Practical application of viscous-flow calculations for the simulation of manoeuvring ships

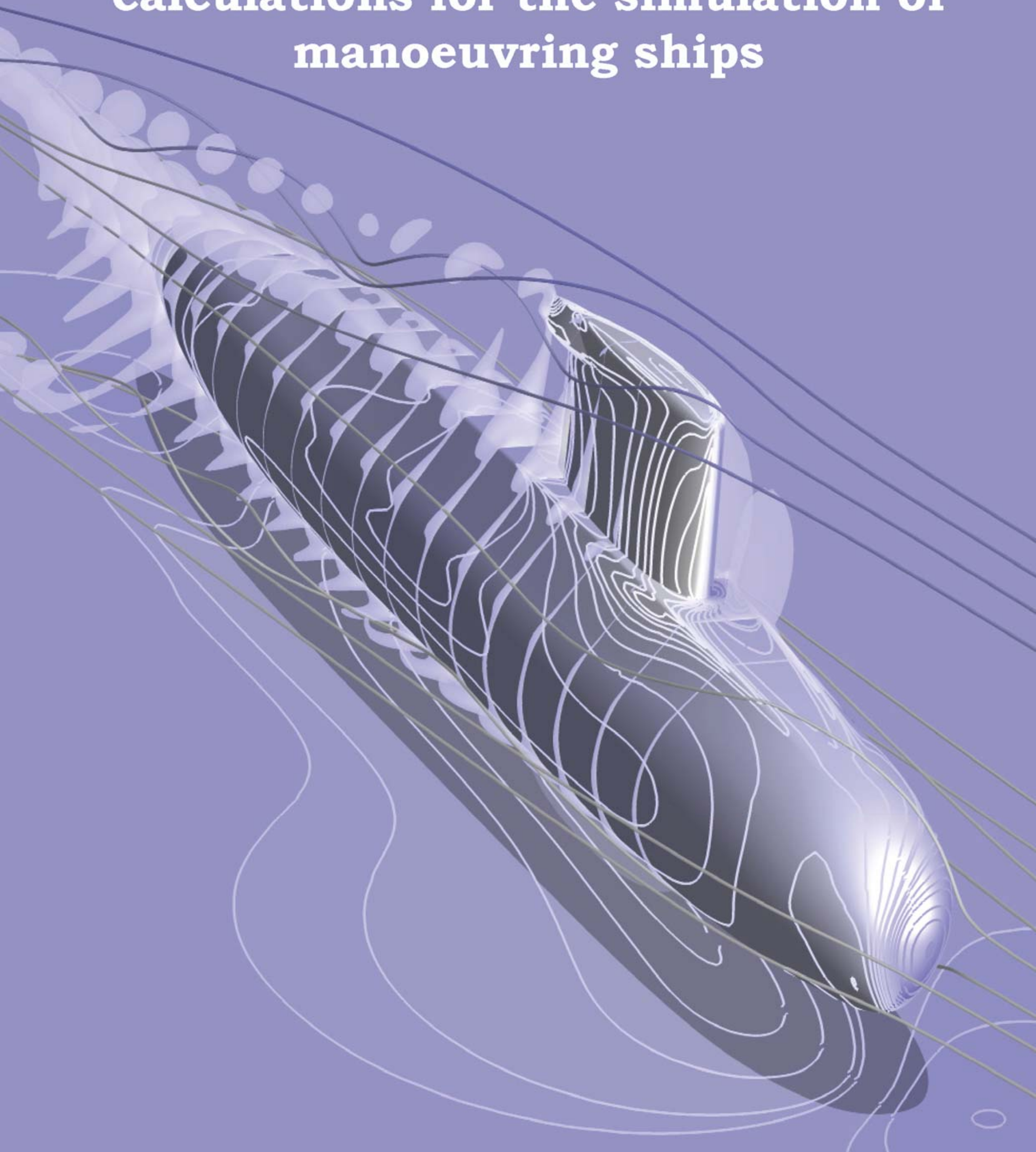

Serge Toxopeus

Practical application of viscous-flow calculations for the simulation of manoeuvring ships

Proofschrift

ter verkrijging van de graad van doctor
aan de Technische Universiteit Delft,
op gezag van de Rector Magnificus prof.ir. K.C.A.M. Luyben,
voorzitter van het College voor Promoties,
in het openbaar te verdedigen op maandag 9 mei 2011 om 15:00 uur

door

Serge Leon TOXOPEUS

Maritiem Ingenieur
geboren te Alkmaar

Dit proefschrift is goedgekeurd door de promotor:

Prof. dr. ir. R.H.M. Huijsmans

Samenstelling promotiecommissie:

Rector Magnificus,	voorzitter
Prof. dr. ir. R.H.M. Huijsmans,	Technische Universiteit Delft, promotor
Prof. dr. ir. M. Vantorre,	Universiteit Gent
Prof. Dr.-Ing. A. Cura Hochbaum,	Technische Universität Berlin
Prof. dr. A.E.P. Veldman,	Rijksuniversiteit Groningen
Prof. B. Pettersen,	Norwegian University of Science and Technology
Prof. ir. J.J. Hopman,	Technische Universiteit Delft
Dr. S.R. Turnock,	University of Southampton
Prof. dr. ir. T.J.C. van Terwisga,	Technische Universiteit Delft, reservelid

Published by the Maritime Research Institute Netherlands (MARIN)
ISBN 978-90-75757-05-7 (print)

Summary

Practical application of viscous-flow calculations for the simulation of manoeuvring ships

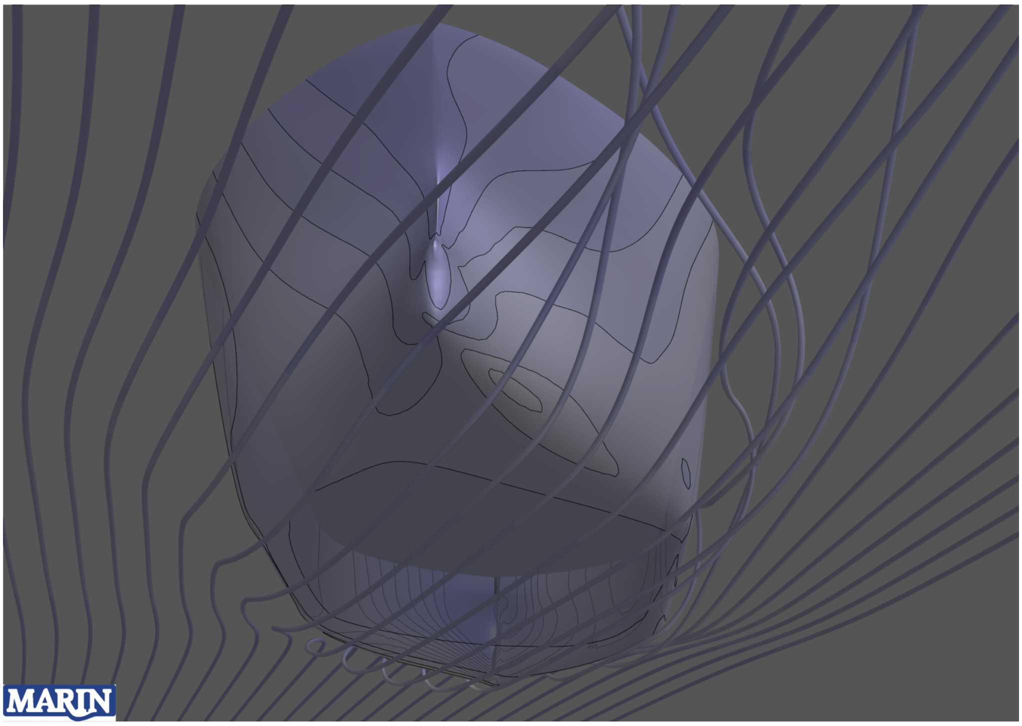

Figure 1: Impression of the flow field and hull surface pressures, KVLCC2, $\beta = -10°$

The present work was initiated in order to improve traditional manoeuvring simulations based on empirical equations to model the forces and moments on the ship. With the evolution of the capability of viscous-flow solvers to predict forces and moments on ships, it was decided to develop a practical method to simulate the manoeuvrability of ships in which viscous-flow solvers are utilised and to investigate whether this improves the accuracy of manoeuvring predictions.

To achieve this goal, the *virtual captive test* approach is adopted, because of the efficient use of computational resources compared to other methods. This procedure mimics the approach for manoeuvring simulations in which experimental PMM is used to obtain the forces and moments on the ship. This study extends the work of other researchers by providing extensive verification and validation of the predicted forces and moments on the hull and a detailed study of the sensitivity of the manoeuvring characteristics of the ship to changes in the hydrodynamic coefficients in the simulation model.

Changes in the flow solvers were required to be able to calculate the flow around ships in rotational motion. These changes are discussed as well as the acceleration techniques that were developed to reduce the effort spent on grid generation and during the computations.

In this thesis, it is demonstrated that good predictions of the loads on the hull in manoeuvring motion can be obtained for a wide range of ship types. The trends in the forces and moments as a function of the drift angle or yaw rate are simulated well.

The verification studies provide useful insight into the influence of grid density on the predicted forces and moments. In several cases, validation of the calculations failed, indicating modelling errors in the numerical results. In these cases, it was generally seen that the magnitude of the transverse force was under-predicted, while the magnitude of the yaw moment was over-predicted. For manoeuvring studies in the early design, the comparison errors are within acceptable levels. However, improvements remain desired and may be obtained using finer grids, larger domain sizes, different grid topologies with refinement in the wake of the ship, other turbulence models or incorporating free surface deformation.

The manoeuvring prediction program SurSim has been used to simulate the manoeuvrability of the HTC. A procedure is proposed to derive the hydrodynamic coefficients required to model the forces and moments on the bare hull. This procedure is chosen to enable accurate modelling of the linearised behaviour for course-keeping as well as realistic modelling of the harbour manoeuvring characteristics, and to enable the modelling of non-linear manoeuvres accurately.

To generate validation data for the manoeuvring predictions presented in this thesis, free sailing manoeuvring tests for the HTC were performed. This test campaign resulted in a very valuable data set which can be used for public validation studies. Besides obtaining general characteristics of the manoeuvrability of a single-screw container ship, unique information has been obtained on the drift angles and rates of turn combined with propeller and rudder forces. Furthermore, repeat tests have been conducted for selected manoeuvres. Based on these tests, the uncertainty in the characteristic manoeuvring properties has been estimated.

By using hydrodynamic manoeuvring coefficients derived from the CFD calculations, it has been shown that it is possible to improve the prediction of ship manoeuvres compared to predictions using coefficients based on empirical equations. A considerable improvement in the turning circle predictions was obtained. The prediction of the yaw checking and course keeping and initial turning abilities based on zig-zag simulations improved as well, but further improvements are required for more reliable assessment of the manoeuvring performance.

The sensitivity of the manoeuvring predictions to changes in the hydrodynamic coefficients was studied. It was found that for accurate predictions of the manoeuvrability using coefficients derived from CFD calculations, accurate predictions of especially the yawing moment must be made.

Contents

Summary **iii**

Review of tables **viii**

Review of figures **x**

List of Symbols **xiii**

Acronyms **xix**

1 Introduction **1**

1.1 Problem definition and objectives 2
1.2 Outline of the thesis 2

2 Background of manoeuvring simulation **5**

2.1 Introduction 5
2.2 Standard mathematical models 8
2.3 Virtual captive tests 9
2.4 RANS coupled to ship motions 10
2.5 Validation cases for captive manoeuvring 12
2.5.1 Series 60 12
2.5.2 DARPA SUBOFF 13
2.5.3 KVLCC1, KVLCC2 and KVLCC2M 14
2.5.4 HTC 17
2.5.5 Other cases 20
2.6 Validation cases for free sailing manoeuvring 21
2.6.1 Esso Osaka 21
2.6.2 KVLCC1, KVLCC2 22
2.6.3 KCS 22
2.6.4 5415M 22
2.7 Conclusion 23

3 **Mathematical model** **25**
3.1 Coordinate system and nomenclature . . . 25
3.2 Manoeuvring simulation program SurSim . . . 26
3.2.1 Introduction . . . 26
3.2.2 Equations of motion . . . 27
3.2.3 Hull forces . . . 27
3.2.4 Propeller forces . . . 29
3.2.5 Rudder forces . . . 30
3.3 Deriving the hydrodynamic coefficients for the user-defined hull forces . . . 34
3.4 Conclusion . . . 35

4 **Viscous flow solvers** **37**
4.1 Background . . . 37
4.2 Parnassos . . . 37
4.3 ReFRESCO . . . 38
4.4 Turbulence closure models . . . 38
4.5 Implementation of rotational motion . . . 38
4.5.1 Background . . . 38
4.5.2 Governing equations . . . 39
4.5.3 Boundary conditions . . . 39
4.6 Grid generation . . . 40
4.6.1 Parnassos . . . 40
4.6.2 ReFRESCO . . . 40
4.7 Boundary conditions . . . 42
4.8 Conclusion . . . 43

5 **Verification and validation of steady motion calculations** **45**
5.1 Introduction to verification and validation . . . 45
5.2 KVLCC1, KVLCC2 and KVLCC2M . . . 47
5.2.1 Iterative error . . . 48
5.2.2 Discretisation error . . . 49
5.2.3 Local quantities . . . 51
5.2.4 Global quantities . . . 51
5.2.5 Validation . . . 53
5.3 HTC . . . 55
5.3.1 Iterative error . . . 55
5.3.2 Discretisation error for steady drift motion . . . 56
5.3.3 Discretisation error for steady yaw motion . . . 62
5.3.4 Local quantities . . . 63
5.3.5 Global quantities . . . 68
5.3.6 Validation . . . 71
5.4 DARPA SUBOFF . . . 73

5.4.1 Iterative error . . . 73
5.4.2 Discretisation error . . . 74
5.4.3 Local quantities . . . 75
5.4.4 Global quantities . . . 79
5.4.5 Validation . . . 82
5.5 Walrus . . . 85
5.5.1 Iterative error . . . 86
5.5.2 Discretisation error . . . 87
5.5.3 Global quantities . . . 87
5.6 Conclusion . . . 91

6 Free sailing manoeuvring tests 93
6.1 Introduction . . . 93
6.2 Ship model . . . 94
6.3 Propulsion and steering system . . . 94
6.4 Experimental facility and measurement system . . . 95
6.5 Data reduction . . . 96
6.6 Test procedures and programme . . . 96
6.7 Uncertainty analysis . . . 98
6.7.1 Introduction . . . 98
6.7.2 Zig-zag tests . . . 98
6.7.3 Turning circle tests . . . 99
6.8 Conclusion . . . 99

7 Simulation of ship manoeuvrability 103
7.1 Introduction . . . 103
7.2 Deriving the hydrodynamic coefficients . . . 104
7.2.1 Resistance curve, wake fraction and thrust deduction fraction . . . 105
7.2.2 Propeller characteristics . . . 105
7.2.3 Rudder forces . . . 106
7.2.4 Hull forces . . . 109
7.3 Standard manoeuvres . . . 112
7.3.1 Programme of simulations . . . 112
7.3.2 RPM-Speed curve . . . 113
7.4 Sensitivity study . . . 113
7.5 Validation . . . 117
7.5.1 Zig-zag manoeuvres . . . 117
7.5.2 Turning circle manoeuvres . . . 119
7.6 Conclusion . . . 119

8 Conclusions and recommendations **123**
8.1 Conclusions . . . 123
8.2 Recommendations . . . 125

References **127**

Samenvatting **143**

Acknowledgements **145**

Curriculum Vitae **147**

Appendices **149**
Table pages . . . 151
Figure pages . . . 177

Review of tables

2.1 Main particulars of Series 60 . . . 13
2.2 Main particulars of DARPA SUBOFF submarine . . . 14
2.3 Main particulars of KVLCC1, KVLCC2 and KVLCC2M . . . 15
2.4 Main particulars of HTC . . . 18
2.5 Main particulars of the HTC propeller . . . 20
2.6 Particulars of the HTC rudder . . . 20

3.1 Symbols used for rudder forces . . . 31

5.1 Properties of grids for different drift angles, KVLCC2M, Parnassos . . . 49
5.2 Properties of grids for uncertainty analysis, KVLCC2M, Parnassos, $\beta = 12°$ . . . 49
5.3 Uncertainty analysis, KVLCC2M, Parnassos, $\beta = 12°$ . . . 50
5.4 Measurement uncertainties and validation, KVLCC2M, Parnassos, $\beta = 12°$ . . . 54
5.5 Properties of grids for different drift angles, HTC, Parnassos, $10\,kn$ . . . 55
5.6 Properties of grids for uncertainty analysis, HTC, $\beta = 10°$, Parnassos . . . 57
5.7 Uncertainty analysis, HTC, $\beta = 10°$, $10\,kn$, Parnassos . . . 57
5.8 Properties of grids for uncertainty analysis, HTC, $18\,kn$, ReFRESCO . . . 59
5.9 Uncertainty analysis, HTC, $\beta = 10°$, $18\,kn$, ReFRESCO . . . 59
5.10 Uncertainty analysis, HTC, $\beta = 30°$, $18\,kn$, ReFRESCO . . . 60
5.11 Properties of grids for uncertainty analysis, HTC, $\gamma = -0.2$, Parnassos . . . 62
5.12 Uncertainty analysis, HTC, $\gamma = -0.2$, $10\,kn$, Parnassos . . . 62
5.13 Uncertainty analysis, HTC, $\gamma = 0.2$, $18\,kn$, ReFRESCO . . . 64
5.14 Uncertainty analysis, HTC, $\gamma = 0.4$, $18\,kn$, ReFRESCO . . . 65
5.15 Validation, HTC, $10\,kn$, Parnassos . . . 72
5.16 Validation, HTC, $18\,kn$, ReFRESCO . . . 72
5.17 Properties of grids for uncertainty analysis, SUBOFF, $\beta = 0°$, $18°$ . . . 74
5.18 Uncertainty analysis, SUBOFF, $\beta = 0°$ . . . 75
5.19 Uncertainty analysis, SUBOFF, $\beta = -18°$ . . . 76
5.20 SUBOFF, longitudinal force X, $Re = 1.4 \times 10^7$, $\beta = 0°$ . . . 81
5.21 SUBOFF, longitudinal force X, $Re = 1.4 \times 10^7$, $\beta = 18°$ . . . 81
5.22 SUBOFF, transverse force Y, $Re = 1.4 \times 10^7$, $\beta = 18°$ . . . 82
5.23 SUBOFF, yawing moment N, $Re = 1.4 \times 10^7$, $\beta = 18°$ . . . 82
5.24 Validation, SUBOFF . . . 83
5.25 Designations and descriptions of Walrus experimental configurations . . . 85
5.26 Uncertainty analysis, Walrus, $\beta = 0°$, $\alpha = 0°$, deep water . . . 87

5.27 Walrus grid refinement study 88

6.1 Experimental uncertainty estimate, zig-zag, 95% confidence interval, all tests . . 100
6.2 Experimental uncertainty estimate, zig-zag, 95% confidence interval, set 1 101
6.3 Experimental uncertainty estimate, turning circle, 95% confidence interval, all tests 101
6.4 Experimental uncertainty estimate, turning circle, 95% confidence interval, set 1 102

7.1 Summary of zig-zag manoeuvre results, original simulations 104
7.2 Summary of turning circle manoeuvre results, original simulations 104
7.3 Propeller No. 5286, open water test No. 45127 106
7.4 Hydrodynamic bare hull and added mass coefficients, HTC 110
7.5 Simulation matrix, HTC 112
7.6 Sensitivity study, HTC, 10 kn 116
7.7 Summary of zig-zag manoeuvre results 117
7.8 Summary of turning circle manoeuvre results 120

Review of figures

1 Impression of the flow field and hull surface pressures, KVLCC2, $\beta = -10°$ . . . iii

2.1 Flow chart of manoeuvring simulations . . . 6
2.2 Body plan of Series 60 . . . 12
2.3 Geometry of DARPA SUBOFF (AFF-1) . . . 14
2.4 Body plans of KVLCC1 and KVLCC2 . . . 15
2.5 Body plans of KVLCC2 and KVLCC2m . . . 16
2.6 Teresa del Mar . . . 17
2.7 Body plan of HTC . . . 19
2.8 HTC model during oblique motion test using CPMC . . . 19
2.9 Drawing of the HTC rudder, T=10.3 m . . . 21

3.1 Ship-fixed coordinate system . . . 25
3.2 Nomenclature and sign convention for rudder forces . . . 30
3.3 The axial actuator disk model . . . 31

4.1 Example grid, Parnassos, HTC, $\gamma = 0.556$ . . . 41
4.2 Example grid, ReFRESCO, HTC . . . 42
4.3 Verification of drift sweep procedure, SUBOFF . . . 43

5.1 Convergence history Y-force, KVLCC2, ReFRESCO . . . 48
5.2 Uncertainty analysis, KVLCC2M, Parnassos, $\beta = 12°$ . . . 51
5.3 Comparison with experiments, KVLCC2M, WAKE1 . . . 52
5.4 Comparison between experiments and calculations, KVLCC hull forms . . . 54
5.5 Convergence history Y-force, HTC, ReFRESCO . . . 56
5.6 Uncertainty analysis, HTC, $\beta = 10°$, 10 kn, Parnassos . . . 58
5.7 Uncertainty analysis, HTC, $\beta = 10°$, 18 kn, ReFRESCO . . . 60
5.8 Uncertainty analysis, HTC, $\beta = 30°$, 18 kn, ReFRESCO . . . 61
5.9 Uncertainty analysis, HTC, $\gamma = -0.2$, 10 kn, Parnassos . . . 63
5.10 Uncertainty analysis, HTC, $\gamma = 0.2$, 18 kn, ReFRESCO . . . 64
5.11 Uncertainty analysis, HTC, $\gamma = 0.4$, 18 kn, ReFRESCO . . . 65
5.12 Comparison between ReFRESCO and Parnassos, HTC, $x = 0.48L_{\mathrm{pp}}$ . . . 66
5.13 Comparison with experiments, HTC, $x = -0.48L_{\mathrm{pp}}$ . . . 67
5.14 Comparison between experiments and calculations, HTC, 18 kn, steady drift . . . 69
5.15 Comparison between experiments and calculations, HTC, 18 kn, steady yaw . . . 70
5.16 Uncertainty analysis, SUBOFF, $\beta = 0°$ . . . 75

5.17 Uncertainty analysis, SUBOFF, $\beta = -18°$ 76
5.18 Pressure (top) and friction (bottom) coefficients along the hull, $\beta = 0°$ 77
5.19 Velocities (top) and Reynolds stresses (bottom) at $x = 0.978L_{\mathrm{oa}}$, $\beta = 0°$ 78
5.20 Pressure (top) and friction (bottom) coefficients along the hull, $\beta = 2°$ 79
5.21 Velocities (top) and Reynolds stresses (bottom) at $x = 0.978L_{\mathrm{oa}}$, $\beta = 2°$ 80
5.22 Comparison between experiments and calculations, SUBOFF, steady drift 84
5.23 Iterative convergence, Walrus, $\beta = 0°$, $\alpha = 0°$ 86
5.24 Convergence history Y-force, Walrus, ReFRESCO 86
5.25 Uncertainty analysis, Walrus, $\beta = 0°$, $\alpha = 0°$, deep water 88
5.26 Comparison between configuration 2 experiments and calculations, Walrus 90

6.1 HTC ship model for free sailing tests 94
6.2 Overview of Seakeeping and Manoeuvring Basin 95
6.3 HTC ship model during free sailing manoeuvring test 97

7.1 Comparison between the original simulations and the free sailing experiments, 18 kn 103
7.2 Estimated resistance curve (model scale values) 105
7.3 Estimated propeller open water curves 106
7.4 Forces on the ship as function of rudder angle, HTC without propeller 107
7.5 Forces on the ship as function of rudder angle and propeller revolutions 108
7.6 Forces on the ship as function of rudder angle, 18 kn, $\beta = -10°$, $n = n_s$ 109
7.7 Forces on the ship as function of rudder angle, 18 kn, $\gamma = 0.4$, $n = n_s$ 110
7.8 Forces on the bare hull as function of yaw rate or drift angle 111
7.9 RPM-Speed relation for HTC, scale 1:30.02, model scale values 113
7.10 Sensitivity study, HTC, zig-zag, 10 kn 114
7.11 Sensitivity study, HTC, turning circle, 10 kn 115
7.12 Comparison between the simulations and the free sailing zig-zag experiments, 10 kn 118
7.13 Comparison between the simulations and the free sailing 20°/20° zig-zag experiments, 18 kn 118
7.14 Comparison between the simulations and the free sailing turning circle experiments, 18 kn 121

8.1 Omstroming en druk op het rompoppervlak, KVLCC2, $\beta = -14°$ 143

List of Symbols

β	drift angle at origin (midship) $(= \arctan \frac{v}{u})$	$[rad]$
β_G	drift angle at centre of gravity $\left(= \arctan \frac{v_G}{u_G}\right)$	$[rad]$
β_{stc}	drift angle during steady turning circle	$[rad]$
δ	(mechanical) rudder angle	$[rad]$
δ_D	error in the experimental value	[various]
δ_{input}	error caused by errors in the input parameter	[various]
δ_{model}	modelling error in the simulated value	[various]
δ_{model}	modelling error	[various]
δ_{req}	required rudder angle	$[rad]$
δ_{SN}	numerical error in the simulated value	[various]
$\dot{\delta}$	rudder turning rate	$[rad/s]$
$\dot{\delta}_{\max}$	maximum rudder turning rate	$[rad/s]$
γ	non-dimensional yaw rate $\left(= \frac{rL_{\mathrm{pp}}}{V}\right)$	$[-]$
Λ	rudder aspect ratio	$[-]$
λ	scale factor	$[-]$
μ	dynamic viscosity $(= \rho\nu)$	$[kg/(sm)]$
∇	displacement volume moulded	$[m^3]$
ν	kinematic viscosity $(= \mu/\rho)$	$[m^2/s]$
$\overline{\Omega}$	vector of rotation	$[rad/s]$
ϕ	roll angle	$[rad]$
ϕ	variable used in verification	[various]
$\overline{\phi}$	arithmetic mean or average of realisations of result ϕ	[various]

ϕ_0	extrapolated value of variable ϕ for infinitely fine grid	[various]
ϕ_1	value of variable ϕ for finest grid	[various]
ϕ_{exact}	exact solution for variable ϕ	[various]
ψ	yaw angle	$[rad]$
ρ	density of the fluid	$[kg/m^3]$
θ	pitch angle	$[rad]$
A_0	propeller disc area	$[m^2]$
A_E	expanded propeller blade area	$[m^2]$
A_R	rudder area	$[m^2]$
B	breadth max. moulded	$[m]$
c	bottom clearance	$[m]$
C_b	block coefficient $\left(= \frac{\nabla}{L_{\text{pp}} B T_m}\right)$	$[-]$
C_f	friction coefficient $\left(= \frac{\vec{\tau}}{\frac{1}{2}\rho V_\infty^2}\right)$	$[-]$
C_p	pressure coefficient $\left(= \frac{p-p_\infty}{\frac{1}{2}\rho V_\infty^2}\right)$	$[-]$
C_{db}	flow straightening factor for drift motion	$[-]$
C_{dr}	flow straightening factor for yaw motion	$[-]$
C_{rue}	propeller-rudder interaction coefficient	$[-]$
D	experimental value	[various]
D_p	propeller diameter	$[m]$
E	comparison error $(= S - D)$	[various]
f_i	force per unit volume	$[N/m^3]$
F_s	safety factor in uncertainty quantification	[-]
Fn	Froude number $\left(= \frac{V}{\sqrt{g L_{\text{pp}}}}\right)$	$[-]$
G	centre of gravity	$[-]$
$\overline{GM}$	metacentric height	$[m]$
h	water depth	$[m]$
J	advance coefficient	$[-]$

K	roll moment around intersection of waterplane/centreplane	$[Nm]$
K_Q	torque coefficient $\left(= \frac{Q_p}{n^2 D_p^5}\right)$	$[-]$
K_T	thrust coefficient $\left(= \frac{T_p}{n^2 D_p^4}\right)$	$[-]$
L_2	root-mean-square of change of variable between iterations	[various]
L_∞	maximum change/value of variable between iterations	[various]
L_{oa}	length overall	$[m]$
L_{pp}	length between perpendiculars	$[m]$
M	pitch moment around intersection of midship/waterplane	$[Nm]$
m	mass	$[kg]$
m_{ij}	added mass/inertia in direction i due to acceleration in direction j	$[kg,\ kgm,\ kgm^2]$
N	yaw moment around intersection of midship/centreplane	$[Nm]$
n	rate of revolution	$[1/s]$
$\overline{n}$	surface normal vector	$[m]$
n_η	number of grid nodes in the normal direction	$[-]$
n_ξ	number of grid nodes in the stream-wise direction	$[-]$
n_ζ	number of grid nodes in the girth-wise direction	$[-]$
N_G	longitudinal force in centre of gravity	$[N]$
n_s	rate of revolution at self propulsion point	$[1/s]$
O	origin of forces and moments	$[-]$
p	apparent order of convergence	$[-]$
p	pressure	$[N/m^2]$
p	roll velocity	$[rad/s]$
p_∞	undisturbed far-field pressure	$[N/m^2]$
$P_{0.7}$	propeller pitch at $0.7R$	$[m]$
q	pitch velocity	$[rad/s]$
Q_p	propeller torque	$[Nm]$
R	radius	$[m]$

R	resistance	$[N]$
r	yaw velocity	$[rad/s]$
$\dot{r}$	yaw acceleration	$[rad/s^2]$
r_{stc}	yaw rate during steady turning circle	$[rad/s]$
Re	Reynolds number $\left(= \frac{V L_{\mathrm{ref}}}{\nu}\right)$	$[-]$
S	simulation value	[various]
s_ϕ	standard deviation of realisations of result q	[various]
S_{wa}	wetted surface area	$[m^2]$
t	thrust deduction fraction	$[-]$
T_a	draught moulded at aft perpendicular	$[m]$
T_f	draught moulded at fore perpendicular	$[m]$
T_m	draught moulded at midship $(= (T_a + T_f)/2)$	$[m]$
T_p	propeller thrust	$[N]$
$t_{\alpha/2}$	Student t-distribution coverage factor	$[-]$
u	longitudinal velocity	$[m/s]$
$\dot{u}$	longitudinal acceleration	$[m/s^2]$
U_ϕ	discretisation uncertainty for variable ϕ	[various]
U_D	uncertainty of the experiment	[various]
U_G	uncertainty due to discretisation error	[various]
U_I	uncertainty due to iterative error	[various]
U_{input}	uncertainty due to possible uncertainties in the input parameters	[various]
U_{val}	validation uncertainty $\left(= \sqrt{U_D^2 + U_{SN}^2 + U_{\mathrm{input}}^2}\right)$	[various]
U_{SN}	numerical uncertainty of the simulation $(= U_I + U_G)$	[various]
V	total velocity $\left(= \sqrt{u^2 + v^2 + w^2}\right)$	$[m/s^2]$
v	transverse velocity	$[m/s]$
$\dot{v}$	transverse acceleration	$[m/s^2]$
V_0	approach speed	$[m/s]$
V_∞	undisturbed far-field velocity	$[m/s]$

V_{stc}	speed during steady turning circle	$[m/s]$
w	vertical velocity	$[m/s]$
w	wake fraction	$[-]$
X	longitudinal force	$[N]$
x	longitudinal position	$[m]$
x_B	position centre of buoyancy forward of midship	$[m]$
x_E	earth-fixed longitudinal position	$[m]$
X_G	longitudinal force in centre of gravity	$[N]$
x_G	position centre of gravity forward of midship	$[m]$
$\overline{x}_R$	centre of rotation	$[m]$
Y	transverse force	$[N]$
y	transverse position	$[m]$
y^+	non-dimensional distance to the wall	$[-]$
y_2^+	non-dimensional wall distance of first cell away from the wall	$[-]$
y_E	earth-fixed transverse position	$[m]$
Y_G	longitudinal force in centre of gravity	$[N]$
Z	number of propeller blades	$[-]$
Z	vertical force	$[N]$
z	vertical position	$[m]$
$\mathrm{res}_{p,\mathrm{max}}$	maximum non-dimensional residual of the pressure	[-]

Page intentionally left blank

Acronyms

AD	Advance. 101, 102, 114
AFF	Anechoic Flow Facility. 13, 14, 73
ANEP	Allied Naval Engineering Publication. 5
APP	Aft Perpendicular Plane. 94
ASME	American Society Of Mechanical Engineers. 46, 47
AVT	Applied Vehicle Technology. 23
CFD	Computational Fluid Dynamics. iv, 7–11, 15–17, 33, 53, 75, 77, 79, 87, 89, 103, 116, 119, 125, 144, 161–175
CMT	Circular Motion Test. 9, 16
CPMC	Computerised Planar Motion Carriage. 9, 95
DARPA	Defense Advanced Research Projects Agency. 13, 73, 75, 91, 145
DES	Detached Eddy Simulation. 11, 13, 17
DMI	Danish Maritime Institute (now FORCE). 22
DMO	Defence Materiel Organisation. 145
DOF	Degrees Of Freedom. 9, 27, 96
GCI	Grid Convergence Index. 47
HSVA	Hamburgische Schiffbau-Versuchanstalt. 17, 18, 38, 66, 105–107, 109, 146
HTC	Hamburg Test Case. iv, 17, 18, 20, 23, 26, 40, 41, 45, 55, 71, 92–94, 99, 102–106, 109, 114, 117, 119, 123, 124, 126, 144–146
IIHR	Iowa Institute of Hydraulic Research. 12
IMO	International Maritime Organization. 1, 5, 7, 104, 117, 119, 120
INSEAN	Istituto Nazionale Per Studi Ed Esperienze Di Architettura Navale. 16, 22, 146
ISO	International Organization for Standardization. 47
IST	Instituto Superior Técnico, Portugal. 145
ITA	Initial Turning Ability. 114, 117
ITTC	International Towing Tank Conference. 21, 85
KCS	KRISO Container Ship. 15, 22
KRISO	Korean Research Institute of Ships and Ocean Engineering. 14
LED	Light-Emitting Diode. 96
LES	Large Eddy Simulation. 13
MARIN	Maritime Research Institute Netherlands. 7, 9, 11, 22, 23, 26, 27, 38, 93–95, 97, 105, 123, 145, 147

MCR	Maximum Continuous Rating. 95
MMG	Mathematical Manoeuvring model Group. 8, 9, 11
MOERI	Maritime & Ocean Engineering Research Institute. 14
MPI	Message Passing Interface. 38
NATO	North Atlantic Treaty Organization. 1, 5, 23
NMRI	National Maritime Research Institute. 51, 146
NNemo	Newport News Experimental Model. 10, 20
NSWCCD	Naval Surface Warfare Center, Carderock Division. 146
osa	Overshoot Angle. 114
PIV	Particle Image Velocimetry. 14, 17, 66
PMM	Planar Motion Mechanism. iii, 6, 7, 9, 10, 16, 17, 143
PS	Port Side. 97, 100–102, 104, 117, 120
QUICK	Quadratic Upwind Interpolation for Convective Kinematics. 74
RANS	Reynolds-Averaged Navier-Stokes. 10, 11, 13, 14, 17, 38, 47, 55, 73, 81, 109, 126
RMS	Root mean square. 46
RNLN	Royal Netherlands Navy. 85, 145
RPM	Revolutions Per Minute. 22, 93, 95–97, 113
RTO	Research and Technology Organisation. 23
SA	Spalart-Allmaras. 73, 76–81
SB	Starboard. 97, 100–102, 104, 117, 120
SHWG	Submarine Hydrodynamics Working Group. 75, 77, 79
SIMPLE	Semi-Implicit Method for Pressure Linked Equations. 38
SMB	Seakeeping and Manoeuvring Basin. 95
SST	Shear Stress Transport. 38, 48, 55, 73, 76–81, 85, 91
STANAG	Standardization Agreement. 5
TD	Tactical Diameter. 101–103, 114
TNT	Turbulent/Non-Turbulent. 38, 73
TUHH	Technische Universität Hamburg-Harburg. 38
UMF	Uncertainty Magnification Factor. 114, 116
V&V	Verification & Validation. 13, 17, 45–47
VIRTUE	VIRtual Tank Utility in Europe. 17, 18, 23, 38, 55, 68, 71, 93, 105, 123, 145, 147
VLCC	Very Large Crude Carrier. 10, 11, 14–17, 22, 23, 47, 48, 51

Chapter 1

Introduction

An increase in ship sizes can be seen in the last decades. One reason for the increase of cargo ships is the improved economy of transporting goods with larger ships. For cruise ships, the increase in size is probably also driven by the need to provide more diverse amusement for passengers and the competition of cruise operators to provide cruises on the largest cruise ship in the world. Furthermore, more and more goods are distributed using ships and therefore an increase of traffic density is observed.

The enlargement of ships and the increased traffic density lead to new challenges in the design of the ship, one of which is the demand for better manoeuvrability. Since large ships must operate in existing harbours, they will experience shallow water effects more severely and the traffic density requires better controllability of the ships. In the past, the interest in improved manoeuvrability has resulted in requirements posed by the International Maritime Organization (IMO), while recently also the North Atlantic Treaty Organization (NATO) started working on manoeuvring criteria for naval ships.

Several methods are available to assess whether a ship's manoeuvrability complies with the requirements. When conducted properly, full scale trials will provide information about ship manoeuvres free of scaling effects or other assumptions. However, due to weather conditions or current, it may be difficult to obtain accurate trial results and when the manoeuvrability is deemed insufficient, modifications to the ship will be extremely expensive. Therefore, assessment of the manoeuvrability is generally made in the design stage, using model tests or simulations. This approach is much less expensive and provides more flexibility in the selection of e.g. the steering arrangements, with the drawback that scale effects will influence the results (model tests) and inaccuracies may be present in the simulations due to improper selection of the mathematical model or hydrodynamic coefficients used.

For training purposes of the crew of ships, or feasibility studies regarding entries of large ships in existing harbours, an increasing demand for full-mission bridge simulations is observed. Furthermore, the manoeuvrability with new propulsors (e.g. pods), or new control strategies or operations (joystick control, dynamic tracking, side-by-side operations) are more and more tried out in simulators before the application in the real ship.

To represent reality as much as possible, the mathematical model of the ship should mimic the response of the ship to rudder or engine commands as well as possible. This also poses new requirements on the accuracy of the mathematical models used in the simulation of ship manoeuvres.

In the last decade, considerable developments have been made in simulation of the viscous-flow around ships in order to predict the flow in manoeuvring conditions and to determine the associated forces and moments. With these developments, the possibility to improve manoeuvring simulations and to partly replace model tests with simulations emerged.

1.1 Problem definition and objectives

The empirical methods used in manoeuvring simulations to predict the hull forces are only reliable when the hull under consideration matches the hulls that were included in the database underlying the empirical formulae, and when the manoeuvring conditions match those as used when the empirical relations were derived. Application outside the range of applicability, e.g. for novel hull concepts, requires alternative methods of predicting the hull forces. For the study which forms the basis of this thesis, the recent developments in viscous-flow calculations provide an attractive means of improving the accuracy of ship manoeuvrability predictions.

The objective of the present work is therefore to develop a practical method to simulate the manoeuvrability of ships in which viscous-flow solvers are utilised to improve the accuracy of the predicted forces and moments on the hull. In this thesis the feasibility of the method is demonstrated.

The method presented here will extend the work of other researchers, see chapter 2, by providing extensive verification and validation of the predicted forces and moments on the hull and a detailed study of the sensitivity of the manoeuvring characteristics of the ship to changes in the hydrodynamic coefficients in the simulation model.

1.2 Outline of the thesis

The outline of this thesis is as follows: first, the background of manoeuvring simulation is presented in chapter 2. An overview of existing mathematical manoeuvring models is given. Then, based on this overview, the so-called *virtual captive tests* approach is selected to predict the forces and moments on a manoeuvring ship. Additionally, test cases available in literature that can be used to validate manoeuvring predictions are summarised.

The fast-time simulation program SurSim will be used to predict the ship manoeuvres. A description of this program is given in chapter 3. A method to derive the hydrodynamic coefficients for the bare hull forces and moments is also proposed. In section 3.1, the coordinate system and nomenclature used in this thesis are presented.

The viscous-flow solvers used for the present study are briefly discussed in chapter 4, together with the grid procedures and boundary conditions used for the current work.

Subsequently, verification and validation of the predicted forces and moments on several different ship hulls in manoeuvring motions will be presented in chapter 5 using validation data available in literature. It is demonstrated that for a wide range of ship types, accurate predictions of the loads on the hull in manoeuvring motion can be obtained.

Free sailing manoeuvring model tests were performed within the context of this thesis to provide detailed validation data for the manoeuvring simulations. The tests and an estimation of the uncertainty in the manoeuvring parameters are discussed in chapter 6.

Coefficients will be derived from these virtual captive tests and will be used in the simulation program SurSim to model the forces on the hull and subsequently simulate standard manoeuvres. The modifications of the mathematical model and the results of the simulations will be presented and discussed in chapter 7.

Finally, conclusions are drawn and recommendations for further work are given in chapter 8.

For descriptions of the symbols and abbreviations used in this thesis, the reader is referred to page xiii and page xix, respectively.

Page intentionally left blank

Chapter 2

Background of manoeuvring simulation

This chapter provides the background of manoeuvring simulations, a review of available standard mathematical manoeuvring models, and gives information regarding the data available in literature that can be used to validate predictions of the forces and moments on a ship in manoeuvring conditions and predictions of ship's manoeuvrability.

2.1 Introduction

Traditionally, ship manoeuvring studies have focused on assessing compliance with the manoeuvring standards set by the IMO [69]. However, due to emerging owner and operational requirements, the need has arisen for assessment of manoeuvring capabilities in operations other than the manoeuvring conditions prescribed by the IMO requirements, see, for example, Quadvlieg and Van Coevorden [111] or Dand [32]. For naval ships, the NATO Specialist Team in Naval Ship Manoeuvrability is developing a Standardization Agreement (STANAG) regarding common manoeuvring capabilities for NATO warships for specific missions. Örnfelt [103] provides an overview of the NATO efforts towards this STANAG. Preliminary criteria have been published in NATO Allied Naval Engineering Publication (ANEP) 70 [96]. In Armaoğlu et al. [8] and Quadvlieg et al. [110], demonstrations are given of the use of prediction tools to verify compliance with the STANAG criteria.

The assessment of the manoeuvrability of ships in the design stage can be done experimentally or numerically, or by combining both. For most engineers, free sailing model tests are generally the preferred option, since they provide immediate insight into the manoeuvring characteristics of the ship and no assumptions are made regarding the hydrodynamics of the model. However, due to scaling of the model, deviations between model scale and full scale manoeuvres may occur. Additionally, free sailing model tests do not give quantitative insight into the forces and moments acting on the hull, which is required when full mission bridge simulator studies, e.g. for training or feasibility studies, are to be conducted.

Furthermore, sometimes different design variants need to be compared before constructing and testing physical models of the ship. In those cases, the use of manoeuvring simulation programs is preferred. However, to obtain reliable simulations, reliable models of the forces and moments acting on the ship are required, since these are needed to calculate the accelerations, velocities and trajectories of the ship during the manoeuvre. A flow chart of manoeuvring simulations is given in Figure 2.1. It is seen that to obtain the forces on the ship, either experimental (mostly Planar Motion Mechanism (PMM)) or numerical (mostly empirical) techniques can be used. These forces are fed into a manoeuvring simulation program in the form of coefficients or tables and with the program the manoeuvring characteristics of the ship can be determined. If needed, modifications to the design can be made in order to ensure compliance with manoeuvring requirements. When the results are found to be satisfactory, the mathematical model can be used in a simulator for e.g. training.

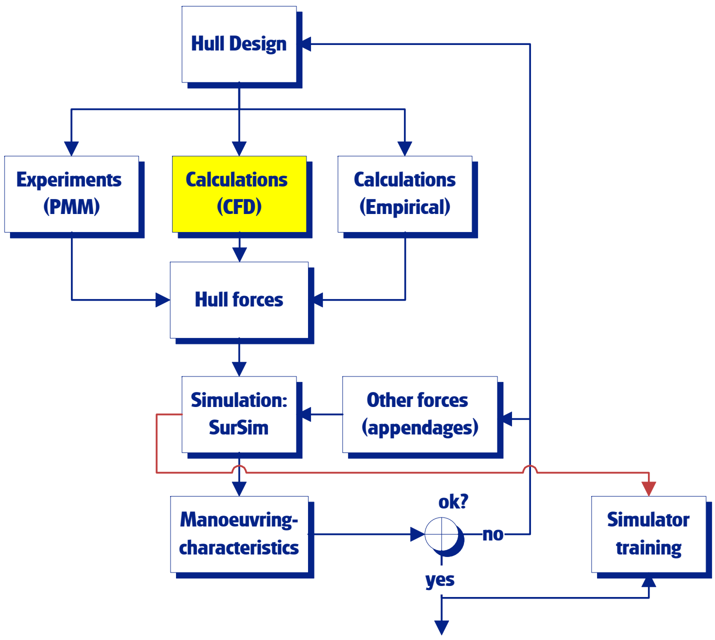

Figure 2.1: Flow chart of manoeuvring simulations

The traditional simulation tools use empirical descriptions of the forces and moments on the ship's hull and are generally based on regression analysis of captive manoeuvring test data for a (preferably wide) range of ships. Due to the lack of resolution of hull details or application outside the range of the regression database, the prediction of the manoeuvrability may be unreliable. On the other hand, empirical simulation tools can provide valuable information regarding the manoeuvring characteristics in a cost-effective way during the early stages of the design.

Other methods to obtain mathematical models of the forces and moments on the ship comprise conducting captive model tests for the ship under consideration, or by conducting a series of free sailing model tests and subsequent system identification. Although these techniques may yield accurate predictions of the manoeuvring characteristics of the ship, the construction of the physical model and the use of the experimental facilities can be costly. Furthermore, the data needs to be analysed and fed into a simulation program, before the actual manoeuvring characteristics of the design can be assessed.

Therefore, new methods are required to obtain reliable and accurate manoeuvring simulation models in a cost-effective manner. Such methods should not only be suitable to predict the yaw checking and turning ability of the ship according to the IMO requirements, but also be applicable to operation in confined waterways or harbour manoeuvring assessment studies, for example.

Recently, viscous-flow calculations provide an attractive means to improve manoeuvring simulations. Two approaches are available to use such calculations in the prediction of the manoeuvring of ships:

virtual captive tests: the forces and moments for a range of forced motions (steady drift, steady rotation, oscillatory sway or yaw, or combinations thereof) are calculated. From the calculations, hydrodynamic coefficients can be derived which are subsequently used in the simulation model to predict the forces and moments. Sometimes, the forces and moments are obtained by interpolation between the data points. This approach resembles the approach taken when using PMM tests and the calculations are therefore referred to as virtual captive tests. This procedure is further discussed in section 2.3.

coupling with body motions: the calculated forces and moments are directly used in the equations of motions to obtain the accelerations, velocities and position of the ship. This procedure is further discussed in section 2.4.

In aerodynamics, similar approaches are used. A thorough overview is given by Salas [120]. In flight dynamics, using the approach of the virtual captive tests is called *flying through the database*, while the coupling with the body motions is called *flying by the equations*. According to Salas, the first method is the easiest to implement, since it relies on existing technology. The second method requires new capabilities, but probably provides more accurate solutions, especially in dynamic conditions.

A concise review of the possible applications of and challenges for Computational Fluid Dynamics (CFD) in aerodynamics is given by McParlin and Tramel [90]. A series of future workshops is proposed in which the applicability of CFD to specific flow phenomena is addressed. Cooperative research efforts are suggested, leading to an understanding of the capabilities of current CFD techniques and to develop best practice guidelines within the context of overall aircraft aerodynamics.

Within Maritime Research Institute Netherlands (MARIN), the method of virtual captive tests is thought to be the most attractive at the moment. The reason for this is that presently the use of viscous-flow calculations coupled with body motions is too computationally intensive. For daily practice the turn-around time of manoeuvring simulations should be in the order of a few days to a week, and in most cases variations of the design have to be considered within this time frame. Furthermore, incorporation of this method in real-time simulators is not yet feasible[1], which means that for simulator studies the method of using virtual captive tests is the only viable solution.

When using existing modular mathematical manoeuvring models, see e.g. section 2.2, it is possible to use the virtual captive tests to improve low-fidelity sub-models and provide manoeuvring advice within a reasonable time frame. For example, when it is expected that the modelling of the propeller or rudder performance in the mathematical model is sufficiently accurate, virtual captive tests need only be conducted for the bare hull. This greatly simplifies the grid generation process and reduces the number of grid points (and thereby computation time) required to arrive at an accurate estimation of the loads on the ship.

2.2 Standard mathematical models

Several standard mathematical models for ship manoeuvrability have been proposed in the past. The models can be divided into integrated models and modular models. Sometimes, the term tabular model is used. In tabular models, expressions for integrated forces/moments or modular components as a function of a given parameter are replaced by look-up tables, see e.g. Eloot and Vantorre [48] and Eloot [47].

The integrated models use single polynomial expressions for each force or moment and are mainly based on series expansions of the forces and moments around an equilibrium condition, see Abkowitz [2]. The model proposed by Norrbin [97] is also an integrated model, but attempts are made to relate the hydrodynamic coefficients in the model to physical phenomena. Tabular or integrated models are very useful for application to a specific ship, but it is difficult to compare the coefficients with those of other ships.

Modular models describe each component of the ship separately: empirical formulations are posed for e.g. the bare hull, propellers and rudders. Most of these models are based on the so-called Mathematical Manoeuvring model Group (MMG) model [98]. The rationale behind the modular models is that this approach will provide the easiest means to incorporate physical background or more complex methods into the modelling of the forces on the ship. For example, while the bare hull forces are generally described using empirical formulae, the rudder forces might be approximated using more advanced predictions such as lifting line or lifting surface methods, without the need to change the modelling of other components in the simulation model[2]. Another advantage is that this approach enables a somewhat easier comparison of the coefficients across different proposed mathematical models.

The first MMG model was proposed by Ogawa and Kasai [98]. Subsequent improvements have been proposed by e.g. Inoue et al. [70] to incorporate changes in loading condition, Lee and Fujino [86] to adapt the model for twin-screw/twin-rudder ships, or

[1]According to Salas [120], real-time CFD simulation will be possible around 2027.
[2]Assuming that errors in one sub-model are not compensated by errors in other sub-models.

Kang and Hasegawa [76] to extend the model to low-speed manoeuvring. For the SIMMAN 2008 workshop [130], several contributions were made in which the MMG model was used to model the manoeuvring of the test case ships.

Other models differing from the MMG model are proposed by e.g. Oltmann [101] and Hooft and Quadvlieg [66]. Both models utilise cross flow drag coefficients (see e.g. Hooft [63]) to model non-linear effects in the forces and moments on the ship. Variations of the model of Hooft and Quadvlieg form the basis of the MARIN in-house manoeuvring simulation programs SurSim, FreSim (see Hooft and Pieffers [65]) and MPP which have been used in submissions for the SIMMAN 2008 workshop [149]. SurSim has been used as a basis for the simulations in this thesis, and is described in detail in section 3.2.

Another attempt to provide a practical but sufficiently accurate, general and physically sound mathematical model was made by Ankudinov and Jakobsen [6]. Guidelines for the development of a standard simulation model are given. More information about manoeuvring models and their applications can be found in Fossen [52] and Eloot [47].

2.3 Virtual captive tests

To obtain the derivatives for a mathematical simulation model, the forces and moments as a function of the flow around the ship need to be obtained. In the past, this was done using captive model tests, but with the evolution of viscous-flow solvers, this can be done numerically as well. In this thesis, the term *virtual captive tests* will be used to designate the simulation of captive tests using viscous-flow solvers. Therefore, virtual captive tests can encompass the simulation of PMM tests, Circular Motion Tests (CMTs) and Computerised Planar Motion Carriage (CPMC) tests, but also steady drift tests.

Although some work on applying viscous-flow solvers to ships in manoeuvring motion was published before, several authors published results concerning surface ships in oblique or rotational motion in the same year, i.e. 1998. Examples are Ohmori et al. [100], Ohmori [99], Alessandrini and Delhommeau [3] and Cura Hochbaum [27]. At this time, the first steps towards simulation of captive tests were made, but complete series of calculations in order to derive coefficients were not yet performed, except by Ohmori. About five years later, Cura Hochbaum and Vogt [29] and Di Mascio et al. [35] presented work regarding their progress towards virtual PMM tests. However, manoeuvring simulations using coefficients derived from the calculations were not yet conducted.

Bellevre et al. [12] study the hydrodynamic derivatives of a submarine. In their calculations, they simulate steady drift and steady rotational motion and determine the rudder effectiveness. With coefficients derived from these results, they simulate 6-Degrees Of Freedom (DOF) manoeuvres and compare the results to experiments and sea trials. Overall, reasonable agreement is found, but restrictions in the number of grid cells that could be used hamper the accuracy of the calculations. Furthermore, improvements of the prediction of the rudder effectiveness were required.

Another example of the application of CFD to actually calculate hydrodynamic coefficients and use these to simulate the manoeuvring behaviour of a ship was presented by Racine and Patterson [112]. For a novel hull form, for which accurate empirical formulae to describe the forces and moments due to manoeuvres were not available, coefficients were derived and the stability and trajectory of the vessel were assessed. The hull form under consideration was the Newport News Experimental Model (NNemo). A sensitivity study was performed to determine the scope of the required calculations and to reduce the size of the CFD matrix. Unfortunately, validation of the simulated behaviour could not be conducted at the time of the study although some of the phenomena found in the simulations were apparently also found during free running model tests.

A detailed study using virtual PMM simulations is presented by Cura Hochbaum [28]. Here, simulations of zig-zag and turning circle manoeuvres are conducted for a twin-screw ferry. The time traces of the PMM simulations are compared to experimental PMM results. Additionally, the coefficients derived from the numerical study are compared to the coefficients derived from the experiments. Finally, the manoeuvre results are compared to the results based on simulations using the experimental hydrodynamic coefficients and to results obtained using free sailing experiments. The validation is encouraging and it is demonstrated that the procedure works well, although some improvements in grid resolution and modelling are proposed.

For the SIMMAN 2008 workshop [130], two participants provided manoeuvring simulations for the KVLCC2 (see section 2.5.3) using coefficients derived from CFD results, i.e. Cura Hochbaum et al. [30] and Toxopeus and Lee [149]. Cura Hochbaum et al. conducted CFD calculations for static drift, oscillatory motion and for rudder deflections to arrive at complete mathematical models for the KVLCC1 and KVLCC2. The agreement of manoeuvring simulations using the mathematical models with the experiments was very promising, especially for the KVLCC2. Toxopeus and Lee calculated the hydrodynamic coefficients using CFD for the bare hull, and used empirical formulae to calculate the forces due to the propeller and rudder. Comparison of the simulated manoeuvres with the free sailing experiments showed that the mathematical model needed to be improved, mainly by extending the range of drift angles and yaw rates used to derive the coefficients.

The present thesis demonstrates a procedure similar to the one used in Toxopeus and Lee [149], but for a different test case and more attention is paid to the correct modelling of the forces and moments on the ship.

2.4 RANS coupled to ship motions

When coupling Reynolds-Averaged Navier-Stokes (RANS) calculations to the ship motions, fewer assumptions about the forces and moments on the ship and its appendages are made, especially when the calculations are performed for the full scale Reynolds number. Although this approach is computationally expensive, progress has been demonstrated in literature. An overview of relevant studies is presented in this section.

Sato et al. [121] conducted a study in which their viscous-flow solver is coupled to the equations motions of the ship. The instantaneous forces on the hull are calculated using CFD, while the forces due to the propeller and rudder are calculated using empirical formulae based on the MMG model. With their model, they perform zig-zag manoeuvres for two Very Large Crude Carrier (VLCC) variants. Comparison with the experiments shows reasonable quantitative agreement.

Pankajakshan et al. [106] apply a coupled procedure to simulate overshoot manoeuvres for the ONR Body-1 submarine model. The control surfaces and rotating propeller are included in the viscous-flow calculations. The propeller is incorporated in the simulation with sliding interfaces. The deflection of the planes is modelled using re-generation of the grid for each deflection angle, based on interpolation between several grids spanning the range of deflection of the control surface. The agreement between the simulated results and the experiments is good.

Jensen et al. [74] show a turning circle simulation for a container ship. The rudder is modelled with sliding interfaces, while the propeller is modelled using body forces. Unfortunately, validation was not performed.

Venkatesan and Clark [160] present simulations for an overshoot manoeuvre for ONR Body-1 (similar to the work by Pankajakshan et al. [106]) and compare the results to experiments. The propeller is modelled using sliding interfaces, while the control surface deflection is modelled using mesh deformation. The agreement is promising, but appears to be slightly less than for Pankajakshan et al.

For the SIMMAN 2008 workshop [130] Carrica and Stern [23] performed Detached Eddy Simulation (DES) of the KVLCC1 performing zig-zag and turning circles with moving propeller and rudder. Overlapping grid techniques are used to model the moving appendages and a level set approach is used to capture the free surface. The simulations were found to be computationally very intensive and could not be finished before the workshop. The results are promising and a good demonstration of the current capabilites of CFD, but some issues remain to be solved. Carrica et al. [22] also conducted free sailing manoeuvring RANS simulations for the 5415M (see section 2.6.4). Also in this case, overlapping grids are used to model the hull, bilge keels, stabiliser fins, shafts, struts and moving rudder and a level set method is used for free surface capturing. The propeller is modelled through the body-force approach, neglecting local velocity effects. The agreement between the simulations and free sailing experiments performed at MARIN [150] was very good, leaving rather limited suggestions for improvements.

Another interesting example of coupling the RANS solution to rigid body motions is given by Bettle et al. [14]. They study the rising stability of a submarine, i.e. the development of the roll angle when a submarine needs to surface quickly. Calculations for full scale Reynolds numbers have been performed. The forces due to the propeller, ballast system and appendages have been incorporated using coefficient based models. The simulations detected the underwater roll instabilities and were consistent with results obtained using fully coefficient-based simulations and with observations during full scale trials. With the CFD results, the main source of the instabilities, i.e. the rolling moment generated by the sail, was identified.

2.5 Validation cases for captive manoeuvring

In literature, several data sets are available that can be used to validate predictions of the forces and moments on a ship in manoeuvring conditions. Some of these test cases also comprise flow field measurements, such that more details about the accuracy of the viscous-flow simulations can be obtained. This section presents some of the available test cases.

2.5.1 Series 60

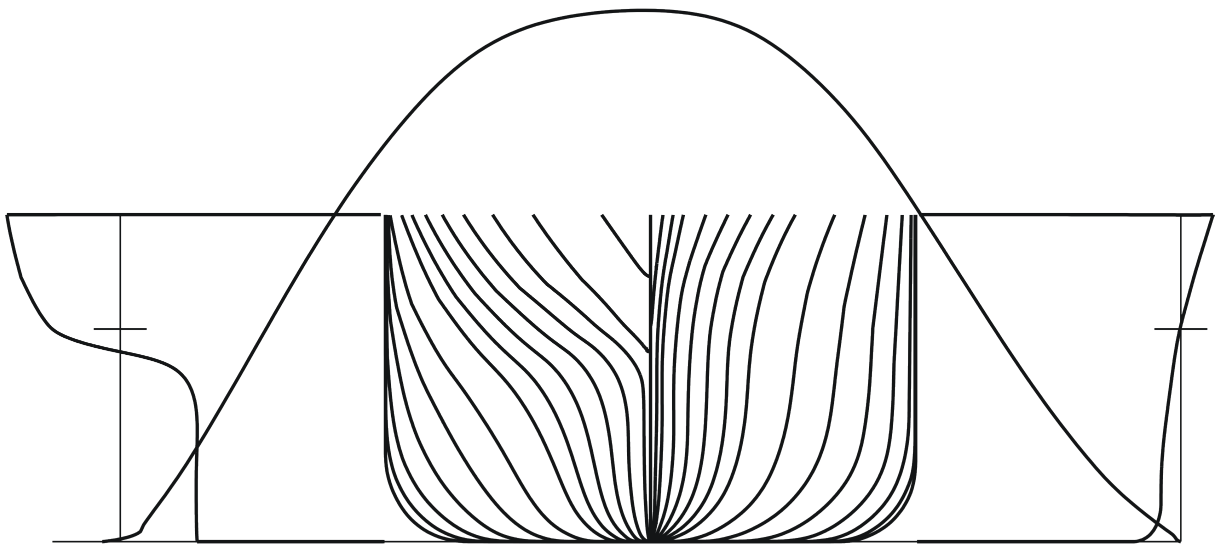

Figure 2.2: Body plan of Series 60

Extensive flow field and force measurements on the well-known Series 60 hull form were conducted at Iowa Institute of Hydraulic Research (IIHR) and the results were made available to the public by Longo [89]. For a range of drift angles and Froude numbers, the forces on the model were measured. Furthermore, wave patterns were measured for a selected set of drift angles and speeds. For a drift angle of 10°, the mean flow was obtained at several longitudinal stations. During the force measurements, the model was free to sink, trim and heel and the displacements were recorded. During all other tests, the model attitude was fixed. The water depth to ship's draught ratio of $h/T_m = 18.7$ represented deep water conditions. The main particulars and body plan of the Series 60 are presented in Table 2.1 and Figure 2.2.

Because of the large amount of data obtained during the measurement campaign, this case is very suitable for validation studies of viscous-flow calculations. Various researchers have already reported such validation studies, such as Alessandrini and Delhommeau [3], Cura Hochbaum [27], Campana et al. [21], Di Mascio and Campana [36], Tahara et al. [140], Toxopeus [141, 142] and Di Mascio et al. [35].

The Series 60 test case is not further considered in this thesis.

Table 2.1: Main particulars of Series 60

Description	Symbol	Magnitude		Unit
		proto	model	
Scale	λ	1:1	1:40	-
Length between perpendiculars	L_{pp}	121.920	3.048	m
Breadth max. moulded	B	16.250	0.406	m
Draught moulded fore	T_f	6.500	0.163	m
Draught moulded aft	T_a	6.500	0.163	m
Displacement volume moulded	∇	7715	0.121	m^3
Wetted surface area bare hull	S_{wa}	2528	1.580	m^2
Position centre of buoyancy forward of midship	x_B	-1.523		$\%L_{pp}$
Block coefficient	C_b	0.600		-
Length-Breadth ratio	L/B	7.503		-
Breadth-Draught ratio	B/T	2.500		-
Length-Draught ratio	L/T	18.757		-

2.5.2 DARPA SUBOFF

For the Defense Advanced Research Projects Agency (DARPA) SUBOFF submarine hull form [57, 88] extensive validation data for flow field variables and integral quantities are available. The test program was initially split into two measurement campaigns. One series was conducted in a wind tunnel (DTRC Anechoic Flow Facility (AFF)), during which the flow field around the aft hull and the pressure and shear stress distributions along the hull length were measured, see Huang et al. [68]. These measurements were conducted at a Reynolds number of $Re = 12 \times 10^6$ and at incidence angles of 0° and 2°. The second series was conducted in a towing basin (DTMB), during which the forces and moments as a function of the flow incidence angle were measured, see Roddy [116]. The towing tank measurements were conducted at a Reynolds number of $Re = 14 \times 10^6$. The main particulars and an impression of the AFF-1 hullform are given in Table 2.2 and Figure 2.3.

In literature, several studies concerning calculations on the bare-hull DARPA SUBOFF (designated Configuration 3 in Roddy [116] and configuration AFF-1 as defined in Liu and Huang [88]) can be found, see e.g. Sung et al. [137, 136, 135], Bull [19], Jonnalagadda et al. [75], Bull and Watson [20] (looking into scale effects), Yang and Löhner [166] (comparisons with the experiments, also for AFF-2), Toxopeus [147] (Verification & Validation (V&V), comparison with the experiments), Toxopeus and Vaz [151] (V&V, comparison with the experiments) and Vaz et al. [158] (V&V, comparison with the experiments, also for AFF-8).

Extensive work on the appended SUBOFF (AFF-8) has been performed by e.g. Alin et al. [4, 5], using Large Eddy Simulation (LES), and comparisons were made with results of DES and RANS calculations. In Fureby [53] an overview is given regarding the application of LES in engineering studies, with application to the SUBOFF, amongst others.

Table 2.2: Main particulars of DARPA SUBOFF submarine

Description	Symbol	Magnitude	Unit
Length overall	L_{oa}	4.356	m
Length between perpendiculars	L_{pp}	4.261	m
Maximum hull radius	R_{max}	0.254	m
Centre of buoyancy (aft of nose)	FB	0.4621 L_{oa}	-
Volume of displacement (AFF-1)	∇	0.708	m^3
Wetted surface (AFF-1)	S_{wa}	5.998	m^2

Figure 2.3: Geometry of DARPA SUBOFF (AFF-1)

Wu et al. [165] conducted studies on the SUBOFF moving close to the sea floor. They found that the bottom effects are proportional to $\frac{B}{c}$, with B the submarine beam and c the clearance between the bottom and the submarine hull. The paper shows that RANS solvers can be used as a practical tool to predict hydrodynamic aspects of submarines.

Etebari et al. [49] present results of a test campaign for the SUBOFF model undergoing a steady turn. Stereo-Particle Image Velocimetry (PIV) was used to obtain the flow field around the model. Pressure measurements at two axial cross sections on the model were conducted and the forces and moments on the model were measured. Three configurations of the SUBOFF were used: the bare hull, the fully appended model and the bare hull with towed-array fairing.

Several series of unsteady measurements using the SUBOFF have been conducted, see e.g. Whitfield [164] or Hosder [67]. Further experiments have been conducted by Granlund and Simpson [56] on the added mass of the SUBOFF (AFF-2). This work has resulted in the thesis by Granlund [55].

2.5.3 KVLCC1, KVLCC2 and KVLCC2M

The KVLCC1 and KVLCC2 (Korean Research Institute of Ships and Ocean Engineering (KRISO)[3] Very Large Crude Carrier) have been subjects of manoeuvrability studies since long. These ships have the same main particulars and bow shape, but slightly different sterns, and should represent typical 300000 t tanker hull forms from around 1997. The KVLCC1 has a fine stern end bulb and the stern frames have more barge type lines, while the stern frames of the KVLCC2 are more U-shaped. During the design of the hull

[3]Now known as Maritime & Ocean Engineering Research Institute (MOERI)

Table 2.3: Main particulars of KVLCC1, KVLCC2 and KVLCC2M

Description	Symbol	Magnitude KVLCC1	KVLCC2	KVLCC2M	Unit
Length between perpendiculars	L_{pp}	320.000	320.000	320.000	m
Breadth max. moulded	B	58.000	58.000	58.000	m
Draught moulded fore	T_f	20.800	20.800	20.800	m
Draught moulded aft	T_a	20.800	20.800	20.800	m
Displacement volume moulded	∇	312631	312635	312650	m^3
Wetted surface area bare hull	S_{wa}	27370	27257	27279	m^2
Position centre of buoyancy forward of midship	x_B	3.494	3.497	3.527	$\%L_{\text{pp}}$
Block coefficient	C_b	0.810	0.810	0.810	-
Length-Breadth ratio	L/B	5.517	5.517	5.517	-
Breadth-Draught ratio	B/T	2.788	2.788	2.788	-
Length-Draught ratio	L/T	15.385	15.385	15.385	-

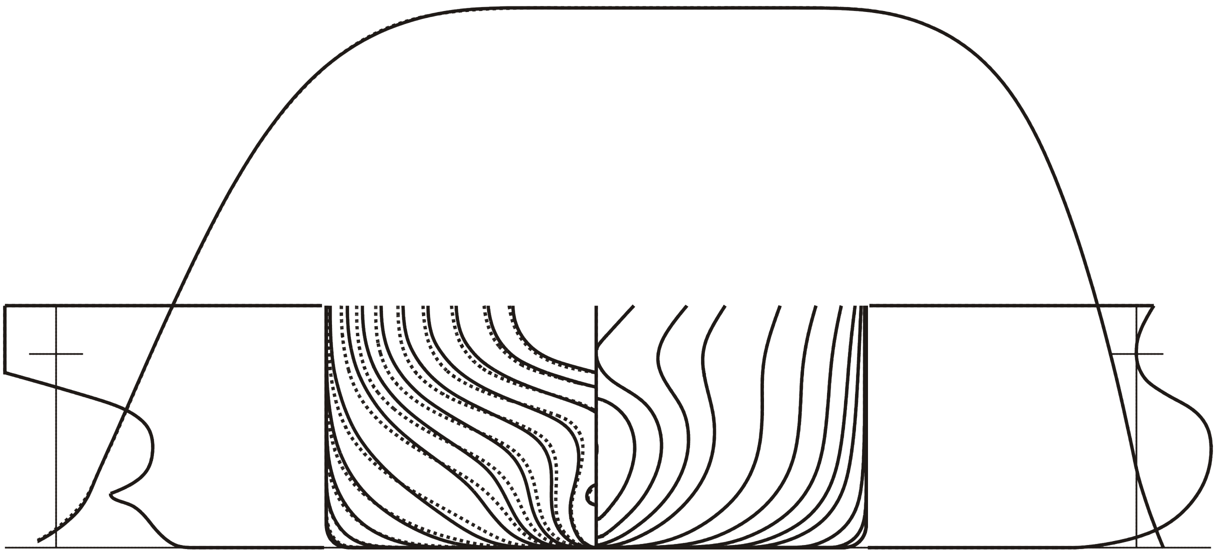

Figure 2.4: Body plans of KVLCC1 and KVLCC2 (dotted: KVLCC1, continuous: KVLCC2)

forms, it was anticipated that the manoeuvrability of these ships would be different. The KVLCC1 and KVLCC2 hull forms were two of the subjects of study during the CFD Workshop Gothenburg 2000 [83] and the SIMMAN 2008 workshop [130]. The KVLCC2 was studied during the CFD Workshop Gothenburg 2010 as well.

Experiments have been conducted by Kim et al. [77]. For the KVLCC1 and KVLCC2 hull forms, they performed wave elevation and flow field measurements around the 1 : 58 scaled ship models. Furthermore, resistance and propulsion tests were conducted. The attitude of the model was fixed, except during the resistance and propulsion tests. During these tests, the trim of the model was modified to arrive at a level running trim during the actual tests. The water depth to ship's draught ratio of $h/T_m = 13.5$ represented deep water conditions. The publication also contains results for the KRISO Container Ship (KCS) (see 2.6.3). Similar flow field measurements have been conducted in a wind

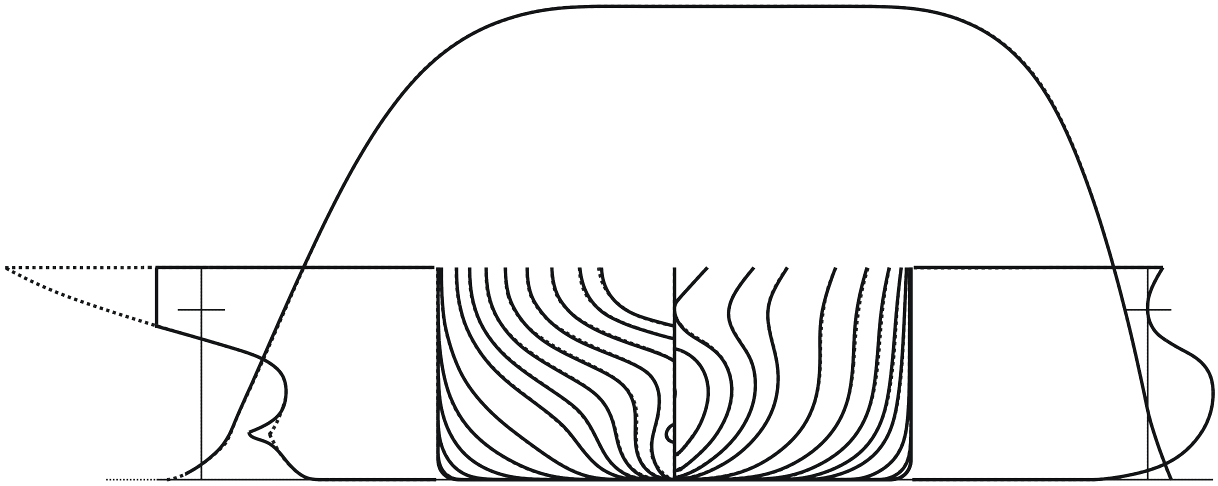

Figure 2.5: Body plans of KVLCC2 and KVLCC2m (dotted: KVLCC2m, continuous: KVLCC2)

tunnel, using double-body models. Tests were only conducted for straight-ahead sailing. The results were published by Lee et al. [85].

Captive model tests for the bare hull KVLCC2 were conducted by Istituto Nazionale Per Studi Ed Esperienze Di Architettura Navale (INSEAN) in preparation for the SIMMAN 2008 Workshop [130], see also Fabbri et al. [50]. A set of PMM tests was performed, comprising amongst others the measurement of the forces and moments for steady drift motion and oscillatory yaw motion. During the tests, the model was free to heave and pitch. The model tests were conducted for deep water (water depth to ship's draught ratio $h/T_m = 8.3$) as well as for restricted water depths using a false bottom: $h/T_m = 1.2$, 1.5 and 3.0. The scale factor was 1 : 45.71.

Additional measurements for the KCS, KVLCC1 and KVLCC2 have been done by Ueno et al. [153]. Using CMT, they obtained the forces and moments on the hull with rudder and propeller as a function of the drift angle and rotation rate. The models were free to trim, sink and heel. For the KVLCCs, the water depth to draught ratio was $h/T_m = 10.6$, representing a deep water condition. The scale factor was 1 : 110.

The KVLCC2M hull form was conceived as a variant of the KVLCC2 but with a slightly modified aft ship to reduce the complexity of the flow and therefore simplify viscous-flow computations. The most visible difference is the fairing of the hull around the propeller shaft position. The KVLCC2M was the main subject of the manoeuvring studies in the CFD Workshop Tokyo 2005 [58]. Model tests for the KVLCC2M have been extensively described by Kume et al. [82]. These tests comprised measurements of forces, surface pressures and stern flow fields for the 1 : 64.4 scaled model at several drift angles. During the tests, the movement of the model with respect to the carriage was fully constrained. The water depth to ship's draught ratio of $h/T_m = 24.8$ represented deep water conditions.

Full scale ships of the KVLCCs do not exist. The main particulars of these ships and body plans are given in Table 2.3, Figure 2.4 and Figure 2.5 respectively.

Several authors have studied the manoeuvrability of these VLCCs, such as the participants of the Tokyo CFD Workshop [58], Toxopeus [143] (KVLCC2M, V&V), Simonsen and Stern [126, 127] (KVLCC2, deep/shallow water, V&V), Broglia et al. [17] (KVLCC2, blockage during PMM), Carrica and Stern [23] (KVLCC1, DES coupled with body motions), Cura Hochbaum et al. [30] (KVLCC1 / KVLCC2, virtual PMM), Toxopeus and Lee [149] (KVLCC2, virtual PMM), Muscari et al. [95] (KVLCC2, RANS coupled with body motions), Stern et al. [132] (KVLCC2, DES at large drift angles) and Phillips et al. [107] (KVLCC2, virtual PMM). More information about the KVLCC results obtained at SIMMAN 2008 can be found in Stern et al. [131].

2.5.4 HTC

Figure 2.6: Teresa del Mar (source: www.shipphotos.es/teresadelmar.htm)

The Hamburg Test Case (HTC) is a model of the container ship built by Bremer Vulkan in 1986 as *Ville de Mercure*, and subsequently named *Teresa del Mar*, see Figure 2.6. *Teresa del Mar* was sold in 2010 and renamed *Maria*. After the *Ville de Mercure* a number of other container ships with the same hull form were built. One of the sister vessels, *Catalina del Mar*, is still sailing.

Captive model experiments were conducted on the HTC within the VIRtual Tank Utility in Europe (VIRTUE) project by Hamburgische Schiffbau-Versuchanstalt (HSVA) in order to provide additional material for CFD validation. These tests comprised force measurements for the bare hull, the hull with rudder and the hull with propeller and rudder. Furthermore, PIV measurements were conducted for the model equipped without rudder, with the model sailing at steady rotational motion. These experiments were reported in VIRTUE deliverable D3.1.3, see Vogt et al. [161]. The scale of the model λ was 1:24 during the HSVA tests. The water depth to ship's draught ratio of $h/T_m = 14$ represented deep water conditions.

The HTC has been studied numerically by several authors, such as Drouet et al. [37], Gao and Vassalos [54] and Toxopeus [144, 145, 148].

Hull form

In Table 2.4, the main particulars of the HTC are presented. Both model scale and full scale (prototype) values are given.

Table 2.4: Main particulars of HTC

Description	Symbol	HTC proto	HTC model		Unit
Scale	λ	1:1	1:24	1:30.02	-
Length between perpendiculars	L_{pp}	153.700	6.404	5.120	m
Breadth max. moulded	B	27.500	1.1458	0.916	m
Draught moulded fore	T_f	10.300	0.4292	0.343	m
Draught moulded aft	T_a	10.300	0.4292	0.343	m
Displacement volume moulded	∇	28342	2.0500	1.048	m^3
Wetted surface area bare hull	S_{wa}	5567	9.6640	6.177	m^2
Position centre of buoyancy forward of midship	x_B	-0.571			$\%L_{pp}$
Block coefficient	C_b	0.650			-
Length-Breadth ratio	L/B	5.582			-
Breadth-Draught ratio	B/T	2.673			-
Length-Draught ratio	L/T	14.922			-

The body plan of the HTC is presented in Figure 2.7. A photograph of the HTC during the model tests at HSVA is presented in Figure 2.8.

The model was tested fixed in all degrees of motion. It was not equipped with bilge keels. For the measurements of the model with rudder, the rudder forces were measured separately. Turbulence was stimulated in all tests. Therefore, in the viscous-flow calculations it was assumed that the flow was fully turbulent.

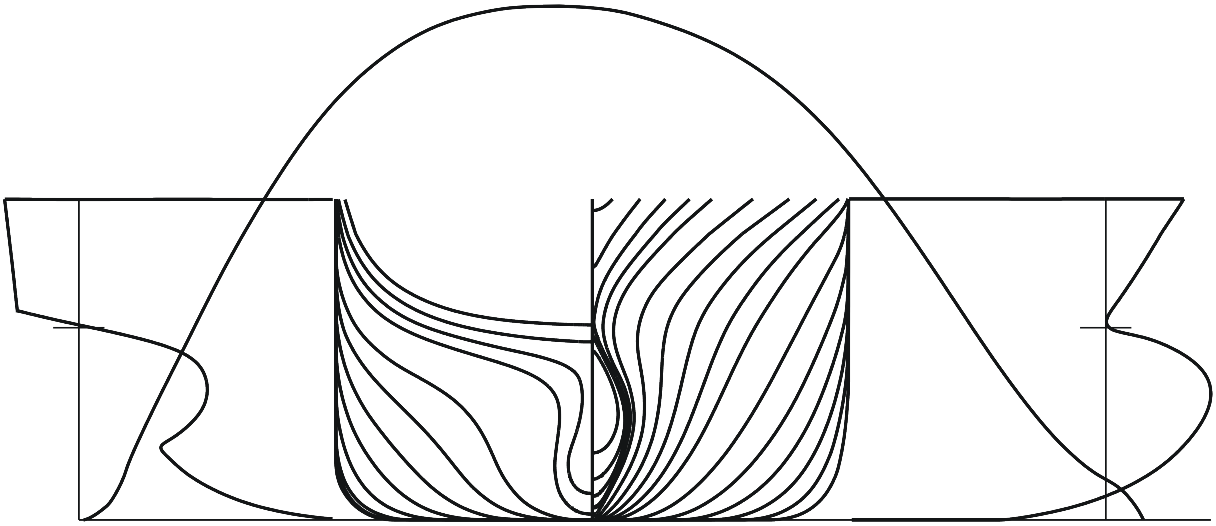

Figure 2.7: Body plan of HTC

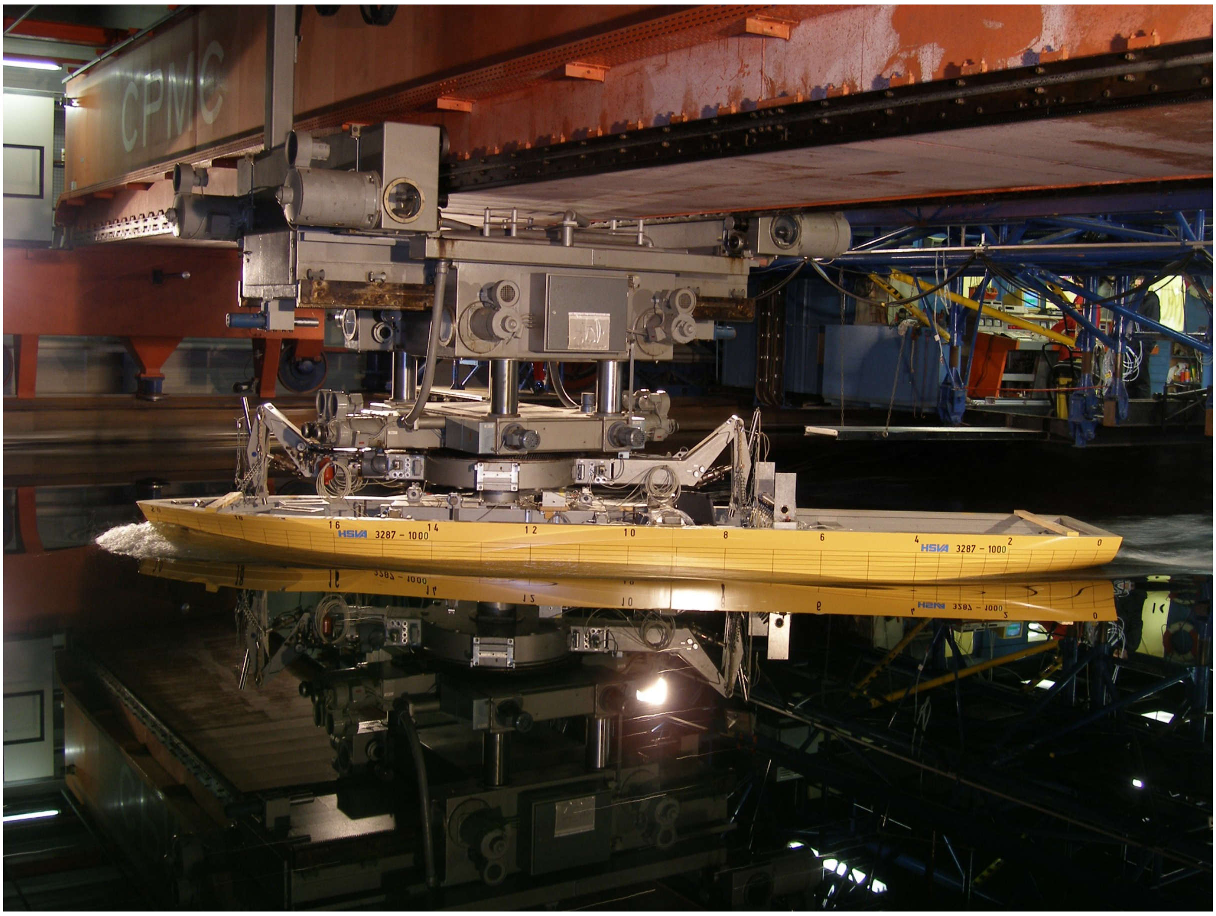

Figure 2.8: HTC model during oblique motion test using CPMC (photograph by HSVA)

Propeller

The particulars of the propellers of the prototype HTC and of the model test propellers (scaled to prototype values) are specified in Table 2.5.

Table 2.5: Main particulars of the HTC propeller

DESIGNATION	SYMBOL	MAGNITUDE			UNIT
		Prototype	Model Scale		
Propeller Id.		-	HSVA 2208	MARIN 5286R	
Diameter	D_p	6.105	6.101	6.100	m
Pitch at $0.7R$	$P_{0.7}$	4.884	4.994	4.642	m
Pitch ratio at $0.7R$	$P_{0.7}/D_p$	0.800	0.818	0.761	-
Expanded blade area ratio	A_E/A_0	0.569	0.580	0.568	-
Number of blades	Z	4	4	4	-
Direction of rotation	-	clockwise when looking ahead			-

Rudder

For the model tests, the rudder was divided into a movable and a fixed (headbox) part in order to allow turning of the rudder without touching the hull surface. The particulars of the rudder and a drawing are presented in Table 2.6 and Figure 2.9.

Table 2.6: Particulars of the HTC rudder

Description	Symbol	Magnitude	Unit
Projected total rudder area	$A_{R,\text{tot}}$	39.76	m^2
Projected movable rudder area	A_R	29.03	m^2
Rudder span	$h_{R,\text{tot}}$	9.20	m
Rudder span of movable part	h_R	7.20	m
Average rudder chord	c_R	4.32	m
Total area ratio	$A_{R,\text{tot}}/L_{\text{pp}}T$	2.51	%
Movable area ratio	$A_R/L_{\text{pp}}T$	1.83	%

2.5.5 Other cases

Other publications presenting data that can be used to validate the forces and moments predicted with viscous-flow calculations for manoeuvring purposes are e.g. the prolate spheroid [24], the NACA 0012 profile (2D case) [1], ONR Body 1 [138, 10], DTMB 5415 [130, 119, 93, 167, 118] and recently the NNemo [112, 33, 117, 55, 108].

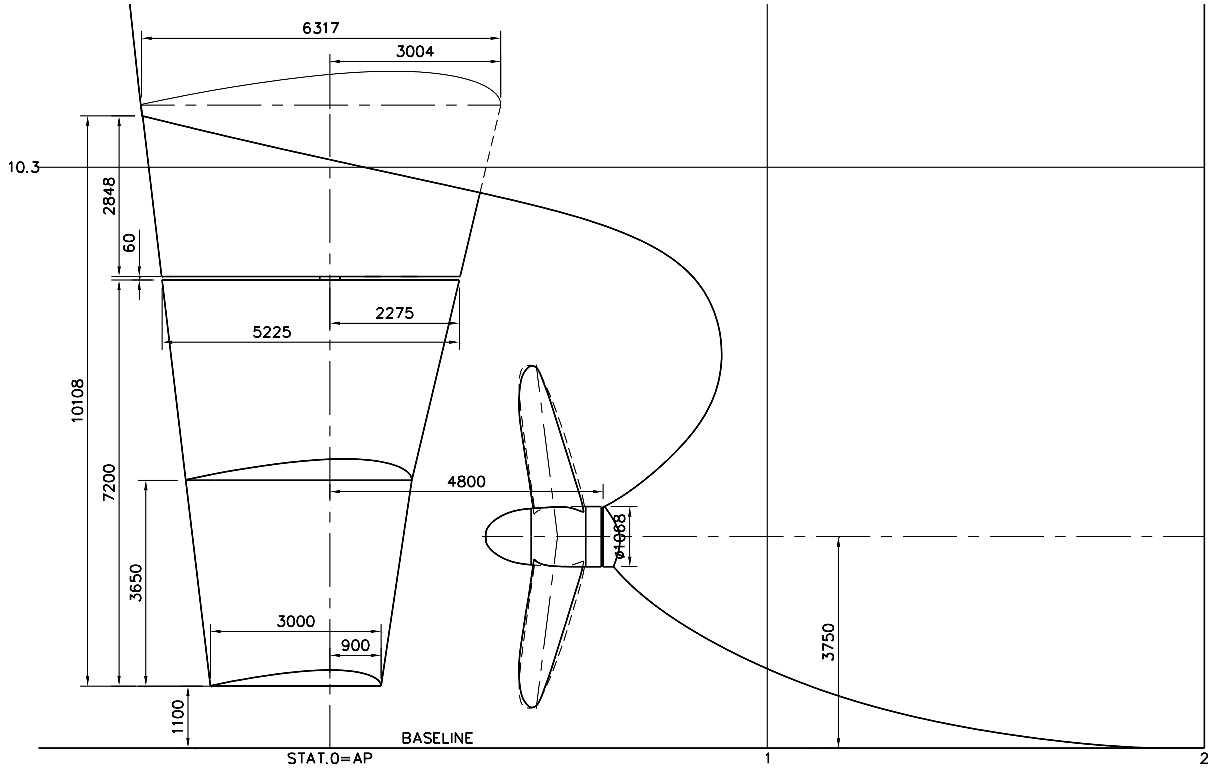

Figure 2.9: Drawing of the HTC rudder, T=10.3 m, dimensions in mm

2.6 Validation cases for free sailing manoeuvring

For validation of the predicted manoeuvres, results from free sailing manoeuvring tests or full scale trials are required. This section presents some of the test cases that are available in literature for which free sailing manoeuvring data is present.

2.6.1 Esso Osaka

The *Esso Osaka* received ample attention due to the existence of well-documented trials in deep and shallow water published by Crane [26], and it was recommended by the 22^{nd} International Towing Tank Conference (ITTC) that this ship was used for validation of force predictions and manoeuvring simulations. However, due to the fact that the hull form is rather outdated and some doubts arose regarding the scatter in the results during analysis of different model test campaigns [25], the interest in this validation case has diminished in the last few years.

Recent studies in which the viscous-flow around the *Esso Osaka* for captive conditions was simulated were published by e.g. El Moctar [46], Simonsen [122], Simonsen and Stern [123, 124, 125] and Van Oers and Toxopeus [155].

2.6.2 KVLCC1, KVLCC2

Information about the hull forms and the captive tests conducted for these KVLCCs is given in section 2.5.3. Free sailing manoeuvring tests, comprising zig-zag and combined turning-circle/pull-out manoeuvres, were conducted at MARIN to supply validation data to the SIMMAN 2008 workshop. The models were manufactured by INSEAN and kindly provided to MARIN for these tests. The tests were reported by Lee [87]. All tests were conducted at model self propulsion point, with constant propeller Revolutions Per Minute (RPM). Several tests were repeated in order to obtain an estimate of the uncertainty in the results. With a model scale of 1 : 45.714, the water depth to ship's draught ratio of $h/T_m = 11$ represented deep water conditions.

2.6.3 KCS

During the SIMMAN 2008 workshop, it was concluded that the existing free sailing manoeuvres with the KCS were not sufficiently accurate to be used as reliable validation data. Therefore, MARIN decided to conduct a new set of free sailing manoeuvres with the KCS. The tests comprised zig-zag and combined turning-circle/pull-out manoeuvres, with variations in $\overline{GM}$ values and for fully loaded and ballast condition, see Overpelt [104]. With a model scale of 1 : 39.89, the water depth to ship's draught ratio of $h/T_m = 17.5$ represented deep water conditions.

2.6.4 5415M

In order to develop new hull form concepts for advanced naval mono-hull ships, a co-operative research programme, called "Thales", was initiated between the Royal Netherlands Navy, the Italian Navy and the Danish Navy. The programme comprised development of design requirements and procedures, determination of assessment procedures and selection of design tools. To be able to select the best design tools, benchmark data were necessary with which design tool data could be compared. Therefore, a model test programme was conducted to generate this data. Model tests were conducted by INSEAN (Italy), DMI (Denmark) and MARIN (The Netherlands). Additional information was obtained from DTMB (USA).

For the model tests, the representative high speed displacement hull form of the US Navy DDG 51 destroyer (in literature often designated DTMB 5415) was selected. This hull form was fitted with a representative twin-propeller / twin-rudder arrangement and centre-line skeg design comparable to European design practice. Furthermore, stabiliser fins were fitted to the model. To distinguish this modified geometry and appendage arrangement to the DTMB 5415, it is designated *5415M*. Standard zig-zag experiments, spiral tests and combined turning circle / pull-out tests were conducted. During these tests, forces on the appendages were measured in order to validate manoeuvring simulation programs in more detail. Several repeat runs for some of the manoeuvres were conducted to assess the uncertainty in the manoeuvring parameters. The tests have been reported by Toxopeus and Lee [150]. With a model scale of 1 : 35.48, the water depth to ship's draught ratio of $h/T_m = 29$ represented deep water conditions.

The 5415M was selected as one of the test cases of the SIMMAN 2008 workshop. The free sailing manoeuvre data are used to validate manoeuvring predictions in Carrica et al. [22], Bhushan et al. [16], and in the SIMMAN 2008 proceedings [130]. Furthermore, the roll decay and seakeeping tests performed with this free sailing model are used as validation data in the NATO Research and Technology Organisation (RTO) Applied Vehicle Technology (AVT)-161 working group.

2.7 Conclusion

Several different methods are given in literature to simulate ship manoeuvres using viscous flow calculations. In this thesis, the *virtual captive test* approach is adopted, since this is at present the most attractive approach when considering the computational costs. Furthermore, this approach can directly be used to improve mathematical models for manoeuvring simulators.

A survey of validation data existing in literature was made. For free sailing manoeuvres as well as for captive tests, data can be found that can be used to validate numerical predictions. Noteworthy is the fact that validation data for captive steady drift motions are much more abundant than validation data for steady rotation or combined motion. Especially for more extreme conditions with large turning rates and drift angles (e.g. non-dimensional turning rates γ of 0.8 - 1.0 and drift angles between 20° and 30°), such as occur during tight turning circles, not much validation data can be found in literature. Furthermore, to the knowledge of the author, cases in which extensive captive test data and free sailing manoeuvring test data are available have only been published for the *Esso Osaka* and the KVLCCs (although the captive tests do not cover the complete range of rotation rates experienced during turning circle manoeuvres). In the work leading up to this thesis, much work was done on simulating the flow around the HTC for captive conditions and simulations of standard free sailing manoeuvres were conducted within the VIRTUE project. To generate validation data for these manoeuvres, MARIN decided to perform free sailing manoeuvring tests for the HTC. Details about these tests will be presented in chapter 6.

The tools used during this study and the procedure to predict the manoeuvrability of the ship are discussed in the following chapters.

Page intentionally left blank

Chapter 3

Mathematical model

The in-house manoeuvring simulation program SurSim will be used to simulate ship manoeuvres within the present study. This chapter presents the system of coordinates adopted in this thesis, details of SurSim and proposes the required steps to derive the hydrodynamic coefficients for the bare hull forces and moments.

3.1 Coordinate system and nomenclature

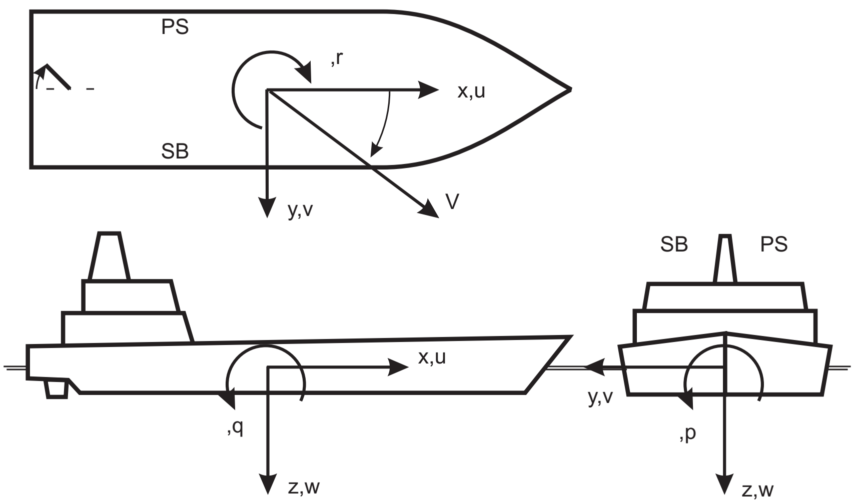

Figure 3.1: Ship-fixed coordinate system

In ship manoeuvring, two reference frames are used. One frame is attached to the ship and is called the ship-fixed coordinate system. The motion of the ship-fixed reference frame is described relative to an earth-fixed inertial reference frame. In the ship-fixed coordinate system, x is directed forward, y to starboard and z vertically down, see Figure 3.1. For captive tests or simulation of captive motions, it is customary to use the intersection of the waterplane, midship and centre-plane as origin O. Therefore, all forces and moments are given with respect to O, with the longitudinal force X directed forward positive and the transverse force Y positive when directed to starboard. A positive drift angle β corresponds to the flow coming from starboard. A positive non-dimensional yaw rate γ corresponds to a turn to starboard when sailing at positive forward speed.

For free sailing manoeuvring tests or simulations, it is however customary to use the centre of gravity G as the origin of the coordinate system. Therefore, the results of all manoeuvres are presented with respect to G. In the results, the drift angle β_G is given relative to the centre of gravity is well.

In the earth-fixed coordinate system, x_E is directed North, while y_E is directed to the East.

All forces and moments are presented non-dimensionally. The longitudinal force X and transverse force Y are made non-dimensional[1] using $\frac{1}{2}\rho V^2 L_{\mathrm{pp}} T$, the vertical force Z using $\frac{1}{2}\rho V^2 L_{\mathrm{pp}} B$, the heeling moment K by $\frac{1}{2}\rho V^2 L_{\mathrm{pp}} T^2$, the pitch moment M by $\frac{1}{2}\rho V^2 L_{\mathrm{pp}}^2 B$ and the yaw moment N by $\frac{1}{2}\rho V^2 L_{\mathrm{pp}}^2 T$. This method of non-dimensionalisation has been applied to all force components presented in this thesis. V is the speed of the ship through the water.

Several subscripts are used to identify separate force components. In this thesis, a subscript H indicates forces on the hull, R forces on the rudder, P forces on the propeller and T total forces. Furthermore, f indicates a force contribution due to friction and p a force contribution due to dynamic pressure (the hydrostatic force component is neglected, since this force is cancelled by the displacement mass when free surface deformation is neglected).

For a complete list of symbols used in this thesis, please refer to page xiii.

3.2 Manoeuvring simulation program SurSim

3.2.1 Introduction

The MARIN in-house developed manoeuvring simulation program SurSim is dedicated to the simulation of the manoeuvrability of mainly twin-screw ferries, cruise ships and motor yachts. Information about SurSim can be found in [149], [66] and [64]. An example of a detailed validation study of SurSim can be found in the SIMMAN proceedings [130].

SurSim is able to predict the heel motion of ships during manoeuvres. Due to the relatively high $\overline{GM}$ value used during the model tests for the HTC, large heel angles during manoeuvres are not expected. To simplify the simulations, it was therefore decided to ignore heel motion for the present study.

SurSim is of the modular type, meaning that the force contributions of the different components of the ship and their interactions (e.g. hull forces, propeller forces and rudder forces) are modelled separately. E.g.:

$$Y_T = Y_H + Y_P + Y_R \tag{3.1}$$

[1]Unless otherwise specified: for submarines forces and moments are generally made non-dimensional using L_{pp}^2 instead of $L_{\mathrm{pp}} T$ as reference area.

in which the subscript T denotes the total forces, H the bare-hull forces, P the propeller forces including hull-propeller interaction and R the rudder forces including hull-propeller-rudder interaction. In this thesis, the results obtained with the bare-hull forces estimated using the original empirical formulae are designated "SurSim". The results with bare-hull coefficients obtained from the viscous-flow calculations will be designated "CFD".

The following sections describe the equations of motions and the different force components. It must be noted that for each force component, user-defined models can also be used.

3.2.2 Equations of motion

Assuming constant added mass coefficients, the equations of motions in three DOF for surge, sway and yaw are (see e.g. Hooft and Nienhuis [64] or the complete derivation in Fossen [52]):

$$\begin{aligned} (m + m_{uu}) \cdot \dot{u} &= m \cdot r \cdot v + X_G \\ (m + m_{vv}) \cdot \dot{v} + m_{vr} \cdot \dot{r} &= -m \cdot r \cdot u + Y_G \\ m_{rv} \cdot \dot{v} + (I_z + m_{rr}) \cdot \dot{r} &= N_G \end{aligned} \tag{3.2}$$

in which $m_{uu} = -X_{\dot{u}}$, $m_{vv} = -Y_{\dot{v}}$, $m_{vr} = -Y_{\dot{r}}$, $m_{rv} = -N_{\dot{v}}$ and $m_{rr} = -N_{\dot{r}}$ are so-called added mass coefficients. The longitudinal force X_G, transverse force Y_G and yaw moment N_G are the excitation and damping forces on the ship, acting in the centre of gravity G.

The yaw moment in the centre of gravity G is obtained by:

$$N_G = N - x_G \cdot Y \tag{3.3}$$

3.2.3 Hull forces

The hull forces are modelled by using the so-called slender-body method to determine the linear manoeuvring derivatives and the cross-flow drag method to determine the non-linear parts of the forces and moments. The linear contributions in these models can be considered to be representative of the lift generated on the hull while the non-linear ones represent the drag. The following paragraphs describe the various components of the hull forces.

Ship resistance

The straight ahead sailing resistance curve of the hull must be given as input to the program. For this, the MARIN in-house program DESP can be used, which is based on an improved version of the method of Holtrop and Mennen [62]. The resistance should be predicted for the appropriate Reynolds numbers, in order to be able to compare the simulation results directly with full scale trials or with model experiments.

Slender body method

The slender-body method is a semi-empirical method to determine the linear force components on the hull. According to this method, the linear manoeuvring coefficients are determined by the rate of change of fluid momentum along the length of the ship. Only a few empirical parameters based on careful validation with experiments are used. Since this method utilises the full description of the hull form, the influence of changes in local details of the hull can be investigated in the early design stage within a short time frame (i.e. a few minutes when the hull form input has been prepared). A more detailed description of the slender-body method can be found in e.g. Toxopeus [145].

Cross-flow drag method

The non-linear contributions to the forces and moments are calculated using e.g. the so-called cross-flow drag theory, presented by e.g. Hooft and Quadvlieg [66] or Hooft [63].

User-defined hull forces

In SurSim, it is possible to override the hull forces by using a user-defined mathematical model. This option has been used to introduce the hydrodynamic coefficients obtained from the viscous-flow calculations into the simulations.

When setting up a mathematical model to describe the forces on a ship due to manoeuvring motion, the intended use of the model determines the structure of the model itself. E.g. when simulator studies incorporating harbour manoeuvres are to be conducted, the model should be able to accurately describe the forces and moments on the ship during transverse motions, turning-on-the-spot and sailing astern. In the present work, it is assumed that the manoeuvring model should be valid for a wide range of applications, including low speed and harbour manoeuvres.

In general, mathematical manoeuvring models for the bare hull consist of three different components: (added) mass coefficients, damping coefficients and spring coefficients. In earlier work by Vassalos et al. [156], Ishiguro et al. [71] and Lee and Shin [84], for example, or more recently, Bulian et al. [18] it was found that the sensitivity of the manoeuvrability to changes in the added mass coefficients is small. Therefore, it is assumed that the added mass coefficients can be approximated reliably by using the empiric formulae existing in SurSim. Due to this assumption, no calculations are required to obtain the added mass coefficients. When only horizontal manoeuvres are considered and neglecting the heel angle, spring coefficients do not have to be taken into account.

The following non-dimensionalised mathematical model for the longitudinal force X, transverse force Y and yawing moment N is adopted:

$$X' = X'_{u'|u'|} \cdot \cos\beta \cdot |\cos\beta| + X'_{\beta\gamma} \cdot \sin\beta \cdot \gamma \tag{3.4}$$

$$Y' = Y'_{\beta} \cdot |\cos\beta| \cdot \sin\beta + Y'_{\gamma} \cdot \cos\beta \cdot \gamma + Y'_{\beta|\beta|} \cdot \sin\beta \cdot |\sin\beta| + Y'_{\gamma|\gamma|} \cdot \gamma \cdot |\gamma|$$

$$+ Y'_{\beta|\gamma|} \cdot \sin\beta\,|\gamma| + Y'_{|\beta|\gamma} \cdot |\sin\beta|\,\gamma + Y'_{ab} \cdot \left|\cos^{a_y}\beta \cdot \sin^{b_y}\beta\right| \cdot \operatorname{sign}\sin\beta \tag{3.5}$$

$$\begin{aligned} N' = {} & N'_{\beta} \cdot \cos\beta \cdot \sin\beta + N'_{\gamma} \cdot |\cos\beta| \cdot \gamma + N'_{u'\gamma c} \cdot |\cos\beta \cdot \gamma^{c_n}| \cdot \operatorname{sign}\gamma \\ & + N'_{\gamma|\gamma|} \cdot \gamma \cdot |\gamma| + N'_{\beta|\beta|} \cdot \sin\beta \cdot |\sin\beta| \\ & + N'_{\beta\beta\gamma} \cdot \sin^2\beta \cdot \gamma + N'_{\beta\gamma\gamma} \cdot \sin\beta \cdot \gamma^2 \cdot \operatorname{sign}\cos\beta \\ & + N'_{ab} \cdot \left|\cos^{a_n}\beta \cdot \sin^{b_n}\beta\right| \cdot \operatorname{sign}(\cos\beta \cdot \sin\beta) \end{aligned} \tag{3.6}$$

The coefficients Y'_{ab} and N'_{ab} are used to describe the relation between the transverse force and yawing moment for drift angles β in the range of approximately $30° < \beta < 60°$. Similarly, $N'_{u'\gamma c}$ describes the relation between the yaw moment and intermediate yaw rates γ. The integer values a_y, b_y, a_n, b_n and c_n should be adapted to match the correct order of the relationship. It should be noted that the orders should not be chosen too high (i.e. 3 or below), to avoid unexpected behaviour at large drift angles.

At zero speed, the non-dimensional yaw rate γ and subsequently the non-dimensional $N'_{\gamma|\gamma|}$ contribution will become infinite and therefore due care has to be taken when implementing this mathematical model in a simulation program. This can be solved by using the $N'_{\gamma|\gamma|}$ term in a fully dimensional form.

3.2.4 Propeller forces

The propeller forces are estimated using information from Strom-Tejsen [134], or on the Wageningen B-Series descriptions, see Oosterveld and Van Oossanen [102]. Alternatively, it is possible to select a user-defined model for the propeller forces. In this case, the thrust T_p and torque Q_p of the propeller with diameter D_p and rotation rate n are obtained as follows (subscript p indicates that a variable applies to the propeller):

$$u_p = u \cdot (1 - w) \tag{3.7}$$

$$J = \frac{u_p}{n \cdot D_p} \tag{3.8}$$

$$K_T = K_{T0} + K_{T1} \cdot J + K_{T2} \cdot J^2 + K_{T3} \cdot J^3 + K_{T4} \cdot J^4 + K_{T5} \cdot J^5 \tag{3.9}$$

$$K_Q = K_{Q0} + K_{Q1} \cdot J + K_{Q2} \cdot J^2 + K_{Q3} \cdot J^3 + K_{Q4} \cdot J^4 + K_{Q5} \cdot J^5 \tag{3.10}$$

$$T_p = K_T \cdot \rho n^2 D_p^4 \tag{3.11}$$

$$Q_p = K_Q \cdot \rho n^2 D_p^5 \tag{3.12}$$

The coefficients K_{Ti} and K_{Qi} in equations (3.9) and (3.10) are to be specified by the user and can be obtained from propeller open-water tests. It should be noted that this user-defined model is not valid for four-quadrant manoeuvre simulations. Based on the formulae above, the longitudinal force on the ship due to the propeller is given by:

$$X_P = (1 - t) \cdot T_p \tag{3.13}$$

The transverse force Y_P which is generated by a propeller rotating in an asymmetrical wake is relatively small and difficult to describe by simple empirical equations. Therefore this force and the related yawing moment are set to zero: $Y_P = 0$ and $N_P = 0$.

3.2.5 Rudder forces

To model the rudder forces, formulae based on publications by e.g. Whicker and Fehlner [163] (rudders in open water), Inoue [70] (rudders behind ships) and Söding [128] (more theoretically based) are used. In SurSim, the nomenclature and sign convention as presented in Figure 3.2 is used. An explanation of the used symbols is given in Table 3.1. A subscript r indicates that a variable applies to the rudder. In this section, the calculation of the rudder forces is presented. However, for simplicity, some details such as heel effects and the angle between the rudder and the vertical axis have not been taken into account in the formulae in this thesis, although they are modelled in SurSim.

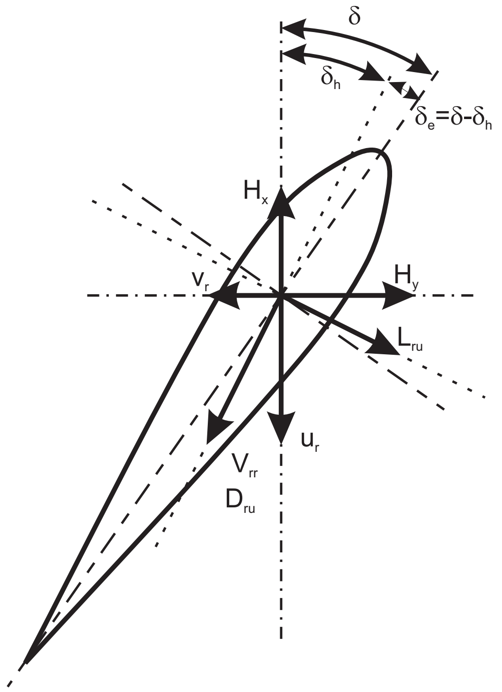

Figure 3.2: Nomenclature and sign convention for rudder forces

One of the most complicated aspects in determining the rudder forces is the determination of the flow velocity and direction at the rudder location as a consequence of the drift angle, yaw rate and propeller action. Therefore, the formulae describing the flow velocity are discussed first. To calculate the longitudinal velocity as a function of the propeller loading, some basic formulae are required. The full analysis can be found in e.g. Kuiper [81], but the basic principles are stated here to demonstrate the physics and to modify the formulae for four-quadrant manoeuvres. A cross section of the flow to be described is given in Figure 3.3.

Table 3.1: Symbols used for rudder forces

Symbol	Description	Unit
δ	(Mechanical) rudder angle	$[rad]$
δ_h	Hydrodynamic inflow angle at rudder stock	$[rad]$
δ_e	Effective inflow angle with respect to the rudder $= \delta - \delta_h$	$[rad]$
x_r	Longitudinal position of rudder	$[m]$
u_r	Longitudinal inflow velocity at rudder stock	$[m/s]$
v_r	Transverse inflow velocity at rudder stock	$[m/s]$
V_{rr}	Rudder inflow velocity $= \sqrt{u_r^2 + v_r^2}$	$[m/s]$
L_{ru}	Rudder lift force	$[N]$
D_{ru}	Rudder drag force	$[N]$
H_x	Ship-fixed longitudinal component of rudder force	$[N]$
H_y	Ship-fixed transverse component of rudder force	$[N]$
A_R	Rudder area	$[m^2]$
Λ	Rudder aspect ratio	$[-]$

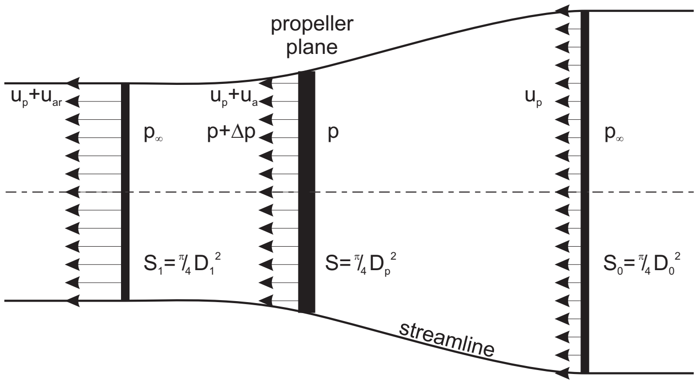

Figure 3.3: The axial actuator disk model

Ahead speed with positive thrust Using axial momentum theory while assuming inviscid and incompressible flow, the first relation is derived using the conservation of mass:

$$u_p \cdot \frac{\pi}{4} D_0^2 = (u_p + u_a) \cdot \frac{\pi}{4} D_p^2 = (u_p + u_{ar}) \cdot \frac{\pi}{4} D_1^2 \tag{3.14}$$

Conservation of momentum leads to:

$$\rho u_p^2 \cdot \frac{\pi}{4} D_0^2 - \rho \left(u_p + u_{ar}\right)^2 \cdot \frac{\pi}{4} D_1^2 + T_p = 0 \tag{3.15}$$

Combining these two relations leads to the following equation for the propeller thrust:

$$T_p = \frac{\pi}{4} D_p^2 \cdot \rho \left(u_p + u_a\right) \cdot u_{ar} \tag{3.16}$$

Applying Bernoulli's law respectively in front and aft of the propeller disc, two additional equations are found:

$$p_\infty + \frac{1}{2} \rho u_p^2 = p + \frac{1}{2} \rho \left(u_p + u_a\right)^2 \tag{3.17}$$

$$p_\infty + \frac{1}{2}\rho\left(u_p + u_{ar}\right)^2 = p + \Delta p + \frac{1}{2}\rho\left(u_p + u_a\right)^2 \tag{3.18}$$

Subtracting equations (3.18) from (3.17) and using $T_p = \Delta p \cdot \frac{\pi}{4} D_p^2$, the propeller thrust is found to be:

$$T_p = \frac{\pi}{4} D_p^2 \cdot \rho\left(u_p + \frac{1}{2}u_{ar}\right) \cdot u_{ar} \tag{3.19}$$

such that $u_{ar} = 2 \cdot u_a$, following from equation (3.16).

Solving equation (3.19) for u_{ar} results in:

$$T_p - \frac{\pi}{4} D_p^2 \cdot \rho u_p \cdot u_{ar} - \frac{\pi}{8} D_p^2 \cdot \rho u_{ar}^2 = 0 \quad \Rightarrow \quad u_{ar} = -u_p \pm \sqrt{u_p^2 + \frac{8T_p}{\rho \pi D_p^2}} \tag{3.20}$$

For positive inflow velocity u_p at the propeller and positive thrust of the propeller, the axial induced velocity u_{ar} is larger than zero. Therefore, equation (3.20) reduces to:

$$u_{ar} = \sqrt{u_p^2 + \frac{8T_p}{\rho \pi D_p^2}} - u_p \tag{3.21}$$

Ahead speed with negative thrust When the forward speed u_p is positive but T_p is negative and assuming that $u_r = u_p + u_{ar} > 0$ (we still do not have flow reversal), equation (3.21) is valid with the additional requirement that $u_{ar} > -u_p$, resulting in:

$$\frac{8T_p}{\rho \pi D_p^2} > -u_p^2 \tag{3.22}$$

If the thrust becomes too negative, we get flow reversal due to the propeller action. In this case, it is assumed that the flow velocity u_r at the rudder becomes zero. This can be obtained by modifying equation (3.21), such that it reads for all conditions with positive ahead speed $u_p \geq 0$:

$$u_{ar} = \sqrt{\max\left(u_p^2 + \frac{8T_p}{\rho \pi D_p^2}, 0\right)} - u_p \tag{3.23}$$

Astern speed with negative thrust For astern speed and negative thrust, it is assumed that there is no induced velocity from the propeller at the rudder location. In that case, the change in axial velocity at the rudder becomes:

$$u_{ar} = 0 \tag{3.24}$$

Astern speed with positive thrust For astern speed but with positive thrust, it is assumed that the inflow velocity at the propeller position u_p equals zero. This results in an axial induced velocity behind the propeller which depends on the propeller thrust and the local undisturbed velocity u_0. The induced velocity is approximated using:

$$u_0 = u \cdot (1 - w_p) \tag{3.25}$$

$$u_{ar} = \max\left(\sqrt{\frac{8T_p}{\rho\pi D_p^2}} + u_0, 0\right) \tag{3.26}$$

and the velocity at the rudder position is calculated with:

$$u_r = u_0 + u_{ar} \tag{3.27}$$

Effective interaction between propeller slipstream and rudder In general, the propeller slipstream at the rudder location will not completely cover the rudder. Furthermore, the slipstream contraction as used in the actuator disc theory presented above will not have fully developed yet at the rudder location. Therefore, corrections to the induced velocity at the rudder need to be made to arrive at the effective induced velocity. This results in the following empirical prediction of the velocity at the rudder location:

$$u_r = u_p + C_{rue} \cdot u_{ar} \tag{3.28}$$

Flow straightening Due to the drift angle of the ship and the rotation rate during manoeuvres, the rudder will also experience a transverse velocity component v_r. However, due to the presence of the ship, the undisturbed flow will be rectified or straightened. Therefore, the flow-straightening coefficients C_{db} for the drift angle and C_{dr} for the yaw rate are introduced:

$$v_r = C_{db} \cdot v + C_{dr} \cdot x_r \cdot r \tag{3.29}$$

It must be noted that with this linear equation the effect of the hull on the flow is strongly simplified (see e.g. Ogawa and Kasai [98]). It can be argued that, for a ship in manoeuvring motion, vortices that are generated upstream may travel to the rudder position, resulting in irregular inflow velocities and flow directions. This effect can be studied using dedicated model tests or with CFD calculations, but is considered to be outside the scope of the present study.

Rudder forces First the lift and drag coefficients are determined, see eq. (10) in [98]:

$$C_L = \frac{6.13 \cdot \Lambda}{2.25 + \Lambda} \tag{3.30}$$

$$C_D = \frac{C_L^2}{\pi \cdot \Lambda} \tag{3.31}$$

The hydrodynamic rudder angle describes the angle between the flow velocity at the rudder position and the ship's longitudinal axis and follows from:

$$\delta_h = \arctan\frac{v_r}{u_r} \tag{3.32}$$

while the velocity at the rudder is calculated with:

$$V_{rr} = \sqrt{u_r^2 + v_r^2} \tag{3.33}$$

The lift and drag on the rudder are calculated using:

$$L_{ru} = \frac{1}{2}\rho V_{rr}^2 A_R \cdot C_L \cdot \cos\delta_e \cdot \sin\delta_e \tag{3.34}$$

$$D_{ru} = \frac{1}{2}\rho V_{rr}^2 A_R \cdot C_D \cdot \sin^2\delta_e \tag{3.35}$$

This results in the longitudinal and transverse forces and the yawing moment on the ship due to the rudder:

$$X_R = H_X = -D_{ru} \cdot \cos\delta_h - L_{ru} \cdot \sin\delta_h \tag{3.36}$$

$$Y_R = H_Y = (1 + a_H) \cdot (L_{ru} \cdot \cos\delta_h - D_{ru} \cdot \sin\delta_h) \tag{3.37}$$

$$N_R = Y_R \cdot x_r - X_R \cdot y_r \tag{3.38}$$

The coefficients C_{rue}, C_{db}, C_{dr} and a_H are ship-dependent coefficients, see section 7.2.

Rudder angle The rudder angle is determined by the required rudder angle δ_{req} and the actual rudder angle δ, mimicking a simplified steering machine. The required rudder angle is set depending on the type of manoeuvre (e.g. auto-pilot, zig-zag, turning-circle). To obtain the actual rudder angle for a new time step, the difference between the required rudder angle and the actual rudder angle at the current time step is determined first:

$$\Delta\delta = \delta_{\text{req}} - \delta \tag{3.39}$$

When $|\Delta\delta|$ is less than a certain threshold (e.g. 3°), then the rudder rate is calculated by:

$$\dot{\delta} = C_r \cdot \Delta\delta \tag{3.40}$$

with C_r a rudder rate constant obtained from $C_r = \dot{\delta}_{max}/3$. For $|\Delta\delta|$ above the threshold, the rudder rate is given by:

$$\dot{\delta} = \dot{\delta}_{\text{max}} \cdot \text{sign}\Delta\delta \tag{3.41}$$

The actual rudder angle at the new time step is obtained by integrating the rudder rate in time.

3.3 Deriving the hydrodynamic coefficients for the user-defined hull forces

In this section, the procedure to derive the coefficients for the user-defined hull force model as presented in section 3.2.3 is described. The damping coefficients in the mathematical model are derived in four steps:

1. The linear coefficients for simple motions (slope of force or moment curves at $\beta = 0°$ resp. $\gamma = 0$) are found as follows: For steady drift manoeuvres, the obtained forces or moments are divided by $\cos\beta \cdot \sin\beta$ and the coefficients are taken from the intersection at $\beta = 0°$ of a linear or polynomial trend line through the data points. For steady rotation, the same procedure is applied to the forces and moments divided by γ.

2. Non-linear coefficients for pure transverse motion ($\beta = 90°$) and pure rotation ($V = 0$) are found using empirical relations (based on the work of Hooft [63], e.g.). Currently, due to the unsteady nature of these manoeuvres and the complexity of the flow around the hull, these motions are not solved using viscous flow calculations.

3. Other non-linear components for simple motions can be determined by subtracting the contributions from the coefficients found in steps 1 and 2 from the calculated total bare hull forces; the non-linear components for the simple motions can then be determined using curve fitting.

4. The cross-terms, based on combined motions, are found in a similar way to step 3. The known contributions of the coefficients from steps 1-3 are subtracted from the calculated bare hull forces and the remainder is used to fit the cross-terms.

This approach is chosen to enable accurate modelling of the linearised behaviour for course-keeping (step 1), realistic modelling of the harbour manoeuvring characteristics (step 2), and accurate modelling of non-linear manoeuvres (steps 3 and 4). To ensure appropriate responses for astern manoeuvres, it is assumed that the forces and moments on the hull during astern manoeuvres are identical to those during ahead manoeuvring. However, if different forces and moments are desired for astern motion, these can be obtained by selecting the linear derivatives based on the sign of the longitudinal ship velocity, for example, as follows for the coefficient Y'_β, with $Y'_{\beta,\text{ahead}}$ the appropriate coefficient for ahead speed and $Y'_{\beta,\text{astern}}$ for astern speed:

$$Y'_\beta = Y'_{\beta,\text{ahead}} \cdot \max(0, \text{sign}(\cos\beta)) + Y'_{\beta,\text{astern}} \cdot \max(0, -\text{sign}(\cos\beta)) \tag{3.42}$$

3.4 Conclusion

In this chapter, the mathematical model used by SurSim to simulate the manoeuvrability of ships has been described. In the program, it is possible to provide user-defined hydrodynamic coefficients for the bare hull forces and moments. This makes the program well suited for the present work to investigate whether the use of viscous-flow calculations can help in improving the prediction accuracy of simulations.

A procedure to derive the coefficients is proposed. This procedure is chosen to enable accurate modelling of the linearised behaviour for course-keeping as well as realistic modelling of the harbour manoeuvring characteristics, and to enable accurate modelling of non-linear manoeuvres.

In the following chapter, the solvers used in the work for this thesis to calculate the viscous flow around a hull in manoeuvring motion will be discussed.

Chapter 4

Viscous flow solvers

This chapter provides short background information regarding the viscous-flow solvers used for the study discussed in this thesis. The grid procedures and the boundary conditions used for the calculations are also presented in this chapter. Since the present work focussed on the practical application of viscous-flow calculations and not on developing the solvers or numerical procedures themselves, the theoretical details of the solvers will not be discussed.

4.1 Background

Two different flow solvers have been used within this study. Initially, the calculations were done with Parnassos, which is a solver optimised to calculate the flow around ships in straight-ahead motion. For ships at drift angles or sailing in rotational motion, it was found that considerable adjustments to the computational parameters (e.g. under-relaxation) were required to reach the desired convergence levels. In the mean time, the developments on the more general purpose solver ReFRESCO were started. With this solver, it appeared to be easier to calculate the flow around ships in manoeuvring motions, especially for larger drift angles and rotation rates, and when using more advanced turbulence models. Therefore, results obtained with both solvers are discussed in this thesis.

4.2 Parnassos

Parnassos is one of MARIN's in-house incompressible viscous-flow solvers. It is based on a finite-difference discretisation of the Reynolds-averaged continuity and momentum equations, using fully collocated variables and discretisation. The equations are solved with a coupled procedure, retaining the continuity equation in its original form. Generally, the governing equations are integrated down to the wall, i.e. no wall functions are used. In Parnassos, multi-block structured grids are used. The implementation of the code is optimised for solving the flow around ships with the mean flow directed along the ship's longitudinal axis. This makes the solver especially suitable for calculating and optimising the resistance or propulsion of ships within a very short time frame, see e.g. Raven et al. [114] or Van der Ploeg and Raven [154].

More detailed information about the solver can be found in Hoekstra and Eça [60], Hoekstra [59], Raven et al. [113] or Eça and Hoekstra [40].

4.3 ReFRESCO

ReFRESCO is a MARIN spin-off of FreSCo [157], which was developed within the VIRTUE EU Project together with Technische Universität Hamburg-Harburg (TUHH) and HSVA. ReFRESCO is an acronym for *Reliable and Fast Rans Equations solver for Ships, Cavitation and Offshore*. It solves the multi-phase unsteady incompressible RANS equations, complemented with turbulence models and volume-fraction transport equations for each phase. The equations are discretised using a finite-volume approach with cell-centred collocated variables. The implementation is face-based, which permits grids with elements with an arbitrary number of faces (hexahedrals, tetrahedrals, prisms, pyramids, etc.). The code is parallelised using Message Passing Interface (MPI) and sub-domain decomposition. Low order and higher-order spatial and temporal discretisation schemes are available in the code. The equations are solved in a segregated approach, and the pressure/velocity coupling is solved using the Semi-Implicit Method for Pressure Linked Equations (SIMPLE) algorithm. The code is targeted, optimised and highly validated for hydrodynamic applications, in particular for obtaining current, wind and manoeuvring coefficients of ships, submersibles and semi-submersibles, see [159, 158, 51, 79]. Automatic wall functions are available. In the present work, however, y_2^+ values below 1 are obtained and all equations are integrated down to the wall.

4.4 Turbulence closure models

Several turbulence closure models are available in both Parnassos and ReFRESCO. The most commonly used are the one-equation turbulence models proposed by Menter [92] (designated MNT) or by Spalart and Allmaras [129] (designated SA), or two versions of the two-equation $k-\omega$ turbulence model, i.e. the Shear Stress Transport (SST) version [91] and the Turbulent/Non-Turbulent (TNT) version [78]. The Spalart correction of the stream-wise vorticity (proposed by Dacles-Mariani et al. see [31]) can be activated.

4.5 Implementation of rotational motion

4.5.1 Background

For ship manoeuvres, not only oblique flow is of interest, but also the flow around the ship when it performs a rotational motion. In RANS, this can be solved in several ways, such as moving the grid in a rotational motion through a stationary flow (inertial reference system), or by letting the flow rotate around the stationary ship (non-inertial reference system). The latter is adopted in Parnassos and ReFRESCO. This approach has been used by several authors, see for example section 3.2 in Batchelor [11] or section 1.15 in Wesseling [162] and the applications to ships of e.g. Alessandrini and Delhommeau [3], Cura Hochbaum [27] or Ohmori [99]. Using this system, the grid is attached to the hull form and rotates with the ship. However, each water particle now should experience centrifugal and Coriolis forces due to the rotation of the coordinate system. These forces have to be added to the momentum equation as source terms.

4.5.2 Governing equations

Originally, the momentum equations in Parnassos read in a Cartesian coordinate system (see equation (2.1) in Hoekstra [59])[1]:

$$\rho u_j u_{i,j} + p_{,i} - \mu u_{i,jj} + \rho \left(\overline{u_i' u_j'}\right)_{,j} = f_i \tag{4.1}$$

with f_i the force per unit volume that is exerted on a discrete flow volume.

Assuming a steady flow, the rotational motion is simulated by implementing the centrifugal and Coriolis force as additional force terms, such that the modified momentum equation reads:

$$\rho u_j u_{i,j} + p_{,i} - \mu u_{i,jj} + \rho \left(\overline{u_i' u_j'}\right)_{,j} = f_i - \rho \left(2\overline{\Omega} \times \overline{u}\right)_i - \rho \left(\overline{\Omega} \times \left(\overline{\Omega} \times \overline{r}\right)\right)_i \tag{4.2}$$

with f_i a remaining force term per unit volume (e.g. propeller forces), $\overline{\Omega}$ the vector of rotation, $\overline{u} = (u_1, u_2, u_3) = (u, v, w)$ the velocity vector and $\overline{r} = (\overline{x} - \overline{x}_R)$ the radius of rotation with $\overline{x}_R$ the position of the centre of rotation. In the equation above, the Coriolis force is represented by $-2\rho\overline{\Omega} \times \overline{u}$ while the centrifugal force is $-\rho\overline{\Omega} \times \left(\overline{\Omega} \times \overline{r}\right)$.

In ReFRESCO the Coriolis and centrifugal contributions are added to the external force f_i: i.e. $f_i = -\rho \left(2\overline{\Omega} \times \overline{u}\right)_i - \rho \left(\overline{\Omega} \times \left(\overline{\Omega} \times \overline{r}\right)\right)_i$.

4.5.3 Boundary conditions

At the outer boundaries in Parnassos calculations, it is assumed that the velocities and pressure correspond to a solution for potential flow, except for the normal velocity, which is left free to account for the displacement effect of the boundary layer. The pressure is based on Bernoulli's law, but a correction for the rotational motion is however required. Using section 3.5 of Batchelor [11], it can be shown that the pressure follows from:

$$\frac{p - p_\infty}{\rho} = \frac{1}{2}\left(\left(\overline{\Omega} \times \overline{r}\right)^2 - |\overline{u}|^2\right) \tag{4.3}$$

[1]In Hoekstra [59] the index notation and summation convention as given by Aris [7] is used. In this notation, whenever a subscript appears twice in a term, summation over the range of that index is implied. A comma in the subscript denotes differentiation.

Such a boundary condition is not available in ReFRESCO. Generally, undisturbed velocities are prescribed at the outer boundary. The modification of the pressure is not required at the outer boundaries in ReFRESCO since for such boundaries the pressure is extrapolated from the interior domain.

4.6 Grid generation

4.6.1 Parnassos

For Parnassos, the grids are generated with in-house tools, see Eça et al. [43]. Use is made of block-structured grids with H-O topology[2], with grid clustering near the bow and propeller plane in order to resolve the large gradients in those regions. In Parnassos, the flow must be more-or-less parallel to far-field boundaries or perpendicular to inflow or outflow planes. This means that to incorporate drift angles or rotational motion the outer boundaries of the computational domain must be adjusted to match the flow direction. Furthermore, calculations for larger drift angles and rotation rates require larger domain sizes. For this, an automated procedure has been made. First, a high-quality base grid is generated around the hull form. Surface grids on the boundaries of the base grid are made first and based on these surface grids the interior 3D grid is generated. The outer boundary of the base grid is located close to the hull, such that the quality of the grid can be controlled easily by adjusting the surface grids.

When the base grid with the desired grid quality is obtained, it is used to generate grids for each drift angle or rotation rate (or combination thereof). This is done by rotating the base grid according to the desired drift angle and subsequently generating the surrounding grid blocks to match the outer boundaries of the domain. Since the surrounding blocks are of relatively simple shapes, no user interaction is required to obtain the desired grid qualities and automatic scripts can be used. This procedure takes just several minutes on a normal PC, even for fine grids. In Figure 4.1 an example grid for the HTC for a steady yaw calculation is given. The base grid is raised with respect to the surrounding blocks to illustrate the procedure.

In Parnassos calculations, the solution from a potential flow calculation is used to set the pressure and tangential velocity at the far-field boundary and the velocities at the inlet. With this approach, the size of the computational domain can be smaller than the size of the computational domain for a calculation with undisturbed velocities at the far-field or inlet boundaries, as was demonstrated by Eça and Hoekstra [42].

4.6.2 ReFRESCO

For best performance of ReFRESCO, multi-block structured O-O grids[3] are used in general. Calculations for ships at drift angles or rotation rates are conducted by setting the

[2]In an H-O grid, one set of grid lines is generally aligned with the incoming flow direction.

[3]In O-O grids, grid lines are aligned perpendicular or parallel to the surface.

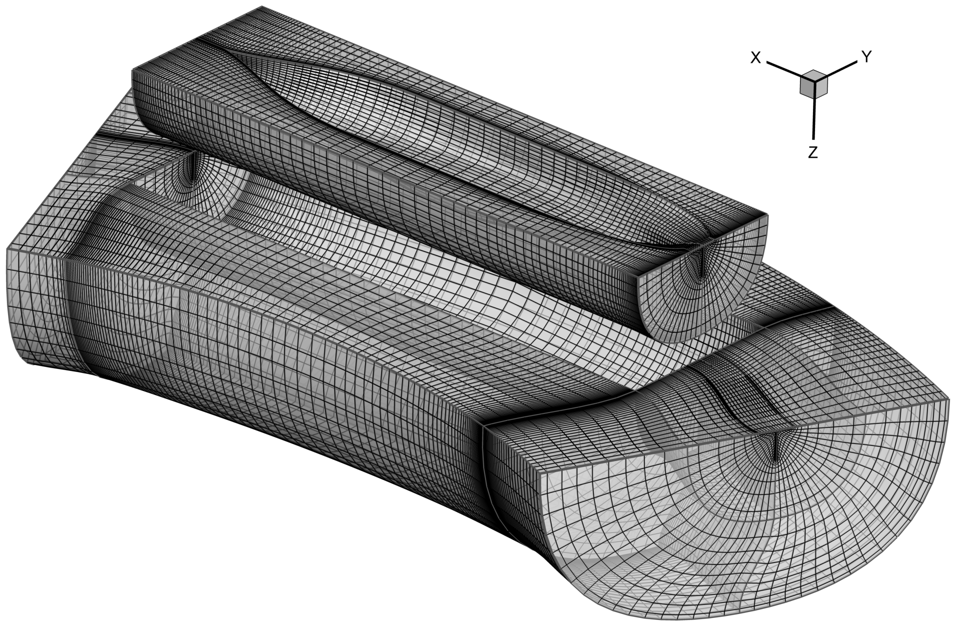

Figure 4.1: Example grid, PARNASSOS*, HTC,* $\gamma = -0.556$ *(coarsened for presentation)*

boundary conditions to the proper inflow velocities. Unlike the grids used in PARNASSOS, the computational domain does not need to be changed for each new calculation. For simple geometries and grid topologies, the grids for REFRESCO can be made using in-house tools. For more generic applications, use is made of commercial grid generation tools, such as ANSYS ICEM CFD, Numeca HEXPRESS, or PDC GridPro. In these tools, the grid can be generated and boundary conditions can be defined. However, when calculations are to be conducted for a range of drift angles or rotation rates, the redefinition of inflow or outflow boundaries to accommodate each computational condition requires user interaction. To avoid this, a new boundary condition has been implemented, designated `BCAutoDetect`. With this type of boundary condition, it is possible to use a single grid for different inflow angles, by automatically determining whether faces on the exterior domain are inflow faces or outflow/pressure faces.

For each face on the exterior boundary, the angle between the velocity $\overline{u}$ and the surface normal $\overline{n}$ is calculated, using:

$$\alpha = \arccos\left(\frac{\overline{u}}{|\overline{u}|} \cdot \frac{\overline{n}}{|\overline{n}|}\right) \tag{4.4}$$

Surface normals on the exterior boundary are always directed outward of the domain. Based on the projected velocity, the boundary condition on a face is either set to inflow ($\alpha \geq \alpha_{ad}$) or outflow/ pressure ($\alpha < \alpha_{ad}$), with α_{ad} an adjustable angle. By default α_{ad} is chosen to be 87°. This appeared to give slightly better convergence properties than an angle of 90°.

To further facilitate the use of a single grid for all computations, the far field boundary is generated as a cylindrical or spherical surface. An example grid for the HTC is given

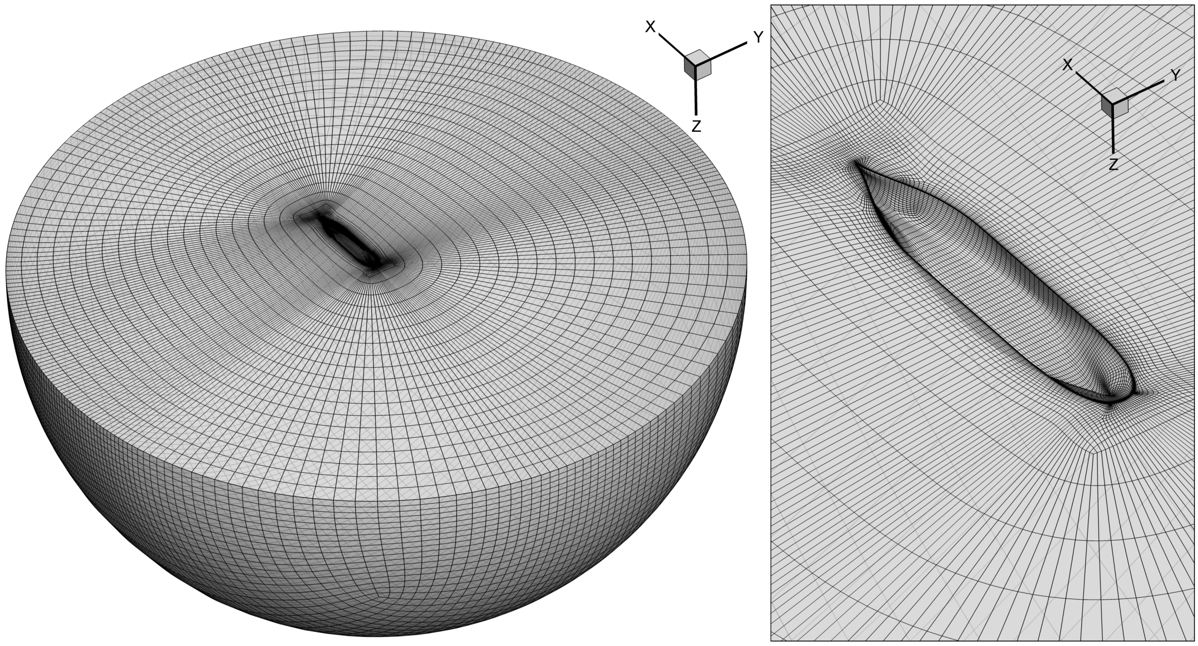

Figure 4.2: Example grid, ReFRESCO*, HTC (coarsest grid)*

in Figure 4.2.

In order to efficiently generate results for many drift angles, a procedure was implemented to automatically increment the drift angle during a single simulation. Simulations begin at a pre-set drift angle, until a specified number of iterations is reached, or when the non-dimensional residuals are less than a specified convergence criterion. Next the drift angle is incremented by $\Delta\beta$, by changing the inflow conditions, and the solution is continued from the solution at the previous drift angle. Starting the calculations from a converged solution at a slightly different drift angle saves time compared to performing each calculation separately. This procedure is repeated until the desired maximum inflow angle is reached. In Figure 4.3, it is demonstrated that this approach (continuous lines) provides the same results as those obtained with multiple single-drift angle calculations (markers). This procedure was designated *drift sweep* and the application has already been presented in e.g. Vaz et al. [158] and Bettle et al. [15].

4.7 Boundary conditions

The calculations presented in this thesis were all conducted without incorporating free-surface deformation. Based on the speeds used during the experiments for each test case and the range of drift angles or rotational rates studied, the effects of speed and free-surface deformation on the forces on the manoeuvring ship are likely to be small and assumed to be smaller than the uncertainties due to e.g. discretisation errors or errors in the experimental results. Therefore, symmetry boundary conditions were applied on the undisturbed water surface. On the hull surface, no-slip and impermeability boundary

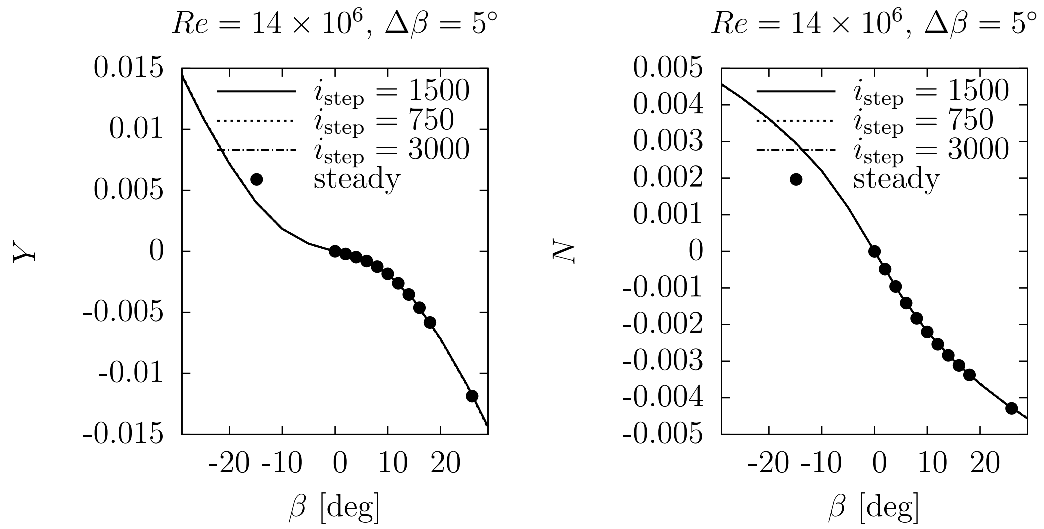

Figure 4.3: Verification of drift sweep procedure, SUBOFF
(i_{step} indicates the maximum number of iterations to perform for one drift angle)

conditions are used. The velocities are set to zero ($\overline{u} = 0$).

The velocity components at the inflow plane and on the external boundary in PARNASSOS calculations are taken from a potential flow calculation. For the inflow boundary, the three velocity components are taken from the potential flow solution, while in the external boundary, the tangential velocities and the pressure are set. During the viscous-flow calculation, the velocity normal to the external boundary is updated to allow for the displacement effect of the boundary layer. Because the velocity and pressure behind the ship are unknown, Neumann boundary conditions are applied on the outflow plane.

For REFRESCO, the boundary conditions on the exterior domain are determined using the `BCAutoDetect` boundary condition, which automatically applies inflow (Dirichlet) or outflow (Neumann) conditions on the cell faces. If a cylindrical domain is used, boundary conditions need to be set on the bottom/lower surface. For shallow water calculations, the boundary condition will be set to moving-wall/fixed slip ($\overline{u} = \overline{V}_\infty$). For unrestricted calculations, the boundary condition on the lower surface can be set to either a pressure boundary condition or to a symmetry boundary condition.

4.8 Conclusion

In this chapter, the viscous-flow solvers used in this thesis have been presented. For ship manoeuvres, not only the flow around the ship in oblique motion is of interest, but also the flow around the ship when it performs a rotational motion. To compute the flow around the ship in rotational motion, the flow solvers had to be modified. For this work, the rotational motion was incorporated by using a non-inertial reference system and supplementing the equations of motions with body forces representing the centrifugal and Coriolis contributions to the flow.

To generate the grids for a range of drift angles and yaw rates, different approaches were adopted depending on the flow solver used. For PARNASSOS, automated scripts were developed with which the desired grids could be generated rapidly. For the more generic solver REFRESCO, all computations are conducted using one grid, but changing the inflow angles and boundary conditions depending on the desired manoeuvring motion. For this, a new boundary condition was developed, which removes the need to pre-process each grid for each new manoeuvring condition.

To further improve the efficiency of the REFRESCO calculations, a so-called drift sweep procedure was developed to automatically calculate the forces and moments on the ship for a range of drift angles.

The following chapter presents verification and validation of the viscous-flow calculations from which the hydrodynamic coefficients for the bare hull forces in the mathematical model can be derived.

Chapter 5

Verification and validation of steady motion calculations

In this chapter, the verification and validation (V&V) of viscous-flow calculations for ship hulls in steady manoeuvring motion are discussed. Results of several test cases will be presented to demonstrate that the flow solvers can be applied to compute the viscous-flow around various hull forms and that accurate predictions of the forces and moments on the manoeuvring ship can be obtained. The results for the HTC will be used in chapter 7 to derive hydrodynamic coefficients for the user-defined mathematical model for the hull forces in SurSim, as presented in chapter 3.

5.1 Introduction to verification and validation

In order to assess whether computational results are reliable and accurate, verification (*solving the equations right* [115]) and validation (*solving the right equations*) studies are required. Two quantities are used: errors and uncertainties, designated by respectively δ and U. An error is defined as the difference between a simulated or measured value and a comparison value (sometimes called the true value), and it is therefore a quantity that has a sign and magnitude. An uncertainty defines an interval containing the true value within a certain degree of confidence. In verification, uncertainties in the results are assessed, while the aim in validation is to show the suitability of the selected model for the problem. Verification can be divided in two parts: code verification in which it is verified whether a code correctly solves the equations of the model; and solution verification in which the numerical uncertainty in a prediction is quantified. This thesis concentrates on solution verification and validation. Code verification is outside of the scope of this thesis and interested readers are referred to e.g. Eça et al. [44] in which the viscous-flow solver Parnassos is subjected to code verification. Similar efforts have been undertaken to verify ReFRESCO.

In solution *verification*, the numerical uncertainty U_{SN} in a solution ϕ is estimated. The exact solution ϕ_{exact} is unknown. The numerical uncertainty is governed by a numerical error multiplied by a factor of safety F_s. The numerical error consists of three components [115]: the round-off error; the iterative error and the discretisation error. The viscous-flow solvers used in this study use double precision and therefore the round-off error becomes negligible compared to the other errors. This means that the numerical uncertainty U_{SN} is obtained by[1]

$$U_{SN} = U_I + U_G \tag{5.1}$$

The uncertainty U_I due to the iterative process depends on whether the equations are sufficiently resolved. In simple flow problems, a reduction of the iterative error to machine accuracy is sometimes possible, but for complex flows this may be too time consuming. Estimations of U_I based on changes in the solution during the iterative process are then required. The discretisation uncertainty U_G is obtained by estimating the discretisation error δ_G and multiplying this with the factor of safety. When the differences between solutions on progressively finer grids reduce (i.e. we are converging towards the exact value), the discretisation error can be estimated with Richardson extrapolation (RE) and the use of the Grid Convergence Index (GCI) [115]:

$$\delta_G \approx \delta_{RE} = \phi_i - \phi_0 = \alpha \cdot h_i^p \tag{5.2}$$

in which ϕ_i stands for the value of a considered quantity, ϕ_0 is the estimate of the exact solution, α is a constant, h is the typical cell size and p is the observed order of accuracy. Additional or alternative error estimators are also used. With this estimator, the uncertainty follows from: $U_G = |\delta_G| \cdot F_s$. See Eça et al. [44, 45] for a complete discussion of the procedure.

The aim of *validation* is to establish the comparison error E and the validation uncertainty U_{val} and to obtain an interval that contains the modelling error δ_{model}. An error δ is supposed to have a magnitude and sign, while an uncertainty U is used to designate an interval containing an error of unknown magnitude and sign. The comparison error is defined by the difference between the simulated value S and the experimental data value D:

$$E = S - D \tag{5.3}$$

This error contains all errors in the experiment as well as in the simulation. The validation uncertainty is estimated by:

$$U_{\text{val}} = \sqrt{U_D^2 + U_{SN}^2 + U_{\text{input}}^2} \tag{5.4}$$

in which U_D is the uncertainty in the experimental result and U_{input} is the uncertainty in the input parameters (e.g. fluid properties, geometry). Evaluation of U_{input} is assumed to be outside the scope of the present work and is taken as zero for simplicity. Therefore U_{val} can be calculated through $U_{\text{val}} = \sqrt{U_D^2 + U_{SN}^2}$. According to the American Society

[1]According to the ASME V&V-20 procedure, Root mean square (RMS) addition cannot be applied to the uncertainties, because of the dependency of e.g. U_G on U_I.

Of Mechanical Engineers (ASME) V&V-20 procedure [9], the modelling error δ_{model} is defined by:

$$\delta_{\text{model}} = E - (\delta_{SN} + \delta_{\text{input}} - \delta_D) \tag{5.5}$$

By comparing E with the validation uncertainty, the following statements can be made:

$|E| >> U_{\text{val}}$: the comparison error is governed by the modelling error ($\delta_{\text{model}} \approx E$), which indicates that the model should be improved to reduce the comparison error.

$|E| < U_{\text{val}}$: the modelling error is within the noise imposed by the uncertainties contained in the validation uncertainties. Conclusions about the modelling error can only be drawn when the uncertainties are reduced. In this case, it is said that the model and its solution are validated at a level of U_{val}.

In this thesis, solutions with $|E| < U_{\text{val}}$ are indicated with a check-mark (✔), while solutions with $|E| >> U_{\text{val}}$ are not validated and therefore indicated with a cross (✘).

In the past, extensive procedures for V&V have been presented, such as the International Organization for Standardization (ISO) Guide to the Expression of Uncertainty in Measurement [72], Stern et al. [133] and recently the ASME Standard for Verification and Validation in Computational Fluid Dynamics and Heat Transfer [9]. In these procedures, guidelines are given, but references to methods which can be used to obtain improved uncertainty estimates are provided. The procedure based on a least-square version of the Grid Convergence Index (GCI) as proposed by Eça et al. [44, 45] is followed in this thesis.

5.2 KVLCC1, KVLCC2 and KVLCC2M

The KVLCC hull forms have been described in section 2.5.3. In this section, RANS calculations for these hulls will be presented and compared to the available experimental validation data. Only the conditions representing deep water will be considered.

With Parnassos, viscous flow calculations have been conducted for the KVLCC2M at several drift angles. These have been reported previously by Toxopeus [143]. The calculations were done with an undisturbed water surface, i.e. neglecting the generation of waves. The Reynolds number was set to $Re = 3.945 \times 10^6$. The Menter one-equation turbulence model was used.

Calculations with Parnassos were performed for the KVLCC1 and KVLCC2 hull forms, see Toxopeus and Lee [149]. Also for these calculations an undisturbed water surface and the Menter one-equation turbulence model were used. Contrary to the model tests, it was assumed that the model attitude was fixed, i.e. dynamic trim, sinkage and heel were not taken into account. The grid consisted of 3.356×10^6 nodes. The Reynolds number was set to $Re = 3.27 \times 10^6$.

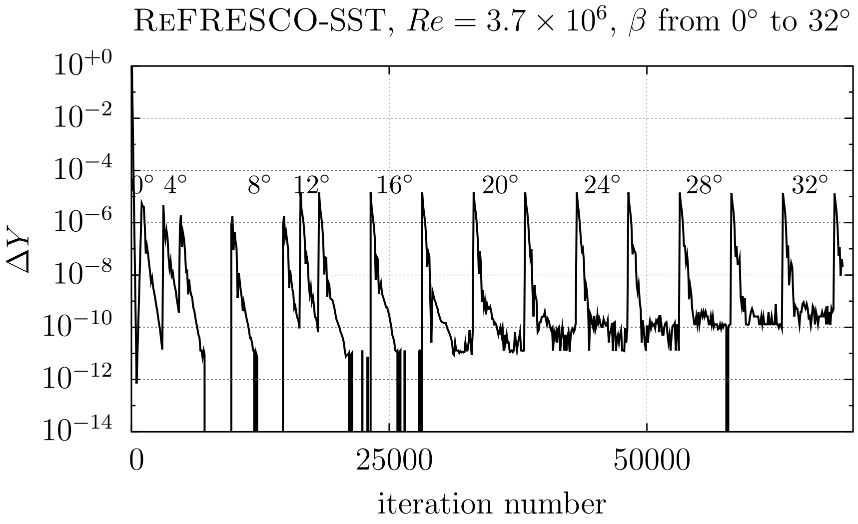

Figure 5.1: Convergence history Y-force, KVLCC2, ReFRESCO

The flow around the KVLCC2 hullform was also studied using ReFRESCO. One grid with 5.388×10^6 cells was used for all drift angles, while the computations for different rotation rates were made with a finer grid of 12.721×10^6 cells. Similar to the Parnassos calculations, an undisturbed water surface and a fixed model attitude were assumed. The Reynolds number was set to the slightly different value of 3.7×10^6 and the SST turbulence model was used. The relation between the drift angle and the forces and moments on the hull was obtained with the drift sweep procedure as introduced in section 4.6.2.

An overview of all experimental and computational results of the forces and moments on the KVLCCs for captive conditions is given in the tables on page 151 through page 156.

5.2.1 Iterative error

In the Parnassos calculations a reduction of the maximum difference in the pressure coefficient between consecutive iterations to 5×10^{-5} was adopted as the convergence criterion. For all cases, the adopted convergence criterion results in a reduction of the difference in the (total) non-dimensional force and moment components between consecutive iterations of well below 5×10^{-5}. This is more than two to three orders of magnitude smaller than the discretisation uncertainty and therefore the iterative uncertainty U_I can be neglected, see Eça et al. [41].

For ReFRESCO, all calculations were run until the maximum non-dimensional residual of the pressure $\mathrm{res}_{p,\max}$ (the so-called L_∞ norm) between successive iterations had dropped well below 1×10^{-5} or when further iterative convergence was not obtained. The changes in the non-dimensional integral quantities (forces and moments) were well below 1×10^{-7}. An example of the convergence history of the transverse force Y is given in Figure 5.1. In this calculation, the drift angle is increased after a predefined number of iterations from 0° to 30° in steps of 2°. Each increase of the drift angle is visible as a spike in the convergence history. For each drift angle, the changes in Y force reduce to below 1×10^{-10}. The convergence of the other force components is similar.

5.2.2 Discretisation error

Several grid topologies have been used for the PARNASSOS calculations of the flow around the KVLCC2M [39]. The results presented in this thesis were all obtained on structured grids with H-O topology with extra grid clustering close to the bow and propeller plane. For each grid, the variation in the number of grid nodes in the stream-wise, normal and girth-wise (n_ξ, n_η and n_ζ) directions is presented in Table 5.1, which also includes the maximum y^+ value for the first cells adjacent to the hull, designated y_2^+, that was obtained during the calculations. It is seen that $y_2^+ < 1$ which is required when the flow is to be resolved down to the wall.

Table 5.1: Properties of grids for different drift angles, KVLCC2M, PARNASSOS

Fn	β	x_{in}	x_{out}	$\lvert y\rvert_{\max}$	$z_{\max}$	n_ξ	n_η	n_ζ	Nodes	y_2^+
	0°	0.73	-0.92	0.18	0.18	449	81	45	1.6×10^6	0.32
	3°	0.74	-0.93	0.42	0.36	449	95	2×45	3.8×10^6	0.40
-	6°	0.75	-0.94	0.49	0.36	449	95	2×45	3.8×10^6	0.55
	9°	0.76	-0.95	0.55	0.36	449	95	2×45	3.8×10^6	0.69
	12°	0.76	-0.95	0.61	0.38	449	95	2×45	3.8×10^6	0.80

For a drift angle of 12°, a series of geometrically similar grids has been generated in order to investigate the discretisation error. The grid coarsening has been conducted in all three directions. For some of the grids, however, the distance of the first node to the hull surface has been maintained in order to capture the velocity gradients in the boundary layer. This might introduce scatter in the results due to non-geometric similarity. Table 5.2 shows the number of nodes and y_2^+ values for these grids.

Table 5.2: Properties of grids for uncertainty analysis, KVLCC2M, PARNASSOS, $\beta = 12°$

id	β	n_ξ	n_η	n_ζ	h_i	Nodes	y_2^+	Comment
1	12	449	95	2×45	1.00	3838950	0.80	
2	12	409	87	2×41	1.10	2917806	0.75	
3	12	361	81	2×37	1.24	2163834	0.62	
4	12	329	74	2×33	1.37	1606836	0.71	
5	12	297	65	2×29	1.51	1119690	0.94	
6	12	249	65	2×25	1.81	809250	0.78	
7	12	225	48	2×23	2.00	496800	1.15	based on grid 1, coarsened by 2×2×2
8	12	177	41	2×19	2.55	275766	1.25	based on grid 3, coarsened by 2×2×2
9	12	145	33	2×15	3.11	143550	1.73	based on grid 5, coarsened by 2×2×2
10	12	121	33	2×13	3.73	103818	1.32	based on grid 6, coarsened by 2×2×2
11	12	113	24	2×12	4.00	65088	2.17	based on grid 1, coarsened by 4×4×4

For grid 5, it was not possible to reach the required convergence criterion. Therefore the results for this grid are dropped from further analysis.

For a drift angle of 12°, the predicted values of the friction (index f) and pressure (index p) components as well as the total force and moment coefficients for each force or moment variable ϕ are given in Table 5.3 with their estimated uncertainties U_ϕ. Based on an analysis of the results for each grid, it was decided to use the 6, 7 or 8 finest grids for the uncertainty analysis. The number of grids n_g used depended on the scatter in the results for the coarsest grids. In the table, ϕ_1 indicates the solution obtained on the finest grid, ϕ_0 the extrapolated solution and p the apparent order of convergence.

Table 5.3: Uncertainty analysis, KVLCC2M, Parnassos, $\beta = 12°$

Item	ϕ_0	ϕ_1	U_ϕ	p
X_p	-	-2.32×10^{-3}	32.3%	[1]
X_f	-1.57×10^{-2}	-1.54×10^{-2}	2.1%	1.45
X	-	-1.78×10^{-2}	7.8%	[2]
Y_p	-6.45×10^{-2}	-6.26×10^{-2}	4.8%	1.25
Y_f	-1.84×10^{-3}	-1.70×10^{-3}	13.4%	1.34
Y	-6.67×10^{-2}	-6.43×10^{-2}	5.6%	1.13
Z_p	3.39×10^{-1}	3.20×10^{-1}	7.7%	0.52
Z_f	-	1.20×10^{-3}	13.2%	[2]
Z	3.41×10^{-1}	3.21×10^{-1}	7.9%	0.51
K_p	-	3.24×10^{-3}	9.3%	[1]
K_f	-2.16×10^{-4}	-1.74×10^{-4}	30.7%	0.44
K	-	3.07×10^{-3}	6.7%	[1]
M_p	-	-3.97×10^{-2}	3.8%	[2]
M_f	1.09×10^{-3}	1.08×10^{-3}	0.7%	1.71
M	-	-3.86×10^{-2}	4.0%	[2]
N_p	-	-2.55×10^{-2}	9.2%	[2]
N_f	-	2.94×10^{-4}	25.4%	[2]
N	-	-2.53×10^{-2}	9.6%	[2]

[1] Oscillatory convergence
[2] Monotonic divergence
[3] Oscillatory divergence

The absolute value of the uncertainty in the pressure components is larger than in the friction components. The uncertainty in the longitudinal friction component X_f is about one-third of the uncertainty in the longitudinal pressure component X_p. For the other forces and moments, the uncertainty in the friction component is at least one order of magnitude smaller than the uncertainty in the pressure component. Since most integral forces and moments are dominated by the pressure component, this results in relatively large uncertainties in the overall forces and moments.

In Figure 5.2, the convergence of the side force and yaw moment coefficients with grid refinement is presented. It is seen that upon grid refinement, the estimated value for Y (indicated by cfd) comes closer to the experimental value (indicated by exp). Considerable scatter is visible in the data and therefore it is not easy to establish whether data points are located in the asymptotic range of convergence. This is typical for this type of calculation, as already observed previously by e.g. Eça et al. [38] and Hoekstra et al. [61].

Looking at the yawing moment N, the maximum difference between the estimated values for all grids is 5.1%. Because the difference between the estimated values is relatively small and scatter on the data is present, monotonic divergence is found and extrapolation to zero step size could not be made. This results in a relatively large uncertainty of 9.6%.

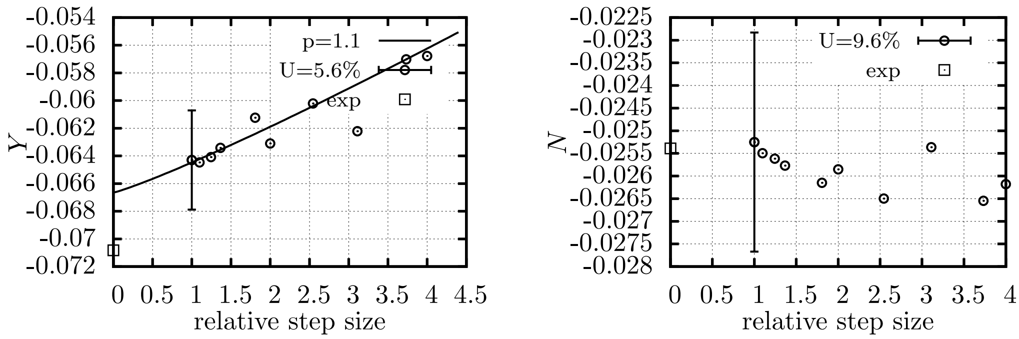

Figure 5.2: Uncertainty analysis, KVLCC2M, Parnassos, $\beta = 12°$

5.2.3 Local quantities

The experimental data of the wake field in the complete WAKE1 plane (near the propeller plane, perpendicular to the incident flow) have kindly been made available by National Maritime Research Institute (NMRI). In Figure 5.3 comparisons of the axial velocity fields between the experiments (dotted lines) and the Parnassos calculations (solid lines) for 0°, 6° and 12° drift angle are made.

This figure shows that in most parts of the plane, the viscous-flow calculations correspond well with the experiments. Even for 12° drift angle, the strength and position of the vortex generated at the starboard bilge (its centre is located at $y = 0.11L_{\mathrm{pp}}$, $z = 0.03L_{\mathrm{pp}}$) is quite accurately captured by the calculations.

In the port side area (windward), discrepancies are found for the 12° drift case, however. In the calculations, the contour lines are straightened while they retain their hook-shape in the experimental results. Also just behind the propeller hub for 0° drift angle, the hook-shape in the measurements appears more pronounced than in the calculations. This can be attributed to the turbulence modelling, as was also observed by Eça et al. [38].

Overall, it is concluded that the flow field around the aft ship is quite accurately predicted.

5.2.4 Global quantities

By comparing the viscous flow calculation results for the KVLCCs, the influence of the stern shape on the forces and moments on the hull can be investigated. In Figure 5.4, a comparison is graphically presented.

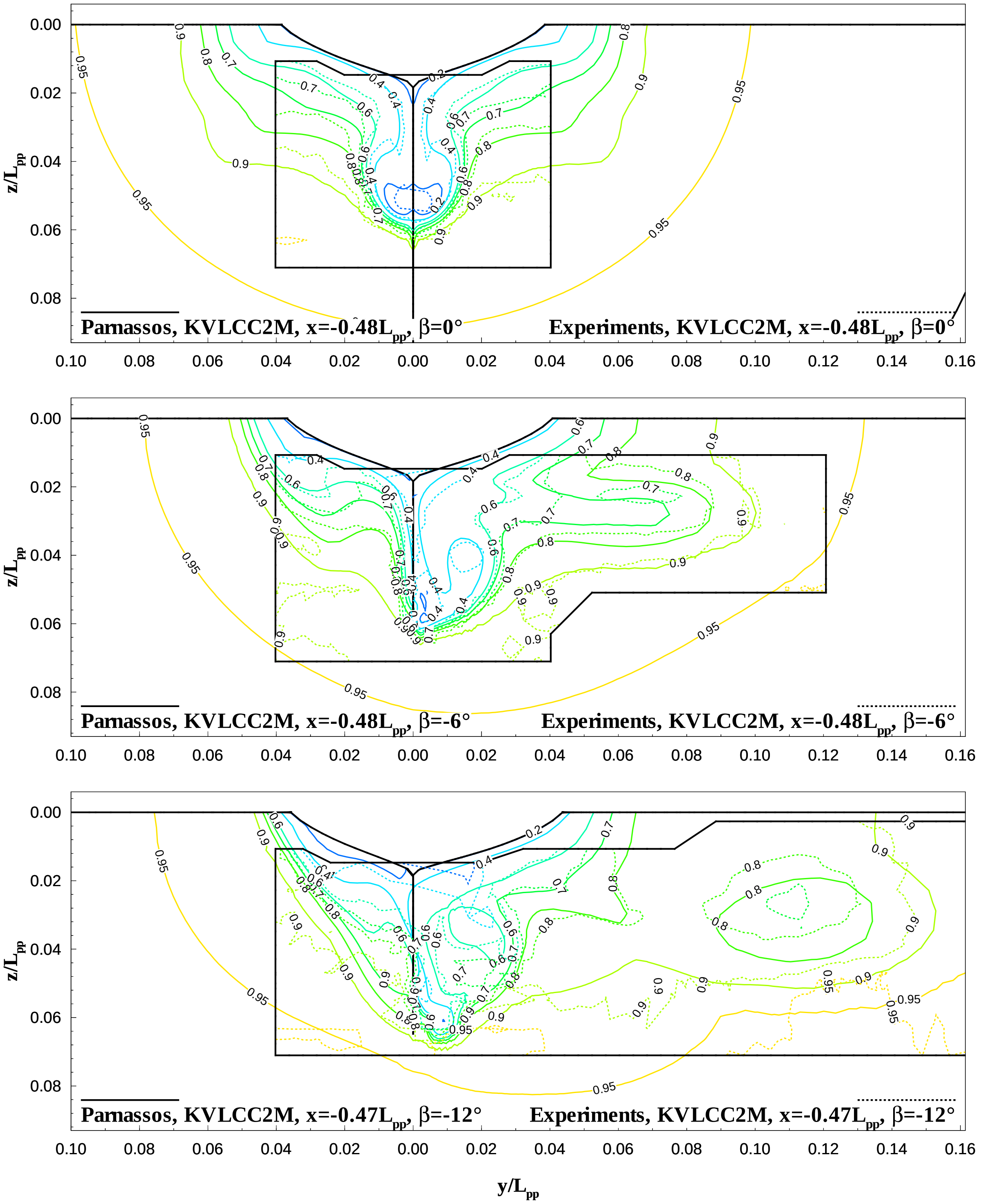

Figure 5.3: Comparison with experiments, KVLCC2M, WAKE1 (solid lines: calculations, dotted lines: experiments)

Based on this comparison, it is seen that a trend may be found in the yaw moment N against the drift angle due to the change in hull form: the yaw moment for the KVLCC1 is slightly higher than for the KVLCC2 and KVLCC2M hulls. This trend is visible in the experiments and in the CFD results. However, no trend can be seen in the transverse force Y or the force or moment against the yaw rate. Furthermore, one would expect the results for the KVLCC2M to be closer to the KVLCC2 results than to the KVLCC1 results. Therefore, it is concluded that the differences between the CFD results for the Y force against the drift angle and Y and N against the yaw rate are within the accuracy of the calculations and are not representative for the differences between the hull forms. Based on the above observations, it is expected that the three hulls will have similar manoeuvring behaviour. This has been demonstrated during the free sailing manoeuvring tests with the KVLCC1 and KVLCC2, see MARIN Report No. 21571-1-SMB [87], in which it was found that indeed there were no significant differences in the manoeuvring performances, other than a small difference in the directional stability derived from pull-out tests.

A comparison between the Parnassos and ReFRESCO results for the KVLCC2 shows only marginal differences, even though a different turbulence model was used. Only in the N moment against γ, a consistent difference between the results of the two solvers is seen. The differences are within the uncertainty of the predictions and a reduction of the uncertainties is required to investigate whether the differences are caused by modelling errors. Therefore, no conclusions can be drawn about the influence of either the solver, the grid layout or the turbulence model on the results.

5.2.5 Validation

The uncertainties in the measurements of the forces and moments are specified by Kume et al. [82] and summarised in Table 5.4. The values for $\beta = 12°$ were calculated by interpolation between the uncertainties for $\beta = 9°$ and $\beta = 18°$. Using the measurement uncertainties and assuming that the simulation numerical uncertainty U_{SN} is only influenced by the discretisation uncertainty U_G (i.e. $U_{SN} = U_I + U_G = U_G$), Table 5.4 can be constructed. The uncertainty U_{input} due to uncertainties in the input parameters (e.g. fluid properties, geometry) is assumed to be zero and therefore U_{val} can be calculated through $U_{\text{val}} = \sqrt{U_D^2 + U_{SN}^2}$.

It is seen that for the longitudinal force X and yaw moment N the comparison error $|E|$ is smaller than the validation uncertainty U_{val} which means that the solution is validated at levels of 8.6% and 10.4% respectively. These levels are judged to be good. If lower validation levels are desired then the numerical uncertainty needs to be reduced. For the transverse force Y validation is not achieved ($|E| > U_{\text{val}}$), which indicates modelling errors. It is seen that the magnitude of the Y force is under-predicted. Changes in turbulence model or domain size or the inclusion of free surface may lead to improvements of the comparison error.

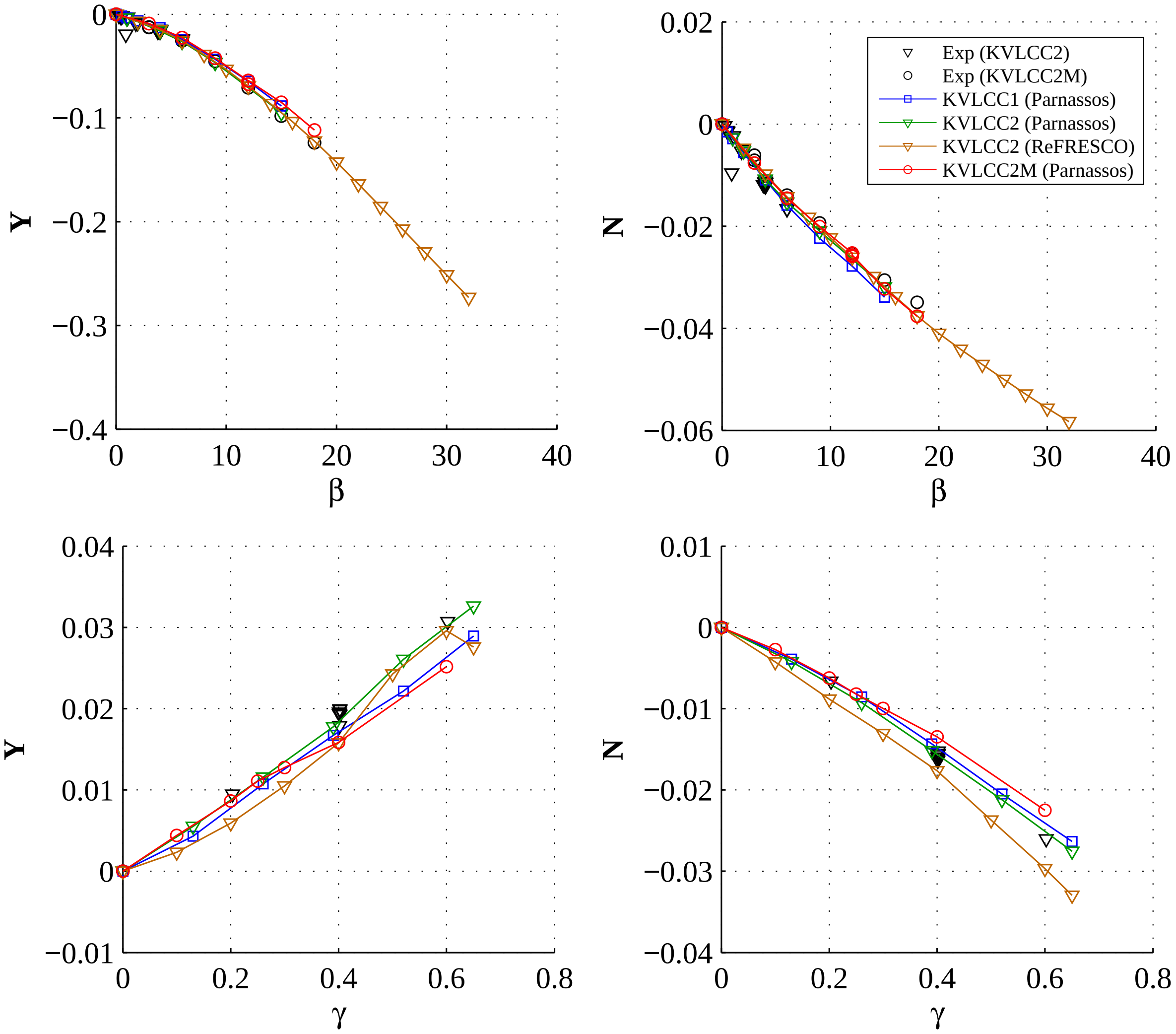

Figure 5.4: Comparison between experiments and calculations, KVLCC hull forms (Lines represent CFD results)

Table 5.4: Measurement uncertainties and validation, KVLCC2M, PARNASSOS, $\beta = 12°$

Measurement uncertainty

β	U_D X ($\%D$)	U_D Y ($\%D$)	U_D N ($\%D$)
0°	3.3	-	-
9°	3.6	3.2	4.3
18°	2.9	3.1	3.7
12°	3.4	3.2	4.1

Validation

	X	Y	N
$D \times 10^3$	-17.5	-70.8	-25.4
$S \times 10^3$	-17.8	-64.3	-25.3
$E = S - D$ ($\%D$)	1.5	-9.2	-0.5
U_D ($\%D$)	3.4	3.2	4.1
U_{SN} ($\%S$)	7.8	5.6	9.6
$U_{\text{val}} = \sqrt{U_D^2 + U_{SN}^2}$ ($\%D$)	8.6	6.0	10.4
Validated?	✔	✘	✔

5.3 HTC

The HTC has been described in section 2.5.4. In this section, RANS calculations for this hull will be presented and compared to available experimental validation data. The captive model tests have been conducted for speeds of $1.05\,m/s$ and $1.89\,m/s$, corresponding to $10\,kn$ and $18\,kn$ on full scale. On model scale ($\lambda = 24$), this results in Reynolds numbers of $Re = 6.29 \times 10^6$ and $Re = 12 \times 10^6$, respectively. All calculations presented in this thesis have been performed at model scale Reynolds numbers. To clearly distinguish the different speeds used for the calculations or model tests and avoid confusion with the speeds for other scale factors and the free sailing tests, calculations for the lower speed will be identified with $10\,kn$, while the calculations for the higher speed will be identified with $18\,kn$.

Calculations using PARNASSOS were made for the HTC hull form, using the Menter one-equation turbulence model. Free surface and appendages were not modelled in the calculations. These calculations were previously documented in VIRTUE Deliverable 3.1.1 [152]. Table 5.5 shows the conditions for the $10\,kn$ computations. The domain sizes and variation in the number of grid nodes in the stream-wise, normal and girth-wise (n_ξ, n_η and n_ζ) directions are given, together with the y_2^+ values that were obtained.

Table 5.5: Properties of grids for different drift angles, HTC, PARNASSOS*, $10\,kn$*

Fn	β	x_{in}	x_{out}	$\lvert y\rvert_{\max}$	$z_{\max}$	n_ξ	n_η	n_ζ	Nodes	y_2^+
	0°	0.70	-0.75	0.16	0.16	329	81	51	1.2×10^6	0.56
	2.5°	0.71	-0.76	0.35	0.31	377	95	2×51	3.7×10^6	0.74
-	5°	0.71	-0.79	0.38	0.31	377	95	2×51	3.7×10^6	0.81
	10°	0.72	-0.91	0.45	0.31	377	95	2×51	3.7×10^6	0.90
	15°	0.73	-1.11	0.52	0.32	377	95	2×51	3.7×10^6	0.90

Calculations have been conducted with REFRESCO as well. Also in this case, free surface and appendages were not modelled. All calculations were conducted for the $18\,kn$ condition and the SST turbulence model was selected for turbulence closure. One single grid was used for all calculations. The steady drift calculations were performed with the drift sweep procedure as introduced in section 4.6.2.

An overview of all experimental and computational results of the forces and moments on the HTC for captive conditions is given in the tables on page 157 and page 158.

5.3.1 Iterative error

In the PARNASSOS calculations a reduction of the maximum difference in the pressure coefficient between consecutive iterations to 5×10^{-5} was adopted as the convergence criterion. For all cases, the adopted convergence criterion results in a reduction of the difference in the (total) non-dimensional force and moment components between consecutive iterations of well below 4×10^{-5}. This is more than two to three orders of magnitude smaller than the discretisation uncertainty and therefore the iterative uncertainty U_I can be neglected, see Eça et al. [41].

For ReFRESCO, all calculations were run until the maximum non-dimensional residual of the pressure $\text{res}_{p,\max}$ (the so-called L_∞ norm) between successive iterations had dropped well below $1 \cdot 10^{-5}$ or when further iterative convergence was not obtained. The changes in the non-dimensional integral quantities (forces and moments) were well below 1×10^{-7}. An example of the convergence history of the transverse force Y is given in Figure 5.5. In this calculation, the drift angle is increased after a predefined number of iterations from 0° to 30° in steps of 2.5°. Each increase of the drift angle is visible as the spikes in the convergence history. For each drift angle, the changes in Y force reduce to below 1×10^{-8}. The convergence of the other force components is similar.

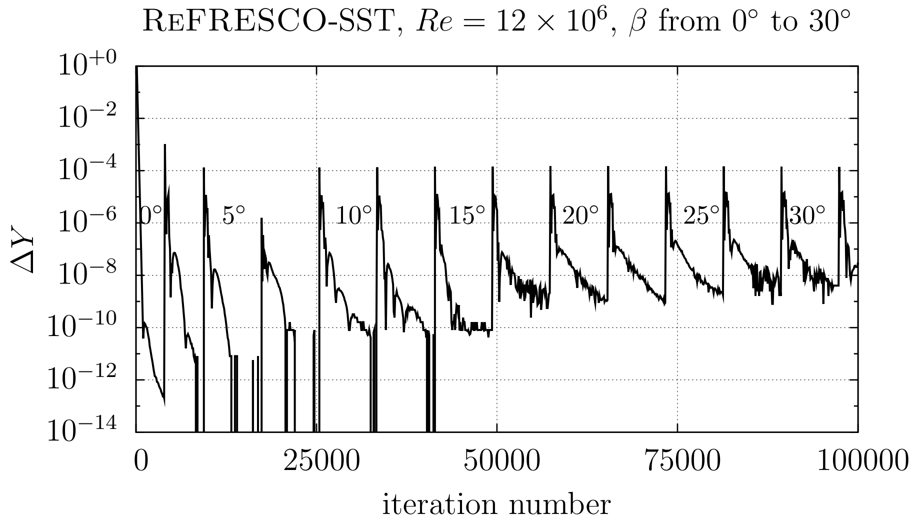

Figure 5.5: Convergence history Y-force, HTC, ReFRESCO

5.3.2 Discretisation error for steady drift motion

For Parnassos, a series of geometrically similar grids has been generated for a drift angle of 10°, in order to investigate the discretisation error. The grid coarsening has been conducted in all three directions. For each grid, the variation in the number of grid nodes in the stream-wise, normal and girth-wise (n_ξ, n_η and n_ζ) directions is presented in Table 5.6, which includes also the y_2^+ values that were obtained during the calculations conducted for the 10 kn condition.

For a drift angle of 10°, the predicted values ϕ_1 of the friction (subscript f) and pressure (subscript p) components as well as the total force and moment coefficients are presented in Table 5.7 with their estimated uncertainties U_ϕ. Based on an analysis of the results for each grid, it was decided to use the eight finest grids for the uncertainty analysis. The number of grids n_g used was chosen based on the scatter in the results for the coarsest grids.

The absolute value of the uncertainty in the pressure components is larger than in the friction components, as was already found during the uncertainty study for the KVLCC2M hull form, see section 5.2. The uncertainty in the longitudinal friction component X_f is about one-third of the uncertainty in the longitudinal pressure component X_p. For the other forces and moments, the uncertainty in the friction component is at least one order of magnitude smaller than the uncertainty in the pressure component. Since most integral forces and moments are dominated by the pressure component, this results in relatively large uncertainties in the overall forces and moments. In Raven, Van der Ploeg and

Table 5.6: Properties of grids for uncertainty analysis, HTC, $\beta = 10°$, PARNASSOS

id	β	n_ξ	n_η	n_ζ	h_i	Nodes	y_2^+	Comment
1	10	377	95	2×51	1.00	3653130	0.90	
2	10	361	91	2×49	1.04	3219398	0.86	
3	10	297	77	2×41	1.25	1875258	0.97	
4	10	257	65	2×35	1.47	1169350	1.19	
5	10	185	48	2×26	2.00	461760	1.48	based on grid 1, coarsened by 2×2×2
6	10	177	46	2×25	2.08	407100	1.51	based on grid 2, coarsened by 2×2×2
7	10	145	39	2×21	2.50	237510	1.76	based on grid 3, coarsened by 2×2×2
8	10	129	33	2×18	2.94	153252	2.28	based on grid 4, coarsened by 2×2×2
9	10	89	23	2×13	4.17	53222	3.08	based on grid 2, coarsened by 2×2×2
10	10	73	19	2×11	5.00	30514	4.06	based on grid 1, coarsened by 2×2×2

Table 5.7: Uncertainty analysis, HTC, $\beta = 10°$, $10\,kn$, PARNASSOS

Item	ϕ_0	ϕ_1	U_ϕ	p
X_p	-5.33×10^{-4}	-3.40×10^{-3}	111.1%	0.67
X_f	-	-1.22×10^{-2}	2.6%	[2]
X	-1.40×10^{-2}	-1.57×10^{-2}	14.1%	0.94
Y_p	-3.68×10^{-2}	-4.31×10^{-2}	19.5%	0.69
Y_f	-1.18×10^{-3}	-1.12×10^{-3}	7.2%	1.80
Y	-3.76×10^{-2}	-4.42×10^{-2}	19.9%	0.65
Z_p	7.86×10^{-2}	8.56×10^{-2}	5.8%	0.22
Z_f	-	3.40×10^{-4}	4.4%	[2]
Z	7.86×10^{-2}	8.60×10^{-2}	5.8%	0.21
K_p	2.07×10^{-2}	1.96×10^{-2}	7.0%	1.46
K_f	-1.79×10^{-3}	-1.76×10^{-3}	3.3%	1.97
K	1.89×10^{-2}	1.79×10^{-2}	7.5%	1.42
M_p	-2.24×10^{-3}	-1.55×10^{-3}	59.7%	0.75
M_f	-	3.03×10^{-4}	1.6%	[2]
M	-1.92×10^{-3}	-1.25×10^{-3}	72.6%	0.76
N_p	-2.45×10^{-2}	-2.44×10^{-2}	1.3%	3.45
N_f	2.78×10^{-5}	2.48×10^{-5}	54.8%	1.98
N	-2.45×10^{-2}	-2.44×10^{-2}	1.2%	3.48

[1] Oscillatory convergence
[2] Monotonic divergence
[3] Oscillatory divergence

Eça [113], an extensive study to improve the uncertainty and accuracy of the pressure resistance component is presented.

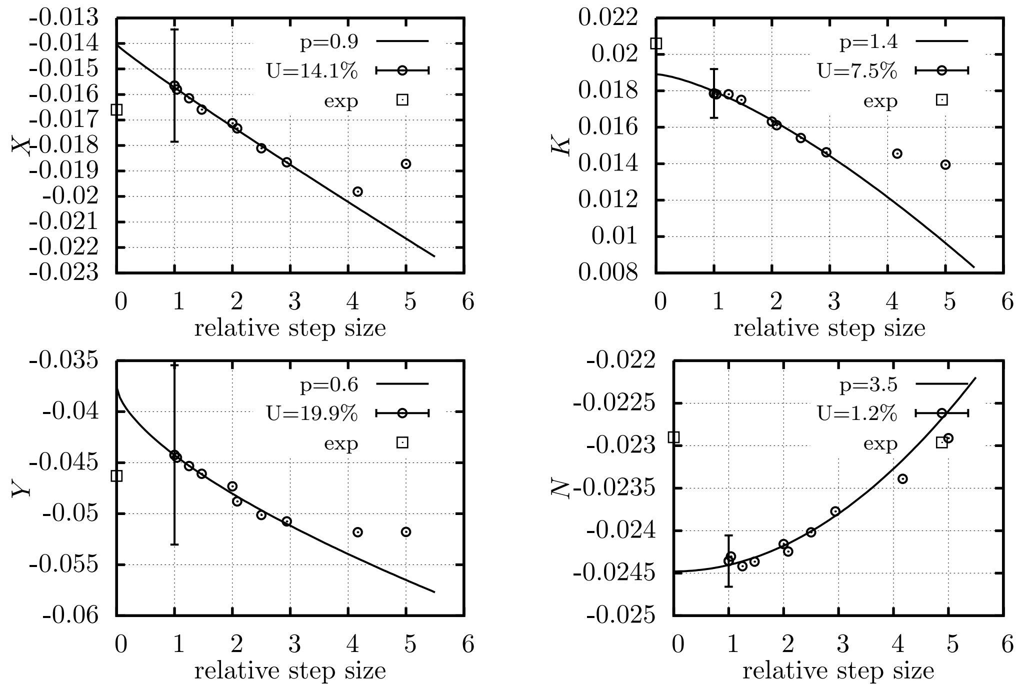

Figure 5.6: Uncertainty analysis, HTC, $\beta = 10°$, $10\,kn$, PARNASSOS

In Figure 5.6 the forces and moments on the ship are shown for the different grids. The scatter in the results is much smaller than found for the KVLCC2M results. For a relative step size below 3, the results appear to converge. The observed convergence rate p, however, is found to be small for both X and Y ($p = 0.9$ and 0.6 respectively). Due to the slow convergence, the difference between the extrapolated value ϕ_0 for zero step-size and the value ϕ_1 is large and hence the uncertainty is relatively large.

Noteworthy is the fact that based on the trends with the current grids, the estimations (indicated by cfd) for X, Y and N for increasing numbers of grid nodes do not converge to the experimental values (indicated by exp). This may be caused by either modelling errors or by uncertainties in the experimental values.

A similar grid study was conducted for REFRESCO. Using an automatic procedure in GridPro, a series of geometrically similar grids was generated, using grid coarsening in all three directions for each block in the grid. For each grid, the number of cells in the grid n_{cells} and the number of faces on the hull surface n_{hull} are given in Table 5.8, which includes also the y_2^+ values that were obtained during the calculations at drift angles of 0° and 30° and a non-dimensional rotation rate of 0.4. For each grid, the full range of drift angles between 0° and 30° was calculated.

For drift angles of 10° and 30°, the uncertainty estimates are presented in Table 5.9 and Table 5.10 respectively. Based on an analysis of the results for each grid, it was decided to use the four finest grids for the uncertainty analysis. The number of grids n_g

used was chosen based on the scatter in the results for the coarsest grid.

In Figure 5.7 and Figure 5.8 the forces and moments on the ship are graphically presented for the different grids. The scatter in the results is relatively large and the results are less consistent than those obtained with PARNASSOS. For a relative step size of 1.6 or below, the results appear to converge. The observed convergence rate p, however, is found to be large for all force components, hence the uncertainty is relatively large due to the use of a larger safety factor F_s. Finer grids are required to reduce the uncertainty in the calculations.

Table 5.8: Properties of grids for uncertainty analysis, HTC, $18\,kn$*,* REFRESCO

id	h_i	n_{cells}	n_{hull}	y_2^+ $(\beta = 0°)$	y_2^+ $(\beta = 30°)$	y_2^+ $(\gamma = 0.4)$
1	1.00	5234432	31872	0.27	0.52	0.42
2	1.27	2564378	19706	0.35	0.64	0.49
3	1.60	1288960	12540	0.46	0.81	0.60
4	1.99	659352	8040	0.59	0.85	0.77
5	2.58	303462	4698	0.78	1.23	0.99

Table 5.9: Uncertainty analysis, HTC, $\beta = 10°$*,* $18\,kn$*,* REFRESCO

Item	ϕ_0	ϕ_1	U_ϕ	p
X_p	-	-3.15×10^{-3}	44.0%	[1]
X_f	-1.17×10^{-2}	-1.14×10^{-2}	4.0%	1.23
X	-	-1.45×10^{-2}	6.6%	[1]
Y_p	-	-3.73×10^{-2}	32.5%	[2]
Y_f	-1.05×10^{-3}	-1.02×10^{-3}	8.9%	3.62
Y	-	-3.84×10^{-2}	31.0%	[2]
Z_p	8.45×10^{-2}	8.65×10^{-2}	6.5%	6.78
Z_f	-	2.58×10^{-4}	13.4%	[2]
Z	8.48×10^{-2}	8.67×10^{-2}	6.4%	6.73
K_p	-	1.60×10^{-2}	14.6%	[2]
K_f	1.54×10^{-3}	1.50×10^{-3}	7.6%	3.36
K	-	1.75×10^{-2}	11.6%	[2]
M_p	-	-1.37×10^{-3}	39.4%	[1]
M_f	-	-2.74×10^{-4}	498.4%	[1]
M	-1.49×10^{-3}	-1.64×10^{-3}	27.2%	5.88
N_p	-	-2.23×10^{-2}	7.0%	[2]
N_f	-7.58×10^{-5}	-5.07×10^{-5}	62.3%	0.64
N	-	-2.23×10^{-2}	6.9%	[2]

[1] Oscillatory convergence
[2] Monotonic divergence
[3] Oscillatory divergence

Table 5.10: Uncertainty analysis, HTC, $\beta = 30°$, $18\,kn$, ReFRESCO

Item	ϕ_0	ϕ_1	U_ϕ	p
X_p	-	6.48×10^{-3}	109.5%	[1]
X_f	-1.22×10^{-2}	-1.18×10^{-2}	9.7%	2.92
X	-	-5.33×10^{-3}	90.0%	[1]
Y_p	-2.27×10^{-1}	-2.34×10^{-1}	9.4%	3.62
Y_f	-3.67×10^{-3}	-3.56×10^{-3}	9.4%	3.16
Y	-2.31×10^{-1}	-2.38×10^{-1}	9.1%	3.63
Z_p	-	2.38×10^{-1}	4.7%	[2]
Z_f	-	1.13×10^{-3}	8.1%	[1]
Z	-	2.39×10^{-1}	4.7%	[2]
K_p	1.10×10^{-1}	1.12×10^{-1}	4.0%	6.56
K_f	4.81×10^{-3}	4.67×10^{-3}	9.1%	3.17
K	1.15×10^{-1}	1.16×10^{-1}	3.5%	7.07
M_p	-7.86×10^{-3}	-6.96×10^{-3}	36.3%	6.52
M_f	-	-3.74×10^{-4}	343.1%	[1]
M	-8.02×10^{-3}	-7.34×10^{-3}	26.2%	5.25
N_p	-7.25×10^{-2}	-7.45×10^{-2}	7.6%	6.16
N_f	-5.97×10^{-5}	-3.77×10^{-5}	179.5%	4.63
N	-7.26×10^{-2}	-7.45×10^{-2}	7.5%	6.18

[1] Oscillatory convergence
[2] Monotonic divergence
[3] Oscillatory divergence

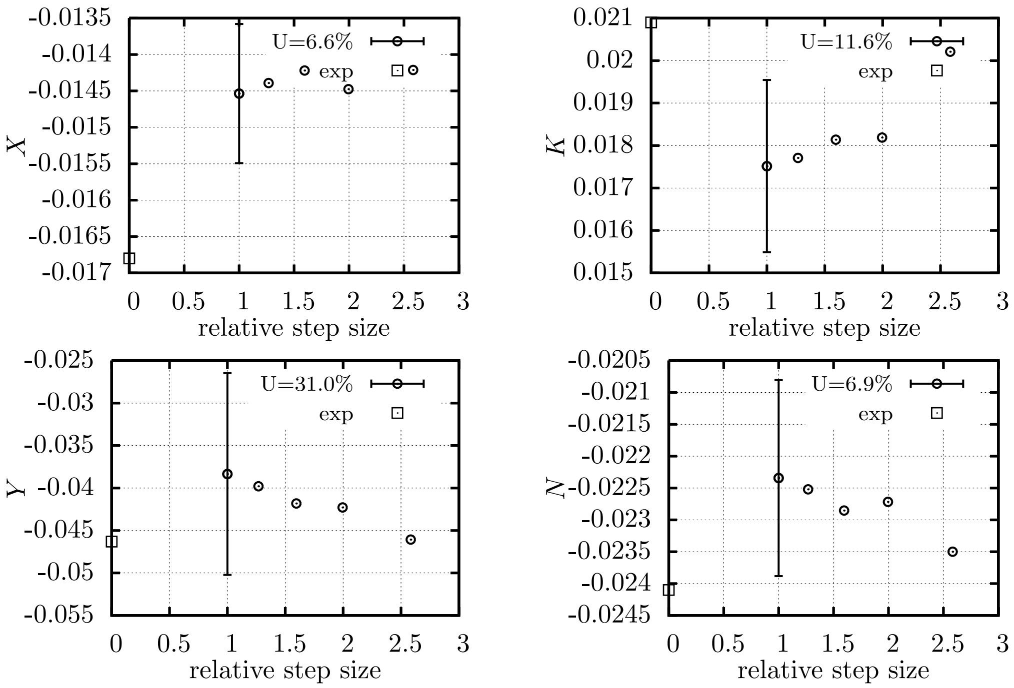

Figure 5.7: Uncertainty analysis, HTC, $\beta = 10°$, $18\,kn$, ReFRESCO

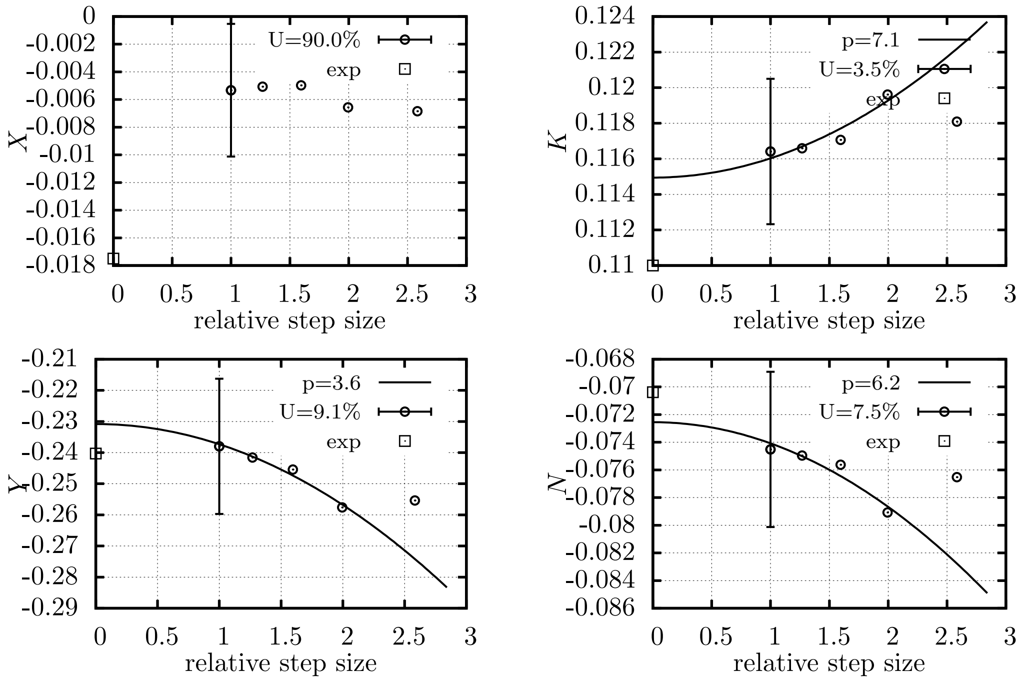

Figure 5.8: Uncertainty analysis, HTC, $\beta = 30°$, $18\,kn$, ReFRESCO

5.3.3 Discretisation error for steady yaw motion

For a non-dimensional rotation rate of $\gamma = -0.2$, a series of geometrically similar grids has been generated in order to investigate the discretisation error for PARNASSOS. The base grids used are the same as those used for the uncertainty estimation for a steady drift angle of 10°. The grid coarsening has been conducted in all three directions. Table 5.11 presents the number of nodes and y_2^+ values for these grids obtained for the 10 kn condition.

Table 5.11: Properties of grids for uncertainty analysis, HTC, $\gamma = -0.2$, PARNASSOS

id	γ	n_ξ	n_η	n_ζ	h_i	Nodes	y_2^+	Comment
3	-0.2	297	77	2×41	1.00	1875258	0.80	
4	-0.2	257	65	2×35	1.18	1169350	0.98	
6	-0.2	177	46	2×25	1.67	407100	1.48	based on grid 2, coarsened by 2×2×2
8	-0.2	129	33	2×18	2.35	153252	1.93	based on grid 4, coarsened by 2×2×2
9	-0.2	89	23	2×13	3.33	53222	2.78	based on grid 2, coarsened by 4×4×4
10	-0.2	73	19	2×11	4.00	30514	3.69	based on grid 1, coarsened by 5×5×5

The predicted values of the friction (index f) and pressure (index p) components as well as the total force and moment coefficients are presented in Table 5.12 with their estimated uncertainties. Based on an analysis of the results for each grid, it was decided to use the four finest grids (grids 3, 4, 6 and 8) for the uncertainty analysis.

Table 5.12: Uncertainty analysis, HTC, $\gamma = -0.2$, 10 kn, PARNASSOS

Item	ϕ_0	ϕ_1	U_ϕ	p
X_p	-1.83×10^{-3}	-2.07×10^{-3}	25.8%	5.46
X_f	-	-1.17×10^{-2}	3.3%	[1]
X	-1.35×10^{-2}	-1.38×10^{-2}	5.1%	6.05
Y_p	-	-5.76×10^{-3}	4.2%	[1]
Y_f	-2.09×10^{-4}	-2.21×10^{-4}	29.5%	2.54
Y	-	-5.98×10^{-3}	6.1%	[1]
Z_p	6.14×10^{-2}	6.04×10^{-2}	2.2%	0.71
Z_f	-	1.62×10^{-4}	4.8%	[1]
Z	6.16×10^{-2}	6.06×10^{-2}	2.2%	0.69
K_p	-2.31×10^{-3}	-2.14×10^{-3}	16.0%	5.00
K_f	-1.77×10^{-4}	-1.94×10^{-4}	25.3%	2.68
K	-2.49×10^{-3}	-2.33×10^{-3}	12.6%	5.60
M_p	-	-1.24×10^{-3}	6.2%	[1]
M_f	-	2.93×10^{-4}	2.7%	[1]
M	-	-9.50×10^{-4}	8.8%	[1]
N_p	-	7.34×10^{-3}	10.7%	[2]
N_f	-1.06×10^{-4}	-1.11×10^{-4}	9.4%	2.24
N	-	7.22×10^{-3}	10.9%	[2]

[1] Oscillatory convergence
[2] Monotonic divergence
[3] Oscillatory divergence

Similar to what was found for steady drift, the absolute uncertainty in the pressure components is larger than in the friction components. Compared to the calculations for steady drift, the relative uncertainties for the rotational motion results are in most cases smaller.

In Figure 5.9 the longitudinal force X, transverse force Y, heel moment K and yawing moment N are given for the different grids. It is seen that the results do not differ much between the individual results, but convergence is not always found due to scatter. For a relative step size below 3, reasonably consistent results are however found.

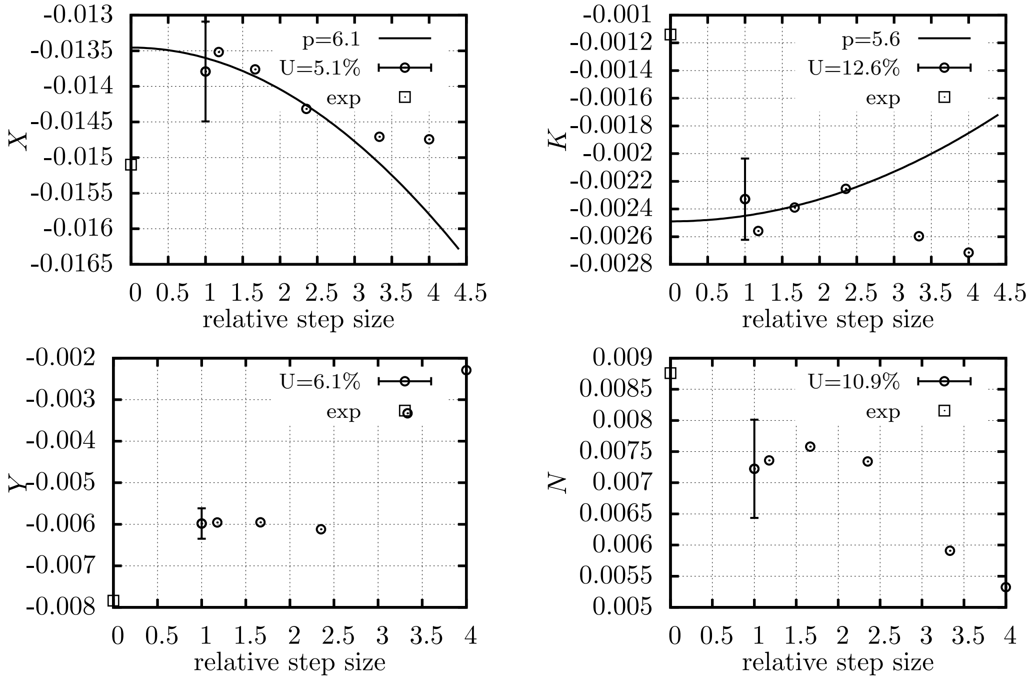

Figure 5.9: Uncertainty analysis, HTC, $\gamma = -0.2$, PARNASSOS
(Experimental values for $18\,kn$ *condition)*

Using the grids summarised in Table 5.8, the uncertainties in the ReFRESCO results for non-dimensional rotation rates of $\gamma = 0.2$ and $\gamma = 0.4$ were determined. Based on an analysis of the results for each grid, it was decided to use the four finest grids for the uncertainty analysis, which is presented in Table 5.13 and Figure 5.10 for $\gamma = 0.2$ and Table 5.14 and Figure 5.11 for $\gamma = 0.4$.

The convergence with grid refinement for rotational motion is slightly better (more realistic apparent orders of convergence) than the grid sensitivity for steady drift presented in Table 5.9.

5.3.4 Local quantities

In both the PARNASSOS and ReFRESCO calculations for drift angles larger than 10°, or as well as for large rotation rates, an area of flow separation was found at the leeward side of the bulbous bow, see Figure 5.12 for $\gamma = 0.4$. This area is probably caused by the

Table 5.13: Uncertainty analysis, HTC, $\gamma = 0.2$, 18 kn, ReFRESCO

Item	ϕ_0	ϕ_1	U_ϕ	p
X_p	-	-2.39×10^{-3}	30.1%	[2]
X_f	-1.14×10^{-2}	-1.10×10^{-2}	4.2%	1.02
X	-1.48×10^{-2}	-1.34×10^{-2}	12.7%	0.54
Y_p	8.53×10^{-3}	7.41×10^{-3}	19.3%	1.61
Y_f	-	1.70×10^{-4}	15.6%	[2]
Y	8.71×10^{-3}	7.58×10^{-3}	19.1%	1.59
Z_p	-	6.56×10^{-2}	3.7%	[1]
Z_f	1.29×10^{-4}	1.31×10^{-4}	2.5%	5.22
Z	-	6.57×10^{-2}	3.7%	[1]
K_p	1.43×10^{-3}	1.98×10^{-3}	35.1%	1.31
K_f	-2.29×10^{-4}	-1.63×10^{-4}	51.2%	0.74
K	1.22×10^{-3}	1.82×10^{-3}	41.7%	1.28
M_p	-	-8.67×10^{-4}	76.5%	[2]
M_f	-2.83×10^{-4}	-2.74×10^{-4}	3.8%	0.91
M	-	-1.14×10^{-3}	56.2%	[2]
N_p	-5.96×10^{-3}	-7.46×10^{-3}	25.4%	0.85
N_f	-1.17×10^{-4}	-1.11×10^{-4}	7.3%	0.70
N	-6.07×10^{-3}	-7.57×10^{-3}	24.9%	0.85

[1] Oscillatory convergence
[2] Monotonic divergence
[3] Oscillatory divergence

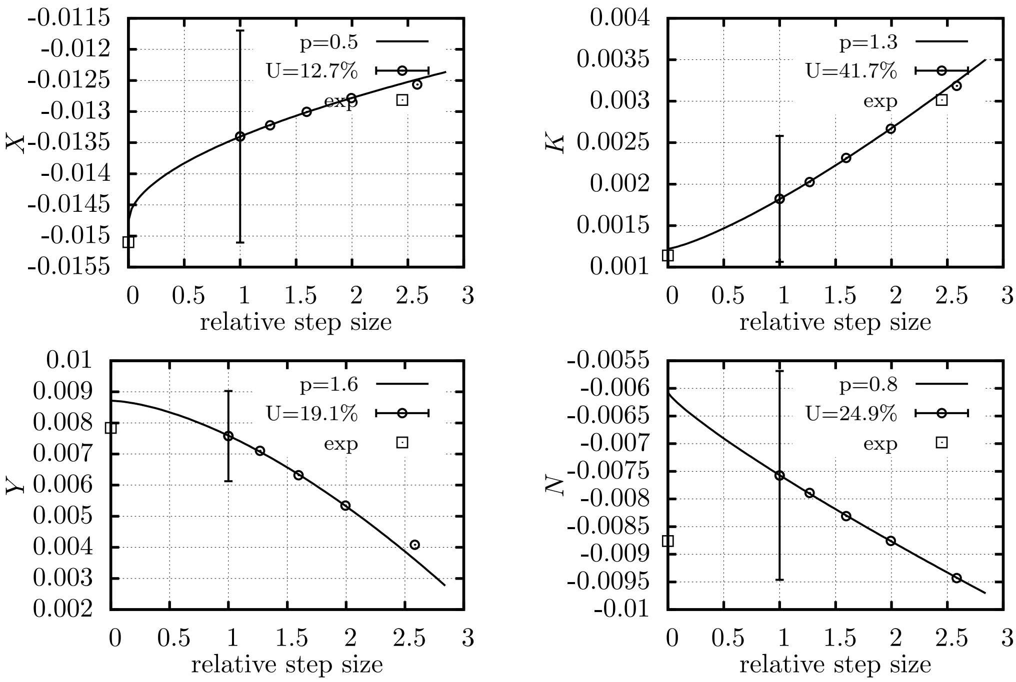

Figure 5.10: Uncertainty analysis, HTC, $\gamma = 0.2$, 18 kn, ReFRESCO

Table 5.14: Uncertainty analysis, HTC, $\gamma = 0.4$, $18\,kn$, REFRESCO

Item	ϕ_0	ϕ_1	U_ϕ	p
X_p	-3.37×10^{-3}	-3.16×10^{-3}	20.5%	2.19
X_f	-1.20×10^{-2}	-1.16×10^{-2}	5.1%	0.96
X	-1.52×10^{-2}	-1.47×10^{-2}	4.3%	1.66
Y_p	1.61×10^{-2}	1.50×10^{-2}	9.7%	2.02
Y_f	3.39×10^{-4}	3.52×10^{-4}	4.9%	1.98
Y	1.64×10^{-2}	1.53×10^{-2}	9.3%	2.02
Z_p	-	7.30×10^{-2}	7.2%	[2]
Z_f	1.60×10^{-4}	1.64×10^{-4}	2.9%	2.01
Z	-	7.32×10^{-2}	7.2%	[2]
K_p	3.33×10^{-3}	3.55×10^{-3}	8.0%	2.03
K_f	-	-3.75×10^{-4}	8.2%	[2]
K	2.95×10^{-3}	3.17×10^{-3}	9.3%	2.01
M_p	-	-1.23×10^{-3}	125.7%	[2]
M_f	-2.96×10^{-4}	-2.87×10^{-4}	3.9%	0.81
M	-	-1.52×10^{-3}	100.6%	[2]
N_p	-1.68×10^{-2}	-1.82×10^{-2}	9.3%	1.35
N_f	-	-2.15×10^{-4}	3.7%	[1]
N	-1.71×10^{-2}	-1.84×10^{-2}	9.1%	1.36

[1] Oscillatory convergence
[2] Monotonic divergence
[3] Oscillatory divergence

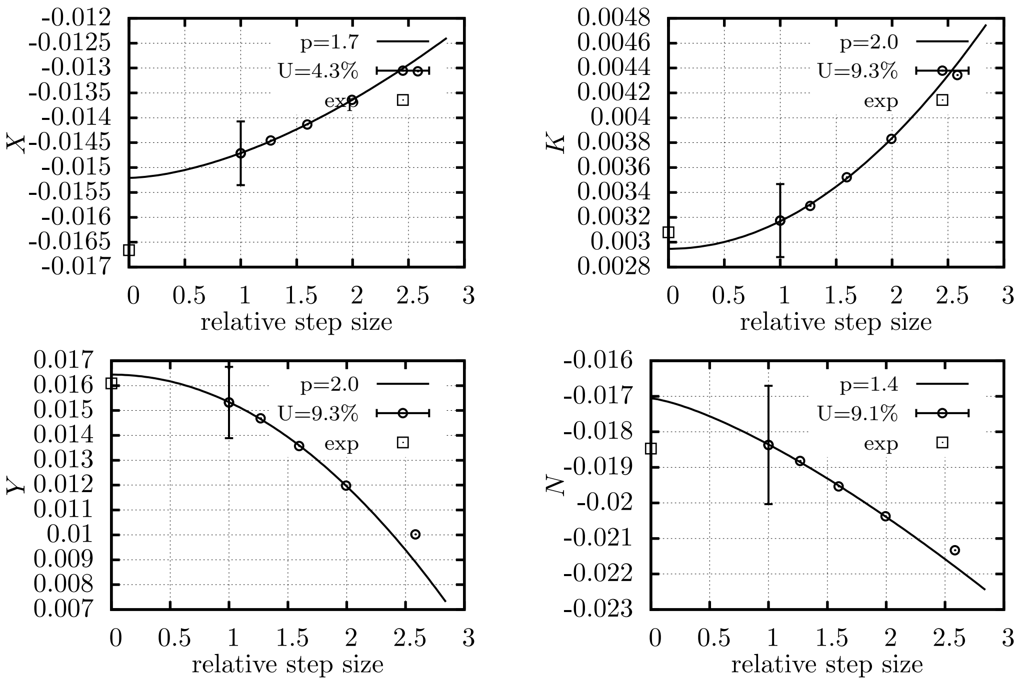

Figure 5.11: Uncertainty analysis, HTC, $\gamma = 0.4$, $18\,kn$, REFRESCO

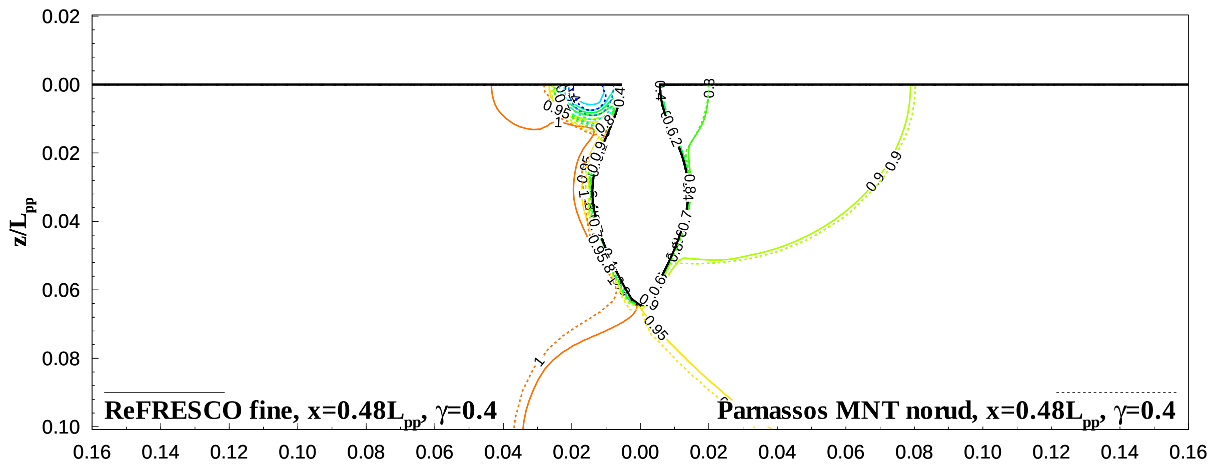

Figure 5.12: Comparison between ReFRESCO *and* Parnassos, *HTC,* $x = 0.48L_{\mathrm{pp}}$, $18\,kn$ *(solid lines:* ReFRESCO, *dotted lines:* Parnassos*)*

neglect of the free water surface and may lead to errors in the prediction of the forces on the hull.

The experimental data of the wake field in a plane $0.48L_{\mathrm{pp}}$ aft of midship have kindly been made available by HSVA[2]. In the upper half of Figure 5.13 a comparison of the non-dimensional axial velocity fields between the experiments (dotted lines) and the calculations (solid lines) for a non-dimensional yaw rate γ of 0.4 is presented. The non-dimensional axial velocity along a horizontal line in this plane at $z = 0.05L_{\mathrm{pp}}$ is given in the lower half of the figure. This figure shows that in most parts of the plane, the viscous-flow calculations correspond reasonably well with the experiments, especially at port side (windward). At the leeward side, the wakes of three different vortices are found in the Parnassos results: around $y = 0.01L_{\mathrm{pp}}$ the vortex generated at the stern, around $y = 0.04L_{\mathrm{pp}}$ the vortex generated at the bow and at $y = 0.07L_{\mathrm{pp}}$ the vortex generated at the starboard bilge. In the ReFRESCO results and in the experiments, only the wakes of two vortices are seen. Based on an analysis of the flow along the length of the ship calculated by ReFRESCO, it was observed that the bow vortex merges with the vortex generated at the bilge. Apparently, this effect is not captured by Parnassos. The difference between the experiments and the calculation is mainly caused by the relatively coarse grid used for the Parnassos calculations.

Overall, it is concluded that the flow field at the propeller plane is predicted reasonably well.

[2]The actual immersion of the PIV probe, which served as reference for the position of the field of view during the wake field measurements, was unknown, because the immersion was measured before the final adjustment of the model condition when the model still had a considerable trim by the stern due to the weight of the PIV equipment. Based on the apparent location of the propeller hub and the ship hull, a vertical shift by about $0.011L_{\mathrm{pp}}$ has been applied.

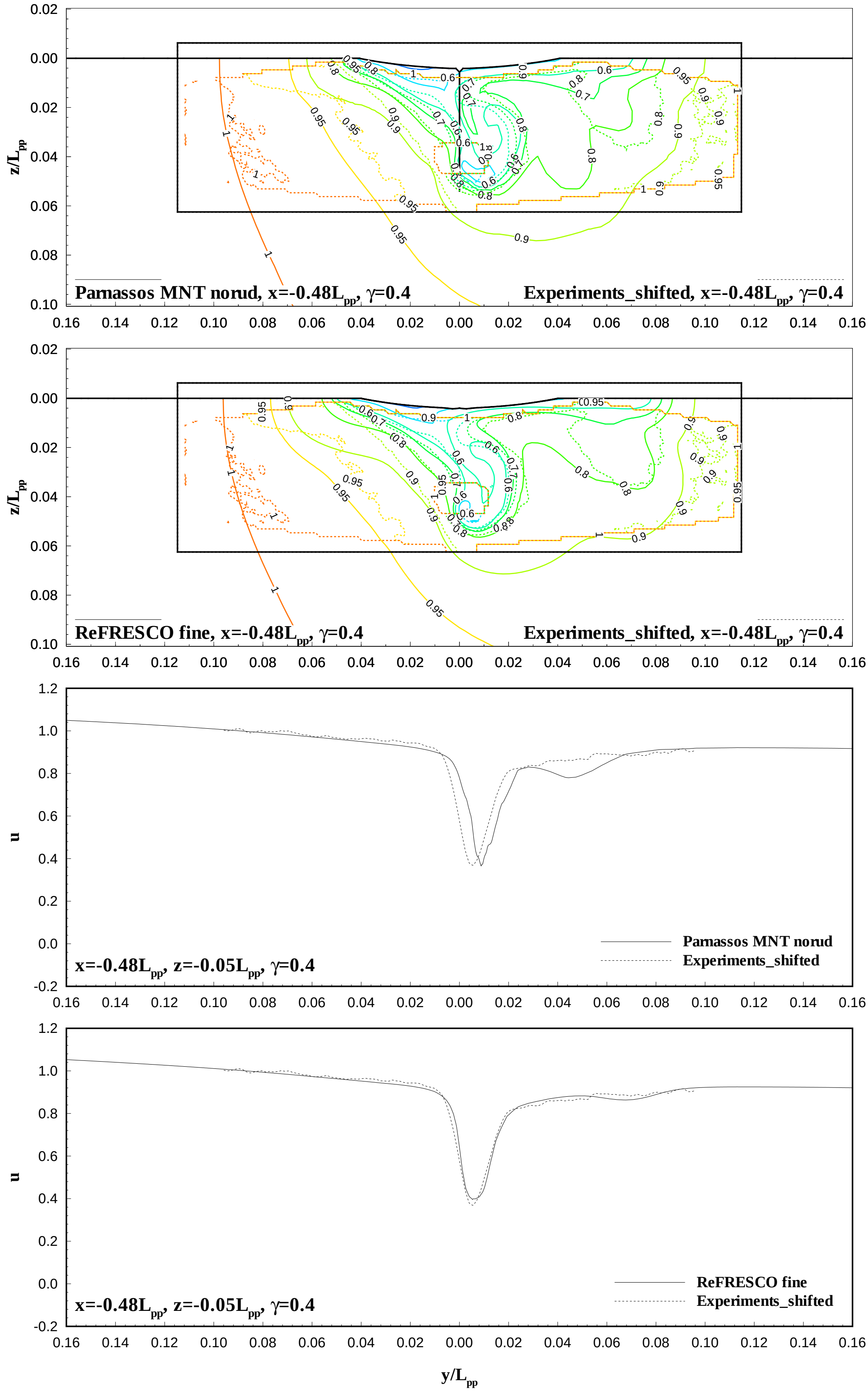

Figure 5.13: Comparison with experiments, HTC, $x = -0.48L_{\mathrm{pp}}$, $18\,kn$ (solid lines: calculations, dotted lines: experiments)

5.3.5 Global quantities

In Figure 5.14 and Figure 5.15 the results for a speed of 18 kn are presented.

For steady drift, good agreement with the experiments is seen for the transverse force Y, heel moment K and yaw moment N results based on the viscous flow calculations using both PARNASSOS and REFRESCO. Only the results for the longitudinal force X deviate from the measured results. Within the VIRTUE project, a similar comparison was made using results from several solvers [152]. There, it was seen that the results from several solvers deviated from the measured X force, but the same solvers showed excellent agreement at a lower speed corresponding to the 10 kn condition. In the calculations using these solvers, the deformation of the free surface was neglected (double body assumption). The discrepancy between the calculations and measurements presented in Figure 5.14 can therefore be caused by the neglect of free surface deformation, and therefore speed effects, or due to uncertainty in the measurements.

For rotational motion, the prediction of the yaw moment N is good, but deviations are seen for the other forces and moment. The magnitudes of the Y force and heel moment K during pure rotation are, however, very small and of less significance than the other forces or moments. Furthermore, it can be expected that the uncertainty in the measurements for the Y force and K moment is relatively high, since the hydrodynamic contribution in these forces or moments is found by subtracting the relatively high centrifugal components from the measured components.

Comparing the PARNASSOS and REFRESCO calculations, some differences can be seen. For steady drift, the differences are small and of the same order of magnitude as the uncertainty in the predictions. In general, the Y force and N moment predicted by PARNASSOS as a function of the drift angle β are slightly closer to the measurements than the REFRESCO results. This may be caused by the use of a different turbulence model.

For steady yaw, the differences are somewhat larger and for these calculations, the REFRESCO calculations are slightly closer to the measurements. This may be caused by either a much finer grid for REFRESCO (i.e. 5.2 million versus 1.9 million for PARNASSOS), or by the different turbulence model.

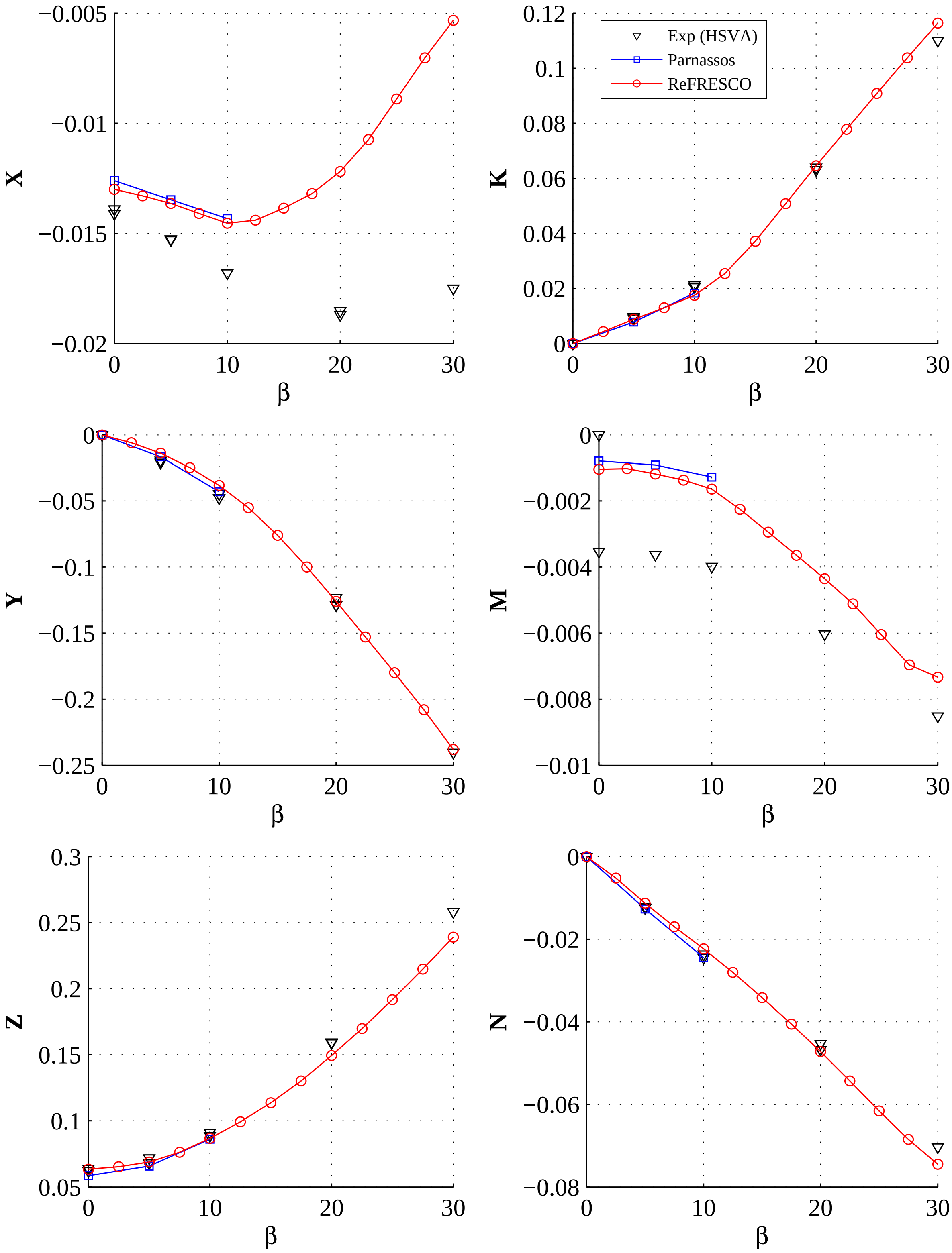

Figure 5.14: Comparison between experiments and calculations, HTC, 18 kn, steady drift

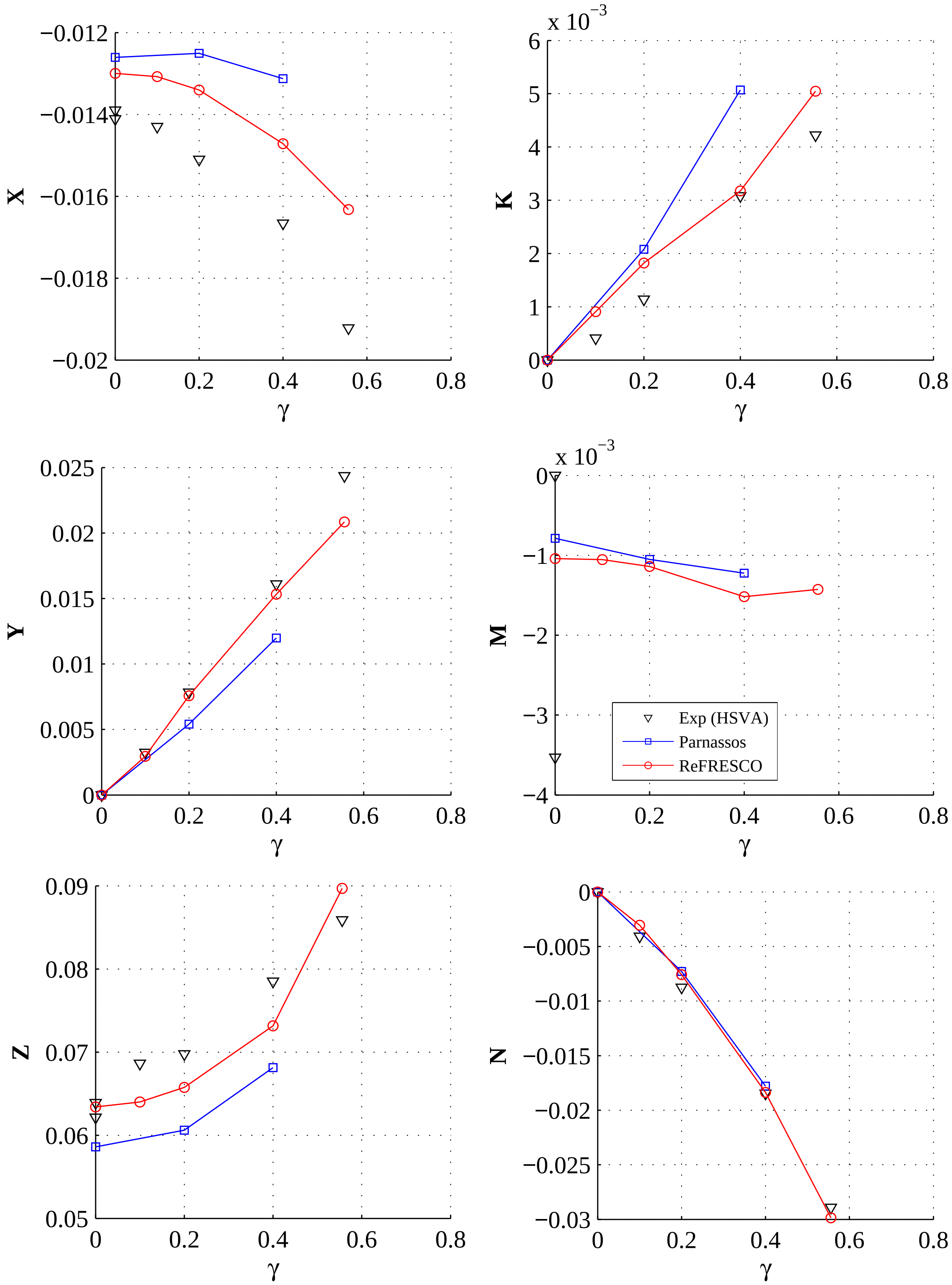

Figure 5.15: Comparison between experiments and calculations, HTC, 18 kn, steady yaw

5.3.6 Validation

The uncertainties in the measurements of the forces and moments have not been specifically determined. However, an estimate of the uncertainty U_D can be made based on results obtained for similar test conditions during measurements at the start of VIRTUE and measurements conducted later in the project. Some tests were repeated and for each test, the uncertainty was estimated using an arbitrary factor of safety of 1.25, i.e. $U_D = 1.25 \times \text{abs}\,(\phi_{\text{test1}} - \phi_{\text{test2}})$. The overall data uncertainty for the HTC experiments is taken from the average of the data uncertainties obtained for several repeat tests. With these estimated data uncertainties and assuming that the simulation numerical uncertainty U_{SN} is only influenced by the discretisation uncertainty U_G (i.e. $U_{SN} = U_I + U_G = U_G$), Table 5.15 and Table 5.16 can be constructed.

The PARNASSOS result for $\beta = 10°$ shows that for the longitudinal and transverse forces X and Y the comparison errors $|E|$ are smaller than the validation uncertainties U_{val} which means that the solution is validated at levels of 13.3% and 21.1% respectively. These levels are judged to be relatively high and indicate that the numerical uncertainty needs to be reduced if lower validation levels are desired. For the heel moment K and the yawing moment N validation is not achieved ($|E| > U_{\text{val}}$), which indicates modelling errors. Changes in turbulence model or domain size or the inclusion of free surface may lead to improvements of the comparison error.

The REFRESCO result for Y for $\beta = 10°$ is validated at a level of 27.2%, which is high. The numerical uncertainty U_{SN} needs to be reduced to reduce the validation level. The yaw moment N is validated at an acceptable level of 8.3%. The other components are not validated and indicate modelling errors. For the higher drift angle $\beta = 30°$, Y and N are validated at levels of 12.8% and 9.5% respectively, which are reasonable values.

For the steady rotation case, $\gamma = 0.2$ with PARNASSOS (the results have been obtained by mirroring the $\gamma = -0.2$ results for comparison with the REFRESCO results), the comparison errors $|E|$ are larger than the validation uncertainties for all forces and moments. Since experimental results for the 10 kn condition with $\gamma = 0.2$ were not available, the experimental values for the 18 kn condition were used for comparison. This mainly introduces an error in the longitudinal force X due to a difference in the frictional resistance and therefore a large comparison error in X is to be expected. For the other components, the influence of the different speed is expected to be of less influence and therefore the validation should still provide insight into the accuracy of the calculations. Even though a comparison between two speed conditions is made, it is concluded based on the validation that the large values of the comparison errors indicate that modelling errors are present in the simulation results.

For REFRESCO, the comparison errors $|E|$ for $\gamma = 0.2$ are smaller than for PARNASSOS. Together with the higher numerical uncertainties U_{SN}, this leads to validation of X, Y, K and N at levels of 11.4%, 20.6%, 66.8% and 22.2%, respectively. These levels are high and U_{SN} needs to be reduced to obtain lower validation levels.

The REFRESCO results for $\gamma = 0.4$ for Y, K and N are validated at levels of 12.7%, 10.5% and 10.5% respectively, which are judged to be reasonable. The comparison errors $|E|$ for all components are found to be small. For X, modelling errors appear to be present, which might be improved by incorporating free surface deformation.

Table 5.15: Validation, HTC, 10 kn, PARNASSOS

Validation, $\beta = 10°$

	X	Y	K	N
$D \times 10^3$	-16.6	-46.3	20.6	-22.9
$S \times 10^3$	-15.7	-44.2	17.9	-24.4
$E = S - D$ (%D)	-5.8	-4.4	-13.2	6.6
U_D (%D)	1.4	9.1	4.3	5.3
U_{SN} (%S)	14.1	19.9	7.5	1.2
$U_{\text{val}} = \sqrt{U_D^2 + U_{SN}^2}$ (%D)	13.3	21.1	7.8	5.4
Validated?	✔	✔	✘	✘

Validation, $\gamma = 0.2$

X	Y	K	N
-15.1	-7.8	-1.1	8.8
-12.5	-5.4	-2.1	7.3
-17.2	-31.1	82.4	-16.8
1.4	9.1	4.3	5.3
6.1	6.1	12.6	10.9
5.2	10.0	23.4	10.5
✘	✘	✘	✘

Table 5.16: Validation, HTC, 18 kn, REFRESCO

Validation, $\beta = 10°$

	X	Y	K	N
$D \times 10^3$	-16.8	-46.3	20.9	-24.1
$S \times 10^3$	-14.5	-38.4	17.5	-22.3
$E = S - D$ (%D)	-13.5	-17.2	-16.1	-7.3
U_D (%D)	1.4	9.1	4.3	5.3
U_{SN} (%S)	6.6	31.0	11.6	6.9
$U_{\text{val}} = \sqrt{U_D^2 + U_{SN}^2}$ (%D)	5.9	27.2	10.6	8.3
Validated?	✘	✔	✘	✔

Validation, $\gamma = 0.2$

X	Y	K	N
-15.1	-7.8	-1.1	8.8
-13.4	-7.6	-1.8	7.6
-11.2	-3.4	59.8	-13.5
1.4	9.1	4.3	5.3
12.7	19.1	41.7	24.9
11.4	20.6	66.8	22.2
✔	✔	✔	✔

Validation, $\beta = 30°$

	X	Y	K	N
$D \times 10^3$	-17.5	-240.3	110.0	-70.4
$S \times 10^3$	-5.3	-238.0	116.4	-74.5
$E = S - D$ (%D)	-69.6	-1.0	5.8	5.9
U_D (%D)	1.4	9.1	4.3	5.3
U_{SN} (%S)	90.0	9.1	3.5	7.5
$U_{\text{val}} = \sqrt{U_D^2 + U_{SN}^2}$ (%D)	27.4	12.8	5.6	9.5
Validated?	✘	✔	✘	✔

Validation, $\gamma = 0.4$

X	Y	K	N
-16.7	-16.1	-3.1	18.5
-14.7	-15.3	-3.2	18.4
-11.7	-4.8	3.1	-0.6
1.4	9.1	4.3	5.3
4.3	9.3	9.3	9.1
4.0	12.7	10.5	10.5
✘	✔	✔	✔

5.4 DARPA SUBOFF

The DARPA SUBOFF hull form has been described in section 2.5.2. In this thesis, only the bare hull (AFF-1) configuration is considered. This section presents RANS calculations for the bare hull and a comparison is made with the experimental validation data.

In earlier work, calculations were made using PARNASSOS with Menter's one-equation turbulence model. First, an H-O grid topology was used and large comparison errors in the longitudinal force X were found, see Toxopeus [147]. Subsequently, an alternative grid-layout, i.e. an axi-symmetric grid, was used. It was found that this reduced the comparison error considerably, but not completely. By using the axi-symmetric grid together with the TNT version of the $k-\omega$ turbulence model, the comparison error became smaller than the validation uncertainty. This work demonstrated the large influence of the grid layout and the turbulence model.

Inspired by this earlier work, new calculations for the DARPA SUBOFF bare hull form were made using REFRESCO. Some of these calculations were compared to the PARNASSOS results. This comparison was presented in Toxopeus and Vaz [151] and is not repeated here for brevity. For all REFRESCO calculations, use was made of Menter's SST version of the two-equation $k-\omega$ turbulence model. Some additional calculations were performed with the one-equation Spalart-Allmaras (SA) turbulence model.

The governing equations were integrated down to the wall, i.e. no wall-functions are used. The flow was solved using a steady approach. Two sets of calculations were conducted: a first set for $Re = 12 \times 10^6$ at $\beta = 0°$ and $\beta = 2°$ for comparison with the flow field, pressure and friction measurements in the wind tunnel by Huang et al. [68], and a second set for $Re = 14 \times 10^6$ at a range of drift angles between 0° and 18° for comparison with force measurements in the towing tank by Roddy [116].

It should be noted that for the SUBOFF results the coordinate system and non-dimensionalisation of the forces and moments differs from those adopted in the rest of this thesis: all forces and moments are made non-dimensional using a reference area of L_{pp}^2 instead of $L_{\mathrm{pp}}T$ and the yaw moment is given relative to the centre of buoyancy, instead of with respect to midship. Additionally, the coordinate x indicates the distance along the ship length from the bow, positive aft.

An overview of all experimental and computational results of the forces and moments on the SUBOFF AFF-1 configuration for captive conditions is given in the table on page 159.

5.4.1 Iterative error

All calculations were run until the maximum non-dimensional residual of the pressure $\mathrm{res}_{p,\max}$ (the so-called L_∞ norm) between successive iterations had dropped well below $1 \cdot 10^{-5}$ or when further iterative convergence was not obtained. The changes in the non-dimensional integral quantities (forces and moments) were well below 1×10^{-7}. This is more than two to three orders of magnitude smaller than the discretisation uncertainty and therefore the iterative uncertainty U_I can be neglected, see Eça et al. [41].

5.4.2 Discretisation error

The results were all obtained on structured axi-symmetric grids with O-O topology. For each grid, the variation in the number of grid nodes in the stream-wise, normal and girth-wise (n_ξ, n_η and n_ζ) directions is given in Table 5.17.

Table 5.17: Properties of grids for uncertainty analysis, SUBOFF, $\beta = 0°$, 18°

id	β	n_ξ	n_η	n_ζ	h_i ($\beta = 0°$)	h_i ($\beta = 18°$)	Nodes $\times 10^{-3}$	Comment
1	0	275	119	129	1.00	-	4222	
2	0,18	241	105	113	1.14	1.00	2859	
3	0,18	201	87	93	1.39	1.22	1626	
4	0,18	171	75	81	1.60	1.40	1039	
5	0,18	138	60	65	2.00	1.75	538	
6	0,18	121	53	57	2.29	2.00	366	based on grid 2, coarsened by 2×2×2
7	0,18	101	31	47	2.78	2.43	147	based on grid 3, coarsened by 2×2×2
8	0,18	86	38	41	3.20	2.80	134	based on grid 4, coarsened by 2×2×2
9	0,18	61	27	29	4.57	4.00	48	based on grid 2, coarsened by 4×4×4

For $Re = 14 \times 10^6$, the discretisation error has been investigated. In Table 5.18 and Figure 5.16, the results for $\beta = 0°$ are presented. The graphs show that scatter exists in the data: the data points are not exactly aligned along the curve. Reasons for this might be e.g. the non-evenly spaced cell nodes, the use of numerical limiters or lack of perfect geometrical similarity between the grids.

For this high Reynolds number, i.e. when convection dominates, and when using an unstructured-grid Quadratic Upwind Interpolation for Convective Kinematics (QUICK) scheme for convective fluxes, it is expected that ReFRESCO will be second order accurate [45]. The observed order of convergence p depends on the force component under consideration. For the friction force, a value just below 1 is found, indicating that the convergence with grid refinement follows a linear order of accuracy. For the other components, a much higher order is found, which is most probably caused by scatter and insufficiently fine grids.

In the previous study by Toxopeus and Vaz [151], the convergence appeared to be better. However, comparing the old (FreSCo) results with the new (ReFRESCO) results with a finer grid added, it is seen that now the four finest grids show a more consistent trend than the four finest grids in the previous study. The present results are therefore judged to be more reliable. The overall uncertainty U in X is 4.5% which is judged to be small.

In Table 5.19 and Figure 5.17, the results for $\beta = 18°$ are presented. In this case, the apparent order of convergence p ranges from 0.74 for X_f to 6.07 for X_p. This indicates

Table 5.18: Uncertainty analysis, SUBOFF, $\beta = 0°$

Item	ϕ_0	ϕ_1	U_ϕ	p
X_p	-1.22×10^{-4}	-1.29×10^{-4}	12.2%	6.71
X_f	-1.00×10^{-3}	-9.67×10^{-4}	4.4%	0.97
X	-1.11×10^{-3}	-1.10×10^{-3}	4.5%	5.05

[1] Oscillatory convergence
[2] Monotonic divergence
[3] Oscillatory divergence

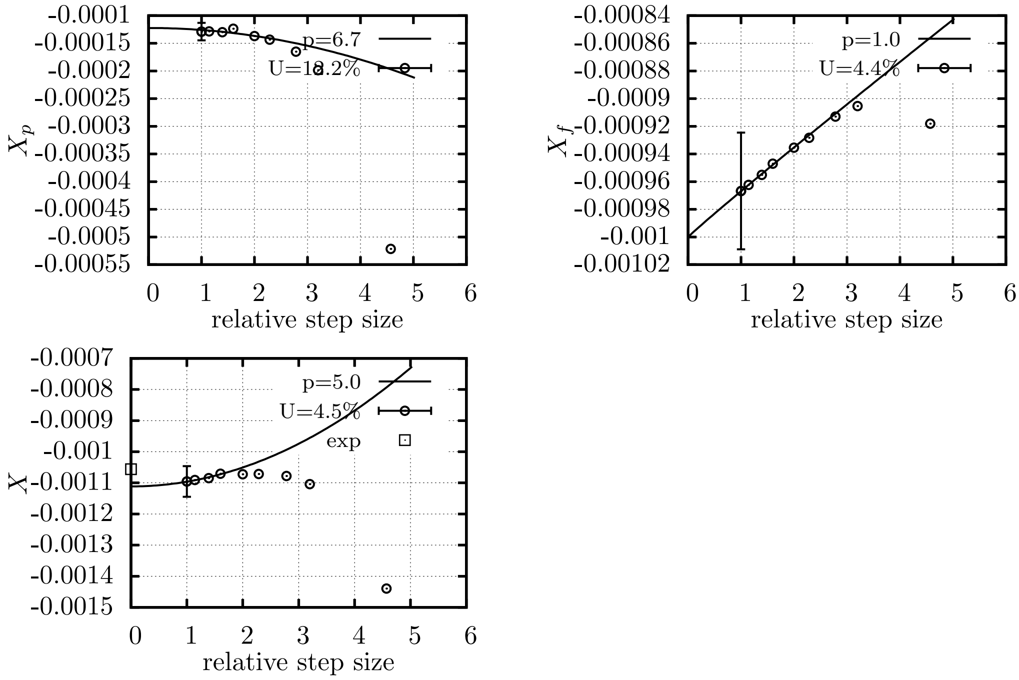

Figure 5.16: Uncertainty analysis, SUBOFF, $\beta = 0°$

that a finer grid needs to be used to obtain a solution closer to the so-called asymptotic range, where the order of convergence will be equal to or lower than the order of the discretisation scheme.

For the components of the transverse force Y and yaw moment N the apparent orders of convergence are between 0.62 and 1.21, which may indicate that for the transverse force and yawing moment the grid density is closer to the asymptotic range. The uncertainty in X is found to be relatively large. The large value is caused by the fact that for the overall force X monotonic convergence was not obtained. However, the value is acceptable from an engineering viewpoint. The uncertainty in the overall transverse force or yawing moment is judged to be small.

5.4.3 Local quantities

Sung [139] has written instructions for the Submarine Hydrodynamics Working Group (SHWG), see www.shwg.org, for the post-processing of the DARPA SUBOFF CFD calculations in order to make consistent comparisons between results of different calculations of different solvers, institutions, Reynolds numbers, grid topologies, etc. The figures pre-

Table 5.19: Uncertainty analysis, SUBOFF, $\beta = -18°$

Item	ϕ_0	ϕ_1	U_ϕ	p
X_p	2.70×10^{-4}	2.41×10^{-4}	31.7%	6.07
X_f	-1.13×10^{-3}	-1.06×10^{-3}	7.9%	0.74
X	-	-8.22×10^{-4}	11.3%	[2]
Y_p	5.21×10^{-3}	5.36×10^{-3}	3.6%	1.17
Y_f	3.26×10^{-4}	3.01×10^{-4}	10.3%	0.62
Y	5.53×10^{-3}	5.66×10^{-3}	3.0%	1.21
N_p	3.45×10^{-3}	3.40×10^{-3}	1.9%	0.81
N_f	-	1.75×10^{-5}	8.2%	[2]
N	3.47×10^{-3}	3.41×10^{-3}	2.0%	0.79

[1] Oscillatory convergence
[2] Monotonic divergence
[3] Oscillatory divergence

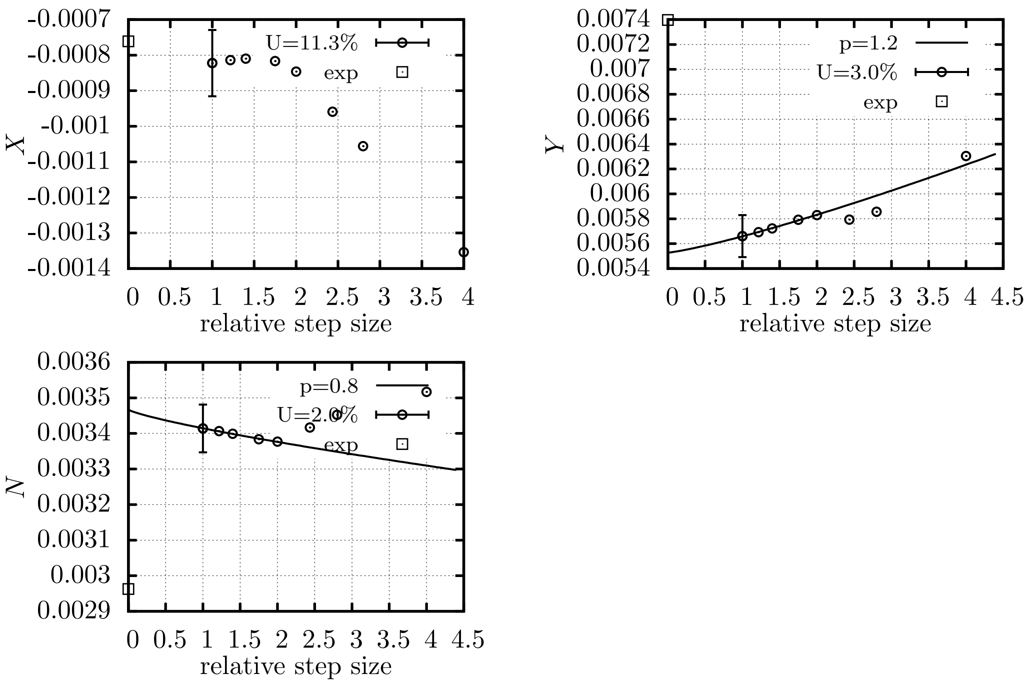

Figure 5.17: Uncertainty analysis, SUBOFF, $\beta = -18°$

sented in this section were made according to these instructions. The experimental values are obtained from flow field and pressure measurements conducted by Huang et al. [68]. These experiments were conducted at a Reynolds number of 12×10^6. The first and second cases defined in the instructions are comparisons of the pressure C_p and friction C_f coefficients along the hull, see Figure 5.18.

These graphs show that the differences in pressure coefficient between the results are negligible. A very small difference between the SST and SA results is found at the stern, which explains the difference in the longitudinal pressure coefficients X_p. For the skin friction coefficient, it is seen that the results with the SA model are in general slightly closer to the experimental data than the SST results. The differences between the results explain the differences in forces found in Table 5.20.

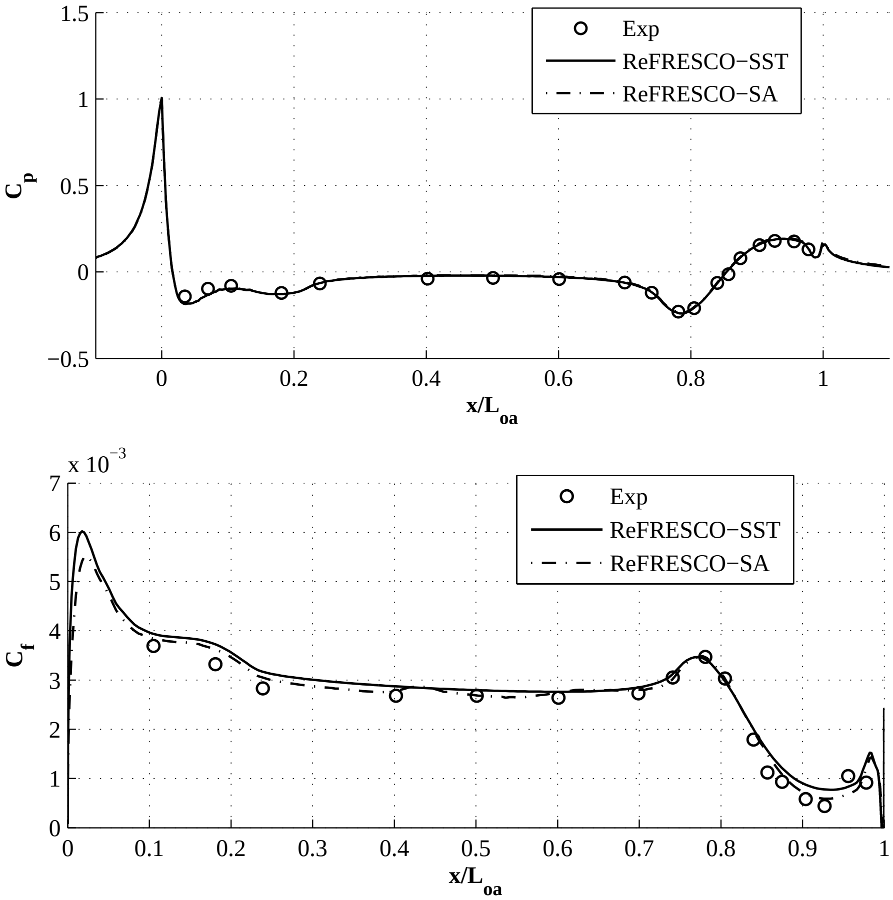

Figure 5.18: Pressure (top) and friction (bottom) coefficients along the hull, $\beta = 0°$

The predicted distribution of the pressure coefficient is close to the experiments. The trends in the predicted distribution of the friction coefficient correspond well to the trends found in the experiments. Although some discrepancies at the bow and stern area are found, it is concluded that the prediction of the pressure and skin friction coefficients is good. It is noted that the discrepancies at the bow and stern were also present in the calculations by Bull [19] and Yang and Löhner [166] and in all results submitted for a collaborative CFD study within the SHWG [146].

The difference between the SST and SA results for the streamwise V_x and radial velocities V_r at $x = 0.978L_{\text{oa}}$ in the aft part of the hull, see Figure 5.19 (top) is considered to be negligible. Comparing the computed results with the experiments, it is observed that the trends in the development of the boundary layer are very well predicted by both solvers, but quantitative discrepancies are seen. Especially the magnitudes of the radial velocities are different. It is seen that in the experiments the radial velocity changes sign between $(r - R_0)/R_{\text{max}} = 2$ and $(r - R_0)/R_{\text{max}} = 0.8$, suggesting outward radial flow in the far field. This may be caused by the use of an open-jet wind tunnel.

In this study, also the correlation between the measured and the predicted Reynolds shear stresses is investigated by comparison of $\frac{-\overline{V_x'V_r'}}{V_0^2}$. Following the eddy-viscosity assumption, the Reynolds stresses are defined by:

$$-\overline{V_x'V_r'} = 2 \cdot \nu_t \cdot S_{ij} \tag{5.6}$$

with eddy viscosity ν_t and strain rate tensor S_{ij}

$$S_{ij} = \frac{1}{2}\left(\frac{\partial u_i}{\partial x_j} + \frac{\partial u_j}{\partial x_i}\right). \tag{5.7}$$

In Figure 5.19 (bottom), the Reynolds shear stresses for the aft-most longitudinal station are presented. It is observed that the curve representing the SST results corresponds very well with the measurements. The results using the SA turbulence model are also close to the measurements, but under-predict the peak of the distribution.

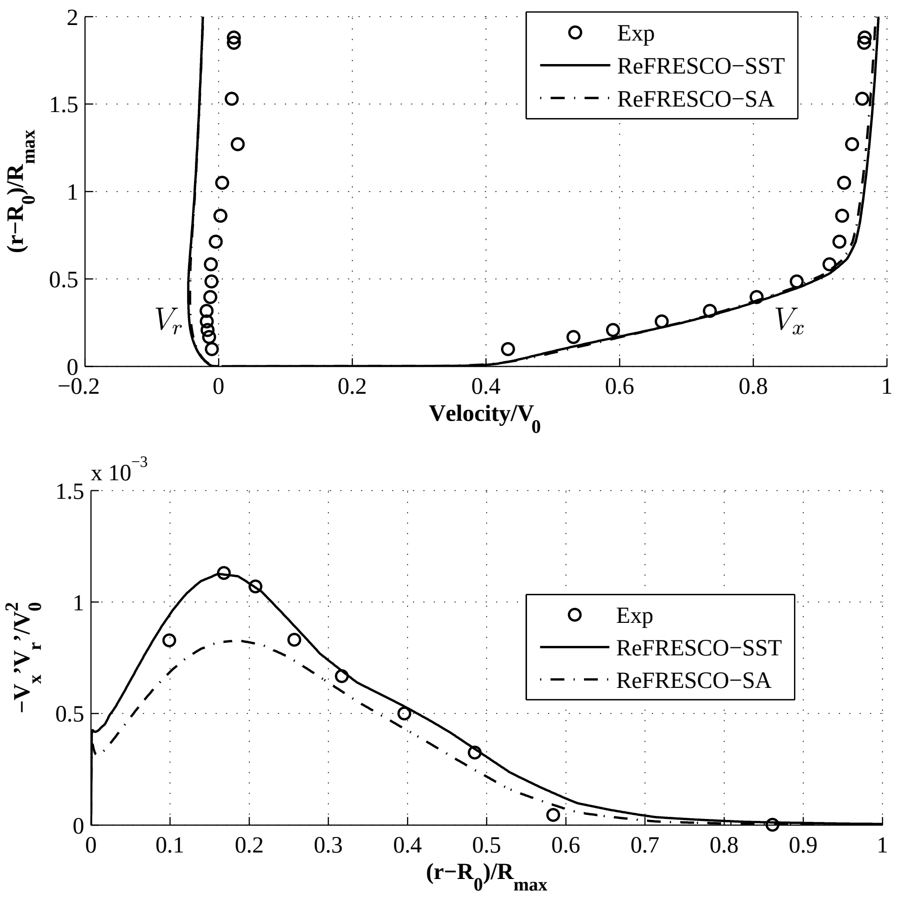

Figure 5.19: Velocities (top) and Reynolds stresses (bottom) at $x = 0.978L_{\rm oa}$, $\beta = 0°$

Figure 5.20 presents comparisons of the pressure C_p and friction C_f coefficients along the hull at the leeward plane of symmetry. Figure 5.21 shows the axial V_x, tangential V_α and radial V_r velocities (top part of the figure) and Reynolds shear stress (lower part of the figure), given for the leeward symmetry plane located at $x = 0.978L_{\rm oa}$. These graphs show that the distribution of the pressure coefficient along the length of the ship and the velocity distribution at the stern is quite well represented. The difference between the

SST and SA results is considered to be small. However, with the SA turbulence model, the radial velocity V_r appears to be too negative compared to the SST results and the results obtained using other solvers and turbulence models during the SHWG CFD study [146]. The distribution of the Reynolds shear stress shows reasonable correspondence with the measurements.

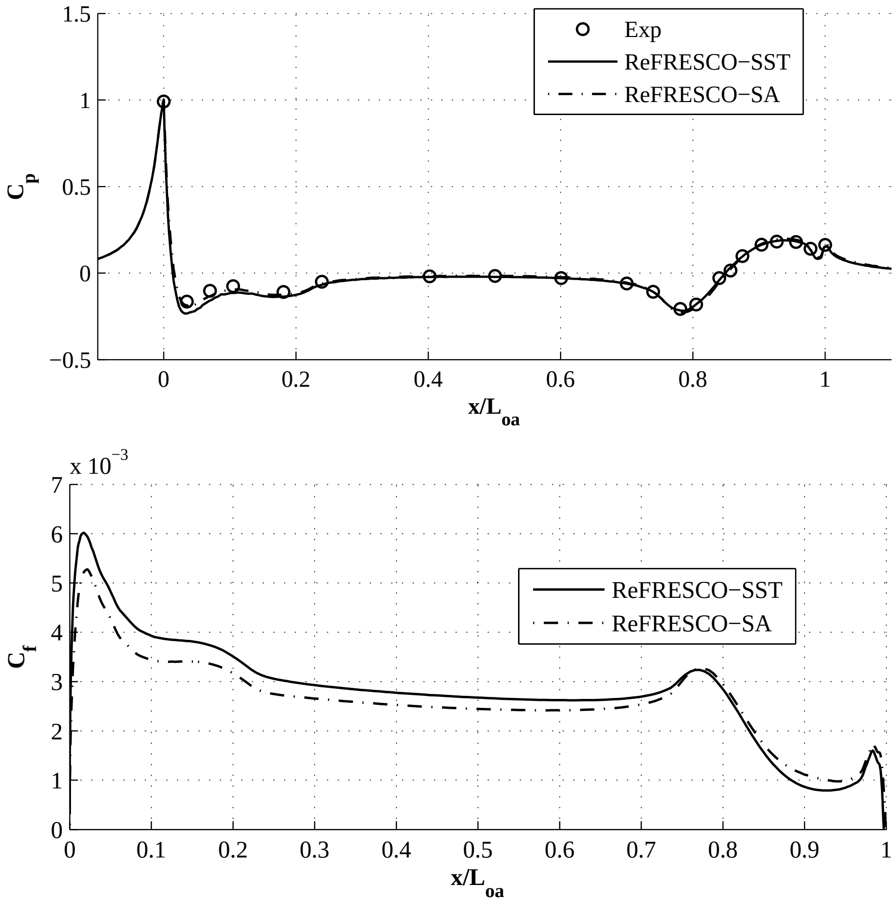

Figure 5.20: Pressure (top) and friction (bottom) coefficients along the hull, $\beta = 2°$ (leeward meridian)

5.4.4 Global quantities

Experimental force measurement results are available for the straight-ahead condition and for oblique motion and were published by Roddy [116]. The experiments were conducted in the towing basin of the David Taylor Research Center. During the tests, the model was supported by two struts. The speed in the experiments resulted in a Reynolds number of 14×10^6. For the straight-flight condition the experimental value of the longitudinal force was found to be:

$$\begin{aligned} X &= \text{average}(X_{\text{test1}}, X_{\text{test2}}) = \text{average}(-1.061, -1.051) \times 10^{-3} \\ &= -1.056 \times 10^{-3} \end{aligned} \tag{5.8}$$

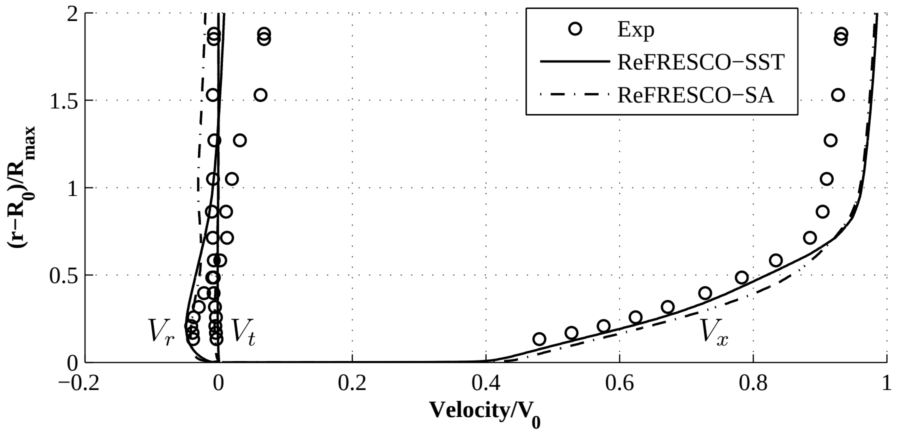

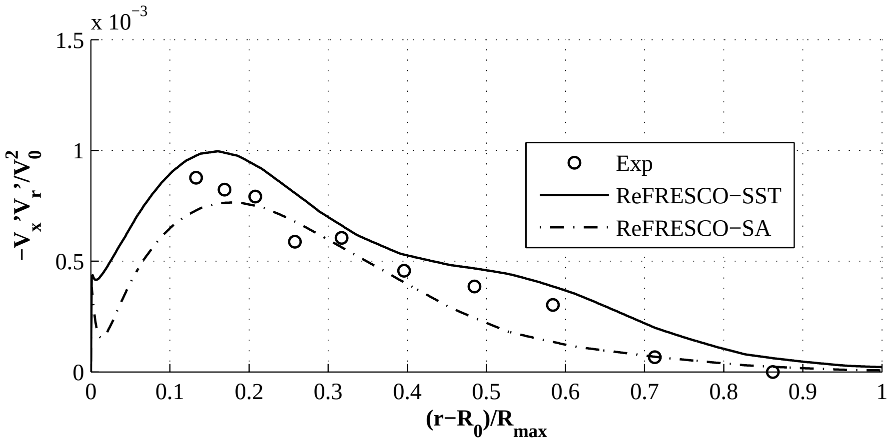

Figure 5.21: Velocities (top) and Reynolds stresses (bottom) at $x = 0.978L_{\text{oa}}$, $\beta = 2°$ (leeward meridian)

The longitudinal force components obtained from the calculations for $\beta = 0°$ are given in Table 5.20. As can be expected for submarine hull forms, the largest part (about 90%) of the total resistance is caused by friction. This means that for the bare hull, the form factor is relatively low, i.e. $(1 + k) = X/X_f = 1.13$ for SST and 1.07 for SA. From the experiments, the form factor is estimated to be $(1 + k) = X/X_{f\,(\text{ITTC})} = 1.13$. This is a normal value for a bare hull submarine.

The comparison error E between the ReFRESCO prediction of X and the measurement is about 3.7%, which is judged to be good for practical applications when also the uncertainty in the experimental data is taken into consideration. It is found that the total resistance predicted using the SST turbulence model is slightly higher than the experimental value, while the SA results are slightly lower. The skin friction coefficient predicted using SA is lower than the coefficient found using SST, as can also be observed in Figure 5.18. In the aft ship, the pressure coefficient predicted using SA is marginally higher than the pressure predicted with the SST model. This explains the lower pressure resistance found in the SA results.

Figure 5.22 presents the force and moment components obtained from the calculations and the values from the experiments for oblique inflow. In Tables 5.21 through 5.23 the

Table 5.20: SUBOFF, longitudinal force X, $Re = 1.4 \times 10^7$, $\beta = 0°$

Solver	Grid	Integral values $\times 10^3$			
		X	X_f	X_p	E (%D)
Exp (DTRC)	-	-1.061	-	-	-
Exp (DTRC)	-	-1.051	-	-	-
Mean μ_{exp}		-1.056	-	-	-
ITTC-57		-	-0.936	-	-
Schoenherr		-	-0.919	-	-
Katsui		-	-0.905	-	-
Grigson		-	-0.932	-	-
ReFRESCO-SST	4138×10^3	-1.096	-0.967	-0.129	3.7
ReFRESCO-SA	4138×10^3	-1.017	-0.950	-0.067	-3.7

results for $\beta = 18°$ are shown.

The comparison error E is about 13%, which is within the uncertainty band of the measurements. With the SA turbulence model, better agreement is found. The trends in the transverse force Y and yaw moment N are predicted reasonably well. The deviation from the measurements may be caused by the modelling error of using a steady RANS approach, which with increasing inflow angle may be disputable. Furthermore, with the O-O grid topology the grid density away from the hull reduces considerably, such that the wake may be insufficiently resolved.

The comparison shows that the turbulence model plays an important role in the prediction of the forces on the SUBOFF. This was also found during a study in which PARNASSOS was used with two different turbulence models: the SST turbulence model and the Menter one-equation model (MNT) [147]. It was found that by changing the turbulence model from MNT to SST, the comparison error in X between the experiments and the simulations reduced from 40.8% to 6.8%. Interestingly, the influence is mostly visible in X: the other forces or moments only change marginally when different turbulence models are used. This means that either more advanced turbulence models are required or that other factors such as grid layout or resolution of the grid in the wake of the submarine affect the results.

Table 5.21: SUBOFF, longitudinal force X, $Re = 1.4 \times 10^7$, $\beta = 18°$

Solver	Grid	Integral values $\times 10^3$			
		X	X_f	X_p	E (%D)
Exp (DTRC)	-	-0.670	-	-	-
Exp (DTRC)	-	-0.852	-	-	-
Mean μ_{exp}		-0.761	-	-	-
ReFRESCO-SST	4138×10^3	-0.860	-1.067	0.207	13.0
ReFRESCO-SA	4138×10^3	-0.767	-1.074	0.307	0.8

Table 5.22: SUBOFF, transverse force Y, $Re = 1.4 \times 10^7$, $\beta = 18°$

Solver	Grid	Integral values $\times 10^3$			
		Y	Y_f	Y_p	E (%D)
Exp (DTRC)	-	-7.355	-	-	-
Exp (DTRC)	-	-7.438	-	-	-
Mean μ_{exp}		-7.397	-	-	-
ReFRESCO-SST	4138×10^3	-5.383	-0.297	-5.086	-27.2
ReFRESCO-SA	4138×10^3	-5.678	-0.307	-5.371	-23.2

Table 5.23: SUBOFF, yawing moment N, $Re = 1.4 \times 10^7$, $\beta = 18°$

Solver	Grid	Integral values $\times 10^3$			
		N	N_f	N_p	E (%D)
Exp (DTRC)	-	-2.986	-	-	-
Exp (DTRC)	-	-2.939	-	-	-
Mean μ_{exp}		-2.962	-	-	-
ReFRESCO-SST	4138×10^3	-3.370	-0.017	-3.353	13.8
ReFRESCO-SA	4138×10^3	-3.383	-0.017	-3.366	14.2

5.4.5 Validation

The uncertainties in the measurements of the forces and moments have not been determined. However, validation of the solution can still be performed, when a data uncertainty U_D is assumed. To obtain an estimate of the uncertainty in the experimental data, the uncertainty U_D in the experimental data is estimated using the difference between two measurements for the same condition and a factor of safety of 1.25. For example, the uncertainty in the longitudinal force X for $\beta = 0°$ is estimated by:

$$U_D = 1.25 \times \text{abs}\left(X_{\text{test1}} - X_{\text{test2}}\right) = 1.25 \times 10^{-5} = 1.2\% \times X \tag{5.9}$$

For other incidence angles, the same procedure can be applied. With this estimated uncertainty and assuming that the simulation numerical uncertainty U_{SN} is only influenced by the discretisation uncertainty U_G (i.e. $U_{SN} = U_I + U_G = U_G$), Table 5.24 can be constructed. For $\beta = 18°$, it is seen that for the longitudinal force X the comparison error $|E|$ is smaller than the validation uncertainty U_{val} which means that the solution of X is validated at a level of 27.2%. This level is judged to be high and indicates that especially the experimental uncertainty needs to be reduced if lower validation levels are desired.

For all other forces and moments validation is not achieved ($|E| > U_{\text{val}}$), which indicates modelling errors. The magnitude of the Y force is under-predicted, while the magnitude of the N moment is over-predicted. Changes in turbulence model or in the domain size but also using higher grid densities in the wake or time accurate solution procedures may lead to improvements of the comparison error.

Table 5.24: Validation, SUBOFF

Validation, $\beta = 0°$

	X
$D \times 10^3$	-1.06
$S \times 10^3$	-1.10
$E = S - D$ (%D)	3.7
U_D (%D)	1.2
U_{SN} (%S)	4.5
$U_{\text{val}} = \sqrt{U_D^2 + U_{SN}^2}$ (%D)	4.8
Validated?	✔

Validation, $\beta = 18°$

	X	Y	N
$D \times 10^3$	-0.76	-7.40	-2.96
$S \times 10^3$	-0.86	-5.38	-3.37
$E = S - D$ (%D)	13.0	-27.2	13.8
U_D (%D)	24.0	1.1	1.6
U_{SN} (%S)	11.3	3.0	2.0
$U_{\text{val}} = \sqrt{U_D^2 + U_{SN}^2}$ (%D)	27.2	2.5	2.8
Validated?	✔	✘	✘

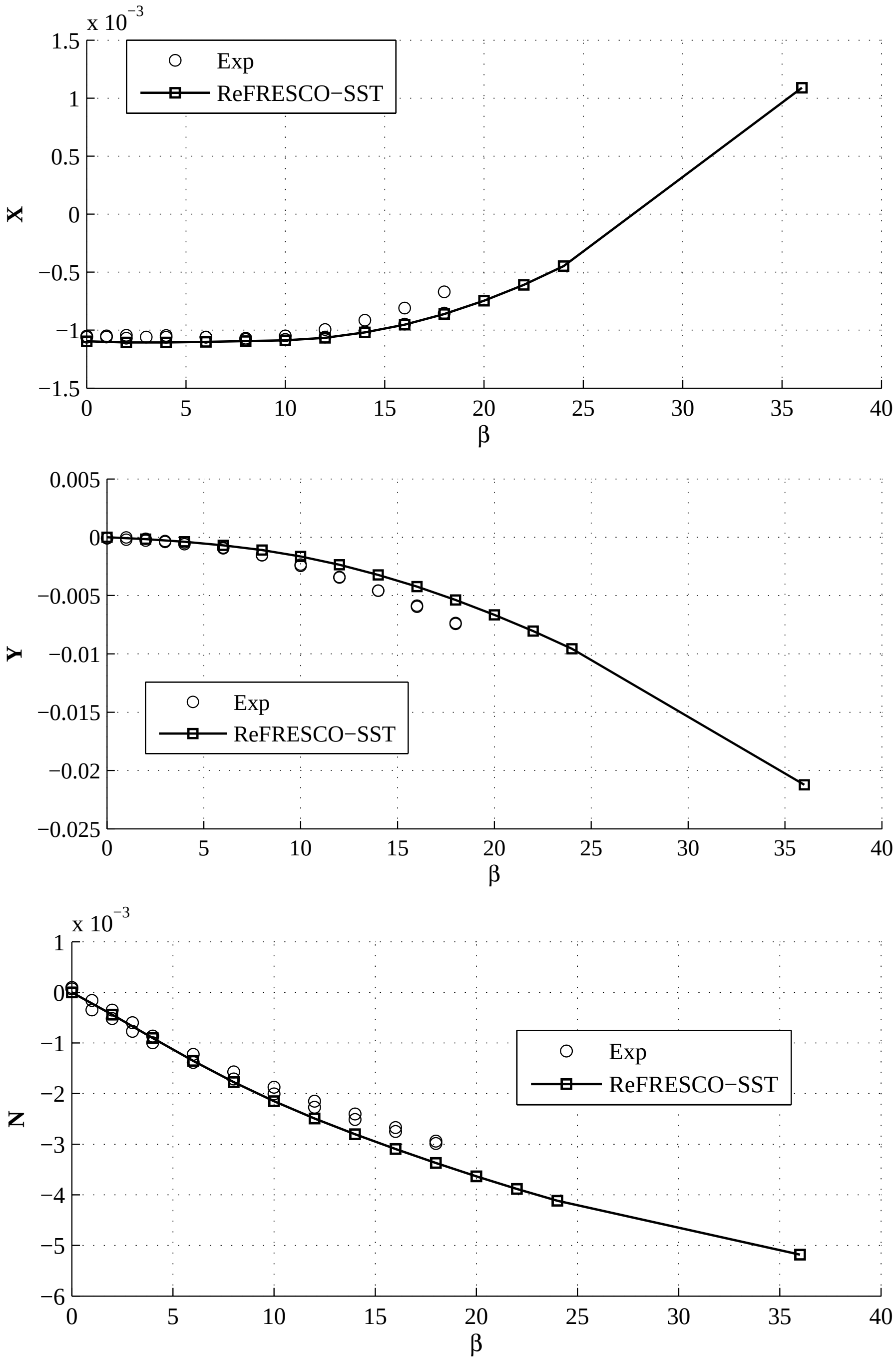

Figure 5.22: Comparison between experiments and calculations, SUBOFF, steady drift

5.5 Walrus

In work conducted for the Royal Netherlands Navy (RNLN) into the influence of the seafloor on the manoeuvrability of submarines, validation studies were performed by Bettle under the supervision of Toxopeus [15]. The flow around the Walrus bare hull form, with deck and sail was computed with ReFRESCO. Other appendages were not included in the study. The SST turbulence model was used and all equations were integrated down to the wall (y_2^+ values were below 1). Calculations have been done for a range of clearances c between the sea bottom and the submarine. In this thesis, only the deep water calculations are considered. For the steady drift calculations, the drift sweep procedure as introduced in section 4.6.2 was used.

It should be noted that for the Walrus results the coordinate system and non-dimensionalisation of the forces and moments differ from those adopted in the rest of this thesis: all forces and moments are made non-dimensional using a reference area of L_{pp}^2 instead of $L_{\mathrm{pp}}T$. The origin of the right-handed coordinate system is located at the intersection of the longitudinal axis of symmetry of the hull, midship and centre-plane.

The experiments for the Walrus-class submarine were conducted by the David W. Taylor Naval Ship Research and Development Center (DTNSRDC) [34]. Experimental results were obtained for the three configurations of the early Walrus design listed in Table 5.25.

Table 5.25: Designations and descriptions of Walrus experimental configurations [34]

♯	Hull with deck	Bridge fairwater (sail), sailplanes, sonar dome	X-tail, propeller
1	✔	✔	✔
2	✔	✔	
3	✔		

It should be noted that the design of the Walrus as used for the DTNSRDC model tests differs slightly from the real Walrus class submarine design, which was used for the present study. The largest differences compared to the real design are a slightly smaller length ($0.9\% L_{\mathrm{oa}}$) and the absence of the *Toekan* (exhaust diffuser). It is expected that this discrepancy will have only a small effect on the overall forces and moments.

The calculations were performed at $Re = 5.2 \times 10^6$ (to resemble the condition of the free sailing experiments) whereas the DTNSRDC experiments were conducted at two higher Reynolds numbers: 9 million and 14 million. The main effect of Reynolds number in this range is to reduce the viscous drag. In order to better compare the results, the axial force evaluated in the calculations at zero drift angle was scaled to $Re = 14$ million using the ITTC 1957 friction line:

$$X_{Re=14\times10^6} = X_p + X_{f,Re=5.2\times10^6} \cdot \frac{C_{f,\mathrm{ITTC},Re=14\times10^6}}{C_{f,\mathrm{ITTC},Re=5.2\times10^6}} \tag{5.10}$$

This was done for the overall force on the hull and sail as well as on the hull surface alone.

5.5.1 Iterative error

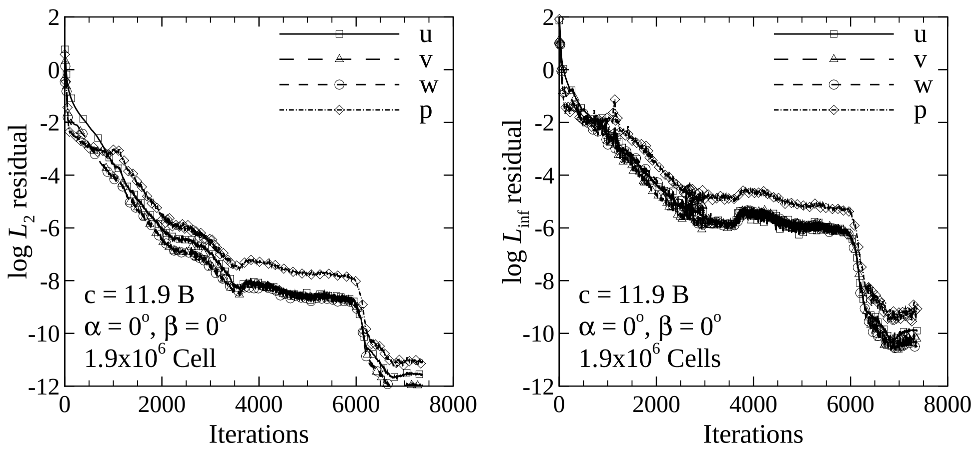

Figure 5.23: Iterative convergence, Walrus, $\beta = 0°$, $\alpha = 0°$

Excellent convergence was achieved, with L_∞ and L_2 norms of the residuals dropping below 10^{-5} and 10^{-7}, respectively, in all cases of $\beta = 0°$. The integrated forces and moments were unchanging to 7 significant digits (the precision with which this data was written to the results file) for the last several hundred iterations. Figure 5.23 shows the convergence histories of a selected calculation with a drift angle of zero.

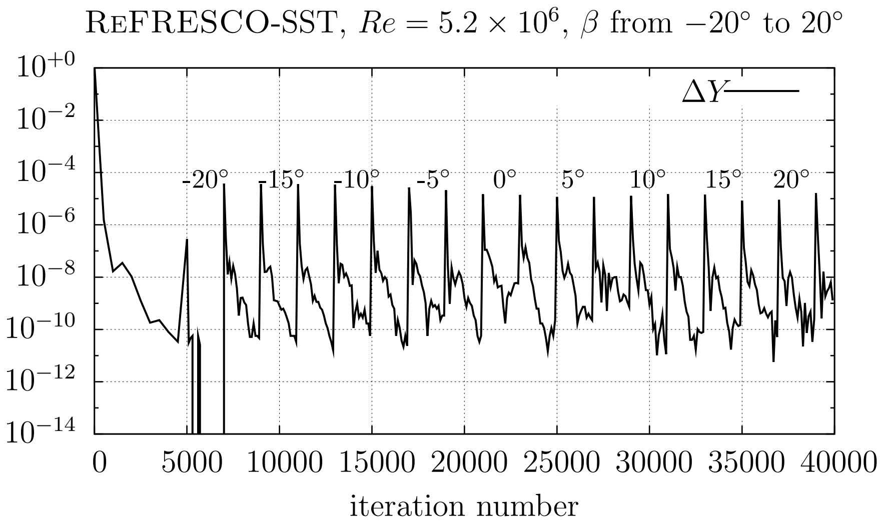

Figure 5.24: Convergence history Y-force, Walrus, ReFRESCO

For non-zero drift angles, the L_2 residuals dropped at least four orders of magnitude. The effect on the integral quantities is small: the non-dimensional changes in the forces and moments were well below 1×10^{-8}. This is more than two to three orders of magnitude smaller than the discretisation uncertainty and therefore the iterative uncertainty U_I can be neglected, see Eça et al. [41]. An example of the convergence history of the non-dimensional Y force for the drift-sweep calculation is shown in Figure 5.24. Each spike in the line indicates the beginning of a new drift angle.

5.5.2 Discretisation error

The results of the discretisation error analysis are presented in Table 5.26 and Figure 5.25. For this analysis, the results for the coarsest grid were taken as an outlier and the least-squares method was applied to the four finest grids only. It is seen that the uncertainties in X and M are small. The uncertainty in the vertical force Z (due to the asymmetry of the hull with deck and sail) is found to be large. This is mainly caused by scatter in the results, which can be attributed to the fact that it is difficult to manually generate grids with ICEM CFD which are exactly geometrically similar. Furthermore, the magnitude of this out-of-plane force is small compared to the vertical forces experienced when sailing close to the sea floor or when sailing at a pitch angle.

Table 5.26: Uncertainty analysis, Walrus, $\beta = 0°$, $\alpha = 0°$, deep water

Item	ϕ_0	ϕ_1	U_ϕ	p
X_p	-2.09×10^{-4}	-2.16×10^{-4}	11.2%	7.56
X_f	-1.32×10^{-3}	-1.31×10^{-3}	1.0%	1.98
X	-	-1.53×10^{-3}	1.7%	2
Z_p	-2.62×10^{-5}	-2.72×10^{-5}	9.9%	0.49
Z_f	-	-4.86×10^{-6}	38.5%	1
Z	-3.04×10^{-5}	-3.20×10^{-5}	10.2%	0.69
M_p	-5.47×10^{-5}	-5.44×10^{-5}	2.4%	5.45
M_f	2.39×10^{-5}	2.38×10^{-5}	2.1%	3.22
M	-3.08×10^{-5}	-3.06×10^{-5}	2.6%	6.83

1 Oscillatory convergence
2 Monotonic divergence
3 Oscillatory divergence

5.5.3 Global quantities

Table 5.27 compares the scaled CFD results with experimental values (Re = 14 million) for the hull-sail (configuration 2) and hull only (configuration 3) configurations. The computations predict the resistance on the hull to within 3% of the experimental data. This is expected to be within experimental error bounds based on the scatter in the experimental data. The total resistance of hull and sail was predicted to be 9% lower than configuration 2. It was expected that the calculated resistance would be lower than the experimental value because the computations do not account for the drag on the sailplanes, which is present in the experimental results for configuration 2.

The unrestricted-water calculations are also compared with configuration 2 experiments for a range of drift angles in Figure 5.26. The agreement is considered to be very good for all components of forces and moments, with the exception of pitching moment M. The pitching moment in the calculations follows the same trend as the experiments

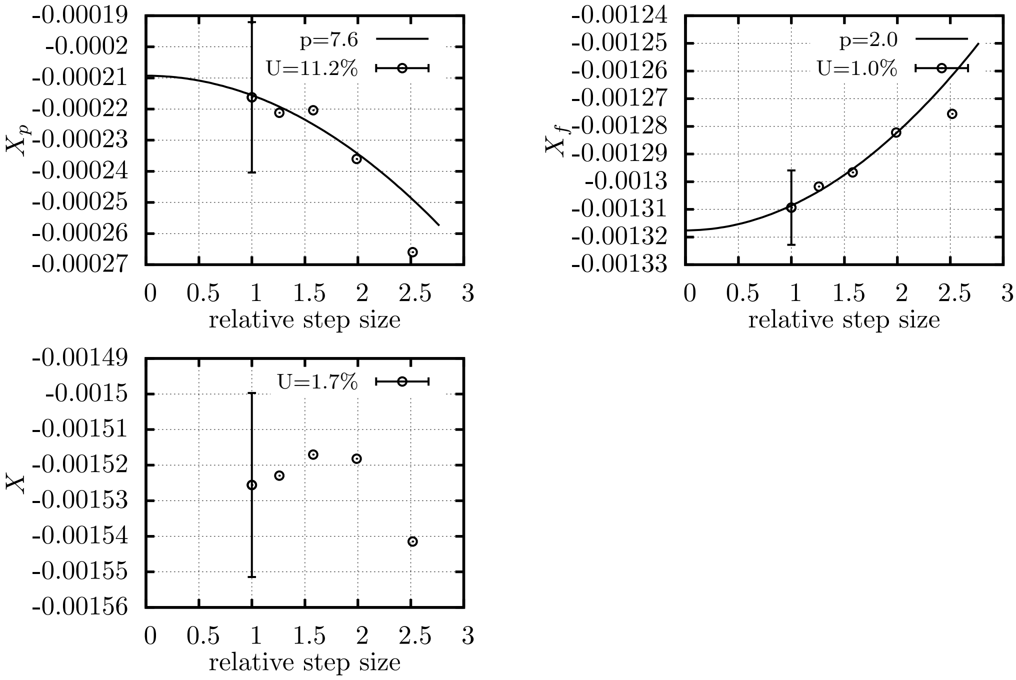

Figure 5.25: Uncertainty analysis, Walrus, $\beta = 0°$, $\alpha = 0°$, deep water

but is shifted down to smaller values. It is possible that this discrepancy is a result of the sailplanes being present in the experiments but not in the calculations. The drag

Table 5.27: Walrus grid refinement study (values $\times 10^3$)

Total forces and moments

Cells	X_p	X_f	X	Form factor $1+k$	$X(Re = 14M)$	X_{exp} Config 2	$E = X - X_{\text{exp}}$ ($\%X_{\text{exp}}$)
470	-0.266	-1.275	-1.546	1.209	-1.295		-8.0
954	-0.236	-1.282	-1.523	1.184	-1.275		-9.4
1909	-0.220	-1.297	-1.521	1.170	-1.274	-1.407	-9.4
3761	-0.221	-1.302	-1.527	1.170	-1.279		-9.1
7509	-0.216	-1.309	-1.530	1.165	-1.281		-8.9

Forces and moments on hull only

Cells	X_p	X_f	X	Form factor $1+k$	$X(Re = 14M)$	X_{exp} Config 3	$E = X - X_{\text{exp}}$ ($\%X_{\text{exp}}$)
470	-0.214	-1.101	-1.314	1.194	-1.104		2.4
954	-0.199	-1.107	-1.306	1.179	-1.097		1.8
1909	-0.190	-1.120	-1.311	1.170	-1.101	-1.078	2.2
3761	-0.187	-1.125	-1.312	1.166	-1.102		2.2
7509	-0.189	-1.131	-1.320	1.167	-1.109		2.9

$C_{f,\text{ITTC},Re=14\times10^6} = 2.832 \times 10^{-3}$ (non-dimensional with wetted surface)
$C_{f,\text{ITTC},Re=5.2\times10^6} = 3.372 \times 10^{-3}$ (non-dimensional with wetted surface)

and lift on the sailplanes would tend to increase M, consistent with the shift observed in Figure 5.26. It also appears from the scatter in the data and the differences between positive and negative drift angles that there is more uncertainty in M (relative to the scale used for the plot) than in the other integral quantities.

The comparison with experiments showed that CFD gives accurate predictions for the forces and moments on the submarine for the case of unrestricted water over a range of drift angles.

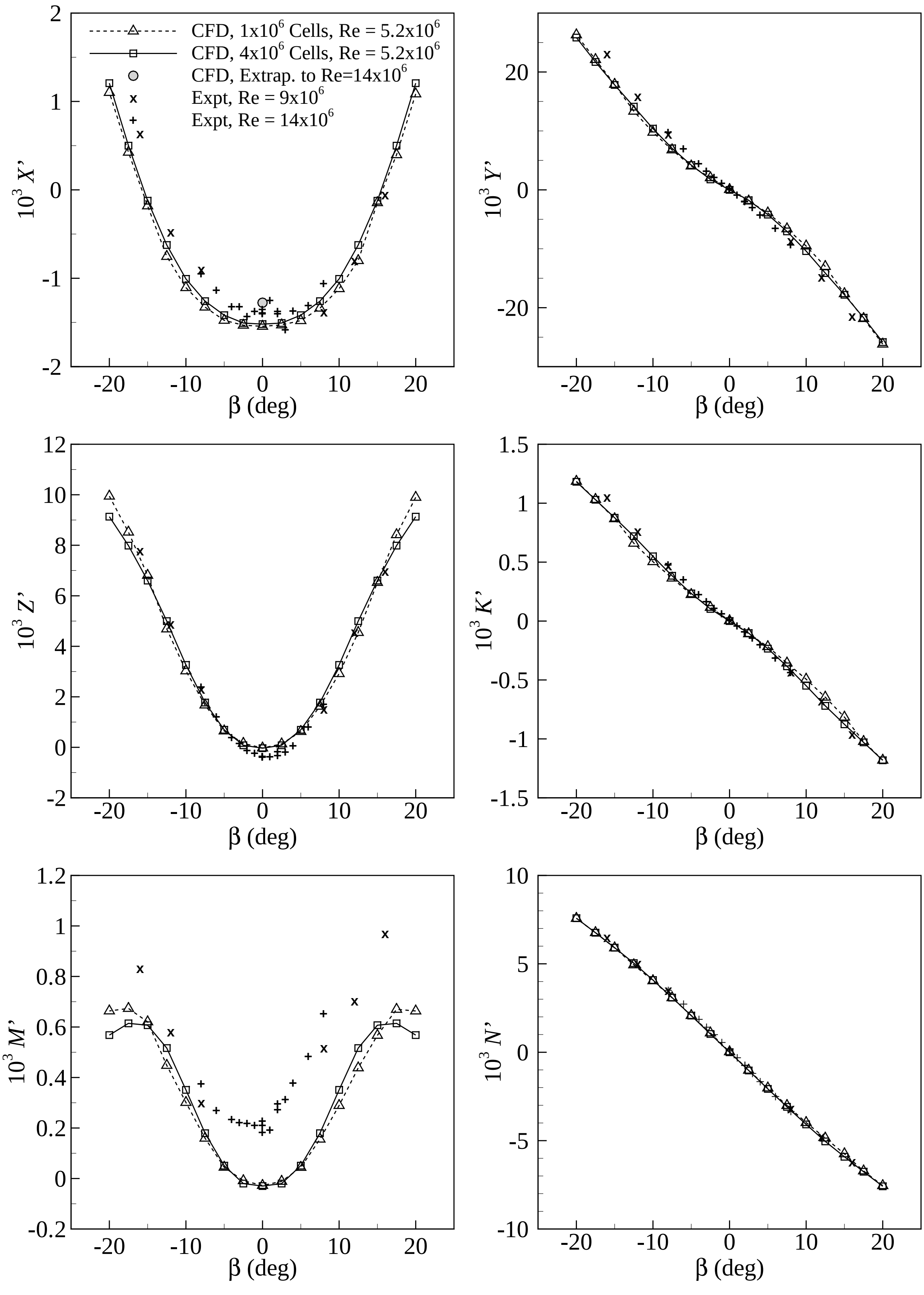

Figure 5.26: Comparison between configuration 2 experiments [34] and calculations, Walrus (deep water, 4×10^6 cells)

5.6 Conclusion

In this chapter, verification and validation of the predicted forces and moments on several different ship hulls in manoeuvring motions have been presented using available validation data from literature. It was demonstrated that for a wide range of ship types, good predictions of the loads on the hull in manoeuvring motion can be obtained. The trends in the forces and moments as a function of the drift angle or yaw rate are simulated well. The results obtained with two different solvers and using different turbulence models were compared. In general, it is concluded that the differences between the results obtained with the two solvers are relatively small and within the numerical uncertainties, except for cases where large differences in grid density were used. In those cases, better results were obviously obtained on the finer grids. In general, it appears that the combination of ReFRESCO with SST provides results that are slightly closer to the experimental values than the combination of Parnassos with MNT. Considering the computational effort, some differences exist between the two solvers. Parnassos is very fast when a converged solution can be obtained and needs only two processors for the cases presented in this section. For ReFRESCO a large number of processors is required to solve the flow in a similar time-frame as Parnassos. However, for more complicated flows, such as found at large drift angles or rotation rates, it becomes more difficult to converge a solution with Parnassos, since this code is optimised for ships sailing in straight-ahead conditions. The combination of ReFRESCO as a general code and the possibility to use high-quality multi-block structured grids is more robust for these conditions and requires much less manual interaction to arrive at a converged solution.

The verification studies provide useful insight into the influence of the grid density on the predicted forces and moments. Summarizing, the numerical uncertainties in the forces and moments obtained by the viscous-flow calculations were found to be about 10% to 15% on average. The uncertainties in Y and K appear to be somewhat higher than in X or N. In several cases, validation of the calculations failed, indicating modelling errors in the numerical results. In these cases, it was generally seen that the magnitude of the transverse force was under-predicted, while the magnitude of the yaw moment was over-predicted. For manoeuvring studies in the early design, the comparison errors are within acceptable levels. However, improvements remain desired and might be obtained using finer grids, larger domain sizes, different grid topologies with refinement in the wake of the ship, other turbulence models or incorporating free surface deformation. Furthermore, unsteady phenomena in the flow have been ignored. In future studies, the influence of instationary flow on the forces and moments needs to be investigated.

For one of the hull forms presented in this chapter, the DARPA SUBOFF, the influence of a variation of the turbulence model was studied. By changing the turbulence model from MNT to the more complex SST model, a considerable reduction of the comparison error in X was found. Unfortunately, the changes in the other forces and moments were small and therefore this did not lead to the desired overall improvements. Further study is therefore required to determine the cause of the modelling error.

The drift-sweep procedure as proposed in section 4.6.2 and implemented in ReFRESCO was used and the verification and validation studies shows that the procedure provides good results in comparison with the Parnassos calculations and with the experiments. With this procedure, the amount of manual interaction for the user decreases considerably. Furthermore, the convergence for the different drift angles is faster than when each drift angle would be calculated separately.

In the following chapter, free sailing model tests for the HTC will be presented, which will be used for validation of the manoeuvring predictions presented in chapter 7.

Chapter 6

Free sailing manoeuvring tests

6.1 Introduction

Unfortunately, results of free sailing manoeuvres for the HTC (see 2.5.4) were not available at the end of the VIRTUE project and validation of the predicted manoeuvres could not be performed. Therefore, MARIN decided to perform such manoeuvres outside of the scope of VIRTUE. The results of this manoeuvring test programme can be used for public domain comparisons of simulation results and for development of procedural guidelines for free running model tests when it concerns manoeuvring of single propeller ships and engine control during manoeuvres.

The purpose of the manoeuvring tests was to determine the yaw checking and course changing abilities and the turning ability of the ship and provide data for validation of manoeuvring predictions. To determine the manoeuvring characteristics, standard zig-zag and combined turning circle/pull-out experiments were conducted with the following variations:

- with and without bilge keels
- design speed and lower speed
- different procedures for the rudder angle application during zig-zag manoeuvres with respect to the neutral rudder angle
- propeller rate control to simulate the engine behaviour during manoeuvring

This chapter presents details of the model, the experimental facility and equipment, the data reduction procedures and the test programme. In this thesis, only the tests without bilge keels and with constant propeller RPM are considered. More details about the tests and drawings of the propeller and bilge keels can be found in MARIN Report No. 23277-3-SMB [105].

6.2 Ship model

Details of the HTC are already given in section 2.5.4. The main particulars of the hull and a small scale body plan are given in Table 2.4 and Figure 2.7. For the MARIN free sailing manoeuvres, a wooden ship model was built to a scale ratio λ of 1:30.02. The model was designated Ship Model No. 8971 and was tested with and without bilge keels. Bow thruster openings were not modelled. Turbulence on the model was stimulated using studs at the bow and sand strips at the appendages. All experiments described in this thesis were carried out for a loading condition corresponding to a draught of 10.3 m on even keel. The metacentric height $\overline{GM}$ of the model was adjusted to the full-scale value of 1.09 m, which is relatively large for a vessel of this size and type. This results in small heel angles during the manoeuvres such that the influence of heel on the manoeuvrability can be neglected. A photograph of the model is given in Figure 6.1.

Figure 6.1: HTC ship model for free sailing tests

6.3 Propulsion and steering system

The ship model was fitted with a single propeller - single rudder arrangement. The rate of rudder application during the tests corresponded to the full-scale value of $4.6°/s$. The rudder arrangement consists of a spade type rudder with headbox with a total lateral area of approximately 39.76 m^2, or $2.51\% L_{\text{pp}}T$ and a movable area of 29.03 m^2, or $1.83\% L_{\text{pp}}T$. The rudder is positioned at the Aft Perpendicular Plane (APP). MARIN stock propeller No. 5286 R was used to propel the ship model during the manoeuvring tests. The direction of rotation of the propeller was clockwise when looking ahead. The propeller and rudder properties are presented in Table 2.5, Table 2.6 and Figure 2.9. The longitudinal and transverse forces on the rudder and the rudder stock moment have been measured using a three-component force transducer. The propeller thrust and torque have also been measured, using a two-component transducer in the shaft, just ahead of the propeller.

Tests have been performed with a constant RPM setting and with modelling of a concise engine control. In the latter case, a maximum power level that could be delivered to the propeller corresponding to 100% Maximum Continuous Rating (MCR) at full scale was assumed. When the power absorbed by the propeller exceeds this value, the propeller rate of revolutions is decreased, simulating full scale engine behaviour. This method has been validated against full scale feedback and has been found to provide better agreement between model tests and full scale trials. The power level absorbed by the propeller was measured during a speed run corresponding to $18.0\,kn$ at full scale. This power was assumed to be equivalent to 85% MCR.

6.4 Experimental facility and measurement system

The free sailing model tests were performed in MARIN's Seakeeping and Manoeuvring Basin (SMB) [109], which measures $170\,m \times 40\,m$, see Figure 6.2. The water depth in the basin is $5\,m$. The model is followed along the basin length by a main carriage spanning the width of the basin. A sub-carriage travels along the main carriage in transverse direction. The carriage can follow all movements of the model in the horizontal plane. With an extra mountable turntable, the system has a CPMC capability which includes the possibility to mimic rotating arm tests.

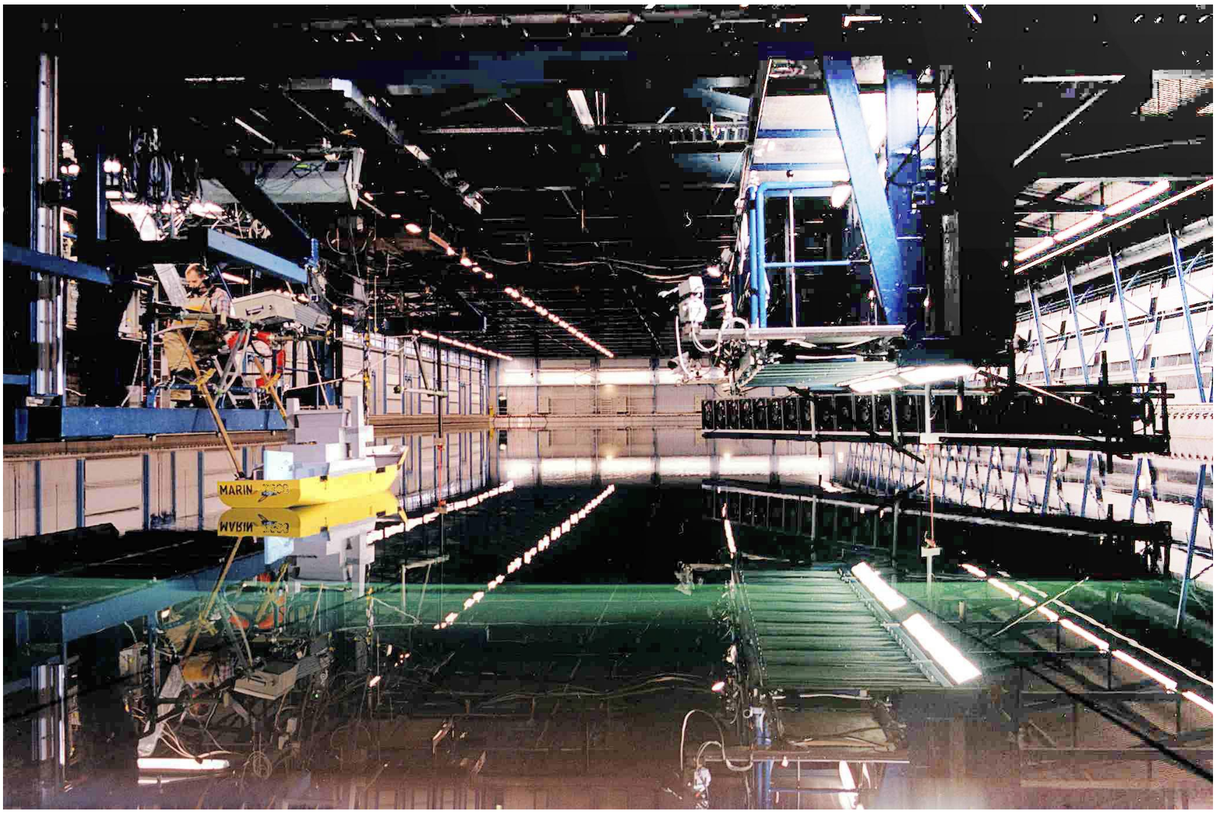

Figure 6.2: Overview of Seakeeping and Manoeuvring Basin

At two adjacent sides of the basin, segmented wave generators consisting of hinged flaps are installed. Each flap is controlled separately by a driving motor and has a width of 60 cm. This set-up makes it possible to generate waves in any direction. The waves can be long and short crested and multi-directional. The wave generator system is equipped with an active wave reflection compensation feature and higher order wave synthesis techniques. Opposite the wave generators, passive sinkable wave absorbers are installed.

A Krypton contact-less optical measurement system (now part of Nikon, see e.g. www.nikonmetrology.com/optical_cmm) is used to determine the position of the model in six DOF. A target consisting of several infra-red Light-Emitting Diodes (LEDs) glued in fixed positions on a non-deformable plate is mounted on the model on a location such that the target is in the Krypton observation area and the location and orientation of the target can be determined. By specifying in Krypton the position of the target relative to the centre of gravity, the system calculates the position of the centre of gravity of the model relative to the sub-carriage based on the measured position and orientation of the target. The Krypton camera is mounted on the subcarriage and consequently moves with the carriage. To obtain the x and y position of the vessel in the basin, the position of the sub-carriage and the relative distance measured with Krypton are combined. All motions are defined in the basin-fixed system of axes, except roll and pitch which are defined in the ship-fixed system of axes.

The rudder angle and propeller RPM are actively controlled by the steering system. The data acquisition consists of recording analogue and digital signals. The analogue signals (e.g. propeller and rudder forces) are sampled before being recorded by the measurement system, while digital signals (e.g. steering system and Krypton output) are recorded directly.

6.5 Data reduction

All results of the model tests are presented as prototype (i.e. full scale) values in the tables and figures in this thesis by applying Froude's law of similitude to the measured data and the assumption of salt water on full scale.

The raw data obtained from the measurements has been filtered before presentation and before parameters were derived. Furthermore, sign conventions according to those presented in section 3.1 have been applied.

6.6 Test procedures and programme

The manoeuvring tests were performed at the self propulsion point of the model. Corrections for scale effects were not made, since some of the scale effects (such as the relatively higher resistance or the relatively higher wake fractions at model scale) tend to even out and because of the lack of worldwide consensus on how to correct for scale effects, see ITTC Recommended Procedures and Guidelines on free sailing manoeuvring tests [73]. Before commencing the manoeuvring tests, the relation between the propeller RPM and the achieved speed was determined. During these tests, the model was steered on a straight course with an autopilot. From the recordings, the average rudder angle required for straight-ahead sailing was obtained. These angles were adopted as the neutral rudder angle to compensate the propeller wheel effect for that specific speed. Based on the RPM-speed relationship, the propeller RPMs to sail at speeds corresponding to 10 kn and 18 kn were derived. These RPMs were used during the remainder of the test programme.

Standard zig-zag and combined turning circle/pull-out manoeuvres have been conducted (see e.g. Bertram [13]). A photograph of the ship model during one of the tests is shown in Figure 6.3. For the zig-zag tests, the rudder execute angle was given relative to the neutral rudder angle. For a neutral angle of e.g. 1° to starboard, the actual mechanical steering angles were 11° to starboard and 9° to port-side for a 10°/10° zig-zag. In the test results, the presented rudder angle is however compensated for the neutral angle and will therefore show rudder angles between 10° PS and 10° SB.

Figure 6.3: HTC ship model during free sailing manoeuvring test

For this thesis, only a subset of the test programme was used. This subset corresponds to the conditions for which simulations were performed and is summarised in Table 7.5 on page 112, where also references are given to the table pages and figure pages with the results. In MARIN Report No. 23277-3-SMB [105] a discussion of all tests is given.

The repeat tests with the ship model equipped with bilge keels were only used to provide further estimates of the uncertainty in the experimental results.

6.7 Uncertainty analysis

6.7.1 Introduction

It is possible to conduct an analysis of the experimental uncertainty using the repeat test results. In this section, the procedure proposed by the Guide to the Expression of Uncertainty in Measurement (ISO-GUM) [72] is followed. In this guide, two methods of evaluation of the uncertainty are given and the Type A method is adopted for this thesis. The Type A method evaluates the uncertainty by statistical analysis of a series of observations. The arithmetic mean or average $\overline{\phi}$ and experimental standard deviation s_ϕ of each result ϕ are determined first. Then, based on the number of observations and the standard deviation, an estimate of the uncertainty is made using a desired level of confidence. Since only a limited number n of identical manoeuvres was realised, an estimate of the experimental uncertainty U of the mean value $\overline{\phi}$ is made using a coverage factor based on the t-value from the Student t-distribution. Using the Student distribution, the uncertainty estimates with 95% confidence ($\alpha = 5\%$) are found.

During the analysis of the model tests, it was observed that scatter existed in the zig-zag test results for an approach speed of $10\,kn$, while the scatter for $18\,kn$ was considerably less. Furthermore, some irregularities were observed in the turning circle results for $18\,kn$. Therefore, a second test series was conducted to generate additional repeat tests to improve the uncertainty estimates of the experimental results. The tests conducted in the first series have test numbers consisting of six digits starting with 1, while the numbers of the tests from the second series start with 2. It should be noted that the second test series has been performed a few months after the first series, and that the setup of the model has been redone for the second test series. This means that the estimated uncertainty values include uncertainties due to the experimental setup. Further uncertainties such as introduced due to model manufacture tolerances or measurement equipment precision are assumed to be much smaller than the uncertainties found in the repeat tests and are therefore not further considered.

6.7.2 Zig-zag tests

Using the repeat tests for $10\,kn$ without bilge keels and $18\,kn$ without and with bilge keels, uncertainty estimates of the zig-zag test results were made. The results are presented in Table 6.1. In Table 6.2 the uncertainty estimate based on the first test series only is given.

It is seen that the uncertainties for the $10\,kn$ zig-zag tests are on average slightly higher than for the $18\,kn$ tests. At $10\,kn$, the second overshoot values for the $10°/10°$ zig-zag appear to be larger than at $18\,kn$, indicating an improving yaw checking and course keeping ability for higher approach speeds. However, this does not apply to the

20°/20° zig-zag test: at the higher approach speed, the higher turning rate during the time required to reverse the rudder angle results in larger overshoot angles.

Interesting to see is the difference between the 18 kn results with and without bilge keels. With bilge keels, the overshoot and initial turning ability values appear to increase (i.e. a deterioration of the yaw checking and initial turning abilities) while also the uncertainties in the results increase.

Comparing the uncertainty estimates based on the first test series (Table 6.2) and those based on all tests (Table 6.1), it is observed that due to the larger number of observations the uncertainty in the mean values of the zig-zag parameters reduced. This is mainly caused by a reduction in the standard deviations s_ϕ and a reduction of the Student t coverage factor. From this, it can be concluded that the Student t coverage factor results in a conservative uncertainty estimate.

6.7.3 Turning circle tests

Using the repeat tests for 18 kn without and with bilge keels, uncertainty estimates of the turning circle test results were made, see Table 6.3. In Table 6.4 the uncertainty estimate based on the first test series only is given.

The uncertainties in the advance and tactical diameter values are found to be small, i.e. 3% or less. There does not appear to be a consistent difference between the uncertainties in the results with or without bilge keels. In general, it is seen that with bilge keels, the turning ability improves (5% smaller tactical diameter) somewhat.

Similar to the uncertainty analysis for the zig-zag, it is observed that due to the larger number of observations the uncertainty in the mean values of the turning circle parameters is generally reduced (see Table 6.3 and Table 6.4). This is mainly caused by a reduction of the Student t coverage factor while the standard deviation s_ϕ remains roughly the same. Also in this case, the Student t coverage factor results in a conservative uncertainty estimation. Only for the steady turning diameter D_{stc} a small increase in uncertainty is obtained by including the additional test.

6.8 Conclusion

Free sailing manoeuvring test on the HTC have been performed. This test campaign resulted in a very valuable data set which can be used for public validation studies. Besides obtaining general characteristics of the manoeuvrability of a single-screw container ship, unique information has been obtained on the drift angles and rates of turn combined with propeller and rudder forces. From this, important information for the development and validation of manoeuvring prediction tools is obtained. Furthermore, repeat tests have been conducted for selected manoeuvres and based on these tests, the uncertainty in the characteristic manoeuvring properties has been estimated. Even when a small number of observations is available, it is concluded that the verification procedure proposed in

Table 6.1: Experimental uncertainty estimate, zig-zag, 95% confidence interval, all tests

Zig-zag 10 *kn, without bilge keels*								
	$\delta/\psi = 10°/10°$						$\delta/\psi = 20°/20°$	
	1st overshoot angle [deg]		2nd overshoot angle [deg]		Initial turning ability [L_{pp}]		1st overshoot angle [deg]	
	PS	SB	PS	SB	PS	SB	PS	SB
Average $\overline{\phi}$	9.8°	10.1°	22.3°	25.0°	1.68	1.81	15.1°	15.4°
Standard deviation s_ϕ	1.3°	1.3°	1.6°	2.8°	0.05	0.25	1.0°	1.5°
Observations n	8	8	8	8	8	8	4	4
$t_{\alpha/2}(n-1)$	2.36	2.36	2.36	2.36	2.36	2.36	3.18	3.18
$U = t \cdot s_\phi/\sqrt{n}$	1.1°	1.1°	1.3°	2.4°	0.05	0.21	1.7°	2.4°
$U/\overline{\phi}$	12%	11%	6%	10%	3%	11%	11%	15%
$\overline{\phi} - U$	8.6°	9.0°	21.0°	22.6°	1.64	1.60	13.4°	13.0°
$\overline{\phi} + U$	10.9°	11.2°	23.6°	27.4°	1.73	2.01	16.7°	17.7°

Zig-zag 18 *kn, without bilge keels*								
	$\delta/\psi = 10°/10°$						$\delta/\psi = 20°/20°$	
	1st overshoot angle [deg]		2nd overshoot angle [deg]		Initial turning ability [L_{pp}]		1st overshoot angle [deg]	
	PS	SB	PS	SB	PS	SB	PS	SB
Average $\overline{\phi}$	10.0°	9.7°	18.9°	21.6°	1.57	1.67	18.6°	18.2°
Standard deviation s_ϕ	0.9°	0.2°	0.6°	0.2°	0.02	0.01	0.2°	0.7°
Observations n	3	3	3	3	3	3	3	3
$t_{\alpha/2}(n-1)$	4.30	4.30	4.30	4.30	4.30	4.30	4.30	4.30
$U = t \cdot s_\phi/\sqrt{n}$	2.1°	0.6°	1.4°	0.6°	0.06	0.03	0.5°	1.7°
$U/\overline{\phi}$	21%	6%	8%	3%	4%	2%	3%	10%
$\overline{\phi} - U$	7.9°	9.2°	17.4°	21.0°	1.51	1.64	18.1°	16.4°
$\overline{\phi} + U$	12.1°	10.3°	20.3°	22.2°	1.63	1.70	19.1°	19.9°

Zig-zag 18 *kn, with bilge keels*								
	$\delta/\psi = 10°/10°$						$\delta/\psi = 20°/20°$	
	1st overshoot angle [deg]		2nd overshoot angle [deg]		Initial turning ability [L_{pp}]		1st overshoot angle [deg]	
	PS	SB	PS	SB	PS	SB	PS	SB
Average $\overline{\phi}$	11.0°	10.2°	23.4°	27.6°	1.68	1.70	21.2°	20.8°
Standard deviation s_ϕ	0.1°	0.2°	1.2°	1.5°	0.01	0.08	0.7°	0.6°
Observations n	3	3	3	3	3	3	3	3
$t_{\alpha/2}(n-1)$	4.30	4.30	4.30	4.30	4.30	4.30	4.30	4.30
$U = t \cdot s_\phi/\sqrt{n}$	0.4°	0.6°	2.9°	3.7°	0.03	0.21	1.8°	1.6°
$U/\overline{\phi}$	3%	6%	12%	13%	2%	12%	8%	8%
$\overline{\phi} - U$	10.6°	9.6°	20.6°	23.9°	1.65	1.49	19.4°	19.2°
$\overline{\phi} + U$	11.3°	10.8°	26.3°	31.3°	1.71	1.91	22.9°	22.4°

Table 6.2: Experimental uncertainty estimate, zig-zag, 95% confidence interval, set 1

Zig-zag 10 *kn, without bilge keels*								
	$\delta/\psi = 10°/10°$						$\delta/\psi = 20°/20°$	
	1st overshoot angle [deg]		2nd overshoot angle [deg]		Initial turning ability [L_{pp}]		1st overshoot angle [deg]	
	PS	SB	PS	SB	PS	SB	PS	SB
Average $\overline{\phi}$	10.6°	10.7°	21.6°	25.6°	1.67	1.61	15.1°	15.4°
Standard deviation s_ϕ	0.3°	1.0°	1.7°	4.6°	0.09	0.03	1.3°	1.8°
Observations n	3	3	3	3	3	3	3	3
$t_{\alpha/2}(n-1)$	4.30	4.30	4.30	4.30	4.30	4.30	4.30	4.30
$U = t \cdot s_\phi/\sqrt{n}$	0.6°	2.5°	4.2°	11.4°	0.22	0.07	3.2°	4.5°
$U/\overline{\phi}$	6%	23%	19%	45%	13%	4%	21%	29%
$\overline{\phi} - U$	10.0°	8.2°	17.4°	14.2°	1.46	1.54	11.9°	10.9°
$\overline{\phi} + U$	11.2°	13.1°	25.8°	36.9°	1.89	1.68	18.3°	19.8°

Table 6.3: Experimental uncertainty estimate, turning circle, 95% confidence interval, all tests

Turning circle 18 *kn*, $\delta = 35°$, *without bilge keels*						
	Advance AD/L_{pp}		Tactical diam. TD/L_{pp}		Diameter D_{stc}/L_{pp}	
	PS	SB	PS	SB	PS	SB
Average $\overline{\phi}$	2.72	2.86	2.56	2.79	2.10	2.33
Standard deviation s_ϕ	0.03	0.03	0.02	0.03	0.03	0.03
Observations n	4	4	4	4	4	4
$t_{\alpha/2}(n-1)$	3.18	3.18	3.18	3.18	3.18	3.18
$U = t \cdot s_\phi/\sqrt{n}$	0.04	0.04	0.04	0.04	0.05	0.05
$U/\overline{\phi}$	2%	2%	1%	2%	2%	2%
$\overline{\phi} - U$	2.68	2.81	2.53	2.75	2.05	2.28
$\overline{\phi} + U$	2.77	2.90	2.60	2.84	2.15	2.38

Turning circle 18 *kn*, $\delta = 35°$, *with bilge keels*						
	Advance AD/L_{pp}		Tactical diam. TD/L_{pp}		Diameter D_{stc}/L_{pp}	
	PS	SB	PS	SB	PS	SB
Average $\overline{\phi}$	2.72	2.76	2.50	2.57	2.13	2.18
Standard deviation s_ϕ	0.03	0.03	0.01	0.02	0.02	0.00
Observations n	3	3	3	3	3	3
$t_{\alpha/2}(n-1)$	4.30	4.30	4.30	4.30	4.30	4.30
$U = t \cdot s_\phi/\sqrt{n}$	0.07	0.08	0.02	0.04	0.04	0.01
$U/\overline{\phi}$	2%	3%	1%	2%	2%	1%
$\overline{\phi} - U$	2.66	2.68	2.48	2.53	2.09	2.17
$\overline{\phi} + U$	2.79	2.84	2.52	2.61	2.16	2.19

Table 6.4: Experimental uncertainty estimate, turning circle, 95% confidence interval, set 1

Turning circle 18 *kn*, $\delta = 35°$, *without bilge keels*						
	Advance $\mathrm{AD}/L_{\mathrm{pp}}$		Tactical diam. $\mathrm{TD}/L_{\mathrm{pp}}$		Diameter $D_{\mathrm{stc}}/L_{\mathrm{pp}}$	
	PS	SB	PS	SB	PS	SB
Average $\overline{\phi}$	2.71	2.86	2.55	2.80	2.08	2.34
Standard deviation s_{ϕ}	0.02	0.03	0.02	0.02	0.01	0.02
Observations n	3	3	3	3	3	3
$t_{\alpha/2}(n-1)$	4.30	4.30	4.30	4.30	4.30	4.30
$U = t \cdot s_{\phi}/\sqrt{n}$	0.05	0.08	0.05	0.05	0.02	0.04
$U/\overline{\phi}$	2%	3%	2%	2%	1%	2%
$\overline{\phi} - U$	2.66	2.78	2.50	2.75	2.07	2.30
$\overline{\phi} + U$	2.76	2.94	2.61	2.86	2.10	2.39

this chapter provides good estimates of the uncertainty in the measurements, provided a Student t coverage factor is used.

In the following chapter, hydrodynamic coefficients will be derived and manoeuvring simulations will be conducted for the HTC. The model tests results will be used to validate these simulations.

Chapter 7

Simulation of ship manoeuvrability

7.1 Introduction

When SurSim is used to predict the manoeuvrability of the HTC, results as shown in Figure 7.1, Table 7.1 and Table 7.2 are obtained[1]. It is clearly seen that in order to reliably assess the manoeuvring behaviour of the ship an improvement of the mathematical formulae is required: the comparison error for the first overshoot angle during the 20°/20° zig-zag manoeuvre is −72% of the experimental value and the comparison error in the Tactical Diameter (TD) is +46%. In earlier studies, it was already seen that the forces and moments on the bare hull predicted by SurSim were insufficiently accurate, see [148]. To improve the empirical formulations in the mathematical model, CFD calculations will be used.

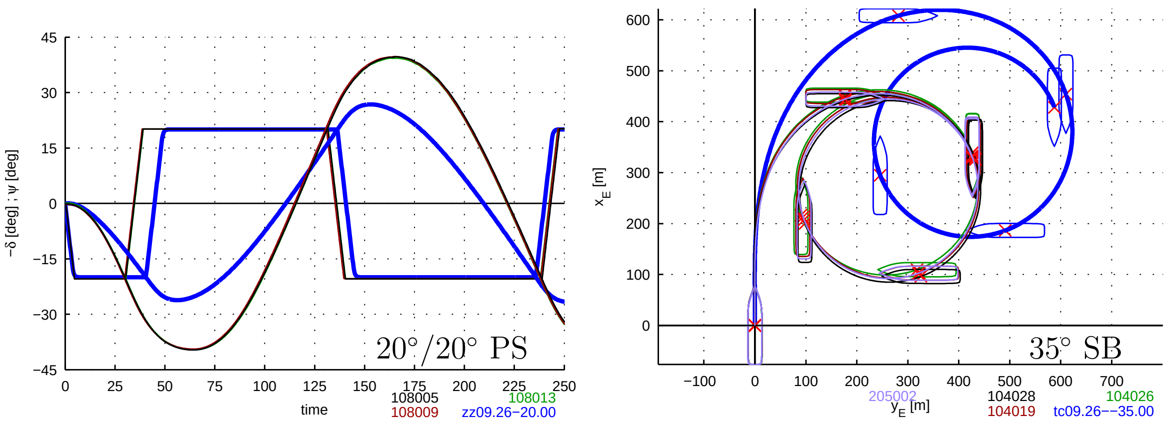

Figure 7.1: Comparison between the original simulations and the free sailing experiments, 18 kn (thick blue lines: simulation, others: experiments)

In this chapter, hydrodynamic coefficients for the modelling of the HTC bare hull

[1] In this chapter, modifications to some of the empirical hull-propeller-rudder coefficients will be made. In the original SurSim predictions here, the same modifications were made. This means that any differences between these simulations and the simulations presented later in this chapter are only caused by changes in the mathematical model for the bare hull forces.

forces and moments as presented in chapter 5 will be derived. Only the results computed using Parnassos will be considered, to limit the scope of the work. The procedure proposed in section 3.3 is followed. With the obtained coefficients, manoeuvring simulations will be conducted with SurSim. The results of the simulations will be compared to the free sailing manoeuvring experiments to demonstrate the feasibility of the approach and the improvement of the simulations compared to the original fully empiric SurSim simulations. See section 2.5.4 and chapter 6 for more information on the HTC and the free sailing manoeuvring experiments.

Table 7.1: Summary of zig-zag manoeuvre results, original simulations, 18 *kn (average from repeat tests)*

V_0 [kn]	L_{pp}/V_0 [s]		$\delta/\psi = 10°/10°$						$\delta/\psi = 20°/20°$	
			1st overshoot angle [deg]		2nd overshoot angle [deg]		Initial turning ability [L_{pp}]		1st overshoot angle [deg]	
			Result	IMO	Result	IMO	Result	IMO	Result	IMO
		Exp PS	10.0°±2.1°		18.9°±1.4°		1.57±0.06		18.6°±0.5°	
		Exp SB	9.7°±0.6°	13.3	21.6°±0.6°	29.9	1.67±0.03	2.5	18.2°±1.7°	25°
18	16.6	SurSim	2.8°		3.6°		2.25		6.2°	
		E PS	-7.2°		-15.3°		0.68		-12.4°	
		E SB	-6.9°		-18.0°		0.58		-12.0°	

Table 7.2: Summary of turning circle manoeuvre results, original simulations, 18 *kn (average from repeat tests)*

V_0 [kn]	L_{pp}/V_0 [s]	δ [deg]		Advance AD/L_{pp}		Tactical diameter TD/L_{pp}	
				Result	IMO	Result	IMO
			Exp PS	2.72±0.04		2.56±0.04	
			Exp SB	2.86±0.04	4.5	2.79±0.04	5.0
18	16.6	35°	SurSim	3.96		3.97	
			E PS	1.24		1.41	
			E SB	1.10		1.18	

7.2 Deriving the hydrodynamic coefficients

In this section, the coefficients for the mathematical model in SurSim as described in chapter 3 will be derived. The forces and moments predicted with this mathematical model will be compared to the available validation data. First, the resistance curve is estimated, while subsequently, the ship-dependent interaction coefficients between the hull, propeller and rudder will be derived. Finally, the procedure as presented in section 3.3 will be followed to obtain the hydrodynamic coefficients for the hull forces.

7.2.1 Resistance curve, wake fraction and thrust deduction fraction

The resistance curve, wake fraction and thrust deduction fraction are obtained from experiments conducted by HSVA prior to the VIRTUE project. Since validation of the simulations will be done using model experiments, the model scale resistance curve must be used. The resistance curve was obtained for a loading condition (trimmed by the stern) that did not completely correspond to the loading condition during the VIRTUE captive experiments for the manoeuvring workpackage. Therefore, a new resistance curve for the different loading condition was predicted using DESP, see section 3.2.3. Furthermore, the resistance curve for the free sailing manoeuvring model was obtained, i.e. for a scale of $\lambda = 30.02$. In Figure 7.2, the original resistance curve (HSVA trimmed), the estimated resistance curve for the captive condition (est. even keel) and the estimated resistance for scale 1:30.02 are shown.

Since the simulation program SurSim uses the input values corresponding to the full-scale HTC, the resistance curve is scaled by λ^3 to arrive at values suitable for the simulation. For all comparison between the SurSim results and the captive measurements the resistance curve for scale $\lambda = 24$ is used, while for the comparisons with the free sailing tests the resistance curve for scale $\lambda = 30.02$ is used.

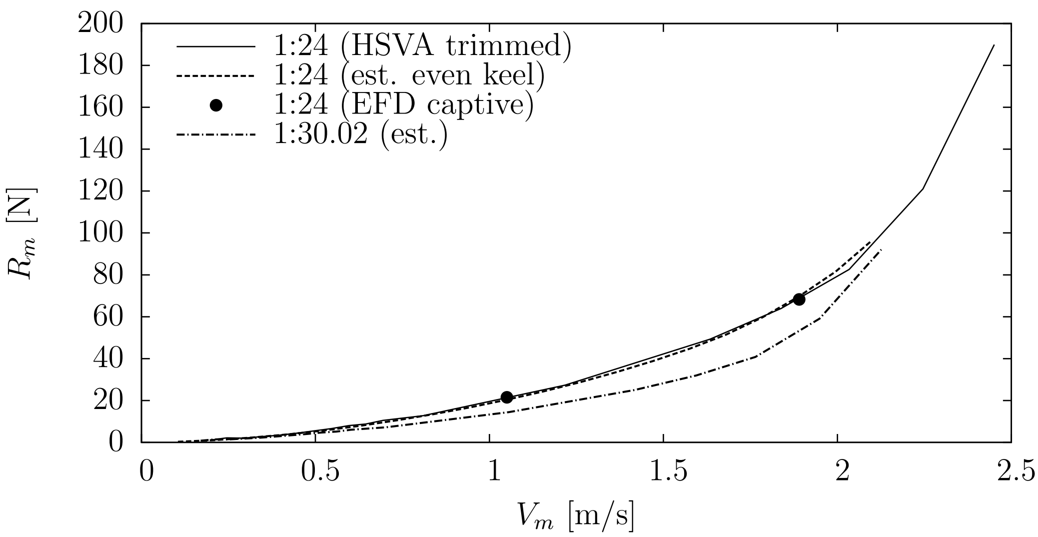

Figure 7.2: Estimated resistance curve (model scale values)

The wake fraction w and thrust deduction fraction t for the captive condition are estimated based on DESP predictions. The predicted values are: $w = 0.38$ and $t = 0.22$.

7.2.2 Propeller characteristics

Using the Strom-Tejsen propeller model [134] for the HSVA 2208 propeller and open water test results for MARIN propeller No. 5286, the propeller open-water curves as presented in Figure 7.3 are obtained. For all comparisons between the SurSim results and the captive measurements propeller 2208 is modelled, while for the comparisons with the free sailing tests propeller 5286 is modelled. The coefficients derived from the open water tests with propeller No. 5286 are as given in Table 7.3.

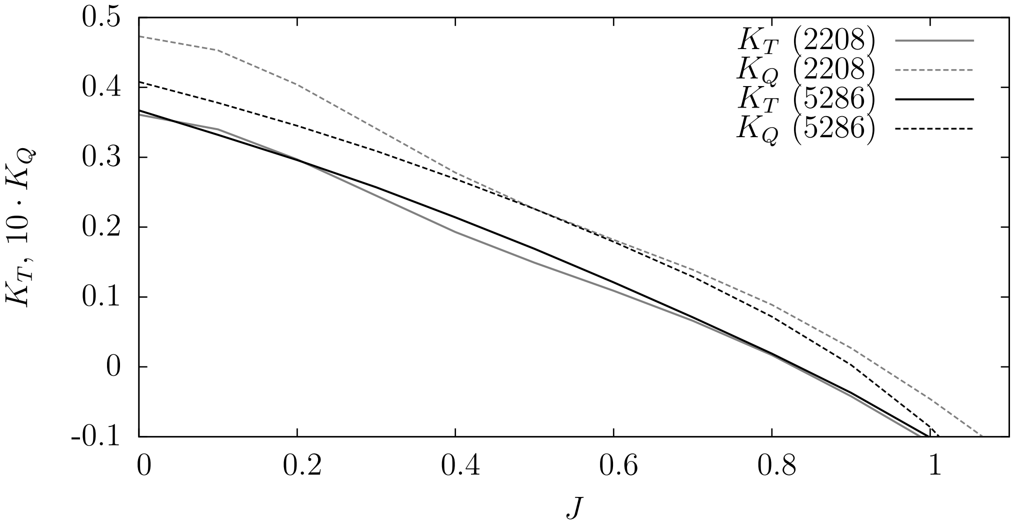

Figure 7.3: Estimated propeller open water curves

Table 7.3: Propeller No. 5286, open water test No. 45127

Coefficient	Value	Coefficient	Value
K_{T0}	0.366897	K_{Q0}	0.040802
K_{T1}	-0.345036	K_{Q1}	-0.029636
K_{T2}	0.068841	K_{Q2}	0.000525
K_{T3}	-0.710991	K_{Q3}	-0.066086
K_{T4}	0.948559	K_{Q4}	0.105238
K_{T5}	-0.428915	K_{Q5}	-0.059477

7.2.3 Rudder forces

Rudder-to-hull interaction

Based on the HSVA captive experiments, the relation between the side force on the rudder and its effect on the total side force on the ship was validated. The value calculated by SurSim for $(1 + a_H)$ (see Equation 3.37) appears to correctly model the rudder force on the ship. For the HTC, a value of $(1 + a_H) = 1.255$ is found. For the ship without rudder, a relation between the rudder angle and the force on the ship as shown in Figure 7.4 is obtained. It is seen that this modelling closely approximates the experimental values, except for the largest rudder angles, where stall appears to be present in the experiments.

However, during the manoeuvres studied in this thesis, the rudder operates in the propeller race, and it is known that for those conditions, the stall angle increases considerably, see Kracht [80] or Molland and Turnock [94], and a lift curve as modelled by SurSim is more appropriate.

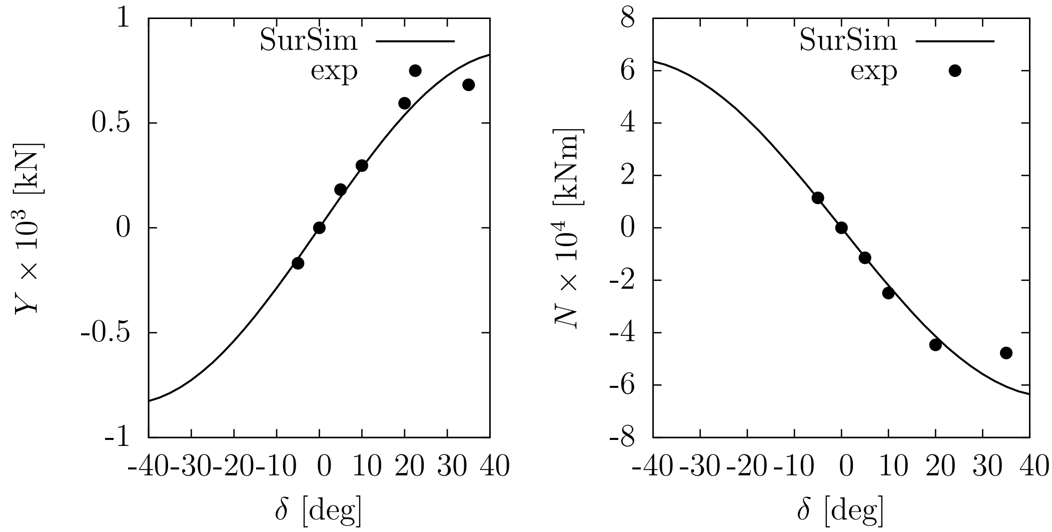

Figure 7.4: Forces on the ship as function of rudder angle, HTC without propeller, $18\,kn$, $\beta = 0°$

Propeller-to-rudder interaction

Based on the HSVA captive experiments, the relation between the propeller thrust and induced velocity on the rudder was estimated (see Equation 3.28). To correlate the forces predicted by SurSim to the measured forces on the ship, the following value is used: $C_{rue} = 0.55$. A relation between the rudder angle and the force on the ship for different propeller revolutions n as given in Figure 7.5 is obtained. The revolutions at model self propulsion are designated n_s. It is seen that this modelling closely approximates the experimental values, except for the largest rudder angles.

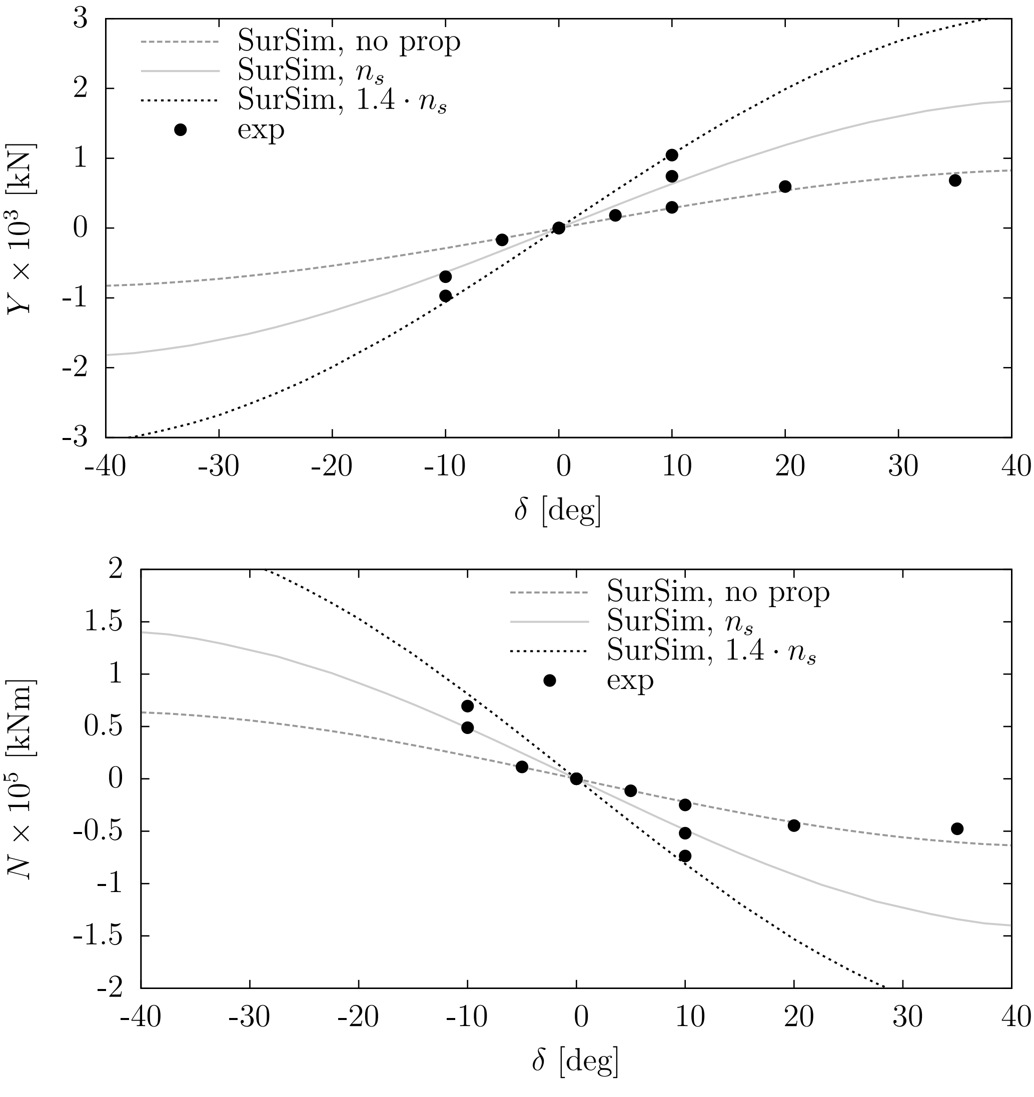

Figure 7.5: Forces on the ship as function of rudder angle and propeller revolutions, $18\,kn$, $\beta = 0°$

Flow straightening

The relation between the drift angle β and rotation rate γ and the effective inflow at the rudder was validated with the HSVA captive experiments. The last two free parameters in the SurSim rudder model are the coefficients for the flow straightening for drift (C_{db}) and the flow straightening for rotation (C_{dr}), see Equation 3.29. These needed to be modified to obtain better agreement with the tests. For the HTC, the following values were adopted: $C_{db} = 0.9$, $C_{dr} = 0.8$. Figure 7.6 and Figure 7.7 show the relation between the rudder angle and the force on the ship for a drift angle of $\beta = -10°$ and for a yaw rate of $\gamma = 0.4$ respectively. With these settings, the rudder forces are modelled reasonably well, although some discrepancies still remain. Further improvement to the rudder modelling is however judged to be outside of the scope of the present work, since the main focus is to demonstrate the influence of the bare hull force model on the manoeuvrability of the ship.

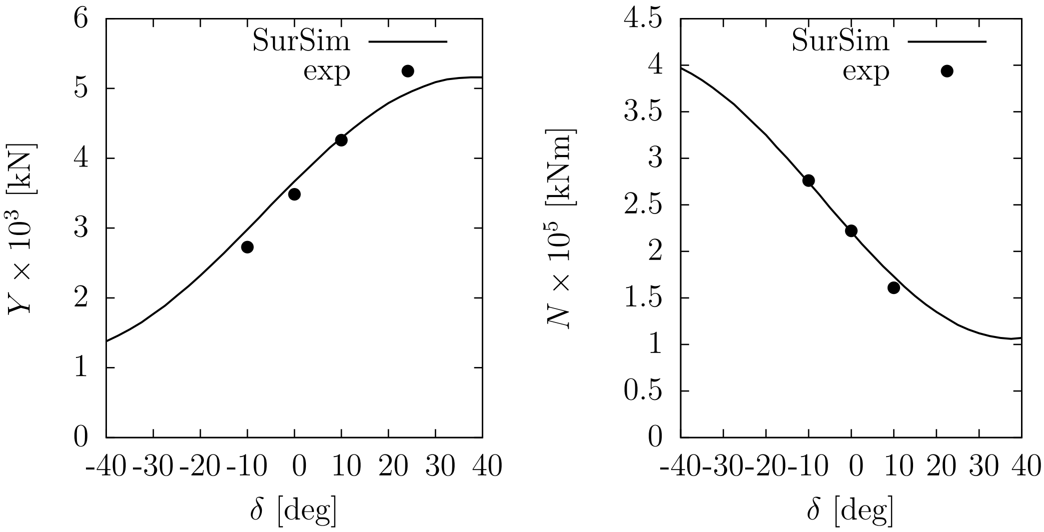

Figure 7.6: Forces on the ship as function of rudder angle, 18 kn, $\beta = -10°$, $n = n_s$

7.2.4 Hull forces

The forces and moments on the bare hull are based on a fit through the RANS calculations with Parnassos for steady drift, steady rotation and combined motion. These calculations were presented in section 5.3 and an overview of the results can be found in the tables on page 157 and page 158. The procedure of deriving the coefficients has been described in section 3.3. Coefficients for pure sideway motion ($Y_{\beta|\beta|}$, $N_{\beta|\beta|}$) or turning on the spot ($Y_{\gamma|\gamma|}$, $N_{\gamma|\gamma|}$) were based on the default values in SurSim. The hydrodynamic damping coefficients derived from the viscous-flow calculations and the added mass coefficients estimated by SurSim are given in Table 7.4, while the transverse forces and yawing moments as a function of drift or yaw motion are given in Figure 7.8. The (added) masses are made non-dimensional using $\frac{1}{2}\rho L_{\mathrm{pp}}^2 T$ and the (added) inertias by $\frac{1}{2}\rho L_{\mathrm{pp}}^4 T$.

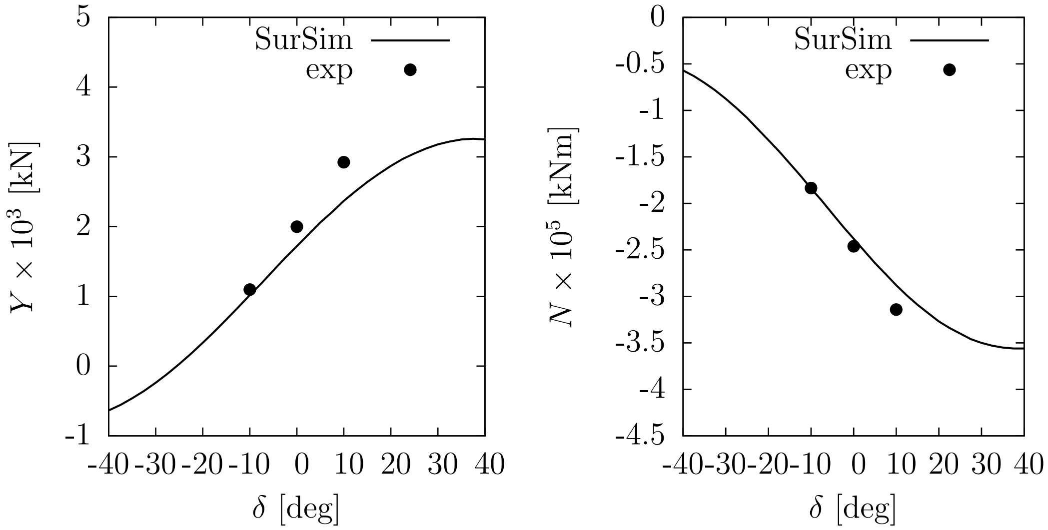

Figure 7.7: Forces on the ship as function of rudder angle, $18\,kn$, $\gamma = 0.4$, $n = n_s$

Table 7.4: Hydrodynamic bare hull and added mass coefficients, HTC

Coefficient	Value	Coefficient	Value
$X'_{u\|u\|}$	-0.0141	$X'_{\beta\gamma}$	0.1025
Y'_{β}	-0.1735	N'_{β}	-0.1442
Y'_{γ}	0.0338	N'_{γ}	-0.0276
$Y'_{\beta\|\beta\|}$	-1.1378	$N'_{\beta\|\beta\|}$	-0.0375
$Y'_{\gamma\|\gamma\|}$	0.0123	$N'_{\gamma\|\gamma\|}$	-0.0386
$Y'_{\beta\|\gamma\|}$	-0.0537	$N'_{\beta\beta\gamma}$	-0.9037
$Y'_{\|\beta\|\gamma}$	0.1252	$N'_{\beta\gamma\gamma}$	-0.2679
Y'_{ab}	0.6747	N'_{ab}	-0.0300
		$N'_{\|u\|\gamma c}$	-0.0075
a_y	3	a_n	1
b_y	2	b_n	3
		c_n	2

Coefficient	Value
m'	0.2328
I'_{zz}	0.0134
m'_{uu}	0.0247
m'_{vv}	0.2286
m'_{rr}	0.0150
m'_{vr}	0.0074
m'_{rv}	0.0074
$m' + m'_{uu}$	0.2575
$m' + m'_{vv}$	0.4614
$I'_{zz} + m'_{rr}$	0.0284

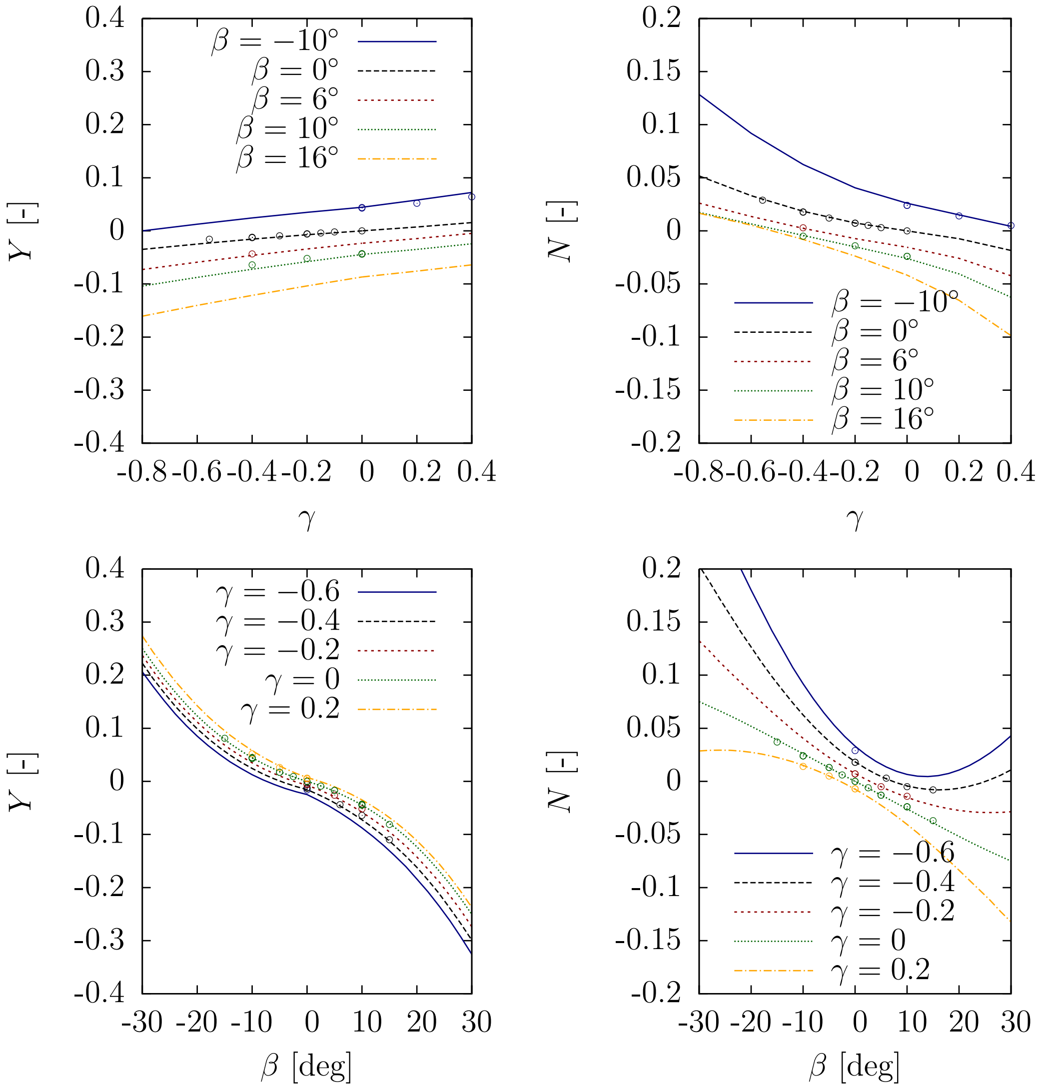

Figure 7.8: Forces on the bare hull as function of yaw rate (top) or drift angle (bottom) (lines: fit, markers: cfd results)

7.3 Standard manoeuvres

7.3.1 Programme of simulations

Calculations were conducted for speeds corresponding to $10\,kn$ and $18\,kn$ on full scale, or $Fn = 0.132$ and $Fn = 0.238$ respectively. All manoeuvres were conducted with a full scale rudder turning rate of $\dot{\delta} = 4.6°/s$. In Table 7.5 the simulations that were performed are indicated, together with the specification of the table and figure pages on which the results are presented. In this section, all values given are presented in full scale values.

Table 7.5: Simulation matrix, HTC

Id	Manoeuvre			Presentation		
	V_0	δ	ψ	Table page	Figure page	
	[kn]	[deg]	[deg]		Timetrace	Track
zz05.14-10.00		10	-10	161	177	178
zz05.14–10.00	10	-10	10	162	179	180
zz05.14-20.00		20	-20	163	181	182
zz05.14–20.00		-20	20	164	183	184
zz09.26-10.00		10	-10	165	185	186
zz09.26–10.00	18	-10	10	166	187	188
zz09.26-20.00		20	-20	167	189	190
zz09.26–20.00		-20	20	168	191	192
tc05.14-35.00		35		169	193	194
tc05.14–35.00		-35			195	196
tc05.14-25.00	10	25	-	170	197	198
tc05.14–25.00		-25			199	200
tc05.14-15.00		15		171	201	202
tc05.14–15.00		-15			203	204
tc09.26-35.00		35		172	205	206
tc09.26–35.00		-35		173	207	208
tc09.26-25.00	18	25	-	174	209	210
tc09.26–25.00		-25			211	212
tc09.26-15.00		15		175	213	214
tc09.26–15.00		-15			215	216

All calculations have been conducted without incorporating heel. The model tests have been performed with a $\overline{GM}$ value that is relatively high for this type of ship and therefore the influence of heel on the manoeuvres is expected to be small. It should be noted that for speeds close to the design speed of the ship, assessment of the heel angle for this type of ship will be important when the $\overline{GM}$ value is small.

7.3.2 RPM-Speed curve

Prior to conducting free sailing model tests for a certain speed, the required RPM to sail this speed needs to be determined. Normally, this is done by applying a pre-defined RPM value to the propeller and measuring the speed of the model obtained with this RPM. This is done for several different RPM settings, resulting in the RPM-Speed relation curve. By interpolating at a given speed, the required RPM is obtained.

With SurSim, the RPM-Speed curve can be predicted, when the proper resistance curve and propeller particulars are available. With the resistance curve and the propeller characteristics as given in sections 7.2.1 and 7.2.2, the RPM-Speed relation as shown in Figure 7.9 is obtained. For a speed of $0.938\,m/s$ (corresponding to $10\,kn$ on full scale), an RPM of 389 is found, while for a speed of $1.69\,m/s$ (corresponding to $18\,kn$ on full scale), an RPM of 700 is found. For the experiments, the values of 400 and 745 are found respectively, resulting in comparison errors of 2.7% and 6.0%. This is judged to be quite small considering the possible uncertainty in the wake and thrust fractions and in the resistance curve used in SurSim.

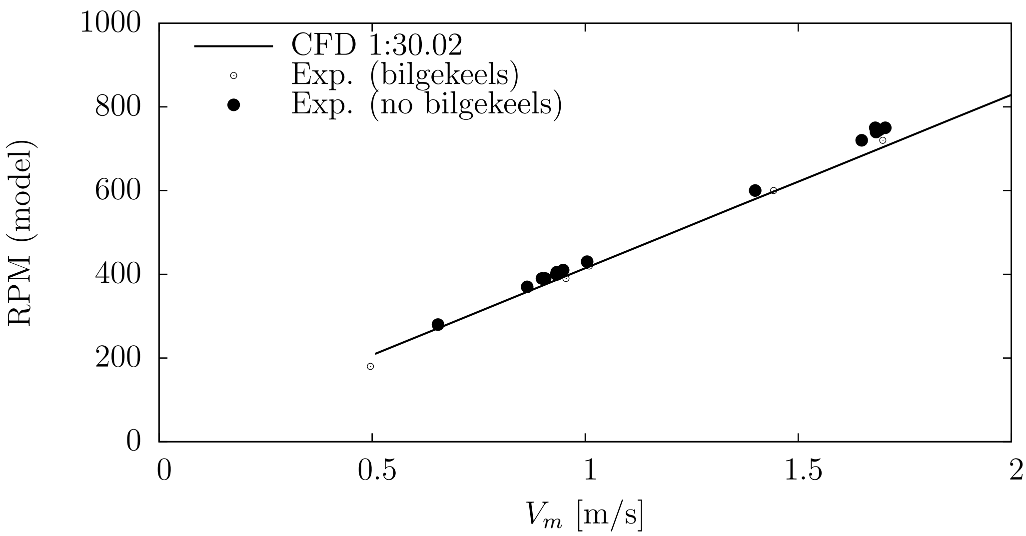

Figure 7.9: RPM-Speed relation for HTC, scale 1:30.02, model scale values

7.4 Sensitivity study

A sensitivity study was conducted in order to determine the influence of estimation errors in each hydrodynamic manoeuvring derivative on the results for standard manoeuvres. In the present study, a set of manoeuvres using the mathematical model described in section 7.2 was simulated during which one of the coefficients was individually multiplied by a factor of 1.1. This value was chosen based on the uncertainties in the order of 10% in the predicted forces and moments, as determined in chapter 5. The changes in the manoeuvring characteristics can be determined and be expressed as percentages of the original values. The resulting factors are the Uncertainty Magnification Factors (UMFs).

Zig-zag manoeuvres were conducted to obtain the first and second Overshoot Angle (osa) and the Initial Turning Ability (ITA) during the 10°/10° manoeuvre and the first overshoot angle during the 20°/20° zig-zag manoeuvre. From turning-circle manoeuvres with 35° steering angle, the Advance (AD) and TD were obtained. From the steady turning circle results, the yaw rate r_{stc}, velocity V_{stc} and drift angle β_{stc} were derived as well.

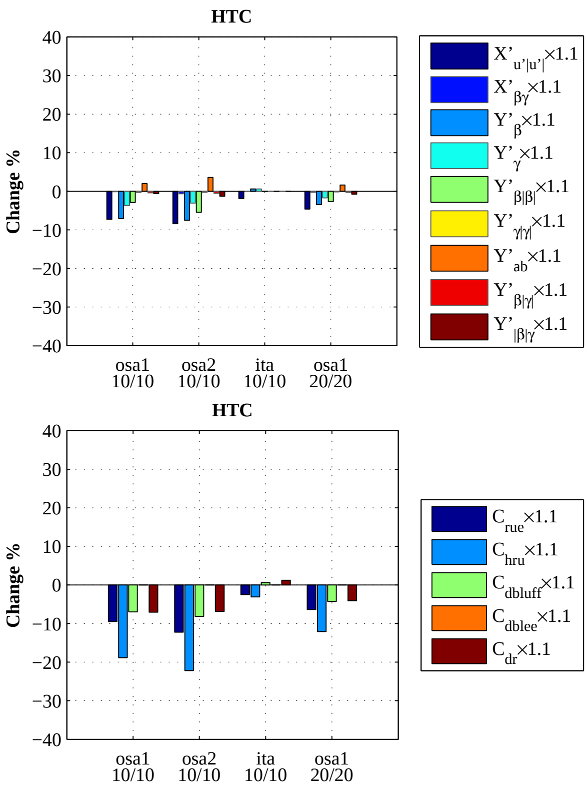

Figure 7.10: Sensitivity study, HTC, zig-zag, 10 *kn*

Based on the sensitivity study, the results as collected in Figure 7.10, Figure 7.11 and Table 7.6 were obtained for an approach speed of 10 *kn*. Another sensitivity study that was conducted for an approach speed of 18 *kn* shows similar results. It is clear that for the HTC deviations in N'_β have the largest impact on the accuracy of the prediction of the yaw checking and course keeping ability, while of all linear coefficients it also has the largest influence on the turning ability. N'_γ is also an important coefficient. Y'_γ is the least important linear coefficient for accurate predictions. Furthermore, it is seen that for the zig-zag manoeuvres, the linear derivatives are more important compared to the non-linear derivatives than during the turning circle manoeuvres. It is also found that the 10°/10° zig-zag manoeuvre is more sensitive to changes in the hydrodynamic derivatives than the 20°/20° zig-zag manoeuvre.

The turning ability is most sensitive to changes in the non-linear coefficients $N'_{\beta\beta\gamma}$

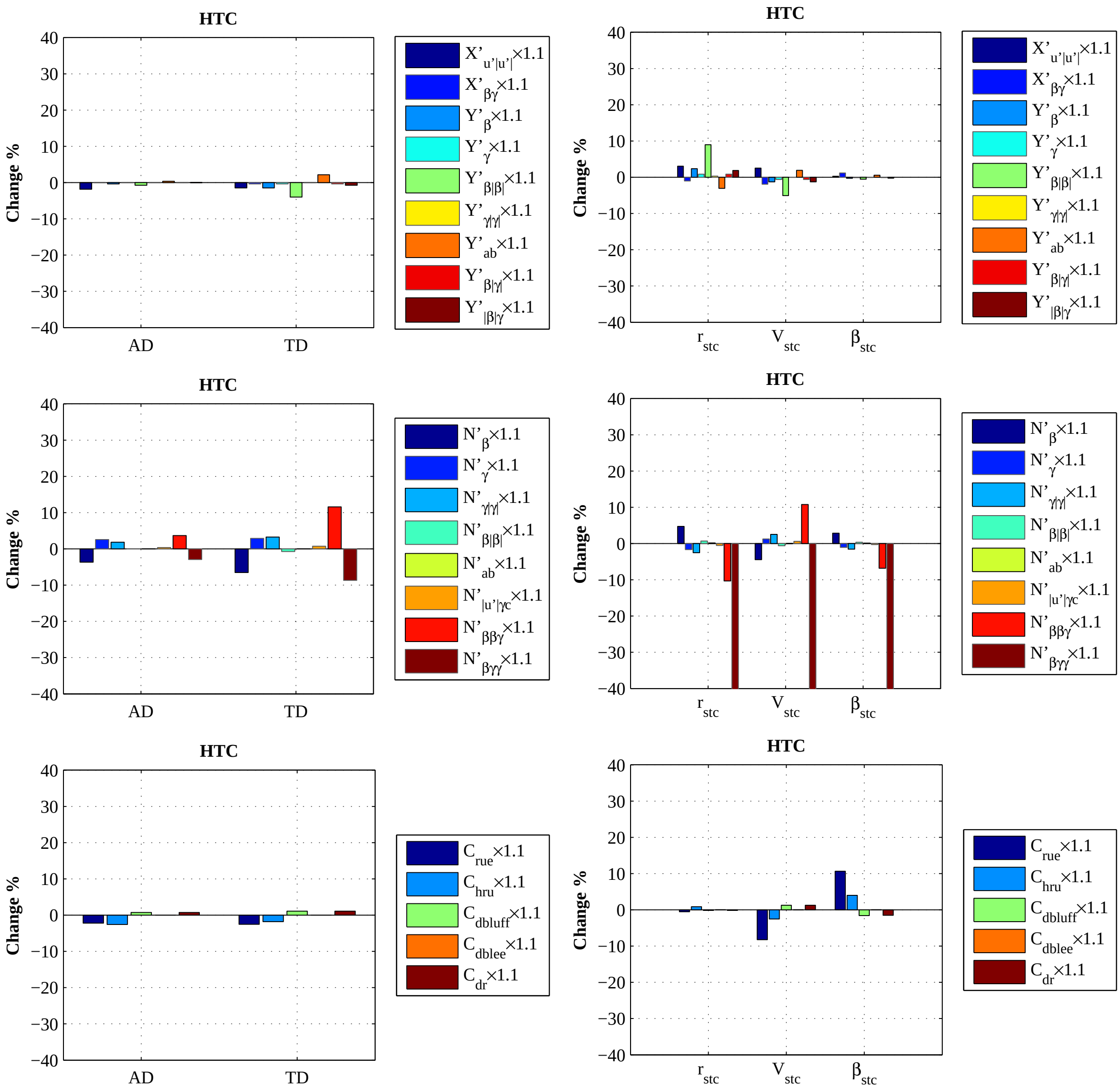

Figure 7.11: Sensitivity study, HTC, turning circle, 10 *kn*

and $N'_{\beta\gamma\gamma}$. The sensitivity of the steady turning circle results to changes in the non-linear coefficient $N'_{\beta\gamma\gamma}$ is large: when this coefficient is increased by 10%, the rate of turn increases and the speed drops such that an unrealistic situation is reached and the simulation is aborted (indicated by a change of 100%).

Similar conclusions were found by Lee and Shin [84] who studied zig-zag manoeuvres for a chemical carrier and two oil tankers and Bulian et al. [18] who conducted a sensitivity study for the *Esso Osaka*.

The hull-propeller-rudder interaction coefficients C_{rue}, $C_{hru}(= 1+a_H)$, $C_{dbluff}(= C_{db})$ and C_{dr} also have a relatively large influence on the yaw checking and course keeping ability of the ship. From these coefficients, the results are most sensitive to changes in C_{hru}.

The sensitivity study demonstrates that for accurate predictions of the manoeuvrability using coefficients derived from CFD calculations, accurate predictions of especially the yawing moment must be made. It should be noted however, that the sensitivity of the results depends on the individual ship, due to different balancing between coefficients.

Changes in coefficients are not necessarily independent of changes in other coefficients. For example, in the procedure used to derive the coefficients, a change in the linear coefficient Y'_γ will lead to changes in the non-linear coefficients $Y'_{\beta|\gamma|}$ and $Y'_{|\beta|\gamma}$, since these are derived after subtracting the linear contribution $Y'_\gamma \cdot \cos\beta \cdot \gamma$ and non-linear contribution $Y'_{\gamma|\gamma|} \cdot \gamma \cdot |\gamma|$ from the total force Y'.

Table 7.6: Sensitivity study, HTC, 10 kn, changes in percentages of the original values (Blue values indicate UMFs larger than 50%, while red values indicate UMFs larger than 100%)

	Zig-zag manoeuvres				Turning circle manoeuvres				
	10/10			20/20	35°				
Variation	osa1	osa2	ita	osa1	AD	TD	r_{stc}	V_{stc}	β_{stc}
$X'_{u'\|u'\|}\times1.1$	-7.25	-8.41	-1.86	-4.63	-1.84	-1.45	3.05	2.53	0.28
$X'_{\beta\gamma}\times1.1$	-0.14	-0.67	0.00	-0.25	0.00	-0.36	-1.02	-1.90	1.18
$Y'_{\beta}\times1.1$	-7.04	-7.52	0.62	-3.45	-0.37	-1.45	2.37	-1.27	-0.28
$Y'_{\gamma}\times1.1$	-3.73	-3.07	0.62	-1.72	0.00	-0.36	0.85	-0.63	-0.14
$Y'_{\beta\|\beta\|}\times1.1$	-2.90	-5.44	0.00	-2.71	-0.74	-3.99	8.97	-5.06	-0.52
$Y'_{\gamma\|\gamma\|}\times1.1$	-0.28	-0.26	0.00	-0.15	0.00	0.00	0.34	0.00	-0.03
$Y'_{ab}\times1.1$	2.00	3.58	0.00	1.62	0.37	2.17	-3.05	1.90	0.56
$Y'_{\beta\|\gamma\|}\times1.1$	-0.41	-0.51	0.00	-0.30	0.00	-0.36	0.85	-0.63	-0.10
$Y'_{\|\beta\|\gamma}\times1.1$	-0.62	-1.25	0.00	-0.74	0.00	-0.72	1.86	-1.27	-0.24
$N'_{\beta}\times1.1$	35.06	33.85	-1.86	20.97	-3.68	-6.52	4.74	-4.43	2.85
$N'_{\gamma}\times1.1$	-10.42	-10.20	1.86	-7.24	2.57	2.90	-1.69	1.27	-1.08
$N'_{\gamma\|\gamma\|}\times1.1$	-2.42	-3.33	0.62	-3.10	1.84	3.26	-2.54	2.53	-1.56
$N'_{\beta\|\beta\|}\times1.1$	0.55	0.96	0.00	0.54	0.00	-0.72	0.68	-0.63	0.38
$N'_{ab}\times1.1$	0.00	0.13	0.00	0.05	0.00	0.00	0.17	0.00	0.14
$N'_{\|u'\|\gamma c}\times1.1$	-0.41	-0.61	0.00	-0.54	0.37	0.72	-0.51	0.63	-0.28
$N'_{\beta\beta\gamma}\times1.1$	-1.73	-4.80	0.00	-3.89	3.68	11.59	-10.32	10.76	-6.81
$N'_{\beta\gamma\gamma}\times1.1$	1.31	3.20	0.00	2.86	-2.94	-8.70	-100.00	-100.00	-100.00
$C_{rue}\times1.1$	-9.45	-12.25	-2.48	-6.35	-2.21	-2.54	-0.51	-8.23	10.63
$C_{hru}\times1.1$	-18.84	-22.20	-3.11	-12.06	-2.57	-1.81	0.85	-2.53	3.99
$C_{dbluff}\times1.1$	-6.97	-8.16	0.62	-4.28	0.74	1.09	-0.17	1.27	-1.60
$C_{dblee}\times1.1$	0.00	0.00	0.00	0.00	0.00	0.00	0.00	0.00	0.00
$C_{dr}\times1.1$	-7.04	-6.85	1.24	-4.09	0.74	1.09	-0.17	1.27	-1.49

Table 7.7: Summary of zig-zag manoeuvre results (average from repeat tests)

V_0 [kn]	L_{pp}/V_0 [s]		$\delta/\psi = 10°/10°$						$\delta/\psi = 20°/20°$	
			1st overshoot angle [deg]		2nd overshoot angle [deg]		Initial turning ability [L_{pp}]		1st overshoot angle [deg]	
			Result	IMO	Result	IMO	Result	IMO	Result	IMO
10	29.9	Exp PS	9.8°±1.1°		22.3°±1.3°		1.68±0.05	-	15.1°±1.7°	
		Exp SB	10.1°±1.1°	-	25.0°±2.4°	-	1.81±0.21	-	15.4°±2.4°	-
		CFD	14.5°		31.3°		1.61		20.3°	
		E PS	4.7°		9.0°		-0.07		5.2°	
		E SB	4.4°		6.3°		-0.20		4.9°	
18	16.6	Exp PS	10.0°±2.1°		18.9°±1.4°		1.57±0.06		18.6°±0.5°	
		Exp SB	9.7°±0.6°	13.3	21.6°±0.6°	29.9	1.67±0.03	2.5	18.2°±1.7°	25°
		CFD	16.2°		32.8°		1.64		23.7°	
		E PS	6.2°		13.9°		0.07		5.1°	
		E SB	6.5°		11.2°		-0.03		5.6°	

7.5 Validation

A comparison between the simulations based on the improved hydrodynamic derivatives and the free sailing experiments is made in Table 7.7, Figure 7.12 and Figure 7.13 for the zig-zag manoeuvres and in Table 7.8 and Figure 7.14 for the turning circles.

7.5.1 Zig-zag manoeuvres

The predicted ITA is within the measurement accuracy, when averaging the results for the manoeuvres started to port side and starboard. For the zig-zag manoeuvres at 10 kn, it is seen that the overshoot angles are considerably over-predicted, especially for the 10°/10° zig-zag. The comparison error E is about 5°, which is judged to be large. When looking at the predicted rate of turn r (see e.g. figure page 179), the physics appear to be very well predicted, since the shape of the rate of turn time trace resembles the measured time trace quite closely. However, the slightly larger value of the rate of turn means a larger build-up of momentum and subsequently larger overshoot angle. The simulations of the 20°/20° zig-zag manoeuvres show a better agreement with the experiments, in particular for 18 kn, see Figure 7.13. In this case, the increase of overshoot angles with increasing speed is captured as well.

Considering the IMO criteria [69] for the yaw checking and course keeping ability, the experiments indicate that the HTC complies with the criteria, although the margin is small: the first overshoot angle for the 10°/10° zig-zag manoeuvre is close to the criterion. According to the simulations, the HTC does not comply with the criteria for the yaw checking and course keeping ability: both the first and second overshoot angles are larger than the limits. Although the simulations provide conservative values, the distinction between whether or not the HTC complies with the IMO zig-zag criteria is not predicted reliably.

Compared to the original simulations with the original bare hull mathematical model of SurSim, see Table 7.1, a considerable improvement is obtained: all comparison errors reduce in magnitude and now the predictions of the overshoot angles are conservative instead of too optimistic in case of the original SurSim predictions.

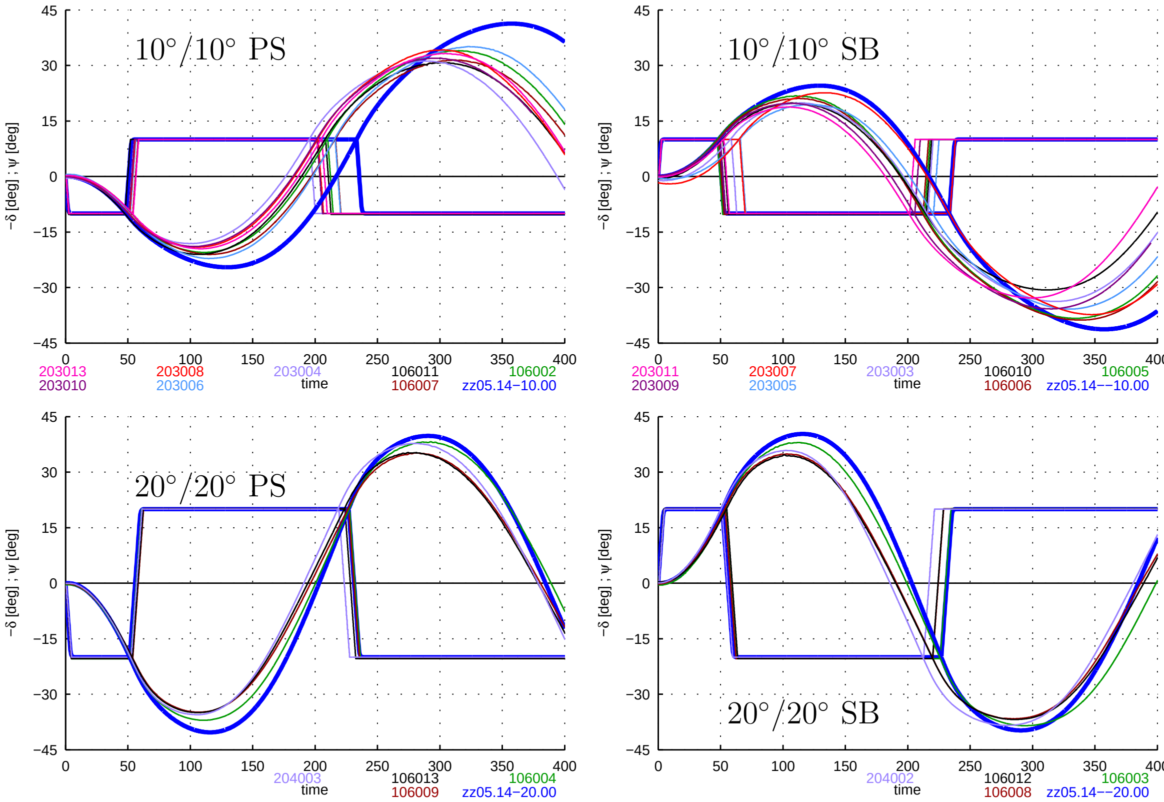

Figure 7.12: Comparison between the simulations and the free sailing zig-zag experiments, 10 *kn (thick blue lines: simulation, others: experiments)*

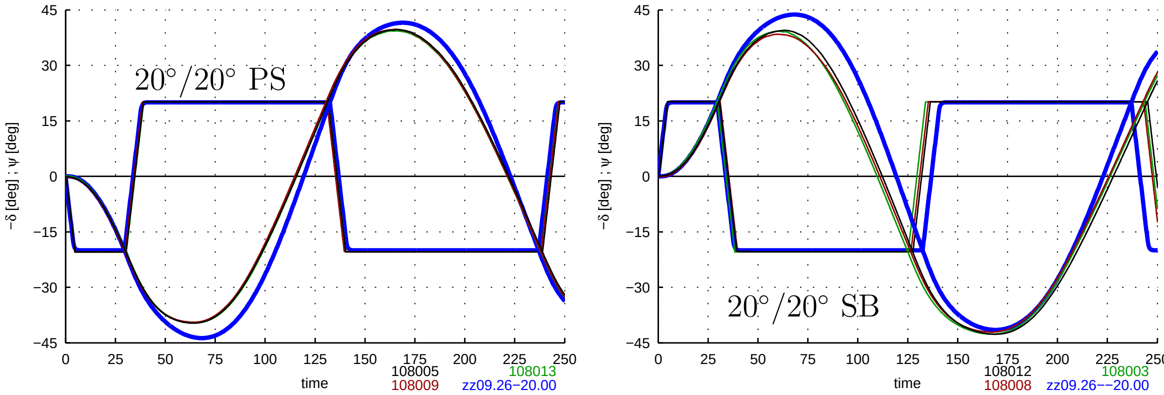

Figure 7.13: Comparison between the simulations and the free sailing 20°/20° *zig-zag experiments,* 18 *kn (thick blue lines: simulation, others: experiments)*

7.5.2 Turning circle manoeuvres

The prediction of the turning ability, and especially of the advance AD and tactical diameter TD is more impressive. The simulation results are very close to the average of the manoeuvres started to port side and starboard. The comparison errors for AD and TD are small, i.e. less than $0.1 \times L_{\text{pp}}$. When the manoeuvre reaches the steady turning circle condition, some deviations from the experiments are seen for steering angles of 35°: in general, the drift angle β and the speed loss $(V_0 - V_{\text{stc}})$ are over-predicted. This results in a slightly smaller turning diameter D_{stc}. These observations apply to the manoeuvres conducted with an approach speed of $10\,kn$ as well as for $18\,kn$.

The distinction whether or not the HTC complies with the IMO turning ability criteria is accurately made using the predictions. This is however not a surprise considering the margin to the limiting values.

Compared to the simulations with the original bare hull mathematical model of SurSim, see Table 7.2, a considerable improvement is obtained with the new hydrodynamic coefficients based on CFD calculations: all comparison errors reduce in magnitude and now the predictions of the tactical diameter values are very close to the experimental ones.

7.6 Conclusion

Using hydrodynamic manoeuvring coefficients derived from CFD calculations of the forces on the bare hull, it has been shown that it is possible to improve the prediction of ship manoeuvres compared to predictions using coefficients based on empirical equations, which was the objective of the present study. In this chapter, it has been demonstrated that a considerable improvement of the turning circle predictions was obtained. The prediction of the yaw checking and course keeping and initial turning abilities based on zig-zag simulations improved as well, but further improvements are required for more reliable assessment of the manoeuvring performance.

The sensitivity of the manoeuvring predictions on changes in the hydrodynamic coefficients was studied. It was found that the linear coefficients mostly determine the sensitivity of the results of the zig-zag manoeuvres, while non-linear coefficients affect mostly the turning circle results. Hull-propeller-rudder coefficients were also found to be important in the sensitivity study. The study demonstrates that for accurate predictions of the manoeuvrability using coefficients derived from CFD calculations, accurate predictions of especially the yawing moment must be made.

Table 7.8: Summary of turning circle manoeuvre results (average from repeat tests)

V_0 [kn]	L_{pp}/V_0 [s]	δ [deg]		Advance AD/L_{pp} Result	Advance AD/L_{pp} IMO	Tactical diameter TD/L_{pp} Result	Tactical diameter TD/L_{pp} IMO
10	29.9	35°	Exp PS	2.76	-	2.70	-
			Exp SB	2.77		2.85	
			CFD	2.72		2.76	
			E PS	-0.04		0.06	
			E SB	-0.05		-0.09	
		25°	Exp PS	3.24	-	3.30	-
			Exp SB	3.10		3.44	
			CFD	3.09		3.27	
			E PS	-0.15		-0.03	
			E SB	-0.01		-0.17	
		15°	Exp PS	3.86	-	4.11	-
			Exp SB	3.73		4.40	
			CFD	3.78		4.15	
			E PS	-0.03		0.04	
			E SB	0.10		-0.25	
18	16.6	35°	Exp PS	2.72±0.04	4.5	2.56±0.04	5.0
			Exp SB	2.86±0.04		2.79±0.04	
			CFD	2.81		2.77	
			E PS	0.09		0.21	
			E SB	-0.05		-0.02	
		25°	Exp PS	3.02	-	3.14	-
			Exp SB	3.35		3.42	
			CFD	3.15		3.27	
			E PS	0.13		0.13	
			E SB	-0.20		-0.15	
		15°	Exp PS	3.64	-	4.00	-
			Exp SB	4.10		4.43	
			CFD	3.83		4.15	
			E PS	0.19		0.15	
			E SB	-0.27		-0.28	

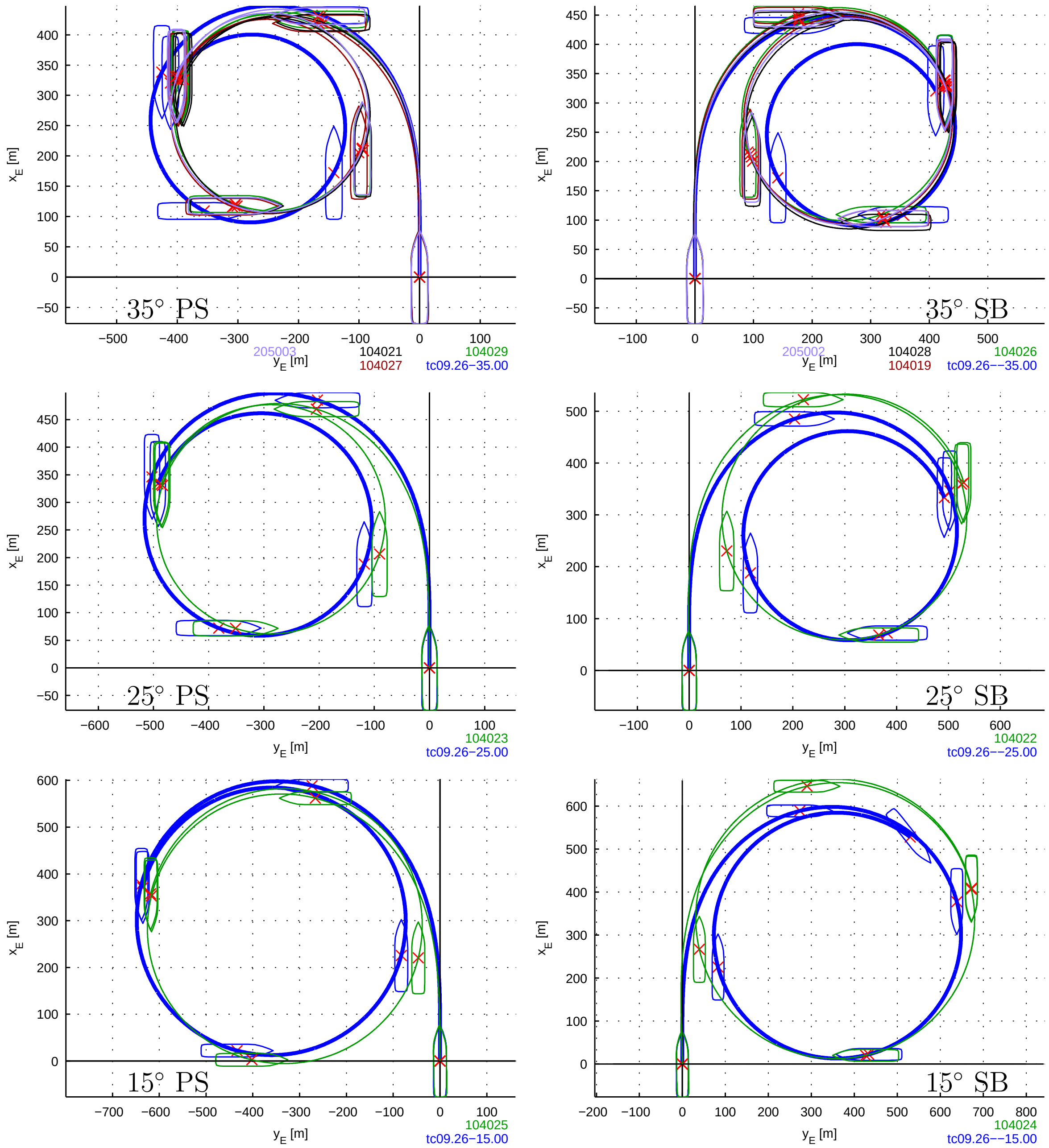

Figure 7.14: Comparison between the simulations and the free sailing turning circle experiments, 18 kn (thick blue lines: simulation, others: experiments)

Page intentionally left blank

Chapter 8

Conclusions and recommendations

8.1 Conclusions

The present work was initiated in order to improve traditional manoeuvring simulations based on empirical mathematical equations to model the forces and moments on the ship. With the evolution of viscous-flow solvers and their promising results in predicting the forces and moments on ships, it was decided to develop a practical method to simulate the manoeuvrability of ships in which viscous-flow solvers are utilised and investigate whether this improves the accuracy of the predicted simulations.

Several different methods are given in literature to simulate ship manoeuvres using viscous-flow calculations, see chapter 2. In this thesis, the *virtual captive test* approach is adopted, because of the efficient use of computational resources compared to other methods. Furthermore, this approach can directly be used to improve mathematical models for manoeuvring simulators. The present study extends the work of other researchers by providing extensive verification and validation of the predicted forces and moments on the hull and a detailed study of the sensitivity of the manoeuvring characteristics of the ship to changes in the hydrodynamic coefficients in the simulation model.

Concerning the forces and moments acting on a ship hull in manoeuvring motions, it is noteworthy that validation data for captive steady drift motions are much more abundant than for steady rotation or combined motion. Especially for more extreme conditions with large turning rates and drift angles, such as occur during tight turning circles, not much validation data can be found in literature. Furthermore, cases in which both extensive captive test data and free sailing manoeuvring test data are available are scarce.

In the work leading to this thesis, much effort was spent on simulating the flow around the HTC for captive conditions and simulations of standard free sailing manoeuvres were conducted within the VIRTUE project. To generate validation data for these manoeuvres, MARIN decided to perform free sailing manoeuvring tests for the HTC. This test campaign resulted in a very valuable data set which can be used for public validation studies, see chapter 6. Besides obtaining general characteristics of the manoeuvrability of a single-screw container ship, unique information has been obtained on the drift angles and rates of turn in combination with propeller and rudder forces. From this, important information for the development and validation of manoeuvring prediction tools is obtained. Furthermore, repeat tests have been conducted for selected manoeuvres and based on these tests, the uncertainty in the characteristic manoeuvring properties has been estimated. Even when a small number of observations is available, it is concluded that the verification procedure proposed in this thesis provides good estimates of the uncertainty in the measurements, provided a Student t coverage factor is used.

The manoeuvring prediction program SurSim has been used to simulate the manoeuvrability of the HTC, see chapter 3. In the program, it is possible to provide user-defined hydrodynamic coefficients for the bare hull forces and moments. This makes the program well suited for the present work to investigate whether the use of viscous-flow calculations can help in improving the prediction accuracy of simulations. A procedure to derive the coefficients is proposed. This procedure is chosen to enable accurate modelling of the linearised behaviour for course-keeping as well as realistic modelling of the harbour manoeuvring characteristics, and to enable accurate modelling of non-linear manoeuvres.

For ship manoeuvres, not only the flow around the ship in oblique motion is of interest, but also the flow around the ship when it performs a rotational motion. To compute the flow around the ship for such conditions, the flow solvers used in the present study had to be modified. For this work, the rotational motion was incorporated by using a non-inertial reference system and supplementing the equations of motions with body forces representing the centrifugal and Coriolis contributions on the flow.

To generate the grids for a range of drift angles and yaw rates, different approaches were adopted depending on the flow solver used. For Parnassos, automated scripts were developed with which the desired grids could be generated rapidly. For the more generic solver ReFRESCO, all calculations are conducted using one grid, but changing the inflow angles and boundary conditions depending on the desired manoeuvring motion. To facilitate this, a new boundary condition was developed, which removes the need to pre-process each grid for each new manoeuvring condition.

In chapter 5, it was demonstrated that for a wide range of ship types, good predictions of the loads on the hull in manoeuvring motion can be obtained. The trends in the forces and moments as a function of the drift angle or yaw rate are simulated well. Two different solvers and using different turbulence models were applied. In general, it is concluded that the differences between the results obtained with the two solvers are relatively small and within the numerical uncertainties, except for cases where large differences in grid density were used. In those cases, better results were obviously obtained on the finer grids.

The verification studies provide useful insight into the influence of the grid density on the predicted forces and moments. In several cases, validation of the calculations failed, indicating modelling errors in the numerical results. In these cases, it was generally seen that the magnitude of the transverse force was under-predicted, while the magnitude of the yaw moment was over-predicted. For manoeuvring studies in the early design, the comparison errors are within acceptable levels. However, improvements remain desired and may be obtained using finer grids, larger domain sizes, different grid topologies with refinement in the wake of the ship, other turbulence models or incorporating free surface deformation.

The verification and validation studies show that the *drift-sweep* procedure proposed in this thesis and implemented in ReFRESCO provides good results in comparison with the Parnassos calculations and with the experiments. By using the procedure, the amount of manual interaction for the user decreases considerably. Furthermore, the convergence for the different drift angles is faster than when each drift angle would be calculated separately.

By using hydrodynamic manoeuvring coefficients derived from CFD calculations of the forces on the bare hull, it has been shown that it is possible to improve the prediction of ship manoeuvres compared to predictions using coefficients based on empirical equations, which was the objective of the present study. In chapter 7, it has been demonstrated that a considerable improvement of the turning circle predictions was obtained. The prediction of the yaw checking and course keeping and initial turning abilities based on zig-zag simulations improved as well, but further improvements are required for more reliable assessment of the manoeuvring performance.

The sensitivity of the manoeuvring predictions on changes in the hydrodynamic coefficients was studied. It was found that the linear coefficients mostly determine the sensitivity of the results of the zig-zag manoeuvres, while non-linear coefficients influence mostly the turning circle results. Hull-propeller-rudder coefficients were also found to be important in the sensitivity study. The study demonstrates that for accurate predictions of the manoeuvrability using coefficients derived from CFD calculations, accurate predictions of especially the yawing moment must be made.

8.2 Recommendations

To improve the accuracy of manoeuvring simulations and to reduce the uncertainty in the simulation results due to small changes in the predicted forces and moments on the hull, the following recommendations are made:

- One of the most promising prospects of the use of viscous-flow solvers is the ability to estimate the hull forces for full scale conditions. This will eliminate possible scale effects and improve the correspondence between the predictions and the actual prototype results. Therefore, calculations for prototype Reynolds numbers should be made.

- The overall accuracy of force and moments predictions on ship hulls should be improved by investigating in more detail the influence on the predictions of turbulence models, domain size, grid density and topology.

- From the set of forces and moments predicted by ReFRESCO as presented in chapter 5 hydrodynamic coefficients for the HTC can be derived. These should be compared to the coefficients derived from the Parnassos results. By using the coefficients, manoeuvring predictions can be made, which can be compared to the simulation results obtained with the Parnassos coefficients. This will give more insight into the sensitivity of the simulation results to changes in the viscous-flow results.

- In this thesis, only the bare hull is considered in the viscous-flow calculations. However, it is possible to include the propeller influence by e.g. using an actuator disc model to model the propeller thrust, or by calculating the flow around the propeller with a potential flow code and to introduce the calculated forces on the propeller as a force field in the RANS calculations. Furthermore, it is possible to include the rudder in the grid, such that the forces due to the rudder can be obtained as well. With such computations, the empirical modules for the propeller and rudder can be substituted by results obtained with the viscous-flow solvers and probably improve the manoeuvring predictions.

- To prepare for future developments (i.e. increase in computing power), the coupling of the RANS equations and the equations of motions should be implemented in ReFRESCO. This will avoid the simplifications made in the *virtual captive test* approach, such as quasi-steadiness, and therefore result in a better reliability of the simulations. In a first stage, this can be done for the bare hull only, with the appendage forces predicted using e.g. a coupling with SurSim, but fully appended in a later stage.

References

[1] I. H. Abbott and A. E. von Doenhoff. *Theory of Wing Sections: Including a Summary of Airfoil Data*. Dover Publications, Inc., New York, 1959.

[2] A. Abkowitz. Lectures on ship hydrodynamics - steering and maneuverability. Technical Report Hy-5, Hydro- og Aerodynamisk Laboratorium, Lyngby, Denmark, 1964.

[3] B. Alessandrini and G. Delhommeau. Viscous free surface flow past a ship in drift and in rotating motion. In *22nd Symposium on Naval Hydrodynamics*, pages 491–507, Fukuoka, Japan, August 1998.

[4] N. Alin, R. E. Bensow, C. Fureby, T. Huuva, and U. Svennberg. Current capabilities of DES and LES for submarines at straight course. *Journal of Ship Research*, 54(3):184–196, September 2010.

[5] N. Alin, C. Fureby, and S. U. Svennberg. LES of the flow past simplified submarine hulls. In *8th International Conference on Numerical Ship Hydrodynamics*, Busan, Korea, September 2003.

[6] V. K. Ankudinov and B. K. Jakobsen. Physically based maneuvering model for simulations and test evaluations. In *MARSIM International Conference on Marine Simulation and Ship Manoeuvring*, number B4, Terschelling, The Netherlands, June 2006.

[7] R. Aris. *Vectors, Tensors and the Basic Equations of Fluid Mechanics*. Prentice-Hall, Inc., Englewood Cliffs, N.J., 1962.

[8] E. Armaoğlu, R. Eggers, F. H. H. A. Quadvlieg, and P. van Coevorden. On the manoeuvrablity of naval surface ships with respect to a new STANAG. In *RINA WARSHIP 2010: Advanced Technologies in Naval Design and Construction*, London, UK, June 2010.

[9] ASME. Standard for verification and validation in computational fluid dynamics and heat transfer. American Society of Mechanical Engineers (ASME) V&V 20 Committee, November 2009.

[10] P. Atsavapranee, T. Forlini, D. Furey, J. Hamilton, S. Percival, and C.-H. Sung. Experimental measurements for CFD validation of the flow about a submarine model (ONR Body-1). In *25th Symposium on Naval Hydrodynamics*, St. Johns, Newfoundland and Labrador, Canada, August 2004.

[11] G. K. Batchelor. *An Introduction to Fluid Mechanics*. Cambridge University Press, 1967. ISBN 0 521 66396 2.

[12] D. Bellevre, A. Diaz de Tuesta, and P. Perdon. Submarine maneuverability assessment using CFD. In *23rd Symposium on Naval Hydrodynamics*, pages 820–832, Val de Reuil, France, September 2000.

[13] V. Bertram. *Practical Ship Hydrodynamics*. Butterworth-Heinemann, 2000.

[14] M. C. Bettle, A. G. Gerber, and G. D. Watt. Unsteady analysis of the six DOF motion of a buoyantly rising submarine. *Computers & Fluids*, 38(9):1833–1849, October 2009.

[15] M. C. Bettle, S. L. Toxopeus, and A. G. Gerber. Calculation of bottom clearance effects on Walrus submarine hydrodynamics. *International Shipbuilding Progress*, 57(3–4):101–125, 2010.

[16] S. Bhushan, T. Xing, P. Carrica, and F. Stern. Model- and full-scale URANS simulations of Athena resistance, powering, seakeeping, and 5415 maneuvering. *Journal of Ship Research*, 53(4):179–198, December 2009.

[17] R. Broglia, R. Muscari, and A. Di Mascio. Numerical analysis of blockage effects in PMM tests. In *26th Symposium on Naval Hydrodynamics*, Rome, Italy, September 17-22 2006.

[18] G. Bulian, R. G. Nicolosi, and A. Francescutto. On the effect of uncertainty modeling in the hydrodynamic derivatives of a ship manoeuvring mathematical model. In *7th ICHD International Conference on Hydrodynamics*, pages 359–368, Ischia, Italy, October 2006.

[19] P. W. Bull. The validation of CFD predictions of nominal wake for the SUBOFF fully appended geometry. In *21st Symposium on Naval Hydrodynamics*, pages 1061–1076, Trondheim, Norway, June 1996.

[20] P. W. Bull and S. Watson. The scaling of high Reynolds number viscous flow predictions for appended submarine geometries. In *22nd Symposium on Naval Hydrodynamics*, pages 1000–1014, Fukuoka, Japan, August 1998.

[21] E. F. Campana, A. Di Mascio, and R. Penna. CFD analysis of the flow past a ship in steady drift motion. In *3rd Osaka Colloquium on advanced CFD applications to ship flow and hull form design*, pages 151–159, Osaka, Japan, May 1998.

[22] P. M. Carrica, F. Ismail, M. Hyman, S. Bhushan, and F. Stern. Turn and zigzag maneuvers of a surface combatant using a URANS approach with dynamic overset grids. In *SIMMAN Workshop on Verification and Validation of Ship Manoeuvring Simulation Methods*, pages F17–22, Copenhagen, Denmark, April 2008.

[23] P. M. Carrica and F. Stern. DES simulations of KVLCC1 in turn and zigzag maneuvers with moving propeller and rudder. In *SIMMAN Workshop on Verification and Validation of Ship Manoeuvring Simulation Methods*, pages F11–16, Copenhagen, Denmark, April 2008.

[24] C. J. Chesnakas and R. L. Simpson. Full three-dimensional measurements of the cross-flow separation region of a 6:1 prolate spheroid. *Experiments in Fluids*, 17(1–2):68–74, June 1994.

[25] D. Clarke and A. P. Mesbahi, editors. *24^{th} International Towing Tank Conference*, Edinburgh, United Kingdom, September 2005.

[26] C. L. Crane. Maneuvering trials of the 278,000 DWT Esso Osaka in shallow and deep water. In *Transactions of the SNAME*, volume 87, pages 251–283, 1979.

[27] A. Cura Hochbaum. Computation of the turbulent flow around a ship model in steady turn and in steady oblique motion. In *22^{nd} Symposium on Naval Hydrodynamics*, pages 550–567, Fukuoka, Japan, August 1998.

[28] A. Cura Hochbaum. Virtual PMM tests for manoeuvring prediction. In *26^{th} Symposium on Naval Hydrodynamics*, Rome, Italy, September 17-22 2006.

[29] A. Cura Hochbaum and M. Vogt. On the prediction of hydrodynamic forces on a manoeuvring ship. In *MARSIM International Conference on Marine Simulation and Ship Manoeuvring*, pages RC–20–1–7, Kanazawa, Japan, August 2003. The Society of Naval Architects of Japan and Japan Institute of Navigation.

[30] A. Cura Hochbaum, M. Vogt, and S. Gatchell. Manoeuvring prediction for two tankers based on RANS simulations. In *SIMMAN Workshop on Verification and Validation of Ship Manoeuvring Simulation Methods*, pages F23–28, Copenhagen, Denmark, April 2008.

[31] J. Dacles-Mariani, G. G. Zilliac, J. S. Chow, and P. Bradshaw. Numerical/experimental study of a wingtip vortex in the near field. *AIAA Journal*, 33:1561–1568, September 1995.

[32] I. Dand. Low-speed manoeuvring criteria: some considerations. In *MARSIM International Conference on Marine Simulation and Ship Manoeuvring*, pages KN–4–1–8, Kanazawa, Japan, August 2003. The Society of Naval Architects of Japan and Japan Institute of Navigation.

[33] J. A. DeMoss. Drag measurements on an ellipsoidal body. Master's thesis, Virginia Polytechnic Institute and State University, Blacksburg, Virginia, August 2007.

[34] E. M. Dempsey. Experimental investigation of the stability and control characteristics of the Walrus class submarine. Technical report, David W. Taylor Naval Ship Research and Development Center, November 1980.

[35] A. Di Mascio, R. Broglia, and R. Muscari. Unsteady RANS simulation of a manoeuvring ship hull. In *25th Symposium on Naval Hydrodynamics*, pages 9–18, St. Johns, Newfoundland and Labrador, Canada, August 2004.

[36] A. Di Mascio and E. F. Campana. The numerical simulation of the yaw flow of a free surface ship. In *7th International Conference on Numerical Ship Hydrodynamics*, pages 6.1–1–10, Nantes, France, July 1999.

[37] A. Drouet, E. Jacquin, B. Alessandrini, P. Ferrant, L. Gentaz, C. Monroy, J. M. Rousset, P. E. Guillerm, and P. Perdon. Simulation of unsteady ship maneuvering on calm water and in waves using free-surface RANS solver. In 27th *Symposium on Naval Hydrodynamics*, volume 2, B29, Seoul, Korea, October 5–10 2008.

[38] L. Eça and M. Hoekstra, editors. *Workshop on CFD Uncertainty Analysis*, Lisbon, Portugal, October 2004. Instituto Superior Técnico.

[39] L. Eça and M. Hoekstra. On the influence of grid topology on the accuracy of ship viscous flow calculations. In *5th Osaka Colloquium on Advanced CFD Applications to Ship Flow and Hull Form Design*, pages 1–10, March 2005.

[40] L. Eça and M. Hoekstra. The numerical friction line. *Journal of Marine Science and Technology*, 13(4):328–345, November 2008.

[41] L. Eça and M. Hoekstra. Evaluation of numerical error estimation based on grid refinement studies with the method of the manufactured solutions. *Computers & Fluids*, 38(8):1580–1591, September 2009.

[42] L. Eça and M. Hoekstra. On the numerical accuracy of the prediction of resistance coefficients in ship stern flow calculations. *Journal of Marine Science and Technology*, 14(1):2–18, March 2009.

[43] L. Eça, M. Hoekstra, and J. Windt. Practical grid generation tools with applications to ship hydrodynamics. In *7th International Conference on Grid Generation and Computational Field Simulations*, Hawaii, February 2002.

[44] L. Eça, G. N. V. B. Vaz, and M. Hoekstra. Code verification, solution verification and validation in RANS solvers. In *29th International Conference on Ocean, Offshore and Arctic Engineering OMAE*, number OMAE2010-20338, Shanghai, China, June 2010.

[45] L. Eça, G. N. V. B. Vaz, and M. Hoekstra. A verification and validation exercise for the flow over a backward facing step. In *Fifth European Conference on Computational Fluid Dynamics*, Lisbon, Portugal, June 2010. ECCOMAS.

[46] O. M. El Moctar. Numerical computations of flow forces in ship manoeuvring. *Schiffstechnik / Ship Technology Research*, 48:98–123, 2001.

[47] K. Eloot. *Selection, Experimental Determination and Evaluation of a Mathematical Model for Ship Manoeuvring in Shallow Water*. PhD thesis, Universiteit Gent, 2006.

[48] K. Eloot and M. Vantorre. Development of a tabular manoeuvring model for hull forces applied to full and slender ships in shallow water. In *MARSIM International Conference on Marine Simulation and Ship Manoeuvring*, pages RC–18–1–9, Kanazawa, Japan, August 2003. The Society of Naval Architects of Japan and Japan Institute of Navigation.

[49] A. Etebari, P. Atsavapranee, J. B. Carneal, A. S. Percival, D. J. Grant, C.-H. Sung, and I.-Y. Koh. Experimental measurements on a SUBOFF model in a turning maneuver. In 27^{th} *Symposium on Naval Hydrodynamics*, volume 2, B30, Seoul, Korea, October 5–10 2008.

[50] L. Fabbri, L. Benedetti, B. Bouscasse, F. L. Gala, and C. Lugni. An experimental study of the maneuverability of a blunt ship: the effect of the water depth. In *9^{th} NuTTS Numerical Towing Tank Symposium*, Le Croisic, France, October 2006.

[51] F. Fathi, C. M. Klaij, and A. H. Koop. Predicting loads on a LNG carrier with CFD. In *29^{th} International Conference on Ocean, Offshore and Arctic Engineering OMAE*, number OMAE2010-20122, Shanghai, China, June 2010.

[52] T. I. Fossen. *Guidance and Control of Ocean Vehicles*. John Wiley and Sons, 1994.

[53] C. Fureby. Towards the use of large eddy simulation in engineering. In *46^{th} AIAA Aerospace Sciences Meeting and Exhibit*, number AIAA 2008-605, Reno, Nevada, January 2008. American Institute of Aeronautics and Astronautics.

[54] Q. Gao and D. Vassalos. Computational hydrodynamic derivatives by numerical PMM. In *Marine CFD*, Southampton, UK, March 2008. Royal Institution of Naval Architects.

[55] K. Granlund. *Steady and Unsteady Maneuvering Forces and Moments on Slender Bodies*. PhD thesis, Virginia Polytechnic Institute and State University, February 2009.

[56] K. Granlund and R. L. Simpson. Modeling unsteady maneuvers on slender bodies. In *AIAA Atmospheric Flight Mechanics Conference and Exhibit*, number AIAA 2007-6721, Hilton Head, South Carolina, August 2007. American Institute of Aeronautics and Astronautics.

[57] N. C. Groves, T. T. Huang, and M. S. Chang. Geometric characteristics of DARPA SUBOFF models (DTRC Model Nos. 5470 and 5471). *Report No. DTRC/SHD-1298-01*, March 1998.

[58] T. Hino, editor. *CFD Workshop Tokyo*, Tokyo, Japan, March 2005. National Maritime Research Institute.

[59] M. Hoekstra. *Numerical Simulation of Ship Stern Flows with a Space-Marching Navier-Stokes Method*. PhD thesis, Delft University of Technology, Faculty of Mechanical Engineering and Marine Technology, October 1999.

[60] M. Hoekstra and L. Eça. PARNASSOS: an efficient method for ship stern flow calculation. In *3rd Osaka Colloquium on advanced CFD applications to ship flow and hull form design*, pages 331–357, Osaka, May 1998.

[61] M. Hoekstra, L. Eça, J. Windt, and H. C. Raven. Viscous flow calculations for KVLCC2 and KCS models using the PARNASSOS code. *Gothenburg 2000 Workshop on Numerical Ship Hydrodynamics*, 2000.

[62] J. Holtrop and G. G. J. Mennen. An approximate power prediction method. *International Shipbuilding Progress*, 29:166–170, July 1982.

[63] J. P. Hooft. The cross flow drag on a manoeuvring ship. *Ocean Engineering*, 21(3):329–342, April 1994.

[64] J. P. Hooft and U. Nienhuis. The prediction of the ship's manoeuvrability in the design stage. *SNAME Annual Meeting*, 102:1–24, November 1994.

[65] J. P. Hooft and J. B. M. Pieffers. Maneuverability of frigates in waves. *Marine Technology*, 25(4):262–271, October 1988.

[66] J. P. Hooft and F. H. H. A. Quadvlieg. Non-linear hydrodynamic hull forces derived from segmented model tests. In *MARSIM International Conference on Marine Simulation and Ship Manoeuvrability*, pages 399–409, Copenhagen, Denmark, September 1996.

[67] S. Hosder. Unsteady skin-friction measurements on a maneuvering Darpa2 Suboff model. Master's thesis, Virginia Polytechnic Institute and State University, June 2001.

[68] T. T. Huang, H.-L. Liu, N. Groves, T. Forlini, J. Blanton, and S. Gowing. Measurements of flows over an axisymmetric body with various appendages in a wind tunnel: the DARPA SUBOFF experimental program. In *19th Symposium on Naval Hydrodynamics*, pages 312–346, Seoul, South Korea, August 1992.

[69] IMO. Resolution MSC. 137(76): Standards for ship manoeuvrability. International Maritime Organisation, London, 2002.

[70] S. Inoue, M. Hirano, and K. Kijima. Hydrodynamic derivatives on ship manoeuvring. *International Shipbuilding Progress*, 28(321):112–125, 1981.

[71] T. Ishiguro, S. Tanaka, and Y. Yoshimura. A study on the accuracy of the recent prediction technique of ship's manoeuvrability at early design stage. In *MARSIM International Conference on Marine Simulation and Ship Manoeuvring*, pages 547–561, Copenhagen, Denmark, September 1996.

[72] Guide to the expression of uncertainty in measurement. International Organization for Standardization (ISO), 1995.

[73] ITTC. Testing and extrapolation methods manoeuvrability - free running model tests. *Recommended Procedures and Guidelines*, 7.5-02, 06-01, September 2008.

[74] G. Jensen, M. Klemt, and Y. Xing-Kaeding. On the way to the numerical basin for seakeeping and manoeuvring. In *9th Symposium on Practical Design of Ships and Other Floating Structures (PRADS)*, number 74, Lübeck-Travemünde, Germany, September 2004.

[75] R. Jonnalagadda, L. K. Taylor, and D. L. Whitfield. Multiblock multigrid incompressible RANS computation of forces and moments on appended SUBOFF configurations at incidence. In *35th Aerospace Sciences Meeting and Exhibit*, number AIAA 1997-624, Reno, Nevada, January 1997.

[76] D. Kang and K. Hasegawa. Prediction method of hydrodynamic forces acting on the hull of a blunt-body ship in the even keel condition. *Journal of Marine Science and Technology*, 12(1):1–14, March 2007.

[77] W. J. Kim, S. H. Van, and D. H. Kim. Measurement of flows around modern commercial ship models. *Experiments in Fluids*, 31(5):567–578, November 2001.

[78] J. C. Kok. Resolving the dependence on free-stream values for the $k-\omega$ turbulence model. *National Aerospace Laboratory, The Netherlands, Report NLR-TP-99295*, July 1999.

[79] A. H. Koop, C. M. Klaij, and G. N. V. B. Vaz. Predicting wind shielding for FPSO tandem offloading using CFD. In *29th International Conference on Ocean, Offshore and Arctic Engineering OMAE*, number OMAE2010-20284, Shanghai, China, June 2010.

[80] A. M. Kracht. On propeller-rudder interaction. In *Intemational Symposium on Propulsors and Cavitation*, Hamburg, Germany, June 22–25 1992.

[81] G. Kuiper. Resistance and propulsion of ships. Delft University of Technology, July 1991.

[82] K. Kume, J. Hasegawa, Y. Tsukada, J. Fujisawa, R. Fukasawa, and M. Hinatsu. Measurements of hydrodynamic forces, surface pressure, and wake for obliquely towed tanker model and uncertainty analysis for CFD validation. *Journal of Marine Science and Technology*, 11(2):65–75, June 2006.

[83] L. Larsson, F. Stern, and V. Bertram. Benchmarking of computational fluid dynamics for ship flows: The Gothenburg 2000 workshop. *Journal of Ship Research*, 47(1):63–81, March 2003.

[84] H.-Y. Lee and S.-S. Shin. The prediction of ship's manoeuvring performance in initial design stage. In *Practical Design of Ships and Mobile Units (PRADS)*, pages 633–639, The Hague, The Netherlands, September 1998.

[85] S.-J. Lee, H.-R. Kim, W.-J. Kim, and S.-H. Van. Wind tunnel tests on flow characteristics of the KRISO 3,600 TEU containership and 300k VLCC double-deck ship models. *Journal of Ship Research*, 47(1):24–38, March 2003.

[86] S. K. Lee and M. Fujino. Assessment of a mathematical model for the manoeuvring motion of a twin-propeller twin-rudder ship. *International Shipbuilding Progress*, 50(1/2):109–123, 2003.

[87] S. W. Lee. Free sailing manoeuvring tests on KVLCC1 and KVLCC2. MARIN Report No. 21571-1-SMB, Wageningen, The Netherlands, December 2007.

[88] H.-L. Liu and T. T. Huang. Summary of DARPA SUBOFF experimental program data. *Report No. CRDKNSWC/HD-1298-11*, June 1998.

[89] J. F. Longo. *Effects of Yaw on Model-Scale Ship Flows.* PhD thesis, University of Iowa, May 1996.

[90] S. C. McParlin and R. W. Tramel. Taxonomy of flight mechanics issues for aircraft, and underlying fluid dynamics phenomena. In 47^{th} *AIAA Aerospace Sciences Meeting Including The New Horizons Forum and Aerospace Exposition*, number AIAA 2009-744, Orlando, Florida, January 2009. American Institute of Aeronautics and Astronautics.

[91] F. R. Menter. Two-equation eddy-viscosity turbulence models for engineering applications. *AIAA Journal*, Vol. 32(8):1598–1605, August 1994.

[92] F. R. Menter. Eddy viscosity transport equations and their relation to the $k - \epsilon$ model. *Journal of Fluids Engineering*, 119(4):876–884, December 1997.

[93] R. W. Miller. PMM calculations for the bare and appended DTMB 5415 using the RANS solver CFDShip-Iowa. In *SIMMAN Workshop on Verification and Validation of Ship Manoeuvring Simulation Methods*, pages F41–49, Copenhagen, Denmark, April 2008.

[94] A. F. Molland and S. R. Turnock. Wind tunnel investigation of the influence of propeller loading on ship rudder performance. *Transactions RINA*, 135:105–120, 1993.

[95] R. Muscari, R. Broglia, and A. Di Mascio. Trajectory prediction of a self propelled hull by unsteady RANS computations. In *27th Symposium on Naval Hydrodynamics*, volume 2, B31, Seoul, Korea, October 5–10 2008.

[96] NATO. ANEP-70 Guidance for naval surface ships mission oriented manoeuvring requirements. Naval Group 6 Specialist Team on Naval Ship Manoeuvrability, September 2003.

[97] N. H. Norrbin. Theory and observations on the use of a mathematical model for ship maneuvering in deep and confined waters. In *8th Symposium on Naval Hydrodynamics*, pages 807–904, Pasadena, California, August 1970.

[98] A. Ogawa and H. Kasai. On the mathematical model of manoeuvring motion of ships. *International Shipbuilding Progress*, 25(292):306–319, December 1978.

[99] T. Ohmori. Finite-volume simulations of flows about a ship in manoeuvring motion. *Journal of Marine Science and Technology*, 3(2):82–93, June 1998.

[100] T. Ohmori, M. Fujino, and H. Miyata. A study on flow field around full ship forms in manoeuvring motion. *Journal of Marine Science and Technology*, 3(1):22–29, March 1998.

[101] P. Oltmann and S. D. Sharma. Simulation of combined engine and rudder manoeuvres using an improved model of hull-propeller-rudder interactions. In *15th Symposium on Naval Hydrodynamics*, pages 83–108, Hamburg, Germany, September 1984.

[102] M. W. C. Oosterveld and P. van Oossanen. Further computer analyzed data of the Wageningen B-screw series. *International Shipbuilding Progress*, 22(251):251–262, July 1975.

[103] M. Örnfelt. Naval mission and task driven manoeuvrability requirements for naval ships. In *10th International Conference on Fast Sea Transportation (FAST)*, pages 505–518, Athens, Greece, October 2009.

[104] B. Overpelt. Manoeuvring tests on KCS. MARIN Report No. 23991-1-SMB, Wageningen, The Netherlands, September 2010.

[105] B. Overpelt and S. L. Toxopeus. Manoeuvring tests on HTC. MARIN Report No. 23277-3-SMB, Wageningen, The Netherlands, January 2011.

[106] R. Pankajakshan, M. G. Remotigue, L. K. Taylor, M. Jiang, W. R. Bridley, and D. L. Whitfield. Validation of control-surface induced submarine maneuvering simulations using UNCLE. In *24th Symposium on Naval Hydrodynamics*, pages 83–97, Fukuoka, Japan, July 2002.

[107] A. B. Phillips, S. R. Turnock, and M. Furlong. Evaluation of manoeuvring coefficients of a self-propelled ship using a blade element momentum propeller model coupled to a Reynolds averaged Navier Stokes flow solver. *Ocean Engineering*, 36(15–16):1217–1225, November 2009.

[108] J. E. Poremba. Hydrodynamics and maneuvering simulations of a non-body-of-revolution submarine. Master's thesis, Pennsylvania State University, December 2009.

[109] F. H. H. A. Quadvlieg. A new combined seakeeping and manoeuvring basin for the third millennium maritime research. In *MARSIM International Conference on Marine Simulation and Ship Manoeuvring*, Orlando, Florida, May 2000.

[110] F. H. H. A. Quadvlieg, E. Armaoğlu, R. Eggers, and P. van Coevorden. Prediction and verification of the maneuverability of naval surface ships. In *SNAME Annual Meeting and Expo*, Seattle/Bellevue, WA, November 2010.

[111] F. H. H. A. Quadvlieg and P. van Coevorden. Manoeuvring criteria: more than IMO A751 requirements alone! In *MARSIM International Conference on Marine Simulation and Ship Manoeuvring*, pages RB–1–1–8, Kanazawa, Japan, August 2003. The Society of Naval Architects of Japan and Japan Institute of Navigation.

[112] B. J. Racine and E. G. Paterson. CFD-based method for simulation of marine-vehicle maneuvering. In *35th AIAA Fluid Dynamics Conference and Exhibit*, number AIAA 2005-4904, Toronto, Ontario, Canada, June 2005. American Institute of Aeronautics and Astronautics.

[113] H. C. Raven, A. van der Ploeg, and L. Eça. Extending the benefit of CFD tools in ship design and performance prediction. In *7th ICHD International Conference on Hydrodynamics*, pages 573–580, October 2006.

[114] H. C. Raven, A. van der Ploeg, and A. R. Starke. Computation of free-surface viscous flows at model and full scale by a steady iterative approach. In *25th Symposium on Naval Hydrodynamics*, August 2004.

[115] P. J. Roache. *Verification and Validation in Computational Science and Engineering*. Hermosa Publishers, Albuquerque, New Mexico, 1998.

[116] R. F. Roddy. Investigation of the stability and control characteristics of several configurations of the DARPA SUBOFF model (DTRC Model 5470) from captive-model experiments. *Report No. DTRC/SHD-1298-08*, September 1990.

[117] R. F. Roddy, R. M. Curphey, and K. P. Delaney. Advances in understanding of maneuvering characteristics for non-body-of-revolution submersibles. In 27^{th} *Symposium on Naval Hydrodynamics*, volume 2, B36, Seoul, Korea, October 5–10 2008.

[118] N. Sakamoto. *URANS and DES Simulations Of Static And Dynamic Maneuvering For Surface Combatant*. PhD thesis, University of Iowa, Iowa City, Iowa, May 2009.

[119] N. Sakamoto, P. M. Carrica, and F. Stern. URANS simulations of static and dynamic maneuvering for surface combatant. In *SIMMAN Workshop on Verification and Validation of Ship Manoeuvring Simulation Methods*, pages F50–55, Copenhagen, Denmark, April 2008.

[120] M. D. Salas. Digital flight: The last CFD aeronautical grand challenge. *Journal of Scientific Computing*, 28(213):479–505, September 2006.

[121] T. Sato, K. Izumi, and H. Miyata. Numerical simulation of maneuvering motion. In *22^{nd} Symposium on Naval Hydrodynamics*, pages 724–737, Fukuoka, Japan, August 1998.

[122] C. D. Simonsen. *Rudder, Propeller and Hull Interaction by RANS*. PhD thesis, Technical University of Denmark, Department of Naval Architecture and Offshore Engineering, May 2000.

[123] C. D. Simonsen and F. Stern. Verification and validation of RANS maneuvering simulation of Esso Osaka: effects of drift and rudder angle on forces and moments. *Computers & Fluids*, 32(10):1325–1356, December 2003.

[124] C. D. Simonsen and F. Stern. Flow pattern around an appended tanker hull form in simple maneuvering conditions. *Computers & Fluids*, 34(2):169–198, February 2005.

[125] C. D. Simonsen and F. Stern. RANS maneuvering simulation of esso osaka with rudder and a body-force propeller. *Journal of Ship Research*, 49(2):98–120, June 2005.

[126] C. D. Simonsen and F. Stern. Flow structure around maneuvering tanker in deep and shallow water. In *26^{th} Symposium on Naval Hydrodynamics*, number M1, Rome, Italy, September 17–22 2006.

[127] C. D. Simonsen, F. Stern, and K. Agdrup. CFD with PMM test validation for manoeuvring VLCC2 tanker in deep and shallow water. In *MARSIM International Conference on Marine Simulation and Ship Manoeuvring*, number M04, Terschelling, The Netherlands, June 2006.

[128] H. Söding. Forces on rudders behind a manoeuvring ship. In *Third Symposium on Numerical Ship Hydrodynamics*, 1980.

[129] P. R. Spalart and S. R. Allmaras. A one-equatlon turbulence model for aerodynamic flows. In *30th Aerospace Sciences Meeting & Exhibit*, Reno, Nevada, January 1992. American Institute of Aeronautics and Astronautics.

[130] F. Stern and K. Agdrup, editors. *SIMMAN Workshop on Verification and Validation of Ship Manoeuvring Simulation Methods*, Copenhagen, Denmark, April 2008.

[131] F. Stern, K. Agdrup, S. Y. Kim, A. Cura Hochbaum, K. P. Rhee, F. H. H. A. Quadvlieg, P. Perdon, T. Hino, R. Broglia, and J. Gorski. Lessons learnt from the workshop on verification and validation of ship manoeuvring simulation methods - SIMMAN 2008. In *International Conference on Marine Simulation and Ship Maneuverability, MARSIM*, pages M–24–1–10, Panama City, Panama, August 2009.

[132] F. Stern, F. Ismail, T. Xing, and P. Carrica. Vortical and turbulent structures using various convection schemes with algebraic reynolds stress-DES model for the KVLCC2 at large drift angles. In 27th *Symposium on Naval Hydrodynamics*, volume 2, B34, Seoul, Korea, October 5–10 2008.

[133] F. Stern, R. V. Wilson, H. W. Coleman, and E. G. Paterson. Comprehensive approach to verification and validation of CFD simulations - part 1: Methodology and procedures. *Journal of Fluids Engineering*, 123(4):793–802, December 2001.

[134] J. Strom-Tejsen and R. R. Porter. Prediction of controllable pitch propeller performance in off-design conditions. In *Third Ship Control Systems Symposium*, 1972.

[135] C.-H. Sung, T.-C. Fu, and M. Griffin. Validation of incompressible flow computation of forces and moments on axisymmetric bodies undergoing constant radius turning. In *21st Symposium on Naval Hydrodynamics*, pages 1048–1060, Trondheim, Norway, June 1996.

[136] C.-H. Sung, T. C. Fu, M. J. Griffin, and T. T. Huang. Validation of incompressible flow computation of forces and moments on axisymmetric bodies at incidence. In *33rd Aerospace Sciences Meeting and Exhibit*, number AIAA 1995-528, Reno, Nevada, January 1995.

[137] C.-H. Sung, M. J. Griffin, J. F. Tsai, and T. T. Huang. Incompressible flow computation of forces and moments on bodies of revolution at incidence. In *31st Aerospace Sciences Meeting and Exhibit*, number AIAA 1993-787, Reno, Nevada, January 1993.

[138] C.-H. Sung, M.-Y. Jiang, B. Rhee, S. Percival, P. Atsavapranee, and I.-Y. Koh. Validation of the flow around a turning submarine. In *24th Symposium on Naval Hydrodynamics*, Fukuoka, Japan, July 2002.

[139] C.-H. Sung, B. Rhee, and E. Ammeen. SHWG CFD benchmark study on DARPA SUBOFF. Part 1. Bare hull. *SHWG Correspondence*, pages 1–26, November 2005.

[140] Y. Tahara, J. F. Longo, and F. Stern. Comparison of CFD and EFD for the Series 60 C_B=0.6 in steady drift motion. *Journal of Marine Science and Technology*, 7(1):17–30, August 2002.

[141] S. L. Toxopeus. Simulation and validation of the viscous flow around the Series 60 hull form at 10° drift angle. In *7th NuTTS Numerical Towing Tank Symposium*, Hamburg, Germany, October 2004.

[142] S. L. Toxopeus. Validation of calculations of the viscous flow around a ship in oblique motion. In *The First MARIN-NMRI Workshop*, pages 91–99, Tokyo, Japan, October 2004.

[143] S. L. Toxopeus. Verification and validation of calculations of the viscous flow around KVLCC2M in oblique motion. In *5th Osaka Colloquium on Advanced CFD Applications to Ship Flow and Hull Form Design*, pages 200–209, Osaka, Japan, March 2005.

[144] S. L. Toxopeus. Calculation of hydrodynamic manoeuvring coefficients using viscous-flow calculations. In *7th ICHD International Conference on Hydrodynamics*, pages 493–502, Ischia, Italy, October 2006.

[145] S. L. Toxopeus. Validation of slender-body method for prediction of linear manoeuvring coefficients using experiments and viscous-flow calculations. In *7th ICHD International Conference on Hydrodynamics*, pages 589–598, Ischia, Italy, October 2006.

[146] S. L. Toxopeus, editor. *SHWG collaborative CFD excercise - Bare hull DARPA SUBOFF submarine at straight flight and drift angle*. MARIN Report 21668-1-CPM, November 2007.

[147] S. L. Toxopeus. Viscous-flow calculations for bare hull DARPA SUBOFF submarine at incidence. *International Shipbuilding Progress*, 55(3):227–251, December 2008.

[148] S. L. Toxopeus. Deriving mathematical manoeuvring models for bare ship hulls using viscous flow calculations. *Journal of Marine Science and Technology*, 14(1):30–38, March 2009.

[149] S. L. Toxopeus and S. W. Lee. Comparison of manoeuvring simulation programs for SIMMAN test cases. In *SIMMAN Workshop on Verification and Validation of Ship Manoeuvring Simulation Methods*, pages E56–61, Copenhagen, Denmark, April 2008.

[150] S. L. Toxopeus and S. W. Lee. Free sailing tests for European Destroyer. MARIN Report No. 22367-5-CPM, Wageningen, The Netherlands, February 2009.

[151] S. L. Toxopeus and G. N. V. B. Vaz. Calculation of current or manoeuvring forces using a viscous-flow solver. In *28th International Conference on Ocean, Offshore and Arctic Engineering OMAE*, number OMAE2009-79782, Honolulu, Hawaii, May 31–June 5 2009.

[152] S. L. Toxopeus (editor). Calculation and validation of hydrodynamic derivatives. *Virtue Deliverable D3.1.1, Revision 4*, April 2009.

[153] M. Ueno, Y. Yoshimura, Y. Tsukada, and H. Miyazaki. Circular motion tests and uncertainty analysis for ship maneuverability. *Journal of Marine Science and Technology*, 14(4):469–484, December 2009.

[154] A. van der Ploeg and H. C. Raven. CFD-based optimization for minimal power and wake field quality. In *11th International Symposium on Practical Design of Ships and Other Floating Structures (PRADS)*, Rio de Janeiro, Brazil, September 2010.

[155] B. J. van Oers and S. L. Toxopeus. On the relation between flow behaviour and the lateral force distribution acting on a ship in oblique motion. In *10th International Cooperation on Marine Engineering Systems ICMES*, London, UK, March 2006.

[156] D. Vassalos, S. H. Park, and B. S. Lee. Developing a manoeuvring design capability for naval vessels. In *The Sixth International Symposium On Practical Design Of Ships And Mobile Units (PRADS)*, pages 1.616–1.628, Seoul, Korea, September 1995.

[157] G. N. V. B. Vaz, F. A. P. Jaouen, and M. Hoekstra. Free-surface viscous flow computations. Validation of URANS code FreSCo. In *28th International Conference on Ocean, Offshore and Arctic Engineering OMAE*, number OMAE2009-79398, Honolulu, Hawaii, May 31–June 5 2009.

[158] G. N. V. B. Vaz, S. L. Toxopeus, and S. Holmes. Calculation of manoeuvring forces on submarines using two viscous-flow solvers. In *29th International Conference on Ocean, Offshore and Arctic Engineering OMAE*, number OMAE2010-20373, Shanghai, China, June 2010.

[159] G. N. V. B. Vaz, O. Waals, F. Fathi, H. Ottens, T. Le Souef, and K. Kwong. Current Affairs - model tests, semi-empirical predictions and CFD computations for current coefficients of semi-submersibles. In *28th International Conference on Ocean, Offshore and Arctic Engineering OMAE*, number OMAE2009-80216, Honolulu, Hawaii, May 31–June 5 2009.

[160] G. Venkatesan and W. Clark. Submarine maneuvering simulations of ONR Body 1. In *26th International Conference on Offshore Mechanics and Arctic Engineering OMAE*, number OMAE2007-29516, San Diego, California, June 10–15 2007.

[161] M. Vogt, A. Cura Hochbaum, M. Schneider, and J. Dautel. Report on model tests. *Virtue Deliverable D3.1.3*, December 2007.

[162] P. Wesseling. *Principles of Computational Fluid Dynamics*. Springer-Verlag, 2000. ISBN 3-540-67853-0.

[163] L. F. Whicker and L. F. Fehlner. Free-stream characteristics of a family of low-aspect-ratio all-movable control surfaces for application to ship design. Technical Report DTNSRDC Report No. 933, David W. Taylor Naval Ship R&D Center, Bethesda, MD., May 1958.

[164] C. C. Whitfield. Steady and unsteady force and moment data on a DARPA2 submarine. Master's thesis, Virginia Polytechnic Institute and State University, August 1999.

[165] B.-S. Wu, F. Xing, X.-F. Kuang, and Q.-M. Miao. Investigation of hydrodynamic characteristics of submarine moving close to the sea bottom with CFD methods. *Journal of Ship Mechanics*, 9(3):19–28, June 2005.

[166] C. Yang and R. Löhner. Prediction of flows over an axisymmetric body with appendages. In *8th International Conference on Numerical Ship Hydrodynamics*, Busan, Korea, September 2003.

[167] H. Yoon. *Phase-Averaged Stereo-PIV Flow Field And Force/Moment/Motion Measurements For Surface Combatant In PMM Maneuvers*. PhD thesis, University of Iowa, Iowa City, Iowa, December 2009.

Page intentionally left blank

Samenvatting

Praktische toepassing van viskeuze omstromingsberekeningen voor het simuleren van manoeuvrerende schepen

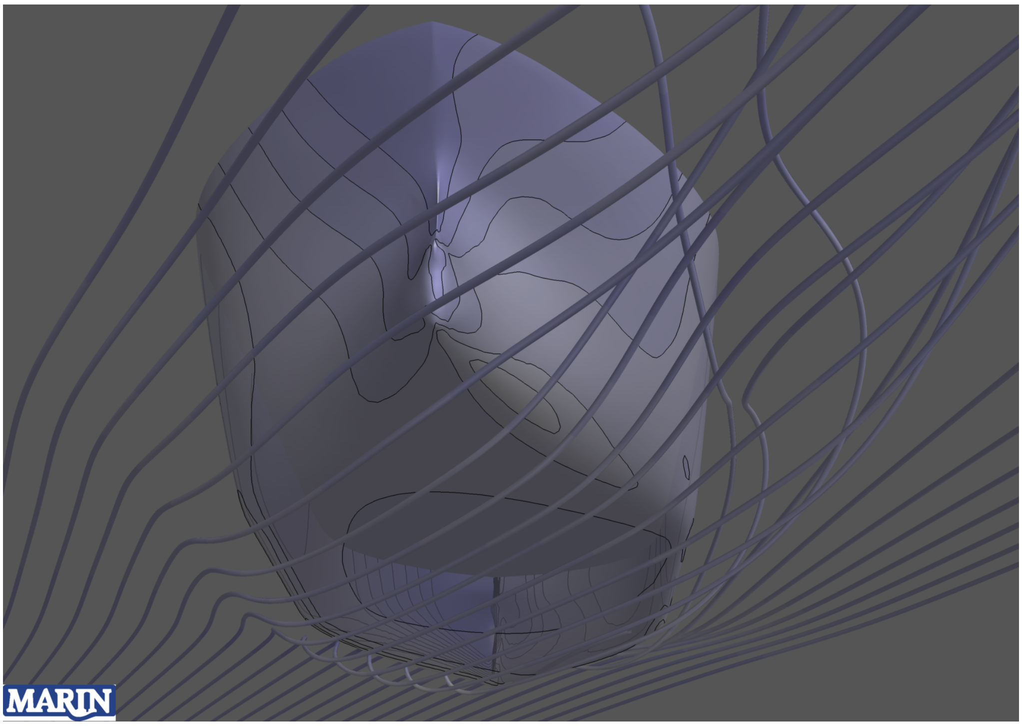

Figure 8.1: Omstroming en druk op het rompoppervlak, KVLCC2, $\beta = -14°$

Het werk dat beschreven is in deze scriptie is gestart om traditionele manoeuvreersimulaties gebaseerd op empirische modellen van de krachten en moment op het schip te verbeteren. Omdat de nauwkeurigheid van viskeuze-omstroming berekeningen om rompkrachten te voorspellen steeds toeneemt, is besloten om een praktische methode voor het simuleren van de scheepsmanoeuvreerbaarheid te ontwikkelen, waarbij viskeuze rekentechnieken gebruikt worden. Het doel is te onderzoeken of hiermee de nauwkeurigheid van manoeuvreerpredicties verbeterd kan worden.

Om dit doel te bereiken, is de *virtual captive test* aanpak gebruikt, vanwege het efficiënte gebruik van rekenkracht van deze aanpak in vergelijking met andere methoden. Deze procedure bootst de traditionele manoeuvreersimulaties na, waarbij experimentele PMM wordt gebruikt om de krachten en momenten op het schip te bepalen. De huidige studie breidt het werk van andere onderzoekers uit, door middel van een uitgebreide verificatie en validatie van de voorspelde krachten en momenten op de romp en een gedetailleerde gevoeligheidsstudie van de manoeuvreereigenschappen van het schip op veranderingen in de hydrodynamische coëfficiënten in het simulatiemodel.

Om de stroming rond schepen in gierbeweging te kunnen berekenen, waren aanpassingen in de rekenprogramma's nodig. Deze veranderingen worden in dit werk beschreven, samen met technieken om de benodigde tijd voor gridgenerering te verkleinen en om sneller geconvergeerde oplossingen te krijgen.

De mogelijkheid om voor een brede range scheepstypes goede voorspellingen van de krachten op het romp te krijgen zal worden gedemonstreerd. Aangetoond zal worden dat de trends in de krachten en momenten als functie van de drifthoek of giersnelheid goed overeenkomen met metingen.

De verificatiestudies leveren bruikbare informatie met betrekking tot de invloed van de griddichtheid op de voorspelde krachten. In een aantal gevallen waren de afwijkingen in de berekeningen groot, wat aantoont dat er modelleerfouten in de numerieke resultaten aanwezig zijn. In deze gevallen bleek vaak dat de dwarskracht te klein voorspeld werd, terwijl het giermoment te groot was. Voor manoeuvreerstudies zijn deze afwijkingen in het algemeen binnen acceptabele grenzen. Toch blijven verbeteringen wenselijk en deze kunnen verkregen worden door het gebruik van fijnere grids, grotere domein groottes, een andere grid topologie met verfijningen van het grid in het zog van het schip, andere turbulentie modellen of het meenemen van het vrije vloeistofoppervlak.

Het predictieprogramma SurSim is gebruikt om de manoeuvreerbaarheid van de HTC te simuleren. Een procedure wordt voorgesteld om de hydrodynamische coefficienten die nodig zijn om de krachten op de romp te beschrijven af te leiden. Deze procedure is gekozen om nauwkeurig zowel het lineaire gedrag tijdens koershouden als het realistische gedrag tijdens havenmanoeuvres te modelleren en tevens niet-lineair gedrag goed te beschrijven.

Ter validatiemateriaal van de manoeuvreersimulaties zijn vrijvarende manoeuvreerproeven met een model van de HTC uitgevoerd. Deze proeven hebben een waardevolle set gegevens opgeleverd die algemeen gebruikt kan worden voor validatie studies. Naast het verkrijgen van de manoeuvreereigenschappen voor een enkelschroef container schip, is door dit proevenprogramma unieke informatie beschikbaar gekomen met betrekking tot de belastingen op de schroef en het roer tijdens manoeuvres. Ook zijn door middel van herhalingsproeven de onzekerheden in de manoeuvreereigenschappen bepaald.

In dit proefschrift zal worden aangetoond dat manoeuvreersimulaties verbeterd kunnen worden, als er hydrodynamische coëfficiënten worden gebruikt die met behulp van CFD zijn bepaald. Vooral in de voorspellingen van de draaicirkel zijn grote verbeteringen zichtbaar ten opzichte van simulaties met coëfficiënten gebaseerd op empirie. Ook de voorspelling van het gedrag tijdens koershouden, op basis van de zig-zag manoeuvres, is verbeterd, maar een verdere verbetering is nodig om meer betrouwbare voorspellingen te krijgen.

De gevoeligheid van de manoeuvreereigenschappen op veranderingen in de hydrodynamische coëfficiënten is onderzocht. Hieruit blijkt dat vooral een nauwkeurige berekening van het giermoment nodig is om betrouwbare voorspellingen te krijgen.

Acknowledgements

The work for this thesis was sponsored by the background research and development of MARIN. I thank MARIN and in particular my former manager Frans Quadvlieg and current manager Henk Prins for their support. I also appreciate the time and effort spent by my supervisor René Huijsmans from Delft University of Technology during this work. Thanks to him I had the opportunity to finalise this work with a PhD degree.

The work presented in this thesis regarding the DARPA SUBOFF and the Walrus submarine was funded through TNO Defence, Security and Safety within the framework of Programma V705 carried out for DMO of the Royal Netherlands Navy. Their support is greatly acknowledged.

Another part (the work on the HTC) was funded by the Commission of the European Communities through the Integrated Project VIRTUE under grant 516201 in the sixth Research and Technological Development Framework Programme (Surface Transport Call). I thank the members of the manoeuvring Work Package of VIRTUE for their discussions and insights during the project.

When starting work at MARIN, I was introduced to the subject of ship manoeuvring by my former colleague Jan Hooft. Thanks to him, I became interested in ship manoeuvring simulations.

Furthermore, this work could not have been done without the support of various colleagues at MARIN. I therefore acknowledge the help of (in random order): Jaap Windt and Chris Klaij for their help in grid generation; Auke van der Ploeg for his efforts in getting difficult Parnassos jobs to converge; Martin Hoekstra and Luís Eça (from Instituto Superior Técnico, Portugal (IST)) for their advice regarding uncertainty analysis; Hoyte Raven for his insight into hydrodynamics in general and discussions about the scope of work; Guilherme Vaz for his development and support of ReFRESCO; Bram Starke for discussions on viscous-flow and help with getting started with Parnassos; Erik van Wijngaarden for his textual suggestions about my thesis and our discussions about being a PhD student; my colleagues at the Helpdesk for keeping the computers and cluster alive. And all others who put up with me when I enthusiastically wanted to show them my ColourFul Diagrams.

Also the work of Mark Bettle from University of New Brunswick is appreciated. He conducted the calculations for the Walrus submarine presented in this thesis. It was a pleasure to have you stay at MARIN and thanks for the great job, Mark!

Bas Overpelt managed and analysed the free sailing experiments for the HTC. Kees Boers supervised also some of the tests. Thanks to both for their efforts and hard work.

Experimental data existing in the public domain has been used to validate the viscous-flow calculations presented in this thesis. This contribution of valuable data of INSEAN, NMRI, HSVA and Naval Surface Warfare Center, Carderock Division (NSWCCD) is greatly appreciated.

Finally, I dearly thank my wife Aisah for her continuous encouragement and support of my PhD work and her valuable advice on planning. Without you, I would still be writing this thesis!

Curriculum Vitae

Serge Toxopeus was born on April 23^{rd}, 1972 in Alkmaar, The Netherlands. He finished high school at the C.S.G. Jan Arentsz in Alkmaar in 1990 and subsequently started to study Maritime Engineering at Delft University of Technology, Faculty of Mechanical Engineering and Marine Technology (currently part of the Faculty of Mechanical, Maritime and Materials Engineering). Serge graduated in 1996 at the Ship Hydromechanics Department with a Master's thesis on the dynamic stability and manoeuvring of planing ships.

In the same year, he became an employee of the Maritime Research Institute Netherlands (MARIN) in Wageningen as Project Leader, Consultant, Project Manager and Senior Project Manager (depending on the year) in the Manoeuvring Department. His main tasks were the development and improvement of mathematical manoeuvring models for surface ships and submarines and the assessment of the manoeuvrability of ships using simulations and model tests. He was actively involved in commercial projects for about eight years.

Around 2002, the desire arose to improve the manoeuvring simulations using advanced techniques and therefore Serge started a PhD study regarding the practical application of viscous-flow calculations for the simulation of manoeuvring ships. Since 2005, most of his time was spent on this PhD study. The work was partly funded as background research by MARIN and partly through the EU project VIRTUE. This thesis is the consolidation of the work done in the past eight years.

To be able to fully concentrate on his research, Serge moved to the Research and Development department in 2007. His present position is Senior Researcher.

Page intentionally left blank

Appendices

Page intentionally left blank

Experimental and computational results of forces, KVLCC1

Id	Re [-]	Fn [-]	β	γ	Solver	Turb.	Grid	X_p	X_f	X	Y_p	Y_f	Y	Z_p	Z_f	Z
01	3.3×10^6	-	0.0	0.00	Parnassos	MNT	1.5×10^6	-0.003	-0.015	-0.018	-	-	-	0.090	0.000	0.090
02	3.3×10^6	-	0.5	0.00	Parnassos	MNT	3.356×10^6	-0.003	-0.015	-0.018	-0.002	-0.000	-0.002	0.080	0.000	0.080
03	3.3×10^6	-	1.0	0.00	Parnassos	MNT	3.356×10^6	-0.003	-0.015	-0.018	-0.003	-0.000	-0.004	0.080	0.000	0.080
04	3.3×10^6	-	2.0	0.00	Parnassos	MNT	3.356×10^6	-0.003	-0.015	-0.018	-0.006	-0.000	-0.006	0.081	0.000	0.081
05	3.3×10^6	-	4.0	0.00	Parnassos	MNT	3.356×10^6	-0.003	-0.015	-0.018	-0.012	-0.001	-0.013	0.084	0.000	0.085
06	3.3×10^6	-	6.0	0.00	Parnassos	MNT	3.356×10^6	-0.004	-0.015	-0.019	-0.023	-0.001	-0.024	0.089	0.000	0.089
07	3.3×10^6	-	9.0	0.00	Parnassos	MNT	3.356×10^6	-0.001	-0.016	-0.018	-0.042	-0.002	-0.043	0.102	0.000	0.102
08	3.3×10^6	-	12.0	0.00	Parnassos	MNT	3.356×10^6	-0.003	-0.016	-0.019	-0.063	-0.002	-0.065	0.117	0.000	0.117
09	3.3×10^6	-	15.0	0.00	Parnassos	MNT	3.356×10^6	-0.002	-0.016	-0.018	-0.086	-0.002	-0.088	0.136	0.001	0.137
10	3.3×10^6	-	0.0	0.13	Parnassos	MNT	3.356×10^6	-0.003	-0.015	-0.018	0.004	-0.000	0.004	0.081	0.000	0.082
11	3.3×10^6	-	0.0	0.26	Parnassos	MNT	3.356×10^6	-0.002	-0.015	-0.017	0.011	-0.000	0.011	0.082	0.000	0.082
12	3.3×10^6	-	0.0	0.39	Parnassos	MNT	3.356×10^6	-0.001	-0.015	-0.017	0.017	-0.000	0.017	0.092	0.000	0.092
13	3.3×10^6	-	0.0	0.52	Parnassos	MNT	3.356×10^6	0.000	-0.015	-0.015	0.022	-0.000	0.022	0.097	0.000	0.097
14	3.3×10^6	-	0.0	0.65	Parnassos	MNT	3.356×10^6	0.002	-0.015	-0.013	0.029	-0.000	0.029	0.105	0.000	0.105
15	3.3×10^6	-	-4.0	0.39	Parnassos	MNT	3.356×10^6	-0.007	-0.015	-0.023	0.033	0.000	0.033	0.096	0.000	0.096
16	3.3×10^6	-	-12.0	0.52	Parnassos	MNT	3.356×10^6	-0.020	-0.017	-0.037	0.104	0.001	0.105	0.124	0.000	0.125

Experimental and computational results of moments, KVLCC1

Id	Re [-]	Fn [-]	β	γ	Solver	Turb.	Grid	K_p	K_f	K	M_p	M_f	M	N_p	N_f	N
01	3.3×10^6	-	0.0	0.00	Parnassos	MNT	1.5×10^6	-	-	-	-0.013	0.000	-0.013	-	-	-
02	3.3×10^6	-	0.5	0.00	Parnassos	MNT	3.356×10^6	0.001	-0.000	0.001	-0.013	0.000	-0.012	-0.002	0.000	-0.002
03	3.3×10^6	-	1.0	0.00	Parnassos	MNT	3.356×10^6	0.003	-0.000	0.002	-0.013	0.000	-0.012	-0.003	0.000	-0.003
04	3.3×10^6	-	2.0	0.00	Parnassos	MNT	3.356×10^6	0.005	-0.001	0.005	-0.013	0.000	-0.012	-0.006	0.000	-0.006
05	3.3×10^6	-	4.0	0.00	Parnassos	MNT	3.356×10^6	0.011	-0.001	0.010	-0.013	0.000	-0.012	-0.011	0.000	-0.011
06	3.3×10^6	-	6.0	0.00	Parnassos	MNT	3.356×10^6	0.018	-0.002	0.017	-0.013	0.000	-0.012	-0.016	0.000	-0.016
07	3.3×10^6	-	9.0	0.00	Parnassos	MNT	3.356×10^6	0.035	-0.002	0.032	-0.015	0.000	-0.015	-0.023	0.000	-0.022
08	3.3×10^6	-	12.0	0.00	Parnassos	MNT	3.356×10^6	0.052	-0.003	0.050	-0.014	0.000	-0.013	-0.028	0.000	-0.028
09	3.3×10^6	-	15.0	0.00	Parnassos	MNT	3.356×10^6	0.076	-0.003	0.073	-0.015	0.000	-0.015	-0.034	0.000	-0.034
10	3.3×10^6	-	0.0	0.13	Parnassos	MNT	3.356×10^6	0.004	-0.000	0.004	-0.013	0.000	-0.012	-0.004	0.000	-0.004
11	3.3×10^6	-	0.0	0.26	Parnassos	MNT	3.356×10^6	0.008	-0.000	0.008	-0.013	0.000	-0.012	-0.009	0.000	-0.009
12	3.3×10^6	-	0.0	0.39	Parnassos	MNT	3.356×10^6	0.012	-0.000	0.011	-0.013	0.000	-0.012	-0.015	0.000	-0.014
13	3.3×10^6	-	0.0	0.52	Parnassos	MNT	3.356×10^6	0.015	-0.000	0.015	-0.013	0.000	-0.013	-0.021	0.000	-0.021
14	3.3×10^6	-	0.0	0.65	Parnassos	MNT	3.356×10^6	0.019	-0.001	0.018	-0.014	0.000	-0.013	-0.027	0.001	-0.026
15	3.3×10^6	-	-4.0	0.39	Parnassos	MNT	3.356×10^6	-0.001	0.001	0.000	-0.010	0.000	-0.009	-0.005	0.000	-0.005
16	3.3×10^6	-	-12.0	0.52	Parnassos	MNT	3.356×10^6	-0.028	0.002	-0.026	-0.003	0.000	-0.002	-0.001	0.000	-0.001

Experimental and computational results of forces, KVLCC2

Id	Re [-]	Fn [-]	β	γ	Solver	Turb.	Grid	X_p	X_f	X	Y_p	Y_f	Y	Z_p	Z_f	Z
01	3.3×10^6	-	0.0	0.00	Parnassos	MNT	1.5×10^6	-0.003	-0.015	-0.018	-	-	-	0.090	0.000	0.090
02	3.7×10^6	0.142	0.3	0.00	Exp (INSEAN)	-	-	-	-	-0.017	-	-	-0.001	-	-	-
03	3.7×10^6	0.142	0.5	0.00	Exp (INSEAN)	-	-	-	-	-0.014	-	-	-0.003	-	-	-
04	3.7×10^6	0.142	0.5	0.00	Exp (INSEAN)	-	-	-	-	-0.018	-	-	-0.002	-	-	-
05	3.7×10^6	0.142	0.9	0.00	Exp (INSEAN)	-	-	-	-	-0.031	-	-	-0.019	-	-	-
06	3.3×10^6	-	1.0	0.00	Parnassos	MNT	3.356×10^6	-0.003	-0.015	-0.018	-0.004	-0.000	-0.004	0.080	0.000	0.080
07	3.7×10^6	0.142	1.0	0.00	Exp (INSEAN)	-	-	-	-	-0.016	-	-	-0.003	-	-	-
08	3.7×10^6	0.142	1.8	0.00	Exp (INSEAN)	-	-	-	-	-0.019	-	-	-0.009	-	-	-
09	3.7×10^6	0.142	2.0	0.00	Exp (INSEAN)	-	-	-	-	-0.015	-	-	-0.008	-	-	-
10	3.3×10^6	-	2.0	0.00	Parnassos	MNT	3.356×10^6	-0.003	-0.015	-0.018	-0.007	-0.000	-0.007	0.081	0.000	0.081
11	3.7×10^6	0.142	3.8	0.00	Exp (INSEAN)	-	-	-	-	-0.020	-	-	-0.017	-	-	-
12	3.7×10^6	0.142	3.9	0.00	Exp (INSEAN)	-	-	-	-	-0.015	-	-	-0.017	-	-	-
13	3.7×10^6	0.142	4.0	0.00	Exp (INSEAN)	-	-	-	-	-0.015	-	-	-0.015	-	-	-
14	3.7×10^6	0.142	4.0	0.00	Exp (INSEAN)	-	-	-	-	-0.015	-	-	-0.015	-	-	-
15	3.7×10^6	0.142	4.0	0.00	Exp (INSEAN)	-	-	-	-	-0.016	-	-	-0.016	-	-	-
16	3.7×10^6	0.142	4.0	0.00	Exp (INSEAN)	-	-	-	-	-0.016	-	-	-0.015	-	-	-
17	3.3×10^6	-	4.0	0.00	Parnassos	MNT	3.356×10^6	-0.004	-0.015	-0.019	-0.015	-0.001	-0.016	0.084	0.000	0.084
18	3.7×10^6	0.142	4.0	0.00	Exp (INSEAN)	-	-	-	-	-0.016	-	-	-0.015	-	-	-
19	3.7×10^6	0.142	4.0	0.00	Exp (INSEAN)	-	-	-	-	-0.014	-	-	-0.015	-	-	-
20	3.7×10^6	0.142	4.0	0.00	Exp (INSEAN)	-	-	-	-	-0.015	-	-	-0.015	-	-	-
21	3.7×10^6	0.142	4.0	0.00	Exp (INSEAN)	-	-	-	-	-0.017	-	-	-0.016	-	-	-
22	3.7×10^6	0.142	4.0	0.00	Exp (INSEAN)	-	-	-	-	-0.017	-	-	-0.016	-	-	-
23	3.7×10^6	0.142	4.0	0.00	Exp (INSEAN)	-	-	-	-	-0.017	-	-	-0.015	-	-	-
24	3.7×10^6	0.142	4.0	0.00	Exp (INSEAN)	-	-	-	-	-0.016	-	-	-0.016	-	-	-
25	3.3×10^6	-	6.0	0.00	Parnassos	MNT	3.356×10^6	-0.004	-0.015	-0.019	-0.025	-0.001	-0.026	0.089	0.000	0.089
26	3.7×10^6	0.142	6.0	0.00	Exp (INSEAN)	-	-	-	-	-0.015	-	-	-0.024	-	-	-
27	3.7×10^6	0.142	6.0	0.00	Exp (INSEAN)	-	-	-	-	-0.020	-	-	-0.025	-	-	-
28	3.3×10^6	-	9.0	0.00	Parnassos	MNT	3.356×10^6	-0.004	-0.016	-0.020	-0.045	-0.001	-0.047	0.101	0.000	0.101
29	3.3×10^6	-	15.0	0.00	Parnassos	MNT	3.356×10^6	-0.002	-0.016	-0.019	-0.093	-0.002	-0.095	0.136	0.001	0.137
30	3.3×10^6	-	0.0	0.13	Parnassos	MNT	3.356×10^6	-0.003	-0.015	-0.018	0.006	-0.000	0.006	0.081	0.000	0.081
31	3.7×10^6	0.142	0.0	0.20	Exp (INSEAN)	-	-	-	-	-0.015	-	-	-0.009	-	-	-
32	3.3×10^6	-	0.0	0.26	Parnassos	MNT	3.356×10^6	-0.002	-0.015	-0.017	0.012	-0.000	0.012	0.082	0.000	0.082
33	3.7×10^6	0.142	0.0	0.40	Exp (INSEAN)	-	-	-	-	-0.015	-	-	-0.020	-	-	-
34	3.7×10^6	0.142	0.0	0.40	Exp (INSEAN)	-	-	-	-	-0.016	-	-	-0.020	-	-	-
35	3.7×10^6	0.142	0.0	0.40	Exp (INSEAN)	-	-	-	-	-0.016	-	-	-0.019	-	-	-
36	3.7×10^6	0.142	0.0	0.40	Exp (INSEAN)	-	-	-	-	-0.015	-	-	-0.018	-	-	-
37	3.7×10^6	0.142	0.0	0.40	Exp (INSEAN)	-	-	-	-	-0.017	-	-	-0.019	-	-	-
38	3.7×10^6	0.142	0.0	0.40	Exp (INSEAN)	-	-	-	-	-0.016	-	-	-0.019	-	-	-
39	3.7×10^6	0.142	0.0	0.40	Exp (INSEAN)	-	-	-	-	-0.014	-	-	-0.019	-	-	-
40	3.7×10^6	0.142	0.0	0.40	Exp (INSEAN)	-	-	-	-	-0.015	-	-	-0.020	-	-	-
41	3.3×10^6	-	0.0	0.39	Parnassos	MNT	3.356×10^6	-0.002	-0.015	-0.017	0.018	-0.000	0.018	0.092	0.000	0.093
42	3.3×10^6	-	0.0	0.52	Parnassos	MNT	3.356×10^6	-0.001	-0.015	-0.016	0.026	-0.000	0.026	0.097	0.000	0.097
43	3.7×10^6	0.142	0.0	0.60	Exp (INSEAN)	-	-	-	-	-0.011	-	-	-0.031	-	-	-
44	3.3×10^6	-	0.0	0.65	Parnassos	MNT	3.356×10^6	0.001	-0.015	-0.014	0.033	-0.000	0.033	0.106	0.000	0.106
45	3.7×10^6	0.142	-4.0	0.40	Exp (INSEAN)	-	-	-	-	0.011	-	-	0.025	-	-	-
46	3.3×10^6	-	-4.0	0.39	Parnassos	MNT	3.356×10^6	-0.008	-0.015	-0.023	0.038	0.000	0.038	0.095	0.000	0.096
47	3.3×10^6	-	-9.0	0.39	Parnassos	MNT	3.356×10^6	-0.026	-0.016	-0.042	0.071	-0.001	0.070	0.107	0.000	0.107
48	3.3×10^6	-	-12.0	0.52	Parnassos	MNT	3.356×10^6	-0.023	-0.017	-0.039	0.113	0.002	0.115	0.129	0.001	0.129
49	3.7×10^6	-	0.0	0.00	ReFRESCO	SST	5.388×10^6	-0.003	-0.015	-0.018	-0.000	0.000	-0.000	0.080	0.000	0.081
50	3.7×10^6	-	2.0	0.00	ReFRESCO	SST	5.388×10^6	-0.003	-0.015	-0.018	-0.007	-0.000	-0.007	0.080	0.000	0.081
51	3.7×10^6	-	4.0	0.00	ReFRESCO	SST	5.388×10^6	-0.003	-0.015	-0.018	-0.014	-0.001	-0.015	0.083	0.000	0.083
52	3.7×10^6	-	6.0	0.00	ReFRESCO	SST	5.388×10^6	-0.003	-0.015	-0.018	-0.025	-0.001	-0.026	0.088	0.000	0.089
53	3.7×10^6	-	8.0	0.00	ReFRESCO	SST	5.388×10^6	-0.003	-0.015	-0.018	-0.038	-0.001	-0.039	0.095	0.000	0.096
54	3.7×10^6	-	10.0	0.00	ReFRESCO	SST	5.388×10^6	-0.003	-0.015	-0.018	-0.052	-0.002	-0.053	0.104	0.000	0.105
55	3.7×10^6	-	12.0	0.00	ReFRESCO	SST	5.388×10^6	-0.002	-0.015	-0.018	-0.067	-0.002	-0.069	0.115	0.000	0.115
56	3.7×10^6	-	14.0	0.00	ReFRESCO	SST	5.388×10^6	-0.002	-0.016	-0.017	-0.084	-0.003	-0.086	0.127	0.001	0.127
57	3.7×10^6	-	16.0	0.00	ReFRESCO	SST	5.388×10^6	-0.001	-0.016	-0.016	-0.101	-0.003	-0.104	0.140	0.001	0.141
58	3.7×10^6	-	18.0	0.00	ReFRESCO	SST	5.388×10^6	0.001	-0.016	-0.015	-0.119	-0.003	-0.122	0.155	0.001	0.156
59	3.7×10^6	-	20.0	0.00	ReFRESCO	SST	5.388×10^6	0.002	-0.016	-0.014	-0.139	-0.004	-0.143	0.171	0.001	0.172
60	3.7×10^6	-	22.0	0.00	ReFRESCO	SST	5.388×10^6	0.004	-0.016	-0.013	-0.160	-0.004	-0.164	0.189	0.001	0.190
61	3.7×10^6	-	24.0	0.00	ReFRESCO	SST	5.388×10^6	0.005	-0.016	-0.011	-0.181	-0.004	-0.185	0.207	0.001	0.208
62	3.7×10^6	-	26.0	0.00	ReFRESCO	SST	5.388×10^6	0.007	-0.017	-0.009	-0.202	-0.005	-0.207	0.227	0.001	0.228
63	3.7×10^6	-	28.0	0.00	ReFRESCO	SST	5.388×10^6	0.010	-0.017	-0.007	-0.224	-0.005	-0.229	0.248	0.001	0.249
64	3.7×10^6	-	30.0	0.00	ReFRESCO	SST	5.388×10^6	0.012	-0.017	-0.005	-0.246	-0.006	-0.251	0.269	0.001	0.271
65	3.7×10^6	-	32.0	0.00	ReFRESCO	SST	5.388×10^6	0.014	-0.017	-0.003	-0.267	-0.006	-0.273	0.291	0.001	0.293
66	3.7×10^6	-	0.0	0.10	ReFRESCO	SST	12.721×10^6	-0.003	-0.015	-0.018	-0.002	0.000	-0.002	0.081	0.000	0.081
67	3.7×10^6	-	0.0	0.20	ReFRESCO	SST	12.721×10^6	-0.002	-0.015	-0.017	-0.006	0.000	-0.006	0.081	0.000	0.081
68	3.7×10^6	-	0.0	0.30	ReFRESCO	SST	12.721×10^6	-0.002	-0.015	-0.017	-0.011	0.000	-0.011	0.081	0.000	0.082
68	3.7×10^6	-	0.0	0.40	ReFRESCO	SST	12.721×10^6	-0.001	-0.015	-0.016	-0.016	0.000	-0.016	0.083	0.000	0.083
69	3.7×10^6	-	0.0	0.50	ReFRESCO	SST	12.721×10^6	0.000	-0.016	-0.016	-0.025	0.001	-0.024	0.090	0.000	0.091
69	3.7×10^6	-	0.0	0.60	ReFRESCO	SST	12.721×10^6	-0.002	-0.017	-0.019	-0.030	0.000	-0.030	0.095	0.000	0.096
70	3.7×10^6	-	0.0	0.65	ReFRESCO	SST	12.721×10^6	-0.002	-0.017	-0.019	-0.028	0.000	-0.028	0.095	0.000	0.096

Experimental and computational results of moments, KVLCC2

Id	Re [-]	Fn [-]	β	γ	Solver	Turb.	Grid	K_p	K_f	K	M_p	M_f	M	N_p	N_f	N
01	3.3×10^6	-	0.0	0.00	Parnassos	MNT	1.5×10^6	-	-	-	-0.013	0.000	-0.013	-	-	-
02	3.7×10^6	0.142	0.3	0.00	Exp (INSEAN)	-	-	-	-	-	-	-	-	-	-	-0.000
03	3.7×10^6	0.142	0.5	0.00	Exp (INSEAN)	-	-	-	-	-	-	-	-	-	-	-0.001
04	3.7×10^6	0.142	0.5	0.00	Exp (INSEAN)	-	-	-	-	-	-	-	-	-	-	-0.001
05	3.7×10^6	0.142	0.9	0.00	Exp (INSEAN)	-	-	-	-	-	-	-	-	-	-	-0.010
06	3.3×10^6	-	1.0	0.00	Parnassos	MNT	3.356×10^6	0.002	-0.000	0.002	-0.012	0.000	-0.012	-0.003	0.000	-0.003
07	3.7×10^6	0.142	1.0	0.00	Exp (INSEAN)	-	-	-	-	-	-	-	-	-	-	-0.002
08	3.7×10^6	0.142	1.8	0.00	Exp (INSEAN)	-	-	-	-	-	-	-	-	-	-	-0.005
09	3.7×10^6	0.142	2.0	0.00	Exp (INSEAN)	-	-	-	-	-	-	-	-	-	-	-0.005
10	3.3×10^6	-	2.0	0.00	Parnassos	MNT	3.356×10^6	0.005	-0.001	0.004	-0.012	0.000	-0.012	-0.005	0.000	-0.005
11	3.7×10^6	0.142	3.8	0.00	Exp (INSEAN)	-	-	-	-	-	-	-	-	-	-	-0.012
12	3.7×10^6	0.142	3.9	0.00	Exp (INSEAN)	-	-	-	-	-	-	-	-	-	-	-0.012
13	3.7×10^6	0.142	4.0	0.00	Exp (INSEAN)	-	-	-	-	-	-	-	-	-	-	-0.011
14	3.7×10^6	0.142	4.0	0.00	Exp (INSEAN)	-	-	-	-	-	-	-	-	-	-	-0.011
15	3.7×10^6	0.142	4.0	0.00	Exp (INSEAN)	-	-	-	-	-	-	-	-	-	-	-0.011
16	3.7×10^6	0.142	4.0	0.00	Exp (INSEAN)	-	-	-	-	-	-	-	-	-	-	-0.011
17	3.3×10^6	-	4.0	0.00	Parnassos	MNT	3.356×10^6	0.010	-0.001	0.009	-0.012	0.000	-0.012	-0.011	0.000	-0.011
18	3.7×10^6	0.142	4.0	0.00	Exp (INSEAN)	-	-	-	-	-	-	-	-	-	-	-0.011
19	3.7×10^6	0.142	4.0	0.00	Exp (INSEAN)	-	-	-	-	-	-	-	-	-	-	-0.011
20	3.7×10^6	0.142	4.0	0.00	Exp (INSEAN)	-	-	-	-	-	-	-	-	-	-	-0.011
21	3.7×10^6	0.142	4.0	0.00	Exp (INSEAN)	-	-	-	-	-	-	-	-	-	-	-0.012
22	3.7×10^6	0.142	4.0	0.00	Exp (INSEAN)	-	-	-	-	-	-	-	-	-	-	-0.012
23	3.7×10^6	0.142	4.0	0.00	Exp (INSEAN)	-	-	-	-	-	-	-	-	-	-	-0.011
24	3.7×10^6	0.142	4.0	0.00	Exp (INSEAN)	-	-	-	-	-	-	-	-	-	-	-0.011
25	3.3×10^6	-	6.0	0.00	Parnassos	MNT	3.356×10^6	0.017	-0.002	0.015	-0.013	0.000	-0.012	-0.015	0.000	-0.015
26	3.7×10^6	0.142	6.0	0.00	Exp (INSEAN)	-	-	-	-	-	-	-	-	-	-	-0.017
27	3.7×10^6	0.142	6.0	0.00	Exp (INSEAN)	-	-	-	-	-	-	-	-	-	-	-0.017
28	3.3×10^6	-	9.0	0.00	Parnassos	MNT	3.356×10^6	0.031	-0.002	0.028	-0.013	0.000	-0.013	-0.021	0.000	-0.021
29	3.3×10^6	-	15.0	0.00	Parnassos	MNT	3.356×10^6	0.072	-0.003	0.069	-0.015	0.000	-0.014	-0.032	0.000	-0.032
30	3.3×10^6	-	0.0	0.13	Parnassos	MNT	3.356×10^6	0.005	-0.000	0.004	-0.012	0.000	-0.012	-0.004	0.000	-0.004
31	3.7×10^6	0.142	0.0	0.20	Exp (INSEAN)	-	-	-	-	-	-	-	-	-	-	0.007
32	3.3×10^6	-	0.0	0.26	Parnassos	MNT	3.356×10^6	0.009	-0.000	0.009	-0.013	0.000	-0.012	-0.010	0.000	-0.009
33	3.7×10^6	0.142	0.0	0.40	Exp (INSEAN)	-	-	-	-	-	-	-	-	-	-	0.015
34	3.7×10^6	0.142	0.0	0.40	Exp (INSEAN)	-	-	-	-	-	-	-	-	-	-	0.016
35	3.7×10^6	0.142	0.0	0.40	Exp (INSEAN)	-	-	-	-	-	-	-	-	-	-	0.016
36	3.7×10^6	0.142	0.0	0.40	Exp (INSEAN)	-	-	-	-	-	-	-	-	-	-	0.016
37	3.7×10^6	0.142	0.0	0.40	Exp (INSEAN)	-	-	-	-	-	-	-	-	-	-	0.016
38	3.7×10^6	0.142	0.0	0.40	Exp (INSEAN)	-	-	-	-	-	-	-	-	-	-	0.016
39	3.7×10^6	0.142	0.0	0.40	Exp (INSEAN)	-	-	-	-	-	-	-	-	-	-	0.016
40	3.7×10^6	0.142	0.0	0.40	Exp (INSEAN)	-	-	-	-	-	-	-	-	-	-	0.016
41	3.3×10^6	-	0.0	0.39	Parnassos	MNT	3.356×10^6	0.014	-0.000	0.013	-0.013	0.000	-0.012	-0.016	0.000	-0.015
42	3.3×10^6	-	0.0	0.52	Parnassos	MNT	3.356×10^6	0.018	-0.000	0.017	-0.013	0.000	-0.013	-0.022	0.000	-0.021
43	3.7×10^6	0.142	0.0	0.60	Exp (INSEAN)	-	-	-	-	-	-	-	-	-	-	0.026
44	3.3×10^6	-	0.0	0.65	Parnassos	MNT	3.356×10^6	0.022	-0.001	0.021	-0.013	0.000	-0.013	-0.028	0.001	-0.028
45	3.7×10^6	0.142	-4.0	0.40	Exp (INSEAN)	-	-	-	-	-	-	-	-	-	-	-0.016
46	3.3×10^6	-	-4.0	0.39	Parnassos	MNT	3.356×10^6	0.003	0.001	0.004	-0.009	0.000	-0.009	-0.006	0.000	-0.006
47	3.3×10^6	-	-9.0	0.39	Parnassos	MNT	3.356×10^6	0.020	-0.000	0.019	-0.006	0.000	-0.005	0.001	0.000	0.001
48	3.3×10^6	-	-12.0	0.52	Parnassos	MNT	3.356×10^6	-0.029	0.003	-0.027	-0.001	0.000	-0.000	-0.003	0.000	-0.003
49	3.7×10^6	-	0.0	0.00	ReFRESCO	SST	5.388×10^6	-0.000	-0.000	-0.000	-0.013	-0.000	-0.013	0.000	-0.000	0.000
50	3.7×10^6	-	2.0	0.00	ReFRESCO	SST	5.388×10^6	0.005	0.001	0.005	-0.013	-0.000	-0.013	-0.005	-0.000	-0.005
51	3.7×10^6	-	4.0	0.00	ReFRESCO	SST	5.388×10^6	0.010	0.001	0.011	-0.013	-0.000	-0.013	-0.010	-0.000	-0.010
52	3.7×10^6	-	6.0	0.00	ReFRESCO	SST	5.388×10^6	0.017	0.001	0.018	-0.013	-0.000	-0.013	-0.014	-0.000	-0.014
53	3.7×10^6	-	8.0	0.00	ReFRESCO	SST	5.388×10^6	0.026	0.002	0.028	-0.013	-0.000	-0.014	-0.018	-0.000	-0.018
54	3.7×10^6	-	10.0	0.00	ReFRESCO	SST	5.388×10^6	0.037	0.002	0.040	-0.014	-0.000	-0.014	-0.022	-0.000	-0.022
55	3.7×10^6	-	12.0	0.00	ReFRESCO	SST	5.388×10^6	0.050	0.003	0.053	-0.014	-0.000	-0.015	-0.026	-0.000	-0.026
56	3.7×10^6	-	14.0	0.00	ReFRESCO	SST	5.388×10^6	0.064	0.003	0.068	-0.015	-0.000	-0.015	-0.030	-0.000	-0.030
57	3.7×10^6	-	16.0	0.00	ReFRESCO	SST	5.388×10^6	0.079	0.004	0.083	-0.016	-0.000	-0.016	-0.033	-0.000	-0.034
58	3.7×10^6	-	18.0	0.00	ReFRESCO	SST	5.388×10^6	0.096	0.005	0.101	-0.017	-0.000	-0.017	-0.037	-0.000	-0.038
59	3.7×10^6	-	20.0	0.00	ReFRESCO	SST	5.388×10^6	0.114	0.005	0.119	-0.018	-0.000	-0.018	-0.041	-0.000	-0.041
60	3.7×10^6	-	22.0	0.00	ReFRESCO	SST	5.388×10^6	0.133	0.006	0.139	-0.019	-0.000	-0.019	-0.044	-0.001	-0.044
61	3.7×10^6	-	24.0	0.00	ReFRESCO	SST	5.388×10^6	0.153	0.006	0.159	-0.020	-0.000	-0.020	-0.047	-0.001	-0.047
62	3.7×10^6	-	26.0	0.00	ReFRESCO	SST	5.388×10^6	0.175	0.007	0.181	-0.021	-0.000	-0.021	-0.049	-0.001	-0.050
63	3.7×10^6	-	28.0	0.00	ReFRESCO	SST	5.388×10^6	0.197	0.007	0.204	-0.022	-0.000	-0.023	-0.052	-0.001	-0.053
64	3.7×10^6	-	30.0	0.00	ReFRESCO	SST	5.388×10^6	0.220	0.008	0.228	-0.024	-0.000	-0.024	-0.055	-0.001	-0.056
65	3.7×10^6	-	32.0	0.00	ReFRESCO	SST	5.388×10^6	0.244	0.008	0.252	-0.025	-0.000	-0.025	-0.057	-0.001	-0.058
66	3.7×10^6	-	0.0	0.10	ReFRESCO	SST	12.721×10^6	-0.004	-0.000	-0.004	-0.013	-0.000	-0.013	0.004	0.000	0.004
67	3.7×10^6	-	0.0	0.20	ReFRESCO	SST	12.721×10^6	-0.008	-0.000	-0.008	-0.013	-0.000	-0.013	0.009	0.000	0.009
68	3.7×10^6	-	0.0	0.30	ReFRESCO	SST	12.721×10^6	-0.011	-0.000	-0.012	-0.013	-0.000	-0.014	0.013	0.000	0.013
68	3.7×10^6	-	0.0	0.40	ReFRESCO	SST	12.721×10^6	-0.014	-0.001	-0.015	-0.014	-0.000	-0.014	0.017	0.000	0.018
69	3.7×10^6	-	0.0	0.50	ReFRESCO	SST	12.721×10^6	-0.019	-0.001	-0.020	-0.015	-0.000	-0.015	0.023	0.001	0.024
69	3.7×10^6	-	0.0	0.60	ReFRESCO	SST	12.721×10^6	-0.021	-0.001	-0.021	-0.014	-0.000	-0.014	0.029	0.001	0.030
70	3.7×10^6	-	0.0	0.65	ReFRESCO	SST	12.721×10^6	-0.023	-0.001	-0.023	-0.014	-0.000	-0.014	0.032	0.001	0.033

Experimental and computational results of forces, KVLCC2M

Id	Re [-]	Fn [-]	β	γ	Solver	Turb.	Grid	X_p	X_f	X	Y_p	Y_f	Y	Z_p	Z_f	Z
01	3.9×10^6	0.142	0.0	0.00	Exp (NMRI)	-	-	-	-	-0.018	-	-	-	-	-	-
02	3.9×10^6	-	0.0	0.00	Parnassos	MNT	1.6×10^6	-0.003	-0.015	-0.017	-	-	-	0.080	0.000	0.080
03	3.9×10^6	0.142	3.0	0.00	Exp (NMRI)	-	-	-	-	-0.018	-	-	-0.013	-	-	-
04	3.9×10^6	0.142	3.0	0.00	Exp (NMRI)	-	-	-	-	-0.018	-	-	-0.012	-	-	-
05	3.9×10^6	-	3.0	0.00	Parnassos	MNT	3.8×10^6	-0.003	-0.015	-0.018	-0.009	-0.001	-0.009	0.082	0.000	0.082
06	3.9×10^6	0.142	6.0	0.00	Exp (NMRI)	-	-	-	-	-0.018	-	-	-0.026	-	-	-
07	3.9×10^6	-	6.0	0.00	Parnassos	MNT	3.8×10^6	-0.003	-0.015	-0.018	-0.022	-0.001	-0.023	0.089	0.000	0.089
08	3.9×10^6	0.142	9.0	0.00	Exp (NMRI)	-	-	-	-	-0.017	-	-	-0.046	-	-	-
09	3.9×10^6	-	9.0	0.00	Parnassos	MNT	3.8×10^6	-0.003	-0.015	-0.018	-0.041	-0.001	-0.042	0.100	0.000	0.100
10	3.9×10^6	0.142	12.0	0.00	Exp (NMRI)	-	-	-	-	-0.018	-	-	-0.071	-	-	-
11	3.9×10^6	-	12.0	0.00	Parnassos	MNT	3.8×10^6	-0.002	-0.015	-0.018	-0.063	-0.002	-0.064	0.115	0.000	0.115
12	3.9×10^6	-	12.0	0.00	Parnassos	SST	3.8×10^6	-0.003	-0.015	-0.018	-0.066	-0.002	-0.067	0.115	0.000	0.115
13	3.9×10^6	-	12.0	0.00	Parnassos	MNT2	3.8×10^6	-0.001	-0.015	-0.017	-0.062	-0.002	-0.064	0.114	0.000	0.114
14	3.9×10^6	0.142	15.0	0.00	Exp (NMRI)	-	-	-	-	-0.016	-	-	-0.098	-	-	-
15	3.9×10^6	-	15.0	0.00	Parnassos	MNT	3.8×10^6	-0.001	-0.016	-0.016	-0.083	-0.002	-0.085	0.133	0.001	0.133
16	3.9×10^6	0.142	18.0	0.00	Exp (NMRI)	-	-	-	-	-0.014	-	-	-0.124	-	-	-
17	3.9×10^6	-	18.0	0.00	Parnassos	MNT	3.8×10^6	0.003	-0.016	-0.013	-0.109	-0.002	-0.112	0.153	0.001	0.154
18	3.9×10^6	-	0.0	0.10	Parnassos	MNT	6.5×10^5	-0.005	-0.015	-0.020	0.004	-0.000	0.004	0.080	0.000	0.081
19	3.9×10^6	-	0.0	0.20	Parnassos	MNT	6.5×10^5	-0.005	-0.015	-0.019	0.009	-0.000	0.009	0.083	0.000	0.083
20	3.9×10^6	-	0.0	0.25	Parnassos	MNT	6.5×10^5	-0.005	-0.015	-0.019	0.011	-0.000	0.011	0.084	0.000	0.084
21	3.9×10^6	-	0.0	0.30	Parnassos	MNT	8.7×10^4	-0.007	-0.014	-0.021	0.013	0.000	0.013	0.085	0.000	0.085
22	3.9×10^6	-	0.0	0.40	Parnassos	MNT	8.7×10^4	-0.004	-0.014	-0.018	0.016	0.000	0.016	0.088	0.000	0.089
23	3.9×10^6	-	0.0	0.60	Parnassos	MNT	8.7×10^4	-0.003	-0.014	-0.017	0.025	0.000	0.025	0.101	0.000	0.101
24	3.9×10^6	-	-12.0	0.10	Parnassos	MNT	8.7×10^4	-0.026	-0.015	-0.041	0.073	-0.002	0.071	0.116	0.000	0.116
25	3.9×10^6	-	-12.0	0.30	Parnassos	MNT	8.7×10^4	-0.035	-0.016	-0.051	0.087	-0.002	0.085	0.119	0.000	0.119
26	3.9×10^6	-	-12.0	0.60	Parnassos	MNT	8.7×10^4	-0.025	-0.016	-0.041	0.123	0.002	0.125	0.131	0.000	0.132

Experimental and computational results of moments, KVLCC2M

Id	Re [-]	Fn [-]	β	γ	Solver	Turb.	Grid	K_p	K_f	K	M_p	M_f	M	N_p	N_f	N
01	3.9×10^6	0.142	0.0	0.00	Exp (NMRI)	-	-	-	-	-	-	-	-	-	-	-
02	3.9×10^6	-	0.0	0.00	Parnassos	MNT	1.6×10^6	-	-	-	-0.013	0.000	-0.012	-	-	-
03	3.9×10^6	0.142	3.0	0.00	Exp (NMRI)	-	-	-	-	-	-	-	-	-	-	-0.006
04	3.9×10^6	0.142	3.0	0.00	Exp (NMRI)	-	-	-	-	-	-	-	-	-	-	-0.007
05	3.9×10^6	-	3.0	0.00	Parnassos	MNT	3.8×10^6	0.007	-0.001	0.006	-0.013	0.000	-0.012	-0.008	0.000	-0.008
06	3.9×10^6	0.142	6.0	0.00	Exp (NMRI)	-	-	-	-	-	-	-	-	-	-	-0.014
07	3.9×10^6	-	6.0	0.00	Parnassos	MNT	3.8×10^6	0.016	-0.001	0.015	-0.013	0.000	-0.013	-0.015	0.000	-0.015
08	3.9×10^6	0.142	9.0	0.00	Exp (NMRI)	-	-	-	-	-	-	-	-	-	-	-0.019
09	3.9×10^6	-	9.0	0.00	Parnassos	MNT	3.8×10^6	0.031	-0.002	0.029	-0.014	0.000	-0.013	-0.020	0.000	-0.020
10	3.9×10^6	0.142	12.0	0.00	Exp (NMRI)	-	-	-	-	-	-	-	-	-	-	-0.025
11	3.9×10^6	-	12.0	0.00	Parnassos	MNT	3.8×10^6	0.050	-0.003	0.047	-0.014	0.000	-0.014	-0.026	0.000	-0.025
12	3.9×10^6	-	12.0	0.00	Parnassos	SST	3.8×10^6	0.054	-0.002	0.051	-0.014	0.000	-0.014	-0.026	0.000	-0.026
13	3.9×10^6	-	12.0	0.00	Parnassos	MNT2	3.8×10^6	0.050	-0.003	0.047	-0.015	0.000	-0.014	-0.026	0.000	-0.026
14	3.9×10^6	0.142	15.0	0.00	Exp (NMRI)	-	-	-	-	-	-	-	-	-	-	-0.031
15	3.9×10^6	-	15.0	0.00	Parnassos	MNT	3.8×10^6	0.074	-0.003	0.071	-0.016	0.000	-0.015	-0.033	0.000	-0.032
16	3.9×10^6	0.142	18.0	0.00	Exp (NMRI)	-	-	-	-	-	-	-	-	-	-	-0.035
17	3.9×10^6	-	18.0	0.00	Parnassos	MNT	3.8×10^6	0.103	-0.004	0.100	-0.017	0.000	-0.017	-0.038	0.000	-0.038
18	3.9×10^6	-	0.0	0.10	Parnassos	MNT	6.5×10^5	0.003	-0.000	0.003	-0.012	0.000	-0.012	-0.003	0.000	-0.003
19	3.9×10^6	-	0.0	0.20	Parnassos	MNT	6.5×10^5	0.007	-0.000	0.007	-0.012	0.000	-0.012	-0.006	0.000	-0.006
20	3.9×10^6	-	0.0	0.25	Parnassos	MNT	6.5×10^5	0.008	-0.000	0.008	-0.012	0.000	-0.012	-0.008	0.000	-0.008
21	3.9×10^6	-	0.0	0.30	Parnassos	MNT	8.7×10^4	0.010	-0.000	0.010	-0.012	0.000	-0.011	-0.010	0.000	-0.010
22	3.9×10^6	-	0.0	0.40	Parnassos	MNT	8.7×10^4	0.014	-0.000	0.014	-0.012	0.000	-0.012	-0.014	0.000	-0.013
23	3.9×10^6	-	0.0	0.60	Parnassos	MNT	8.7×10^4	0.022	-0.000	0.022	-0.013	0.000	-0.012	-0.023	0.000	-0.023
24	3.9×10^6	-	-12.0	0.10	Parnassos	MNT	8.7×10^4	0.050	-0.001	0.049	-0.011	0.000	-0.010	0.023	-0.000	0.023
25	3.9×10^6	-	-12.0	0.30	Parnassos	MNT	8.7×10^4	0.018	-0.001	0.017	-0.006	0.000	-0.006	0.013	-0.000	0.013
26	3.9×10^6	-	-12.0	0.60	Parnassos	MNT	8.7×10^4	-0.028	0.002	-0.025	0.000	0.000	0.001	-0.005	0.000	-0.005

Experimental and computational results of forces, HTC

Id	Re [-]	Fn [-]	β	γ	Solver	Turb.	Grid	X_p	X_f	X	Y_p	Y_f	Y	Z_p	Z_f	Z
01	6.3×10^6	0.132	0.0	0.00	Exp (HSVA)	-	-	-	-	-0.014	-	-	0.000	-	-	0.055
02	6.3×10^6	0.132	0.0	0.00	Exp (HSVA)	-	-	-	-	-0.014	-	-	0.000	-	-	0.063
03	1.1×10^7	0.238	0.0	0.00	Exp (HSVA)	-	-	-	-	-0.014	-	-	0.000	-	-	0.062
04	1.1×10^7	0.238	0.0	0.00	Exp (HSVA)	-	-	-	-	-0.014	-	-	0.000	-	-	0.064
05	6.3×10^6	-	0.0	0.00	Parnassos	MNT	3.7×10^6	-0.002	-0.012	-0.014	-	-	-	0.058	0.000	0.058
06	8.3×10^6	-	0.0	0.00	Parnassos	MNT	1.2×10^6	-0.002	-0.011	-0.013	-	-	-	0.058	0.000	0.059
07	1.2×10^7	-	0.0	0.00	Parnassos	MNT	3.7×10^6	-0.002	-0.011	-0.013	-	-	-	0.058	0.000	0.059
08	6.3×10^6	-	2.5	0.00	Parnassos	MNT	3.7×10^6	-0.003	-0.012	-0.014	-0.008	-0.000	-0.009	0.060	0.000	0.060
09	6.3×10^6	0.132	5.0	0.00	Exp (HSVA)	-	-	-	-	-0.015	-	-	-0.020	-	-	0.064
10	6.3×10^6	0.132	5.0	0.00	Exp (HSVA)	-	-	-	-	-0.015	-	-	-0.017	-	-	0.067
11	1.1×10^7	0.238	5.0	0.00	Exp (HSVA)	-	-	-	-	-0.015	-	-	-0.021	-	-	0.068
12	1.1×10^7	0.238	5.0	0.00	Exp (HSVA)	-	-	-	-	-0.015	-	-	-0.019	-	-	0.072
13	6.3×10^6	-	5.0	0.00	Parnassos	MNT	3.7×10^6	-0.003	-0.012	-0.015	-0.017	-0.000	-0.017	0.065	0.000	0.066
14	1.2×10^7	-	5.0	0.00	Parnassos	MNT	3.7×10^6	-0.003	-0.011	-0.013	-0.016	-0.000	-0.017	0.066	0.000	0.066
15	6.3×10^6	0.132	10.0	0.00	Exp (HSVA)	-	-	-	-	-0.017	-	-	-0.048	-	-	0.097
16	6.3×10^6	0.132	10.0	0.00	Exp (HSVA)	-	-	-	-	-0.017	-	-	-0.045	-	-	0.088
17	1.1×10^7	0.238	10.0	0.00	Exp (HSVA)	-	-	-	-	-0.017	-	-	-0.048	-	-	0.089
18	1.1×10^7	0.238	10.0	0.00	Exp (HSVA)	-	-	-	-	-0.017	-	-	-0.045	-	-	0.091
19	3.7×10^6	-	10.0	0.00	Parnassos	MNT	3.7×10^6	-0.004	-0.013	-0.017	-0.044	-0.001	-0.045	0.086	0.000	0.086
20	6.3×10^6	-	10.0	0.00	Parnassos	MNT	3.7×10^6	-0.003	-0.012	-0.016	-0.043	-0.001	-0.044	0.086	0.000	0.086
21	1.2×10^7	-	10.0	0.00	Parnassos	MNT	3.7×10^6	-0.003	-0.011	-0.014	-0.042	-0.001	-0.043	0.086	0.000	0.086
22	7.4×10^8	-	10.0	0.00	Parnassos	MNT	5.3×10^6	-0.003	-0.006	-0.009	-0.038	-0.001	-0.039	0.087	0.000	0.087
23	6.3×10^6	-	15.0	0.00	Parnassos	MNT	3.7×10^6	-0.003	-0.013	-0.016	-0.079	-0.002	-0.081	0.115	0.001	0.115
24	6.3×10^6	0.132	20.0	0.00	Exp (HSVA)	-	-	-	-	-0.015	-	-	-0.134	-	-	0.152
25	6.3×10^6	0.132	20.0	0.00	Exp (HSVA)	-	-	-	-	-0.015	-	-	-0.127	-	-	0.164
26	1.1×10^7	0.238	20.0	0.00	Exp (HSVA)	-	-	-	-	-0.019	-	-	-0.129	-	-	0.159
27	1.1×10^7	0.238	20.0	0.00	Exp (HSVA)	-	-	-	-	-0.019	-	-	-0.123	-	-	0.160
28	6.3×10^6	0.132	30.0	0.00	Exp (HSVA)	-	-	-	-	-0.008	-	-	-0.244	-	-	0.243
29	1.1×10^7	0.238	30.0	0.00	Exp (HSVA)	-	-	-	-	-0.018	-	-	-0.240	-	-	0.258
30	1.2×10^7	0.238	0.0	0.10	Exp (HSVA)	-	-	-	-	-0.014	-	-	0.003	-	-	0.069
31	6.3×10^6	-	0.0	0.10	Parnassos	MNT	1.2×10^6	-0.002	-0.012	-0.014	0.002	0.000	0.002	0.058	0.000	0.058
32	6.3×10^6	-	0.0	0.15	Parnassos	MNT	1.2×10^6	-0.002	-0.012	-0.014	0.004	0.000	0.004	0.059	0.000	0.059
33	1.2×10^7	0.238	0.0	0.20	Exp (HSVA)	-	-	-	-	-0.015	-	-	0.008	-	-	0.070
34	6.3×10^6	-	0.0	0.20	Parnassos	MNT	1.9×10^6	-0.002	-0.012	-0.014	0.006	0.000	0.006	0.060	0.000	0.061
35	1.2×10^7	-	0.0	0.20	Parnassos	MNT	1.2×10^6	-0.002	-0.011	-0.013	0.005	0.000	0.005	0.060	0.000	0.061
36	6.3×10^6	-	-5.0	0.20	Parnassos	MNT	1.2×10^6	-0.006	-0.012	-0.017	0.025	0.001	0.026	0.067	0.000	0.067
37	6.3×10^6	-	-10.0	0.20	Parnassos	MNT	1.2×10^6	-0.009	-0.012	-0.021	0.051	0.001	0.052	0.088	0.000	0.088
38	6.3×10^6	-	0.0	0.30	Parnassos	MNT	1.2×10^6	-0.003	-0.012	-0.014	0.009	0.000	0.009	0.064	0.000	0.064
39	1.2×10^7	0.238	0.0	0.40	Exp (HSVA)	-	-	-	-	-0.017	-	-	0.016	-	-	0.079
40	6.3×10^6	-	0.0	0.40	Parnassos	MNT	1.2×10^6	-0.003	-0.012	-0.015	0.012	0.000	0.013	0.068	0.000	0.068
41	1.2×10^7	-	0.0	0.40	Parnassos	MNT	1.2×10^6	-0.002	-0.011	-0.013	0.012	0.000	0.012	0.068	0.000	0.068
42	6.3×10^6	-	-6.0	0.40	Parnassos	MNT	1.2×10^6	-0.010	-0.012	-0.022	0.043	0.001	0.044	0.078	0.000	0.079
43	6.3×10^6	-	-10.0	0.40	Parnassos	MNT	1.2×10^6	-0.014	-0.012	-0.026	0.063	0.001	0.064	0.095	0.000	0.095
44	6.3×10^6	-	-15.0	0.40	Parnassos	MNT	1.2×10^6	-0.019	-0.013	-0.032	0.108	0.002	0.110	0.127	0.001	0.128
45	1.2×10^7	0.238	0.0	0.56	Exp (HSVA)	-	-	-	-	-0.019	-	-	0.024	-	-	0.086
46	6.3×10^6	-	0.0	0.56	Parnassos	MNT	1.2×10^6	-0.003	-0.012	-0.015	0.015	0.001	0.016	0.077	0.000	0.078
47	1.2×10^7	-	0.0	0.00	ReFRESCO	SST	5.2×10^6	-0.002	-0.011	-0.013	-	-	-	0.063	0.000	0.063
48	1.2×10^7	-	2.5	0.00	ReFRESCO	SST	5.2×10^6	-0.002	-0.011	-0.013	-0.006	-0.000	-0.006	0.065	0.000	0.065
49	1.2×10^7	-	5.0	0.00	ReFRESCO	SST	5.2×10^6	-0.003	-0.011	-0.014	-0.013	-0.000	-0.014	0.069	0.000	0.069
50	1.2×10^7	-	7.5	0.00	ReFRESCO	SST	5.2×10^6	-0.003	-0.011	-0.014	-0.024	-0.001	-0.025	0.076	0.000	0.076
51	1.2×10^7	-	10.0	0.00	ReFRESCO	SST	5.2×10^6	-0.003	-0.011	-0.015	-0.037	-0.001	-0.038	0.086	0.000	0.087
52	1.2×10^7	-	12.5	0.00	ReFRESCO	SST	5.2×10^6	-0.003	-0.012	-0.014	-0.054	-0.001	-0.055	0.099	0.000	0.099
53	1.2×10^7	-	15.0	0.00	ReFRESCO	SST	5.2×10^6	-0.002	-0.012	-0.014	-0.074	-0.002	-0.076	0.113	0.000	0.114
54	1.2×10^7	-	17.5	0.00	ReFRESCO	SST	5.2×10^6	-0.001	-0.012	-0.013	-0.098	-0.002	-0.100	0.130	0.001	0.130
55	1.2×10^7	-	20.0	0.00	ReFRESCO	SST	5.2×10^6	-0.000	-0.012	-0.012	-0.124	-0.002	-0.126	0.149	0.001	0.149
56	1.2×10^7	-	22.5	0.00	ReFRESCO	SST	5.2×10^6	0.001	-0.012	-0.011	-0.150	-0.003	-0.153	0.169	0.001	0.170
57	1.2×10^7	-	25.0	0.00	ReFRESCO	SST	5.2×10^6	0.003	-0.012	-0.009	-0.177	-0.003	-0.180	0.191	0.001	0.192
58	1.2×10^7	-	27.5	0.00	ReFRESCO	SST	5.2×10^6	0.005	-0.012	-0.007	-0.205	-0.003	-0.208	0.214	0.001	0.215
59	1.2×10^7	-	30.0	0.00	ReFRESCO	SST	5.2×10^6	0.006	-0.012	-0.005	-0.234	-0.004	-0.238	0.238	0.001	0.239
60	1.2×10^7	-	0.0	0.10	ReFRESCO	SST	5.2×10^6	-0.002	-0.011	-0.013	0.003	0.000	0.003	0.064	0.000	0.064
61	1.2×10^7	-	0.0	0.20	ReFRESCO	SST	5.2×10^6	-0.002	-0.011	-0.013	0.007	0.000	0.008	0.066	0.000	0.066
62	1.2×10^7	-	0.0	0.40	ReFRESCO	SST	5.2×10^6	-0.003	-0.012	-0.015	0.015	0.000	0.015	0.073	0.000	0.073
63	1.2×10^7	-	0.0	0.56	ReFRESCO	SST	5.2×10^6	-0.004	-0.012	-0.016	0.020	0.001	0.021	0.089	0.000	0.090
64	1.2×10^7	-	-5.0	0.20	ReFRESCO	SST	5.2×10^6	-0.006	-0.011	-0.017	0.027	0.001	0.027	0.073	0.000	0.073
65	1.2×10^7	-	-10.0	0.20	ReFRESCO	SST	5.2×10^6	-0.009	-0.011	-0.021	0.054	0.001	0.055	0.096	0.000	0.096
66	1.2×10^7	-	-20.0	0.20	ReFRESCO	SST	5.2×10^6	-0.012	-0.012	-0.025	0.138	0.003	0.141	0.169	0.001	0.170
67	1.2×10^7	-	-5.0	0.40	ReFRESCO	SST	5.2×10^6	-0.009	-0.011	-0.021	0.040	0.001	0.041	0.080	0.000	0.080
68	1.2×10^7	-	-10.0	0.40	ReFRESCO	SST	5.2×10^6	-0.015	-0.011	-0.027	0.065	0.001	0.067	0.100	0.000	0.101
69	1.2×10^7	-	-15.0	0.40	ReFRESCO	SST	5.2×10^6	-0.020	-0.012	-0.032	0.108	0.002	0.110	0.138	0.000	0.138
70	1.2×10^7	-	-20.0	0.40	ReFRESCO	SST	5.2×10^6	-0.024	-0.012	-0.036	0.152	0.003	0.155	0.182	0.001	0.182
71	1.2×10^7	-	-30.0	0.40	ReFRESCO	SST	5.2×10^6	-0.028	-0.013	-0.041	0.254	0.004	0.259	0.284	0.001	0.285
72	1.2×10^7	-	-20.0	0.56	ReFRESCO	SST	2.5×10^6	-0.033	-0.013	-0.047	0.183	0.003	0.186	0.200	0.001	0.201

Experimental and computational results of moments, HTC

Id	Re [-]	Fn [-]	β	γ	Solver	Turb.	Grid	K_p	K_f	K	M_p	M_f	M	N_p	N_f	N
01	6.3×10^6	0.132	0.0	0.00	Exp (HSVA)	-	-	-	-	0.000	-	-	-0.004	-	-	0.000
02	6.3×10^6	0.132	0.0	0.00	Exp (HSVA)	-	-	-	-	0.000	-	-	-	-	-	0.000
03	1.1×10^7	0.238	0.0	0.00	Exp (HSVA)	-	-	-	-	0.000	-	-	-0.004	-	-	0.000
04	1.1×10^7	0.238	0.0	0.00	Exp (HSVA)	-	-	-	-	0.000	-	-	-	-	-	0.000
05	6.3×10^6	-	0.0	0.00	Parnassos	MNT	3.7×10^6	-	-	-	-0.001	0.000	-0.001	-	-	-
06	8.3×10^6	-	0.0	0.00	Parnassos	MNT	1.2×10^6	-	-	-	-0.001	0.000	-0.001	-	-	-
07	1.2×10^7	-	0.0	0.00	Parnassos	MNT	3.7×10^6	-	-	-	-0.001	0.000	-0.001	-	-	-
08	6.3×10^6	-	2.5	0.00	Parnassos	MNT	3.7×10^6	0.004	-0.000	0.004	-0.001	0.000	-0.001	-0.006	0.000	-0.006
09	6.3×10^6	0.132	5.0	0.00	Exp (HSVA)	-	-	-	-	0.010	-	-	-0.004	-	-	-0.012
10	6.3×10^6	0.132	5.0	0.00	Exp (HSVA)	-	-	-	-	0.009	-	-	-	-	-	-0.011
11	1.1×10^7	0.238	5.0	0.00	Exp (HSVA)	-	-	-	-	0.009	-	-	-0.004	-	-	-0.012
12	1.1×10^7	0.238	5.0	0.00	Exp (HSVA)	-	-	-	-	0.010	-	-	-	-	-	-0.012
13	6.3×10^6	-	5.0	0.00	Parnassos	MNT	3.7×10^6	0.009	-0.001	0.008	-0.001	0.000	-0.001	-0.013	0.000	-0.013
14	1.2×10^7	-	5.0	0.00	Parnassos	MNT	3.7×10^6	0.009	-0.001	0.008	-0.001	0.000	-0.001	-0.013	0.000	-0.013
15	6.3×10^6	0.132	10.0	0.00	Exp (HSVA)	-	-	-	-	0.021	-	-	-0.005	-	-	-0.023
16	6.3×10^6	0.132	10.0	0.00	Exp (HSVA)	-	-	-	-	0.021	-	-	-	-	-	-0.022
17	1.1×10^7	0.238	10.0	0.00	Exp (HSVA)	-	-	-	-	0.021	-	-	-0.004	-	-	-0.025
18	1.1×10^7	0.238	10.0	0.00	Exp (HSVA)	-	-	-	-	0.021	-	-	-	-	-	-0.024
19	3.7×10^6	-	10.0	0.00	Parnassos	MNT	3.7×10^6	0.019	-0.002	0.017	-0.002	0.000	-0.001	-0.024	0.000	-0.024
20	6.3×10^6	-	10.0	0.00	Parnassos	MNT	3.7×10^6	0.020	-0.002	0.018	-0.002	0.000	-0.001	-0.024	0.000	-0.024
21	1.2×10^7	-	10.0	0.00	Parnassos	MNT	3.7×10^6	0.020	-0.002	0.018	-0.002	0.000	-0.001	-0.024	0.000	-0.024
22	7.4×10^8	-	10.0	0.00	Parnassos	MNT	5.3×10^6	0.021	-0.001	0.020	-0.002	0.000	-0.002	-0.025	0.000	-0.025
23	6.3×10^6	-	15.0	0.00	Parnassos	MNT	3.7×10^6	0.040	-0.003	0.037	-0.002	0.000	-0.002	-0.037	0.000	-0.037
24	6.3×10^6	0.132	20.0	0.00	Exp (HSVA)	-	-	-	-	0.060	-	-	-0.007	-	-	-0.048
25	6.3×10^6	0.132	20.0	0.00	Exp (HSVA)	-	-	-	-	0.062	-	-	-	-	-	-0.047
26	1.1×10^7	0.238	20.0	0.00	Exp (HSVA)	-	-	-	-	0.063	-	-	-0.006	-	-	-0.047
27	1.1×10^7	0.238	20.0	0.00	Exp (HSVA)	-	-	-	-	0.064	-	-	-	-	-	-0.045
28	6.3×10^6	0.132	30.0	0.00	Exp (HSVA)	-	-	-	-	0.110	-	-	-0.011	-	-	-0.073
29	1.1×10^7	0.238	30.0	0.00	Exp (HSVA)	-	-	-	-	0.110	-	-	-0.009	-	-	-0.070
30	1.2×10^7	0.238	0.0	0.10	Exp (HSVA)	-	-	-	-	0.000	-	-	-	-	-	-0.004
31	6.3×10^6	-	0.0	0.10	Parnassos	MNT	1.2×10^6	0.001	0.000	0.001	-0.001	0.000	-0.001	-0.003	0.000	-0.003
32	6.3×10^6	-	0.0	0.15	Parnassos	MNT	1.2×10^6	0.002	0.000	0.002	-0.001	0.000	-0.001	-0.005	0.000	-0.005
33	1.2×10^7	0.238	0.0	0.20	Exp (HSVA)	-	-	-	-	0.001	-	-	-	-	-	-0.009
34	6.3×10^6	-	0.0	0.20	Parnassos	MNT	1.9×10^6	0.002	0.000	0.002	-0.001	0.000	-0.001	-0.007	0.000	-0.007
35	1.2×10^7	-	0.0	0.20	Parnassos	MNT	1.2×10^6	0.002	0.000	0.002	-0.001	0.000	-0.001	-0.007	0.000	-0.007
36	6.3×10^6	-	-5.0	0.20	Parnassos	MNT	1.2×10^6	-0.006	0.001	-0.005	0.001	0.000	0.001	0.005	0.000	0.005
37	6.3×10^6	-	-10.0	0.20	Parnassos	MNT	1.2×10^6	-0.012	0.002	-0.010	0.003	0.000	0.003	0.014	0.000	0.014
38	6.3×10^6	-	0.0	0.30	Parnassos	MNT	1.2×10^6	0.004	0.000	0.004	-0.001	0.000	-0.001	-0.012	0.000	-0.012
39	1.2×10^7	0.238	0.0	0.40	Exp (HSVA)	-	-	-	-	0.003	-	-	-	-	-	-0.018
40	6.3×10^6	-	0.0	0.40	Parnassos	MNT	1.2×10^6	0.005	0.000	0.005	-0.001	0.000	-0.001	-0.018	0.000	-0.018
41	1.2×10^7	-	0.0	0.40	Parnassos	MNT	1.2×10^6	0.005	0.000	0.005	-0.001	0.000	-0.001	-0.018	0.000	-0.018
42	6.3×10^6	-	-6.0	0.40	Parnassos	MNT	1.2×10^6	-0.004	0.001	-0.003	0.004	0.000	0.004	-0.003	0.000	-0.003
43	6.3×10^6	-	-10.0	0.40	Parnassos	MNT	1.2×10^6	-0.007	0.002	-0.005	0.007	0.000	0.007	0.004	0.000	0.005
44	6.3×10^6	-	-15.0	0.40	Parnassos	MNT	1.2×10^6	-0.012	0.003	-0.009	0.010	0.000	0.011	0.008	0.000	0.008
45	1.2×10^7	0.238	0.0	0.56	Exp (HSVA)	-	-	-	-	0.004	-	-	-	-	-	-0.029
46	6.3×10^6	-	0.0	0.56	Parnassos	MNT	1.2×10^6	0.009	0.000	0.009	-0.002	0.000	-0.001	-0.029	0.000	-0.029
47	1.2×10^7	-	0.0	0.00	ReFRESCO	SST	5.2×10^6	-	-	-	-0.001	-0.000	-0.001	-	-	-
48	1.2×10^7	-	2.5	0.00	ReFRESCO	SST	5.2×10^6	0.004	0.000	0.004	-0.001	-0.000	-0.001	-0.005	-0.000	-0.005
49	1.2×10^7	-	5.0	0.00	ReFRESCO	SST	5.2×10^6	0.008	0.001	0.009	-0.001	-0.000	-0.001	-0.011	-0.000	-0.011
50	1.2×10^7	-	7.5	0.00	ReFRESCO	SST	5.2×10^6	0.012	0.001	0.013	-0.001	-0.000	-0.001	-0.017	-0.000	-0.017
51	1.2×10^7	-	10.0	0.00	ReFRESCO	SST	5.2×10^6	0.016	0.002	0.018	-0.001	-0.000	-0.002	-0.022	-0.000	-0.022
52	1.2×10^7	-	12.5	0.00	ReFRESCO	SST	5.2×10^6	0.024	0.002	0.025	-0.002	-0.000	-0.002	-0.028	-0.000	-0.028
53	1.2×10^7	-	15.0	0.00	ReFRESCO	SST	5.2×10^6	0.035	0.002	0.037	-0.003	-0.000	-0.003	-0.034	-0.000	-0.034
54	1.2×10^7	-	17.5	0.00	ReFRESCO	SST	5.2×10^6	0.048	0.003	0.051	-0.003	-0.000	-0.004	-0.040	-0.000	-0.041
55	1.2×10^7	-	20.0	0.00	ReFRESCO	SST	5.2×10^6	0.061	0.003	0.065	-0.004	-0.000	-0.004	-0.047	-0.000	-0.047
56	1.2×10^7	-	22.5	0.00	ReFRESCO	SST	5.2×10^6	0.074	0.003	0.078	-0.005	-0.000	-0.005	-0.054	-0.000	-0.054
57	1.2×10^7	-	25.0	0.00	ReFRESCO	SST	5.2×10^6	0.087	0.004	0.091	-0.006	-0.000	-0.006	-0.062	-0.000	-0.062
58	1.2×10^7	-	27.5	0.00	ReFRESCO	SST	5.2×10^6	0.099	0.004	0.104	-0.007	-0.000	-0.007	-0.068	-0.000	-0.068
59	1.2×10^7	-	30.0	0.00	ReFRESCO	SST	5.2×10^6	0.112	0.005	0.116	-0.007	-0.000	-0.007	-0.074	-0.000	-0.075
60	1.2×10^7	-	0.0	0.10	ReFRESCO	SST	5.2×10^6	0.001	-0.000	0.001	-0.001	-0.000	-0.001	-0.003	-0.000	-0.003
61	1.2×10^7	-	0.0	0.20	ReFRESCO	SST	5.2×10^6	0.002	-0.000	0.002	-0.001	-0.000	-0.001	-0.007	-0.000	-0.008
62	1.2×10^7	-	0.0	0.40	ReFRESCO	SST	5.2×10^6	0.004	-0.000	0.003	-0.001	-0.000	-0.002	-0.018	-0.000	-0.018
63	1.2×10^7	-	0.0	0.56	ReFRESCO	SST	5.2×10^6	0.006	-0.001	0.005	-0.001	-0.000	-0.001	-0.030	-0.000	-0.030
64	1.2×10^7	-	-5.0	0.20	ReFRESCO	SST	5.2×10^6	-0.007	-0.001	-0.008	0.001	-0.000	0.001	0.004	-0.000	0.004
65	1.2×10^7	-	-10.0	0.20	ReFRESCO	SST	5.2×10^6	-0.014	-0.002	-0.016	0.003	-0.000	0.003	0.013	-0.000	0.013
66	1.2×10^7	-	-20.0	0.20	ReFRESCO	SST	5.2×10^6	-0.047	-0.004	-0.050	0.005	-0.000	0.005	0.032	-0.000	0.031
67	1.2×10^7	-	-5.0	0.40	ReFRESCO	SST	5.2×10^6	-0.006	-0.001	-0.007	0.003	-0.000	0.003	-0.006	-0.000	-0.006
68	1.2×10^7	-	-10.0	0.40	ReFRESCO	SST	5.2×10^6	-0.010	-0.002	-0.011	0.007	-0.000	0.007	0.002	-0.000	0.002
69	1.2×10^7	-	-15.0	0.40	ReFRESCO	SST	5.2×10^6	-0.014	-0.003	-0.017	0.011	-0.000	0.011	0.008	-0.000	0.008
70	1.2×10^7	-	-20.0	0.40	ReFRESCO	SST	5.2×10^6	-0.031	-0.004	-0.035	0.014	-0.000	0.013	0.014	-0.000	0.014
71	1.2×10^7	-	-30.0	0.40	ReFRESCO	SST	5.2×10^6	-0.071	-0.006	-0.077	0.018	-0.000	0.018	0.027	-0.000	0.027
72	1.2×10^7	-	-20.0	0.56	ReFRESCO	SST	2.5×10^6	-0.020	-0.004	-0.025	0.021	-0.000	0.020	0.003	-0.000	0.003

Experimental and computational results of forces and moments, SUBOFF

Id	Re [-]	β	γ	Solver	Turb.	Grid	X_p	X_f	X	Y_p	Y_f	Y	N_p	N_f	N
01	1.4×10^7	0	0.0	Exp (DTRC)	-	-	-	-	-1.061	-	-	-0.099	-	-	0.098
02	1.4×10^7	0	0.0	Exp (DTRC)	-	-	-	-	-1.051	-	-	-0.082	-	-	0.070
03	1.4×10^7	0	0.0	ReFRESCO	SST	4138×10^3	-0.129	-0.967	-1.096	0.000	0.000	0.000	0.000	0.000	0.000
04	1.4×10^7	0	0.0	ReFRESCO	SA	4138×10^3	-0.067	-0.950	-1.017	-0.007	0.000	-0.007	0.000	0.000	0.000
05	1.4×10^7	1	0.0	Exp (DTRC)	-	-	-	-	-1.060	-	-	-0.021	-	-	-0.346
06	1.4×10^7	1	0.0	Exp (DTRC)	-	-	-	-	-1.050	-	-	-0.206	-	-	-0.160
07	1.4×10^7	2	0.0	Exp (DTRC)	-	-	-	-	-1.045	-	-	-0.133	-	-	-0.517
08	1.4×10^7	2	0.0	Exp (DTRC)	-	-	-	-	-1.069	-	-	-0.292	-	-	-0.350
09	1.4×10^7	2	0.0	ReFRESCO	SST	4138×10^3	-0.138	-0.969	-1.107	-0.135	-0.029	-0.164	-0.438	-0.001	-0.439
10	1.4×10^7	2	0.0	ReFRESCO	SA	4138×10^3	-0.065	-0.952	-1.017	-0.168	-0.032	-0.199	-0.000	-0.000	-0.000
11	1.4×10^7	3	0.0	Exp (DTRC)	-	-	-	-	-1.060	-	-	-0.321	-	-	-0.771
12	1.4×10^7	3	0.0	Exp (DTRC)	-	-	-	-	-1.060	-	-	-0.408	-	-	-0.598
13	1.4×10^7	4	0.0	Exp (DTRC)	-	-	-	-	-1.061	-	-	-0.449	-	-	-0.996
14	1.4×10^7	4	0.0	Exp (DTRC)	-	-	-	-	-1.046	-	-	-0.592	-	-	-0.864
15	1.4×10^7	4	0.0	ReFRESCO	SST	4138×10^3	-0.132	-0.973	-1.105	-0.330	-0.060	-0.390	-0.899	-0.002	-0.902
16	1.4×10^7	6	0.0	Exp (DTRC)	-	-	-	-	-1.059	-	-	-0.886	-	-	-1.385
17	1.4×10^7	6	0.0	Exp (DTRC)	-	-	-	-	-1.061	-	-	-0.947	-	-	-1.226
18	1.4×10^7	6	0.0	ReFRESCO	SST	4138×10^3	-0.121	-0.980	-1.100	-0.600	-0.094	-0.694	-1.350	-0.003	-1.353
19	1.4×10^7	8	0.0	Exp (DTRC)	-	-	-	-	-1.070	-	-	-1.540	-	-	-1.710
20	1.4×10^7	8	0.0	Exp (DTRC)	-	-	-	-	-1.080	-	-	-1.550	-	-	-1.570
21	1.4×10^7	8	0.0	ReFRESCO	SST	4138×10^3	-0.106	-0.989	-1.095	-0.975	-0.128	-1.102	-1.768	-0.005	-1.773
22	1.4×10^7	10	0.0	Exp (DTRC)	-	-	-	-	-1.049	-	-	-2.450	-	-	-2.008
23	1.4×10^7	10	0.0	Exp (DTRC)	-	-	-	-	-1.079	-	-	-2.337	-	-	-1.875
24	1.4×10^7	10	0.0	ReFRESCO	SST	4138×10^3	-0.086	-1.002	-1.088	-1.487	-0.161	-1.648	-2.144	-0.007	-2.151
25	1.4×10^7	12	0.0	Exp (DTRC)	-	-	-	-	-0.994	-	-	-3.460	-	-	-2.270
26	1.4×10^7	12	0.0	Exp (DTRC)	-	-	-	-	-1.060	-	-	-3.410	-	-	-2.150
27	1.4×10^7	12	0.0	ReFRESCO	SST	4138×10^3	-0.048	-1.018	-1.066	-2.164	-0.195	-2.359	-2.483	-0.009	-2.492
28	1.4×10^7	14	0.0	Exp (DTRC)	-	-	-	-	-0.914	-	-	-4.586	-	-	-2.511
29	1.4×10^7	14	0.0	Exp (DTRC)	-	-	-	-	-1.014	-	-	-4.569	-	-	-2.404
30	1.4×10^7	14	0.0	ReFRESCO	SST	4138×10^3	0.017	-1.036	-1.019	-3.005	-0.229	-3.234	-2.793	-0.012	-2.805
31	1.4×10^7	16	0.0	Exp (DTRC)	-	-	-	-	-0.809	-	-	-5.860	-	-	-2.750
32	1.4×10^7	16	0.0	Exp (DTRC)	-	-	-	-	-0.947	-	-	-5.960	-	-	-2.670
33	1.4×10^7	16	0.0	ReFRESCO	SST	4138×10^3	0.100	-1.052	-0.952	-3.973	-0.263	-4.236	-3.080	-0.014	-3.094
34	1.4×10^7	18	0.0	Exp (DTRC)	-	-	-	-	-0.670	-	-	-7.355	-	-	-2.986
35	1.4×10^7	18	0.0	Exp (DTRC)	-	-	-	-	-0.852	-	-	-7.438	-	-	-2.939
36	1.4×10^7	18	0.0	ReFRESCO	SST	4138×10^3	0.207	-1.067	-0.860	-5.086	-0.297	-5.383	-3.353	-0.017	-3.370
37	1.4×10^7	18	0.0	ReFRESCO	SA	4138×10^3	0.307	-1.074	-0.767	-5.371	-0.307	-5.678	-3.366	-0.017	-3.383
38	1.4×10^7	20	0.0	ReFRESCO	SST	4138×10^3	0.336	-1.082	-0.745	-6.331	-0.330	-6.661	-3.613	-0.020	-3.633
39	1.4×10^7	22	0.0	ReFRESCO	SST	4138×10^3	0.487	-1.096	-0.609	-7.691	-0.363	-8.053	-3.859	-0.024	-3.882
40	1.4×10^7	24	0.0	ReFRESCO	SST	4138×10^3	0.661	-1.109	-0.448	-9.167	-0.395	-9.562	-4.092	-0.027	-4.119
41	1.4×10^7	36	0.0	ReFRESCO	SST	300×10^3	2.162	-1.072	1.089	-20.679	-0.549	-21.228	-5.135	-0.046	-5.180
42	1.4×10^7	60	0.0	ReFRESCO	SST	300×10^3	6.196	-0.881	5.315	-39.279	-0.823	-40.102	-6.565	-0.070	-6.635
43	1.4×10^7	75	0.0	ReFRESCO	SST	300×10^3	6.769	-0.571	6.197	-43.006	-0.928	-43.935	-5.845	-0.060	-5.905
44	1.4×10^7	90	0.0	ReFRESCO	SST	300×10^3	1.859	-0.093	1.766	-43.672	-0.980	-44.653	-0.527	-0.005	-0.531

Note: The forces and moments have been multiplied by 10^3

Page intentionally left blank

ZIG-ZAG 10°/10° PS, V_0 = 10 kn

DESIGNATION	UNIT	MAGNITUDE								
TestNo	-	CFD	106002	106007	106011	203004	203006	203008	203010	203013
Approach speed V_0	kn	10.00	10.00	10.00	10.50	10.00	10.00	10.00	10.00	10.00
Steering angle (δ)	deg	10.00	10.00	10.00	10.00	10.00	10.00	10.00	10.00	10.00
Check angle (ψ)	deg	-10.00	-10.00	-10.00	-10.00	-10.00	-10.00	-10.00	-10.00	-10.00
2^{nd} execute time	s	48.3	50.7	53.4	47.4	50.7	51.1	50.7	50.1	53.4
3^{rd} execute time	s	233.3	209.6	215.9	208.0	195.1	215.3	201.6	200.8	204.7
4^{th} execute time	s	491.0	444.1	442.8	432.3	411.0	451.7	427.9	-	429.3
5^{th} execute time	s	744.0	708.0	672.3	666.8	-	701.9	-	-	-
Reach	s	216.9	190.6	196.7	189.1	174.6	197.9	182.3	181.0	185.9
Period	s	510.8	498.3	456.5	464.9	360.3	486.6	377.2	-	375.9
Overshoot angle (ψ)										
-1^{st} execute	deg	14.5	10.3	10.7	10.8	7.9	11.9	8.8	8.6	9.2
-2^{nd} execute	deg	31.3	23.5	21.1	20.3	20.8	24.6	23.8	21.6	22.7
-3^{rd} execute	deg	29.4	28.1	20.2	20.9	26.1	27.2	25.4	-	22.3
-4^{th} execute	deg	27.8	-	18.4	18.9	-	23.9	-	-	-
Overshoot time										
-1^{st} execute	s	81.2	60.9	60.4	58.5	50.7	62.8	53.5	52.6	53.4
-2^{nd} execute	s	124.2	104.9	94.7	94.3	92.5	106.9	99.9	98.6	99.1
-3^{rd} execute	s	119.2	120.2	93.8	102.3	112.4	113.1	111.5	-	82.4
-4^{th} execute	s	115.6	-	94.5	95.5	-	109.4	-	-	-
Initial turning ability	m	247.4	258.9	269.4	242.9	255.7	263.8	257.6	253.3	266.4
-Relative to L_{pp}	-	1.61	1.68	1.75	1.58	1.66	1.72	1.68	1.65	1.73
Maximum heel angle (ϕ)										
-1^{st} execute	deg	0.0	1.3	1.0	1.0	1.2	1.3	1.0	1.1	0.9
-2^{nd} execute	deg	0.0	-1.6	-1.5	-1.4	-1.3	-1.5	-1.4	-1.4	-1.3
-3^{rd} execute	deg	0.0	1.3	0.8	1.0	1.1	1.0	1.0	-	1.0
-4^{th} execute	deg	0.0	-	-0.9	-1.2	-	-1.4	-	-	-
Maximum drift angle (β)										
-1^{st} execute	deg	4.5	4.3	4.7	4.6	4.2	4.7	4.0	4.8	4.3
-2^{nd} execute	deg	-8.8	-8.4	-8.9	-9.3	-8.3	-9.1	-8.3	-8.0	-8.4
-3^{rd} execute	deg	10.5	10.1	10.5	10.1	9.3	10.0	9.6	-	9.7
-4^{th} execute	deg	-10.3	-	-11.1	-10.5	-	-10.3	-	-	-
Maximum rate of turn (r)										
-1^{st} execute	$deg \cdot s^{-1}$	-0.41	-0.39	-0.40	-0.41	-0.36	-0.42	-0.37	-0.37	-0.37
-2^{nd} execute	$deg \cdot s^{-1}$	0.64	0.58	0.55	0.55	0.56	0.59	0.58	0.57	0.58
-3^{rd} execute	$deg \cdot s^{-1}$	-0.66	-0.60	-0.53	-0.53	-0.60	-0.60	-0.60		-0.58
-4^{th} execute	$deg \cdot s^{-1}$	0.64	-	0.50	0.51		0.58			

clear columns contain CFD results

gray columns contain experimental results

ZIG-ZAG 10°/10° SB, V_0 = 10 kn

DESIGNATION	UNIT	MAGNITUDE								
TestNo	-	CFD	106005	106006	106010	203003	203005	203007	203009	203011
Approach speed V_0	kn	10.00	10.00	10.00	9.50	10.00	10.00	10.00	10.00	10.00
Steering angle (δ)	deg	-10.00	-10.00	-10.00	-10.00	-10.00	-10.00	-10.00	-10.00	-10.00
Check angle (ψ)	deg	10.00	10.00	10.00	10.00	10.00	10.00	10.00	10.00	10.00
2^{nd} execute time	s	48.3	46.9	48.2	51.5	57.8	65.0	64.4	49.0	51.8
3^{rd} execute time	s	233.3	212.8	211.8	214.2	215.3	220.0	232.9	204.9	200.8
4^{th} execute time	s	491.0	469.8	474.5	439.2	446.1	459.4	480.3	-	423.0
5^{th} execute time	s	744.0	721.6	726.0	666.9	685.2	705.4	-	-	-
Reach	s	216.9	194.4	193.6	194.8	198.0	201.3	217.8	185.1	181.3
Period	s	510.8	508.8	514.3	452.6	469.9	485.4	415.9	-	371.2
Overshoot angle (ψ)										
-1^{st} execute	deg	14.5	11.6	10.8	9.6	9.5	9.2	12.3	9.4	8.6
-2^{nd} execute	deg	31.3	28.0	28.4	20.3	23.3	25.3	26.9	25.3	22.4
-3^{rd} execute	deg	29.4	25.5	25.1	18.8	23.8	25.0	24.1	-	22.2
-4^{th} execute	deg	27.8	28.3	-	19.5	25.4	24.2	-	-	-
Overshoot time										
-1^{st} execute	s	81.2	62.4	63.5	54.6	55.8	54.6	65.6	57.0	50.7
-2^{nd} execute	s	124.2	120.2	127.1	96.9	100.9	109.6	113.3	109.4	96.8
-3^{rd} execute	s	119.2	115.2	110.1	95.2	107.5	113.4	111.9	-	99.7
-4^{th} execute	s	115.6	124.5	-	93.4	109.5	108.8	-	-	-
Initial turning ability	m	247.4	242.6	250.4	249.1	292.5	333.4	334.8	254.7	263.2
-Relative to L_{pp}	-	1.61	1.58	1.63	1.62	1.90	2.17	2.18	1.66	1.71
Maximum heel angle (ϕ)										
-1^{st} execute	deg	0.0	-1.5	-1.6	-1.1	-1.3	-1.3	-1.6	-1.5	-1.3
-2^{nd} execute	deg	0.0	1.2	1.4	1.0	1.3	1.3	1.1	1.4	1.1
-3^{rd} execute	deg	0.0	-1.3	-1.3	-1.1	-1.4	-1.2	-1.1	-	-1.2
-4^{th} execute	deg	0.0	1.2	-	0.8	1.0	1.1	-	-	-
Maximum drift angle (β)										
-1^{st} execute	deg	-4.5	-5.0	-4.7	-5.1	-5.1	-4.6	-5.1	-4.7	-4.8
-2^{nd} execute	deg	8.8	8.7	8.8	8.9	8.2	8.6	8.8	8.6	8.0
-3^{rd} execute	deg	-10.5	-10.4	-10.4	-10.1	-10.2	-10.3	-10.4	-	-9.9
-4^{th} execute	deg	10.3	11.0	-	10.4	10.0	9.9	-	-	-
Maximum rate of turn (r)										
-1^{st} execute	$deg \cdot s^{-1}$	0.41	0.42	0.41	0.39	0.41	0.39	0.44	0.40	0.38
-2^{nd} execute	$deg \cdot s^{-1}$	-0.64	-0.59	-0.59	-0.53	-0.58	-0.58	-0.59	-0.57	-0.56
-3^{rd} execute	$deg \cdot s^{-1}$	0.66	0.59	0.59	0.51	0.59	0.60	0.60		0.58
-4^{th} execute	$deg \cdot s^{-1}$	-0.64	-0.59	-	-0.51	-0.59	-0.58			

clear columns contain CFD results

gray columns contain experimental results

ZIG-ZAG 20°/20° PS, V_0 = 10 kn

DESIGNATION	UNIT	MAGNITUDE				
TestNo	-	CFD	106004	106009	106013	204003
Approach speed V_0	kn	10.00	10.00	9.50	10.00	10.00
Steering angle (δ)	deg	20.00	20.00	20.00	20.00	20.00
Check angle (ψ)	deg	-20.00	-20.00	-20.00	-20.00	-20.00
2^{nd} execute time	s	51.3	51.5	53.4	53.2	51.7
3^{rd} execute time	s	226.8	227.1	226.3	223.3	218.1
4^{th} execute time	s	409.8	417.6	413.4	410.4	406.6
5^{th} execute time	s	585.8	619.7	611.1	606.9	601.9
Reach	s	203.3	198.9	195.4	193.3	189.8
Period	s	359.0	386.9	376.7	380.9	379.4
Overshoot angle (ψ)						
-1^{st} execute	deg	20.3	16.6	14.3	14.4	15.0
-2^{nd} execute	deg	19.8	17.6	14.6	14.8	17.2
-3^{rd} execute	deg	17.1	17.5	13.8	14.3	15.5
-4^{th} execute	deg	16.5	15.3	12.0	13.1	14.5
Overshoot time						
-1^{st} execute	s	64.7	57.8	53.5	51.3	54.1
-2^{nd} execute	s	63.8	64.8	55.5	50.5	59.6
-3^{rd} execute	s	57.5	70.1	59.7	62.0	62.5
-4^{th} execute	s	55.7	54.2	51.5	52.1	57.3
Initial turning ability	m	260.1	261.1	253.2	259.8	262.0
-Relative to L_{pp}	-	1.69	1.70	1.65	1.69	1.70
Maximum heel angle (ϕ)						
-1^{st} execute	deg	0.0	2.2	1.4	1.5	2.0
-2^{nd} execute	deg	0.0	-1.7	-1.3	-1.3	-1.1
-3^{rd} execute	deg	0.0	1.2	1.0	0.9	1.2
-4^{th} execute	deg	0.0	-1.6	-1.3	-1.3	-1.4
Maximum drift angle (β)						
-1^{st} execute	deg	8.6	8.7	9.1	8.7	8.6
-2^{nd} execute	deg	-14.5	-13.4	-14.4	-14.2	-13.1
-3^{rd} execute	deg	14.6	13.5	14.0	13.5	14.1
-4^{th} execute	deg	-14.4	-13.6	-14.3	-14.1	-13.0
Maximum rate of turn (r)						
-1^{st} execute	$deg \cdot s^{-1}$	-0.75	-0.71	-0.67	-0.69	-0.71
-2^{nd} execute	$deg \cdot s^{-1}$	0.84	0.75	0.68	0.69	0.74
-3^{rd} execute	$deg \cdot s^{-1}$	-0.79	-0.71	-0.62	-0.63	-0.72
-4^{th} execute	$deg \cdot s^{-1}$	0.78	0.68	0.59	0.61	0.67

clear columns contain CFD results

gray columns contain experimental results

ZIG-ZAG 20°/20° PS, V_0 = 10 kn

DESIGNATION	UNIT	MAGNITUDE				
TestNo	-	CFD	106003	106008	106012	204002
Approach speed V_0	kn	10.00	10.50	9.50	9.50	10.00
Steering angle (δ)	deg	-20.00	-20.00	-20.00	-20.00	-20.00
Check angle (ψ)	deg	20.00	20.00	20.00	20.00	20.00
2^{nd} execute time	s	51.3	53.4	52.9	54.3	49.9
3^{rd} execute time	s	226.8	225.5	219.5	219.2	211.8
4^{th} execute time	s	409.8	428.2	420.3	420.9	410.2
5^{th} execute time	s	585.8	615.9	604.5	603.6	591.2
Reach	s	203.3	199.1	190.5	188.9	184.6
Period	s	359.0	391.0	377.3	379.5	379.4
Overshoot angle (ψ)						
-1^{st} execute	deg	20.3	17.4	14.4	14.2	15.4
-2^{nd} execute	deg	19.8	17.9	16.1	16.3	17.8
-3^{rd} execute	deg	17.1	15.8	13.3	13.1	14.5
-4^{th} execute	deg	16.5	16.5	14.3	14.5	15.1
Overshoot time						
-1^{st} execute	s	64.7	58.6	49.2	46.1	51.6
-2^{nd} execute	s	63.8	67.0	65.8	64.3	66.3
-3^{rd} execute	s	57.5	60.5	55.2	49.9	55.2
-4^{th} execute	s	55.7	68.1	57.0	61.4	56.8
Initial turning ability	m	260.1	282.3	250.1	258.2	251.9
-Relative to L_{pp}	-	1.69	1.84	1.63	1.68	1.64
Maximum heel angle (ϕ)						
-1^{st} execute	deg	0.0	-1.7	-1.6	-1.5	-1.6
-2^{nd} execute	deg	0.0	1.4	1.1	1.2	1.2
-3^{rd} execute	deg	0.0	-1.6	-1.2	-1.4	-1.4
-4^{th} execute	deg	0.0	1.2	1.1	1.3	1.1
Maximum drift angle (β)						
-1^{st} execute	deg	-8.6	-8.9	-9.0	-9.0	-8.5
-2^{nd} execute	deg	14.5	14.0	13.9	14.3	13.8
-3^{rd} execute	deg	-14.6	-13.6	-14.0	-14.0	-13.6
-4^{th} execute	deg	14.4	13.9	13.6	13.7	13.8
Maximum rate of turn (r)						
-1^{st} execute	$deg \cdot s^{-1}$	0.75	0.73	0.67	0.67	0.72
-2^{nd} execute	$deg \cdot s^{-1}$	-0.84	-0.77	-0.71	-0.70	-0.77
-3^{rd} execute	$deg \cdot s^{-1}$	0.79	0.68	0.61	0.63	0.68
-4^{th} execute	$deg \cdot s^{-1}$	-0.78	-0.69	-0.64	-0.63	-0.70

clear columns contain CFD results

gray columns contain experimental results

ZIG-ZAG 10°/10° PS, V_0 = 18 kn

DESIGNATION	UNIT	MAGNITUDE			
TestNo	-	CFD	108002	108007	108011
Approach speed V_0	kn	18.00	17.50	17.50	17.00
Steering angle (δ)	deg	10.00	10.00	10.00	10.00
Check angle (ψ)	deg	-10.00	-10.00	-10.00	-10.00
2^{nd} execute time	s	27.3	27.4	26.9	27.9
3^{rd} execute time	s	134.5	112.6	116.7	113.8
4^{th} execute time	s	280.5	226.3	234.0	227.2
5^{th} execute time	s	422.5	352.9	361.3	-
Reach	s	125.6	101.0	105.3	101.8
Period	s	288.0	240.3	244.7	199.2
Overshoot angle (ψ)					
-1^{st} execute	deg	16.2	9.4	11.0	9.6
-2^{nd} execute	deg	32.8	18.5	19.5	18.6
-3^{rd} execute	deg	30.2	22.5	22.4	23.2
-4^{th} execute	deg	28.8	18.5	19.0	-
Overshoot time					
-1^{st} execute	s	48.0	29.8	33.5	30.3
-2^{nd} execute	s	70.4	45.6	49.0	45.3
-3^{rd} execute	s	66.8	52.3	53.9	55.3
-4^{th} execute	s	65.0	47.1	50.2	-
Initial turning ability	m	251.5	241.0	238.1	245.4
-Relative to L_{pp}	-	1.64	1.57	1.55	1.60
Maximum heel angle (ϕ)					
-1^{st} execute	deg	0.0	3.5	3.5	3.5
-2^{nd} execute	deg	0.0	-4.2	-4.0	-4.2
-3^{rd} execute	deg	0.0	3.0	3.3	3.0
-4^{th} execute	deg	0.0	-3.6	-3.6	-
Maximum drift angle (β)					
-1^{st} execute	deg	4.6	4.7	5.1	4.8
-2^{nd} execute	deg	-9.1	-8.3	-8.2	-8.1
-3^{rd} execute	deg	10.6	9.6	9.7	9.6
-4^{th} execute	deg	-10.4	-9.5	-9.3	-
Maximum rate of turn (r)					
-1^{st} execute	$deg \cdot s^{-1}$	-0.75	-0.69	-0.71	-0.68
-2^{nd} execute	$deg \cdot s^{-1}$	1.17	0.98	0.99	0.98
-3^{rd} execute	$deg \cdot s^{-1}$	-1.19	-1.00	-1.01	-1.01
-4^{th} execute	$deg \cdot s^{-1}$	1.16	0.97	0.97	

clear columns contain CFD results

gray columns contain experimental results

ZIG-ZAG 10°/10° SB, V_0 = 18 kn

DESIGNATION	UNIT	MAGNITUDE			
TestNo	-	CFD	108001	108006	108010
Approach speed V_0	kn	18.00	17.50	17.50	17.50
Steering angle (δ)	deg	-10.00	-10.00	-10.00	-10.00
Check angle (ψ)	deg	10.00	10.00	10.00	10.00
2^{nd} execute time	s	27.3	28.8	29.1	28.8
3^{rd} execute time	s	134.5	113.8	115.1	114.2
4^{th} execute time	s	280.5	236.4	235.9	237.0
5^{th} execute time	s	422.5	-	354.3	355.0
Reach	s	125.6	102.6	103.6	102.7
Period	s	288.0	207.7	239.2	240.9
Overshoot angle (ψ)					
-1^{st} execute	deg	16.2	10.0	9.6	9.6
-2^{nd} execute	deg	32.8	21.6	21.3	21.8
-3^{rd} execute	deg	30.2	19.0	19.1	19.2
-4^{th} execute	deg	28.8	-	21.5	21.4
Overshoot time					
-1^{st} execute	s	48.0	29.4	30.1	29.3
-2^{nd} execute	s	70.4	50.8	50.8	51.9
-3^{rd} execute	s	66.8	46.5	49.7	46.5
-4^{th} execute	s	65.0	-	52.5	51.4
Initial turning ability	m	251.5	257.9	258.5	254.9
-Relative to L_{pp}	-	1.64	1.68	1.68	1.66
Maximum heel angle (ϕ)					
-1^{st} execute	deg	0.0	-4.1	-4.1	-4.0
-2^{nd} execute	deg	0.0	3.6	3.6	3.6
-3^{rd} execute	deg	0.0	-3.6	-3.7	-3.7
-4^{th} execute	deg	0.0	-	3.1	3.0
Maximum drift angle (β)					
-1^{st} execute	deg	-4.6	-4.5	-4.4	-4.6
-2^{nd} execute	deg	9.1	8.5	8.4	8.3
-3^{rd} execute	deg	-10.6	-9.7	-9.2	-9.1
-4^{th} execute	deg	10.4	-	9.6	9.4
Maximum rate of turn (r)					
-1^{st} execute	$deg{\cdot}s^{-1}$	0.75	0.72	0.71	0.71
-2^{nd} execute	$deg{\cdot}s^{-1}$	-1.17	-1.00	-0.99	-1.00
-3^{rd} execute	$deg{\cdot}s^{-1}$	1.19	0.98	0.99	0.99
-4^{th} execute	$deg{\cdot}s^{-1}$	-1.16		-0.97	-0.99

clear columns contain CFD results

gray columns contain experimental results

ZIG-ZAG 20°/20° PS, V_0 = 18 kn

DESIGNATION	UNIT	MAGNITUDE			
TestNo	-	CFD	108013	108009	108005
Approach speed V_0	kn	18.00	17.50	17.50	17.50
Steering angle (δ)	deg	20.00	20.00	20.00	20.00
Check angle (ψ)	deg	-20.00	-20.00	-20.00	-22.00
2^{nd} execute time	s	29.5	29.9	29.3	29.6
3^{rd} execute time	s	132.3	131.2	130.1	130.9
4^{th} execute time	s	237.0	237.5	237.6	238.3
5^{th} execute time	s	337.8	352.0	352.9	353.4
Reach	s	119.3	115.1	113.7	114.3
Period	s	205.5	217.8	222.7	222.4
Overshoot angle (ψ)					
-1^{st} execute	deg	23.7	18.9	18.5	18.6
-2^{nd} execute	deg	21.5	18.3	18.9	18.5
-3^{rd} execute	deg	19.0	19.6	19.4	19.0
-4^{th} execute	deg	18.5	16.3	16.4	16.1
Overshoot time					
-1^{st} execute	s	38.8	33.2	33.0	33.4
-2^{nd} execute	s	36.7	34.1	34.3	34.6
-3^{rd} execute	s	33.2	38.6	39.0	38.0
-4^{th} execute	s	32.4	30.0	31.3	30.6
Initial turning ability	m	269.6	261.3	257.5	258.0
-Relative to L_{pp}	-	1.75	1.70	1.68	1.68
Maximum heel angle (ϕ)					
-1^{st} execute	deg	0.0	5.0	5.1	5.0
-2^{nd} execute	deg	0.0	-3.7	-4.1	-3.8
-3^{rd} execute	deg	0.0	3.1	3.0	3.4
-4^{th} execute	deg	0.0	-3.1	-3.0	-3.1
Maximum drift angle (β)					
-1^{st} execute	deg	9.0	9.1	9.0	9.3
-2^{nd} execute	deg	-14.9	-13.5	-13.8	-13.9
-3^{rd} execute	deg	14.9	14.0	13.7	14.0
-4^{th} execute	deg	-14.7	-13.3	-13.4	-13.4
Maximum rate of turn (r)					
-1^{st} execute	$deg{\cdot}s^{-1}$	-1.36	-1.25	-1.25	-1.25
-2^{nd} execute	$deg{\cdot}s^{-1}$	1.50	1.30	1.29	1.29
-3^{rd} execute	$deg{\cdot}s^{-1}$	-1.40	-1.24	-1.24	-1.22
-4^{th} execute	$deg{\cdot}s^{-1}$	1.39	1.16	1.16	1.16

clear columns contain CFD results

gray columns contain experimental results

ZIG-ZAG 20°/20° SB, V_0 = 18 kn

DESIGNATION	UNIT	MAGNITUDE			
TestNo	-	CFD	108003	108008	108012
Approach speed V_0	kn	18.00	17.50	17.00	17.50
Steering angle (δ)	deg	-20.00	-20.00	-20.00	-20.00
Check angle (ψ)	deg	20.00	20.00	22.00	20.00
2nd execute time	s	29.5	29.0	30.4	30.1
3rd execute time	s	132.3	124.6	126.1	126.8
4th execute time	s	237.0	243.3	242.4	244.4
5th execute time	s	337.8	347.6	347.0	349.6
Reach	s	119.3	108.8	110.0	111.2
Period	s	205.5	219.1	218.9	220.5
Overshoot angle (ψ)					
-1st execute	deg	23.7	18.5	17.3	18.6
-2nd execute	deg	21.5	21.7	20.8	21.8
-3rd execute	deg	19.0	16.3	16.5	16.8
-4th execute	deg	18.5	19.3	18.6	19.3
Overshoot time					
-1st execute	s	38.8	30.6	28.3	32.5
-2nd execute	s	36.7	41.4	39.7	40.8
-3rd execute	s	33.2	30.4	31.0	30.9
-4th execute	s	32.4	39.4	38.2	39.9
Initial turning ability	m	269.6	257.6	264.4	266.1
-Relative to L_{pp}	-	1.75	1.68	1.72	1.73
Maximum heel angle (ϕ)					
-1st execute	deg	0.0	-5.7	-5.6	-5.4
-2nd execute	deg	0.0	3.2	3.0	3.2
-3rd execute	deg	0.0	-3.3	-3.3	-3.4
-4th execute	deg	0.0	3.2	3.3	3.2
Maximum drift angle (β)					
-1st execute	deg	-9.0	-8.6	-8.8	-8.6
-2nd execute	deg	14.9	14.3	14.1	14.4
-3rd execute	deg	-14.9	-13.4	-13.1	-13.2
-4th execute	deg	14.7	13.8	13.8	13.9
Maximum rate of turn (r)					
-1st execute	$deg \cdot s^{-1}$	1.36	1.26	1.24	1.24
-2nd execute	$deg \cdot s^{-1}$	-1.50	-1.34	-1.34	-1.36
-3rd execute	$deg \cdot s^{-1}$	1.40	1.18	1.19	1.19
-4th execute	$deg \cdot s^{-1}$	-1.39	-1.21	-1.22	-1.22

clear columns contain CFD results

gray columns contain experimental results

TURNING CIRCLE 35° PS/SB, V_0 = 10 kn

DESIGNATION	UNIT	MAGNITUDE			
TestNo	-	CFD	107002	CFD	107001
Approach speed V_0	kn	10.00	10.00	10.00	9.50
Steering angle (δ)	deg	35.00	35.00	-35.00	-35.00
Advance (AD)	m	418.4	424.8	418.4	425.8
Transfer (TR)	m	-160.1	161.3	160.1	177.3
Tactical diameter (TD)	m	-424.7	414.3	424.7	437.7
D_{stc}	m	305.9	356.5	305.9	380.2
T_{90}	s	110.2	120.8	110.2	124.9
T_{180}	s	239.5	249.5	239.5	262.6
T_{360}	s	539.6	541.7	539.6	570.3
T_{stc}	s	609.3	567.6	609.3	616.0
$r_{execute}$	$deg{\cdot}s^{-1}$	-1.13	-0.97	1.13	0.96
r_{stc}	$deg{\cdot}s^{-1}$	-0.59	-0.63	0.59	0.58
$r_{residual}$	$deg{\cdot}s^{-1}$	-	0.13	-	0.07
$r_{residual}/r_{stc}$	-	-	-0.21	-	0.12
V_{stc}	kn	3.1	3.8	3.1	3.8
V_{stc}/V_0	-	0.31	0.39	0.31	0.39
$\phi_{max,in}$	deg	0.0	-1.0	0.0	1.0
$\phi_{max,out}$	deg	0.0	0.8	0.0	-1.0
ϕ_{stc}	deg	0.0	-0.2	0.0	0.1
ϕ_{stc}/ϕ_{max}	-	-	-0.22	-	-0.07
Drift angle during turn (β_{stc})	deg	28.8	20.4	-28.8	-19.0
D_{stc}/L_{pp} ratio	-	1.99	2.32	1.99	2.47
AD/L_{pp} ratio	-	2.72	2.76	2.72	2.77
TD/L_{pp} ratio	-	-2.76	2.70	2.76	2.85

clear columns contain CFD results

gray columns contain experimental results

TURNING CIRCLE 25° PS/SB, V_0 = 10 kn

DESIGNATION	UNIT	MAGNITUDE			
TestNo	-	CFD	107005	CFD	107004
Approach speed V_0	kn	10.00	10.50	10.00	9.50
Steering angle (δ)	deg	25.00	25.00	-25.00	-25.00
Advance (AD)	m	474.5	498.6	474.5	476.1
Transfer (TR)	m	-201.7	206.7	201.7	216.3
Tactical diameter (TD)	m	-502.3	507.9	502.3	528.1
D_{stc}	m	399.9	447.6	399.9	476.6
T_{90}	s	123.7	134.3	123.7	143.1
T_{180}	s	252.5	272.9	252.5	295.9
T_{360}	s	546.8	583.0	546.8	630.0
T_{stc}	s	601.6	609.0	601.6	649.3
$r_{execute}$	$deg \cdot s^{-1}$	-0.98	-0.86	0.98	0.81
r_{stc}	$deg \cdot s^{-1}$	-0.60	-0.59	0.60	0.55
$r_{residual}$	$deg \cdot s^{-1}$	-	0.14	-	0.13
$r_{residual}/r_{stc}$	-	-	-0.23	-	0.23
V_{stc}	kn	4.1	4.5	4.1	4.5
V_{stc}/V_0	-	0.41	0.43	0.41	0.48
$\phi_{max,in}$	deg	0.0	-1.3	0.0	0.5
$\phi_{max,out}$	deg	0.0	0.8	0.0	-1.3
ϕ_{stc}	deg	0.0	-0.2	0.0	0.1
ϕ_{stc}/ϕ_{max}	-	-	-0.26	-	-0.09
Drift angle during turn (β_{stc})	deg	21.4	17.1	-21.4	-15.0
D_{stc}/L_{pp} ratio	-	2.60	2.91	2.60	3.10
AD/L_{pp} ratio	-	3.09	3.24	3.09	3.10
TD/L_{pp} ratio	-	-3.27	3.30	3.27	3.44

clear columns contain CFD results

gray columns contain experimental results

TURNING CIRCLE 15° PS/SB, $V_0 = 10$ kn

DESIGNATION	UNIT	MAGNITUDE			
TestNo	-	CFD	107007	CFD	107008
Approach speed V_0	kn	10.00	10.00	10.00	10.00
Steering angle (δ)	deg	15.00	15.00	-15.00	-15.00
Advance (AD)	m	581.7	593.5	581.7	573.3
Transfer (TR)	m	-271.8	275.0	271.8	289.8
Tactical diameter (TD)	m	-638.3	632.3	638.3	676.8
D_{stc}	m	571.3	591.5	571.6	622.0
T_{90}	s	150.0	162.4	150.0	168.2
T_{180}	s	290.0	316.1	290.0	337.2
T_{360}	s	603.1	655.8	603.1	696.3
T_{stc}	s	637.7	685.4	636.9	715.8
$r_{execute}$	$deg \cdot s^{-1}$	-0.80	-0.72	0.80	0.68
r_{stc}	$deg \cdot s^{-1}$	-0.56	-0.53	0.57	0.50
$r_{residual}$	$deg \cdot s^{-1}$	-	-0.04	-	0.03
$r_{residual}/r_{stc}$	-	-	0.08	-	0.06
V_{stc}	kn	5.5	5.3	5.5	5.3
V_{stc}/V_0	-	0.55	0.52	0.55	0.54
$\phi_{max,in}$	deg	0.0	-1.0	0.0	0.3
$\phi_{max,out}$	deg	0.0	0.8	0.0	-1.0
ϕ_{stc}	deg	0.0	-0.2	0.0	-0.1
ϕ_{stc}/ϕ_{max}	-	-	-0.26	-	0.15
Drift angle during turn (β_{stc})	deg	14.9	14.0	-14.9	-12.4
D_{stc}/L_{pp} ratio	-	3.72	3.85	3.72	4.05
AD/L_{pp} ratio	-	3.78	3.86	3.78	3.73
TD/L_{pp} ratio	-	-4.15	4.11	4.15	4.40

clear columns contain CFD results

gray columns contain experimental results

TURNING CIRCLE 35° PS, V_0 = 18 kn

DESIGNATION	UNIT	MAGNITUDE				
TestNo	-	CFD	104029	104027	104021	205003
Approach speed V_0	kn	18.00	18.00	18.50	17.50	18.00
Steering angle (δ)	deg	35.00	35.00	35.00	35.00	35.00
Advance (AD)	m	431.7	419.8	416.0	414.2	423.6
Transfer (TR)	m	-160.4	164.8	162.2	158.2	163.7
Tactical diameter (TD)	m	-425.1	394.7	394.4	389.0	397.7
D_{stc}	m	305.7	320.5	321.1	319.0	330.1
T_{90}	s	62.6	62.5	61.7	62.8	63.0
T_{180}	s	134.3	124.5	123.8	125.4	125.9
T_{360}	s	301.1	262.3	262.9	263.9	265.8
T_{stc}	s	338.4	276.1	277.8	276.5	284.5
$r_{execute}$	$deg \cdot s^{-1}$	-2.04	-1.93	-1.96	-1.93	-1.90
r_{stc}	$deg \cdot s^{-1}$	-1.06	-1.30	-1.30	-1.30	-1.27
$r_{residual}$	$deg \cdot s^{-1}$	-	-0.49	-0.55	-0.55	-0.30
$r_{residual}/r_{stc}$	-	-	0.38	0.43	0.42	0.24
V_{stc}	kn	5.5	7.1	7.1	7.0	7.1
V_{stc}/V_0	-	0.31	0.39	0.39	0.40	0.39
$\phi_{max,in}$	deg	0.0	-2.4	-2.7	-2.6	-2.6
$\phi_{max,out}$	deg	0.0	3.5	3.8	3.0	3.4
ϕ_{stc}	deg	0.0	-1.0	-1.1	-1.1	-0.8
ϕ_{stc}/ϕ_{max}	-	-	-0.29	-0.28	-0.36	-0.23
Drift angle during turn (β_{stc})	deg	28.8	21.2	21.5	21.2	20.6
D_{stc}/L_{pp} ratio	-	1.99	2.09	2.09	2.08	2.15
AD/L_{pp} ratio	-	2.81	2.73	2.71	2.69	2.76
TD/L_{pp} ratio	-	-2.77	2.57	2.57	2.53	2.59

clear columns contain CFD results

gray columns contain experimental results

TURNING CIRCLE 35° SB, V_0 = 18 kn

DESIGNATION	UNIT	MAGNITUDE				
TestNo	-	CFD	104026	104019	104028	205002
Approach speed V_0	kn	18.00	18.00	18.00	18.00	18.50
Steering angle (δ)	deg	-35.00	-35.00	-35.00	-35.00	-35.00
Advance (AD)	m	431.7	443.5	441.4	433.8	438.7
Transfer (TR)	m	160.4	177.3	179.9	180.6	175.0
Tactical diameter (TD)	m	425.1	427.8	431.1	434.2	424.3
D_{stc}	m	305.7	361.7	357.2	362.0	352.1
T_{90}	s	62.6	66.4	66.1	65.9	64.9
T_{180}	s	134.3	133.1	133.1	133.3	132.0
T_{360}	s	301.1	282.2	281.6	283.4	283.4
T_{stc}	s	338.4	304.5	302.4	306.2	304.8
$r_{execute}$	deg·s^{-1}	2.04	1.84	1.84	1.84	1.90
r_{stc}	deg·s^{-1}	1.06	1.18	1.19	1.18	1.18
$r_{residual}$	deg·s^{-1}	-	0.34	0.37	0.37	0.51
$r_{residual}/r_{stc}$	-	-	0.29	0.31	0.31	0.43
V_{stc}	kn	5.5	7.3	7.2	7.2	7.1
V_{stc}/V_0	-	0.31	0.40	0.40	0.40	0.38
$\phi_{max,in}$	deg	0.0	2.1	2.2	2.0	2.1
$\phi_{max,out}$	deg	0.0	-2.9	-3.0	-3.5	-3.2
ϕ_{stc}	deg	0.0	0.3	0.3	0.3	-0.1
ϕ_{stc}/ϕ_{max}	-	-	-0.10	-0.09	-0.08	0.01
Drift angle during turn (β_{stc})	deg	-28.8	-19.9	-19.6	-20.4	-20.1
D_{stc}/L_{pp} ratio	-	1.99	2.35	2.32	2.36	2.29
AD/L_{pp} ratio	-	2.81	2.89	2.87	2.82	2.85
TD/L_{pp} ratio	-	2.77	2.78	2.80	2.83	2.76

clear columns contain CFD results

gray columns contain experimental results

TURNING CIRCLE 25° PS/SB, V_0 = 18 kn

DESIGNATION	UNIT	MAGNITUDE			
TestNo	-	CFD	104023	CFD	104022
Approach speed V_0	kn	18.00	18.50	18.00	18.00
Steering angle (δ)	deg	25.00	25.00	-25.00	-25.00
Advance (AD)	m	484.9	464.6	484.9	515.2
Transfer (TR)	m	-201.9	204.2	201.9	218.4
Tactical diameter (TD)	m	-502.5	482.0	502.5	525.5
D_{stc}	m	400.0	412.3	400.0	486.1
T_{90}	s	69.8	68.7	69.8	75.5
T_{180}	s	141.3	136.3	141.3	149.0
T_{360}	s	304.8	284.8	304.8	311.1
T_{stc}	s	334.3	297.6	334.3	333.3
$r_{execute}$	$deg \cdot s^{-1}$	-1.76	-1.69	1.76	1.57
r_{stc}	$deg \cdot s^{-1}$	-1.08	-1.21	1.08	1.08
$r_{residual}$	$deg \cdot s^{-1}$	-	-0.48	-	0.37
$r_{residual}/r_{stc}$	-	-	0.40	-	0.34
V_{stc}	kn	7.3	8.5	7.3	8.9
V_{stc}/V_0	-	0.41	0.46	0.41	0.49
$\phi_{max,in}$	deg	0.0	-2.0	0.0	2.1
$\phi_{max,out}$	deg	0.0	3.0	0.0	-3.3
ϕ_{stc}	deg	0.0	-0.9	0.0	0.2
ϕ_{stc}/ϕ_{max}	-	-	-0.29	-	-0.06
Drift angle during turn (β_{stc})	deg	21.3	17.5	-21.3	-15.7
D_{stc}/L_{pp} ratio	-	2.60	2.68	2.60	3.16
AD/L_{pp} ratio	-	3.15	3.02	3.15	3.35
TD/L_{pp} ratio	-	-3.27	3.14	3.27	3.42

clear columns contain CFD results

gray columns contain experimental results

TURNING CIRCLE 15° PS/SB, V_0 = 18 kn

DESIGNATION	UNIT	MAGNITUDE			
TestNo	-	CFD	104025	CFD	104024
Approach speed V_0	kn	18.00	18.00	18.00	18.50
Steering angle (δ)	deg	15.00	15.00	-15.00	-15.00
Advance (AD)	m	588.4	560.1	588.4	630.3
Transfer (TR)	m	-271.8	265.1	271.8	300.5
Tactical diameter (TD)	m	-638.2	614.2	638.2	681.3
D_{stc}	m	571.2	577.8	571.4	662.7
T_{90}	s	84.0	82.3	84.0	91.3
T_{180}	s	161.8	160.4	161.8	175.7
T_{360}	s	335.8	331.3	335.8	358.4
T_{stc}	s	354.3	336.0	354.3	373.8
$r_{execute}$	deg·s^{-1}	-1.44	-1.42	1.44	1.28
r_{stc}	deg·s^{-1}	-1.02	-1.07	1.02	0.96
$r_{residual}$	deg·s^{-1}	-	-0.62	-	0.40
$r_{residual}/r_{stc}$	-	-	0.58	-	0.42
V_{stc}	kn	9.8	10.5	9.8	10.8
V_{stc}/V_0	-	0.55	0.58	0.55	0.59
$\phi_{max,in}$	deg	0.0	-1.4	0.0	1.3
$\phi_{max,out}$	deg	0.0	3.2	0.0	-3.2
ϕ_{stc}	deg	0.0	-0.3	0.0	-0.7
ϕ_{stc}/ϕ_{max}	-	-	-0.09	-	0.20
Drift angle during turn (β_{stc})	deg	14.9	13.5	-14.9	-12.4
D_{stc}/L_{pp} ratio	-	3.72	3.76	3.72	4.31
AD/L_{pp} ratio	-	3.83	3.64	3.83	4.10
TD/L_{pp} ratio	-	-4.15	4.00	4.15	4.43

clear columns contain CFD results

gray columns contain experimental results

Page intentionally left blank

ZIG-ZAG 10°/10° PS, V_0 = 10 kn, TIMESERIES

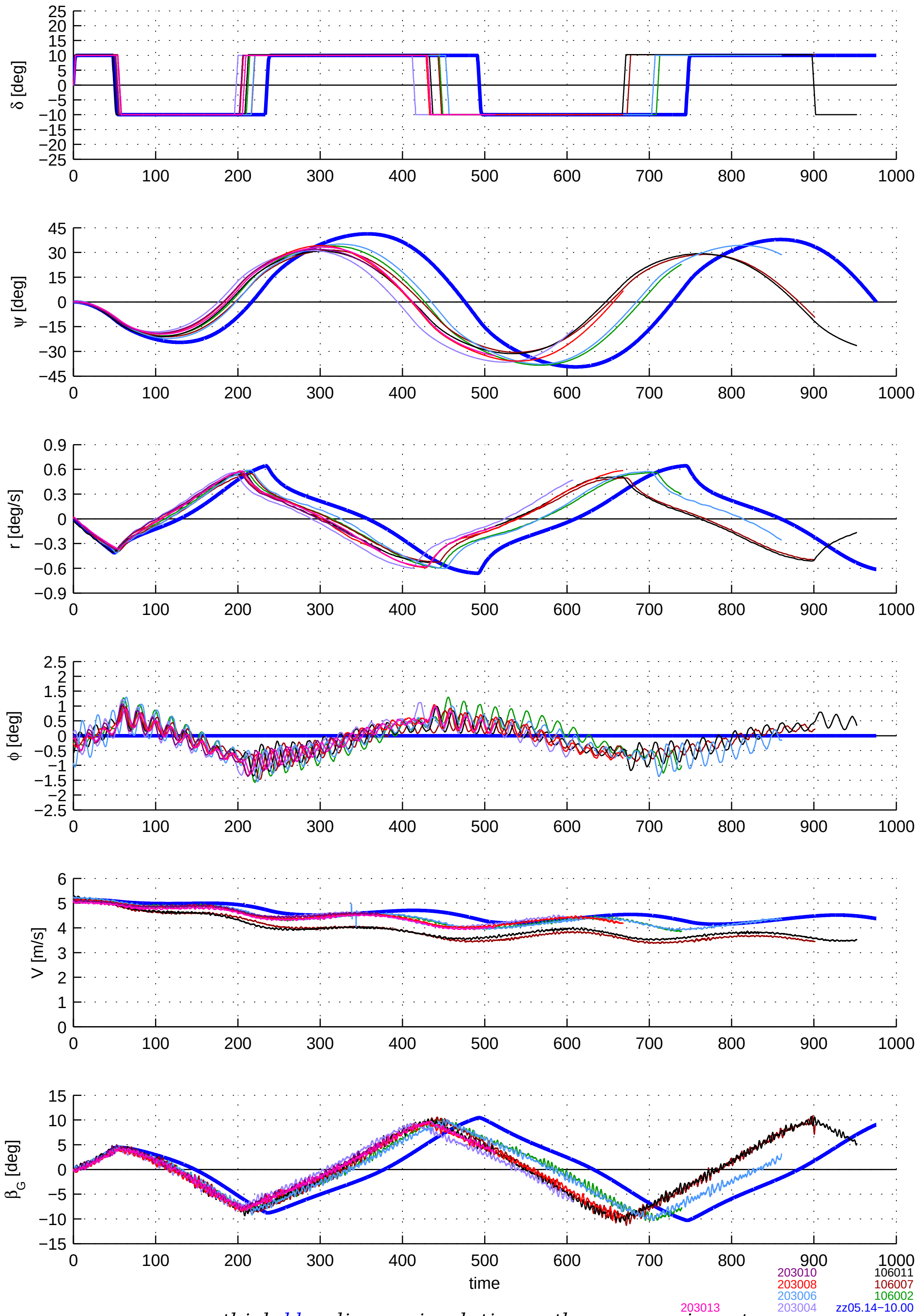

thick blue lines: simulation, others: experiments

ZIG-ZAG 10°/10° PS, V_0 = 10 kn, TRACK

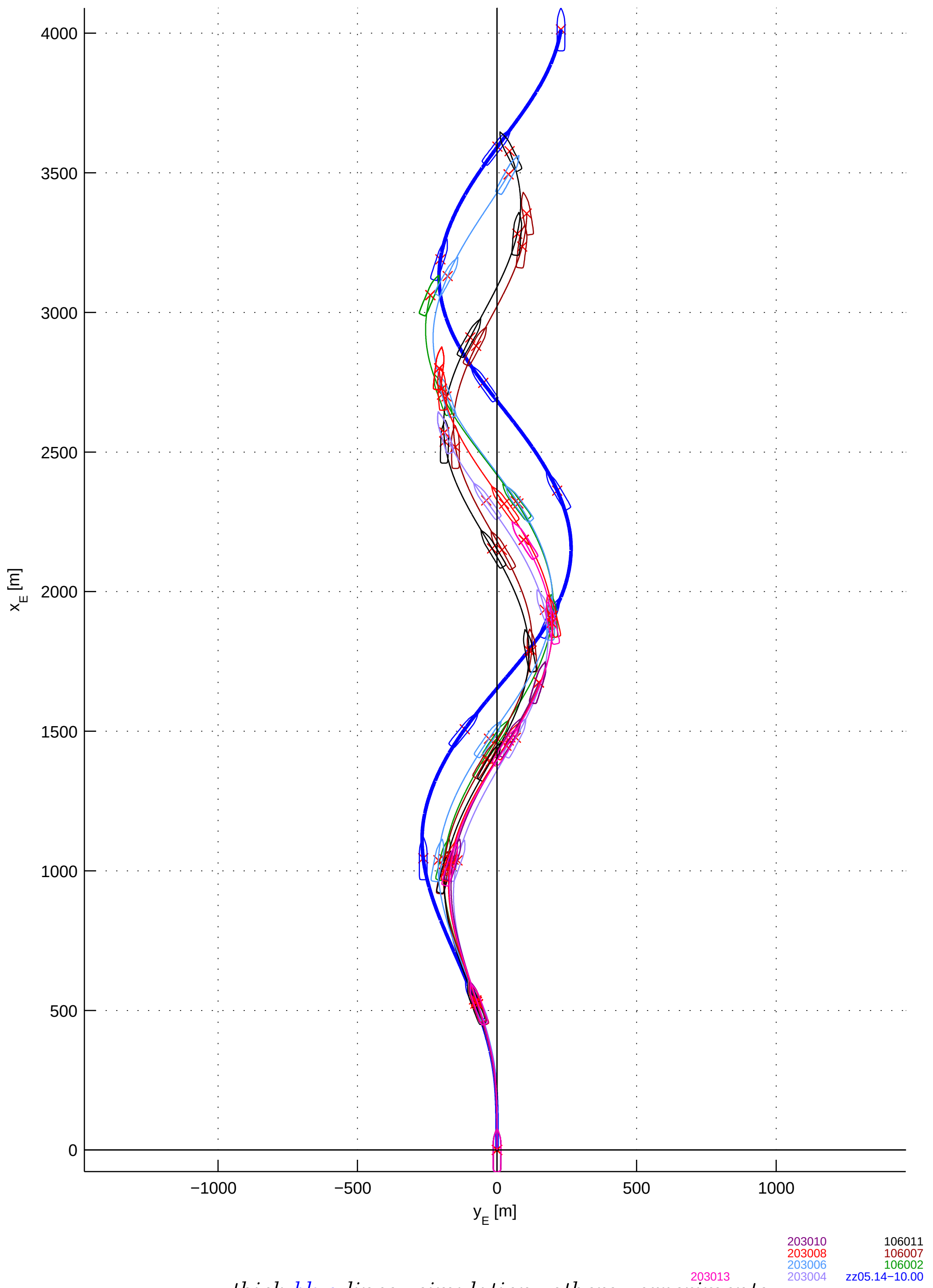

thick blue lines: simulation, others: experiments

ZIG-ZAG 10°/10° SB, V_0 = 10 kn, TIMESERIES

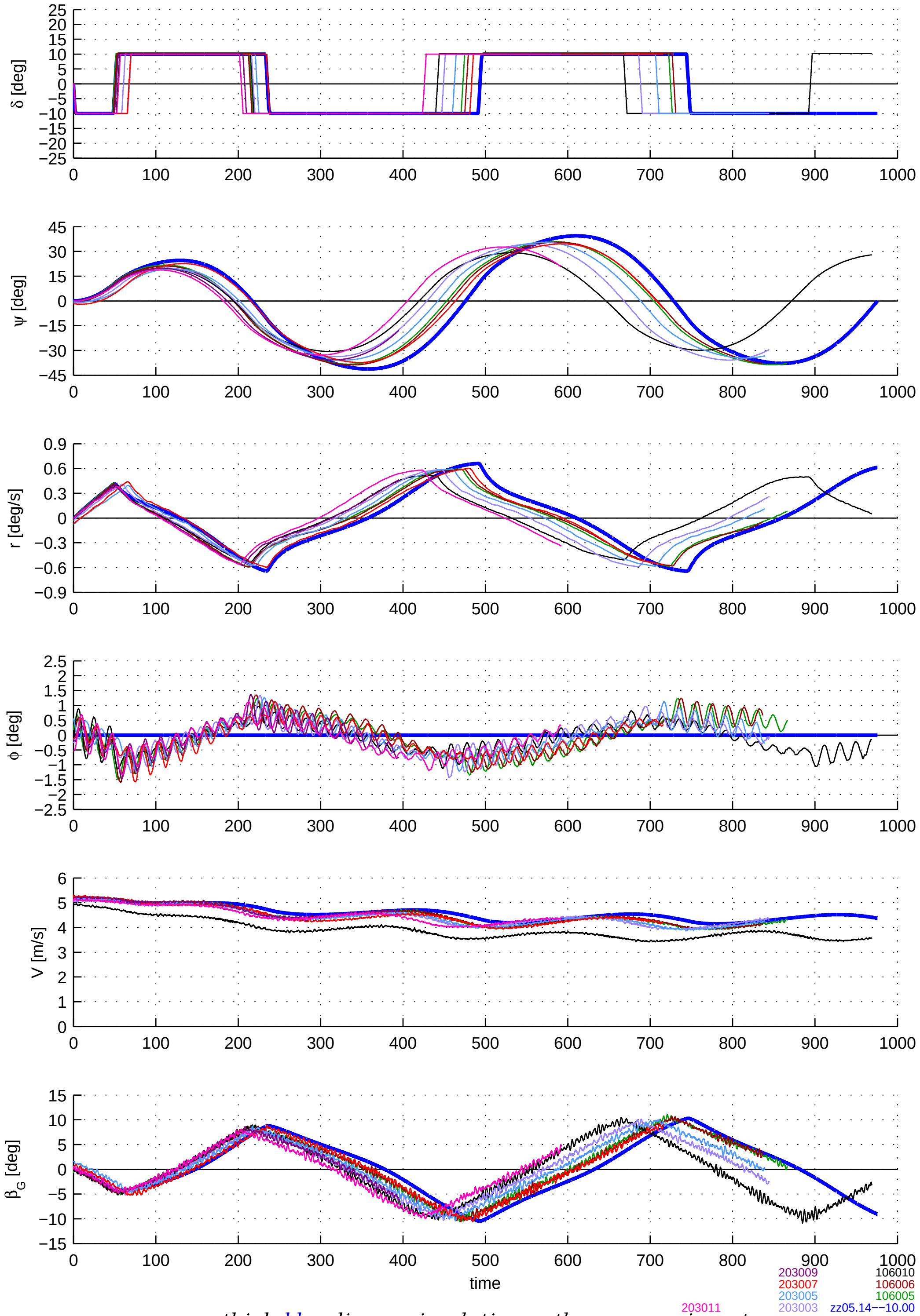

thick blue lines: simulation, others: experiments

ZIG-ZAG 10°/10° SB, V_0 = 10 kn, TRACK

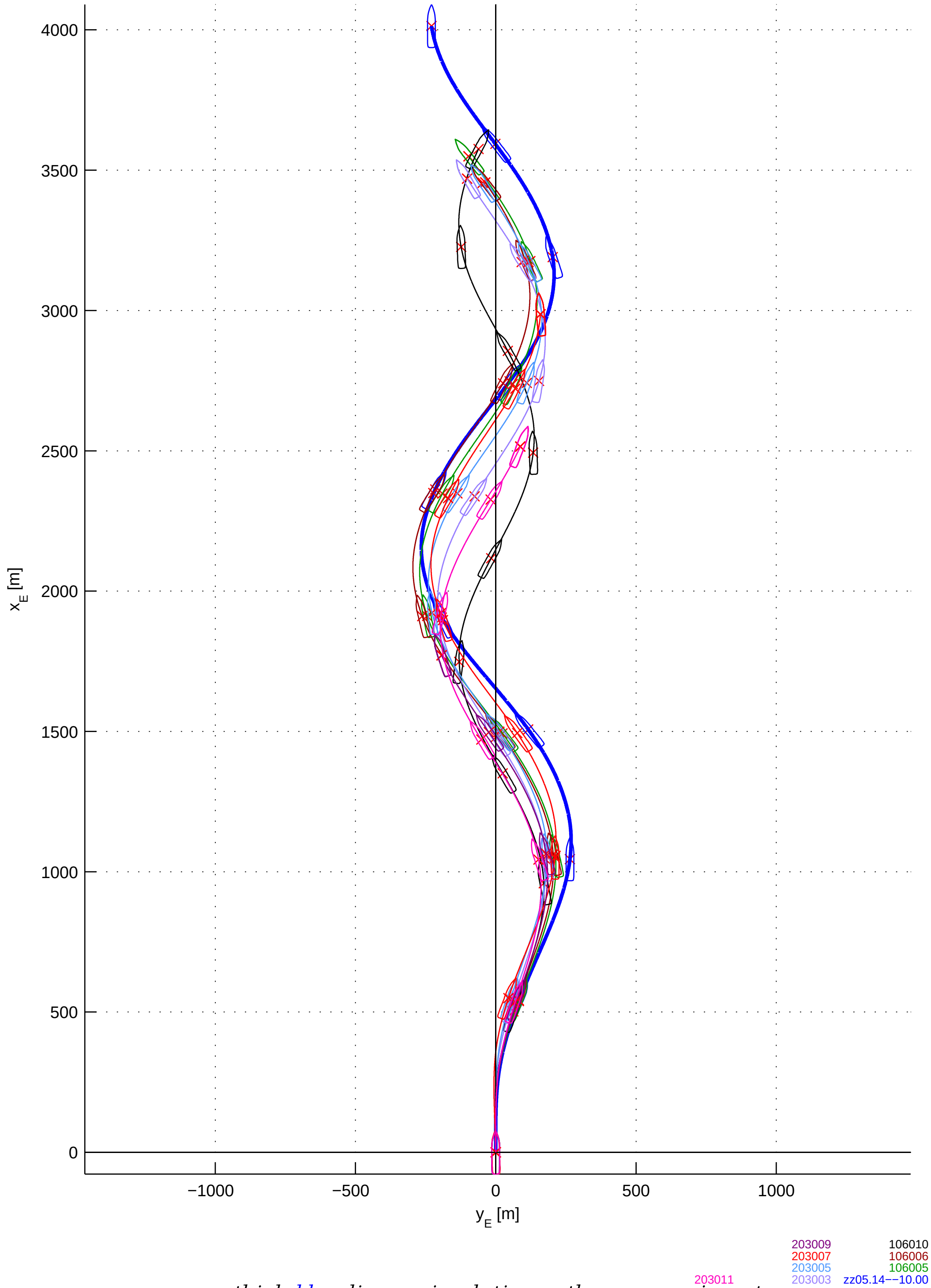

thick blue lines: simulation, others: experiments

ZIG-ZAG 20°/20° PS, V_0 = 10 kn, TIMESERIES

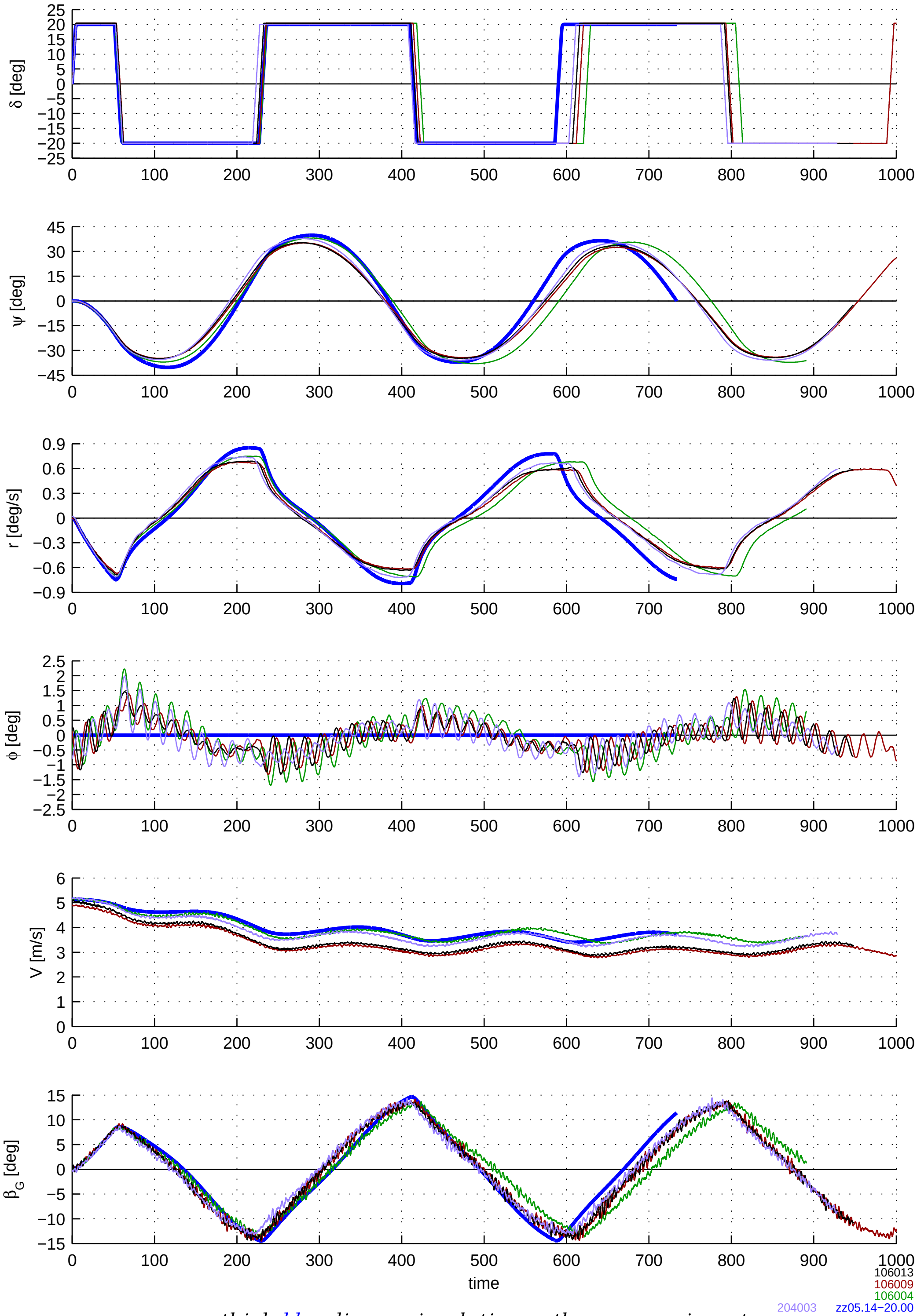

thick blue lines: simulation, others: experiments

ZIG-ZAG 20°/20° PS, V_0 = 10 kn, TRACK

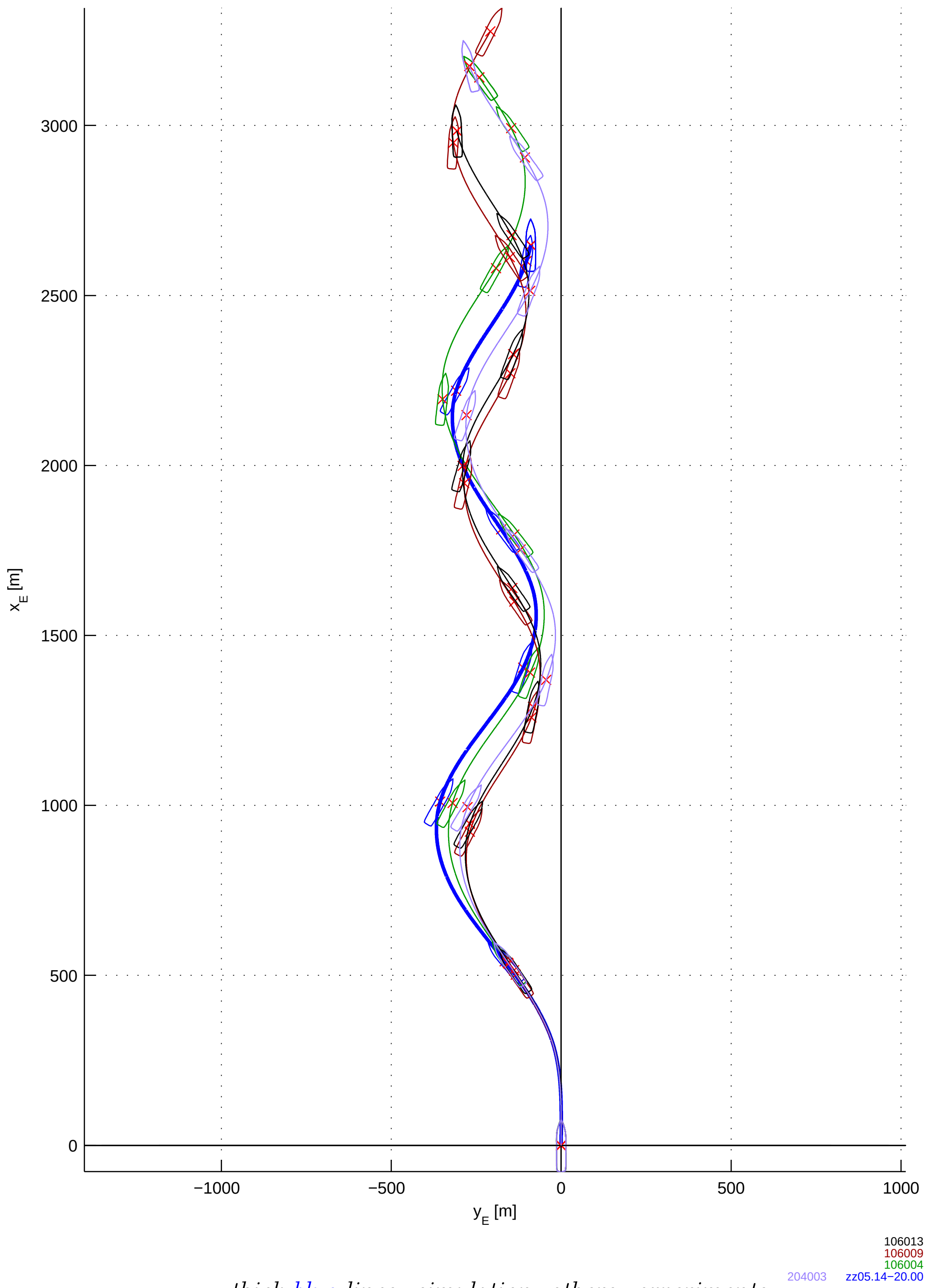

thick blue lines: simulation, others: experiments

ZIG-ZAG 20°/20° SB, V_0 = 10 kn, TIMESERIES

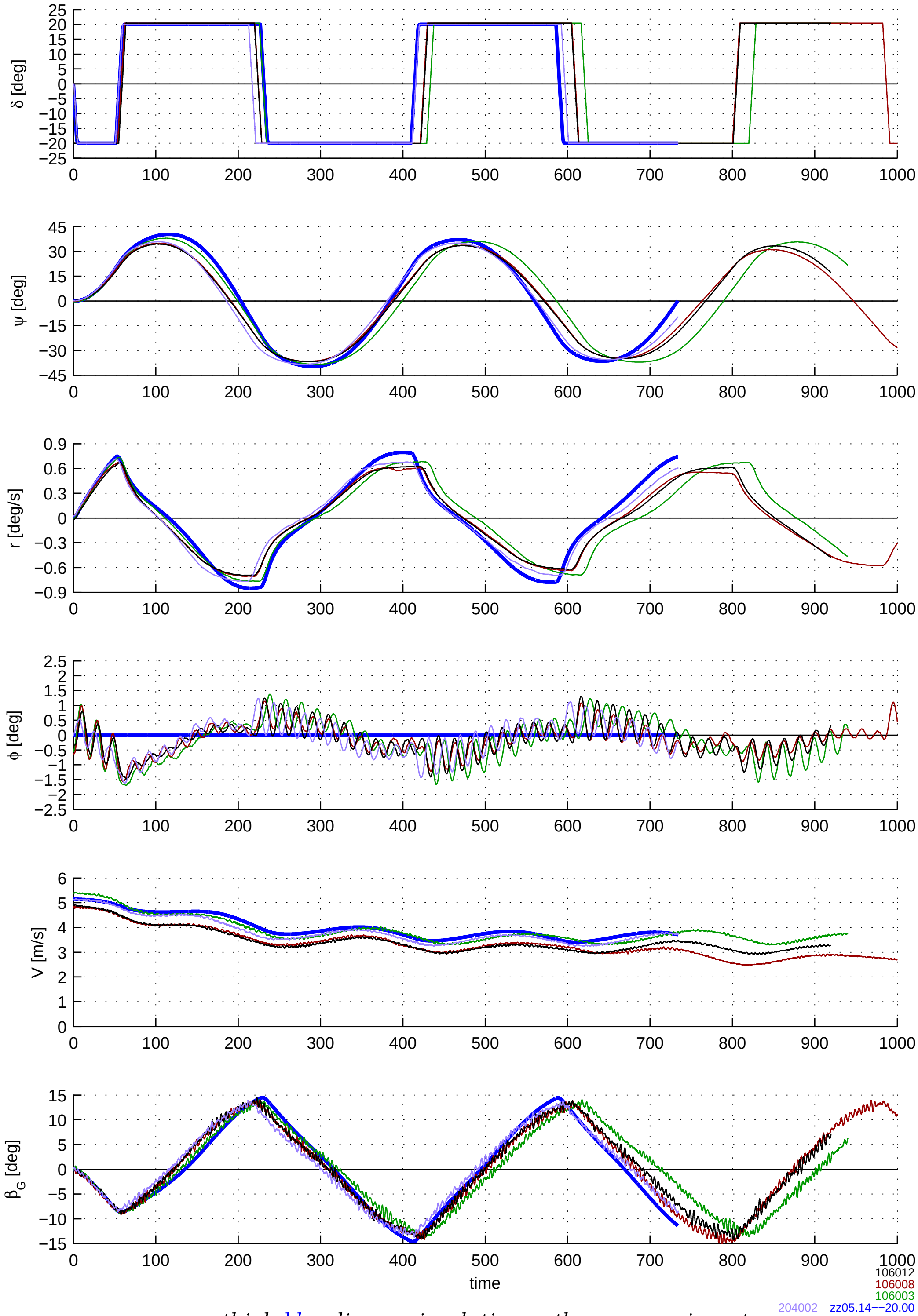

thick blue lines: simulation, others: experiments

ZIG-ZAG 20°/20° SB, V_0 = 10 kn, TRACK

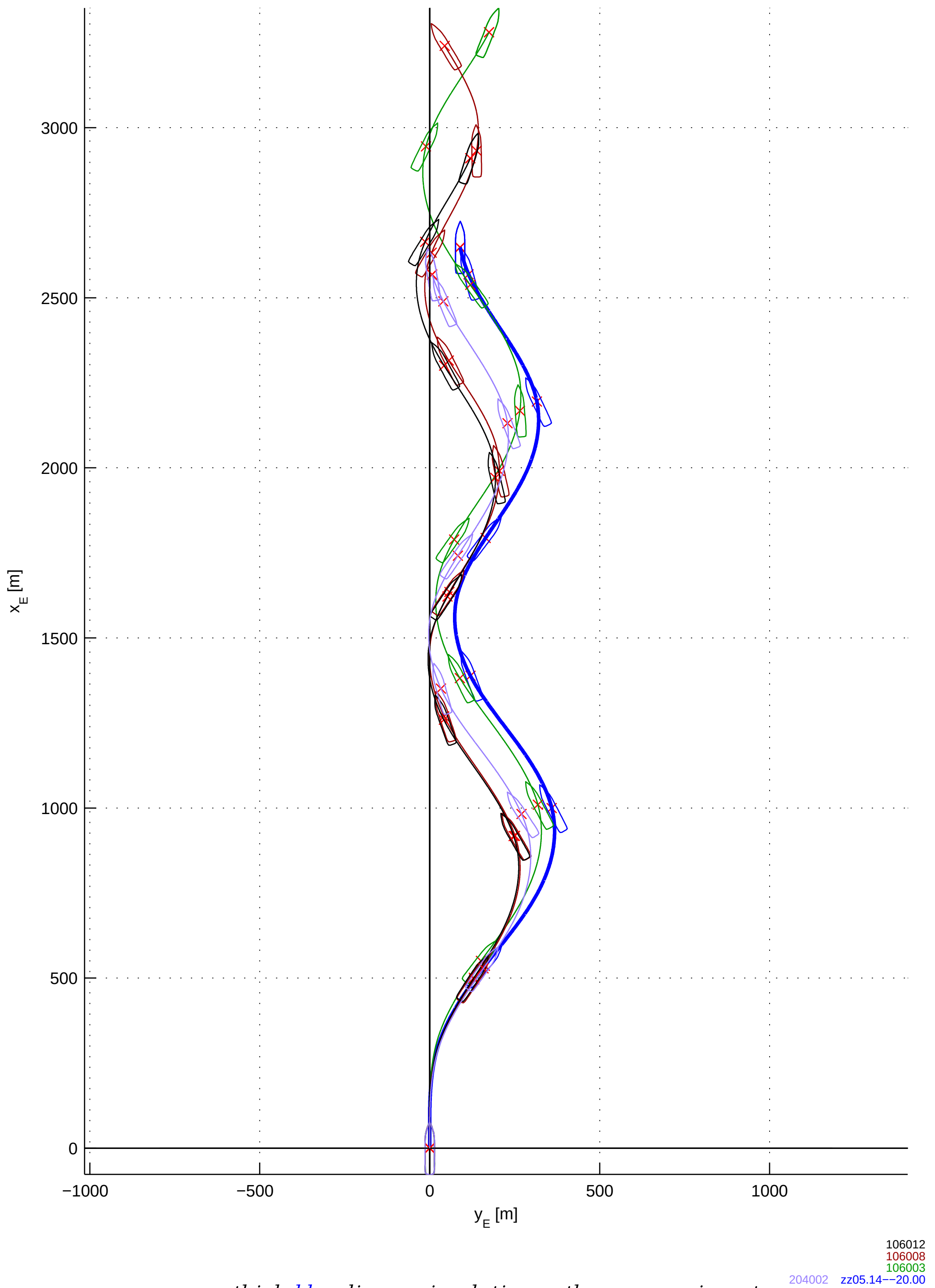

thick blue lines: simulation, others: experiments

ZIG-ZAG 10°/10° PS, V_0 = 18 kn, TIMESERIES

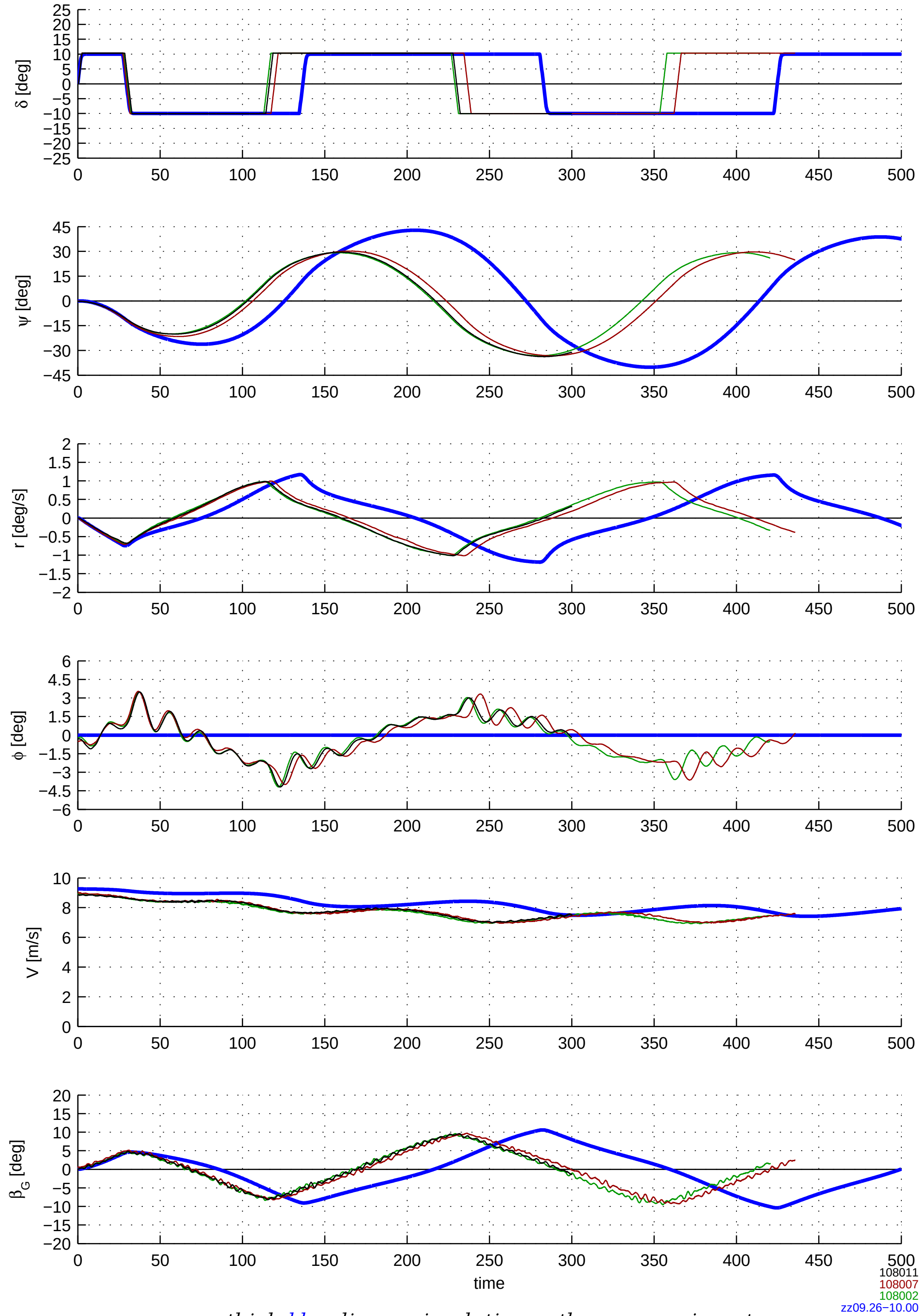

thick blue lines: simulation, others: experiments

ZIG-ZAG 10°/10° PS, V_0 = 18 kn, TRACK

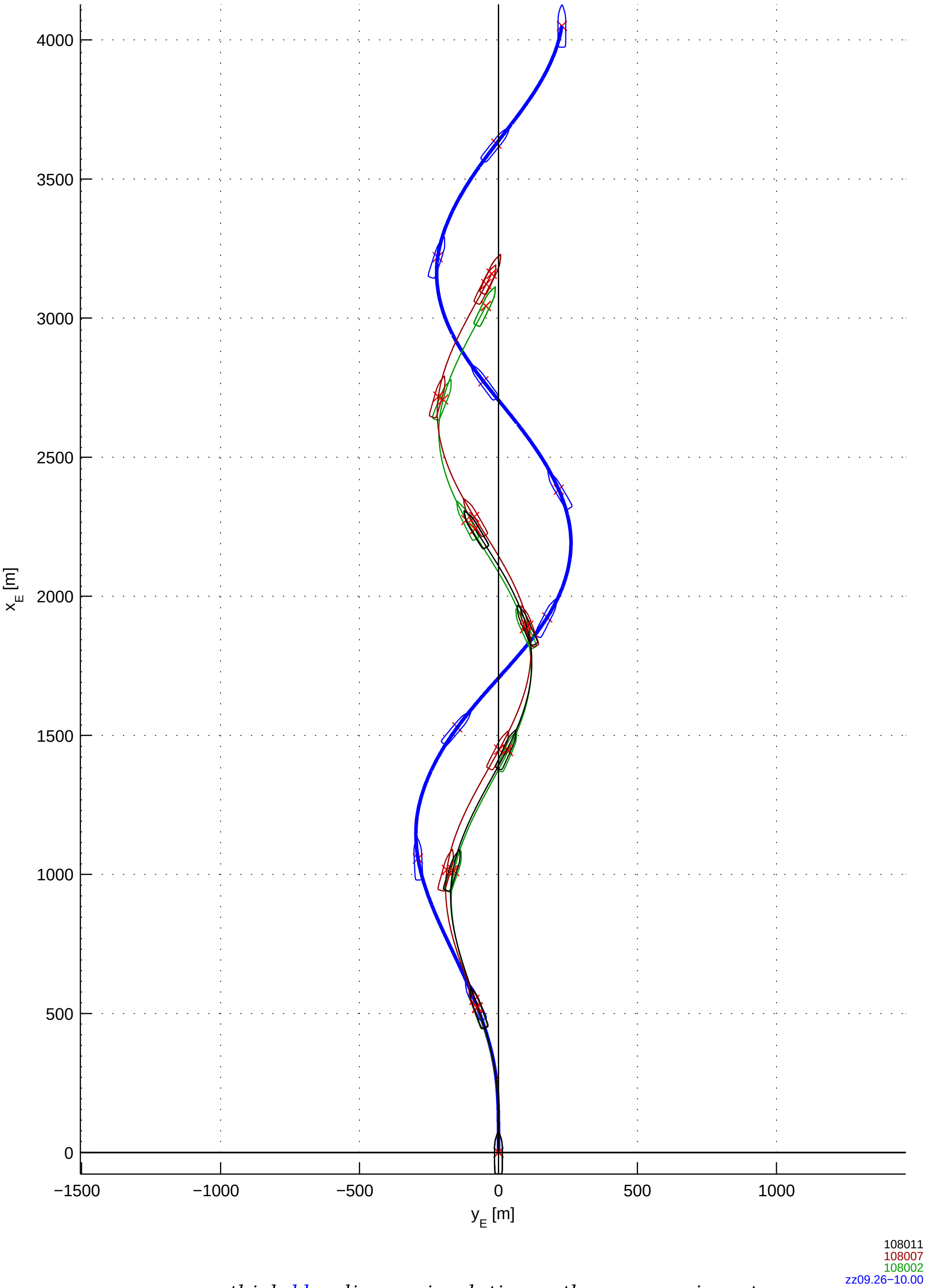

thick blue lines: simulation, others: experiments

ZIG-ZAG 10°/10° SB, V_0 = 18 kn, TIMESERIES

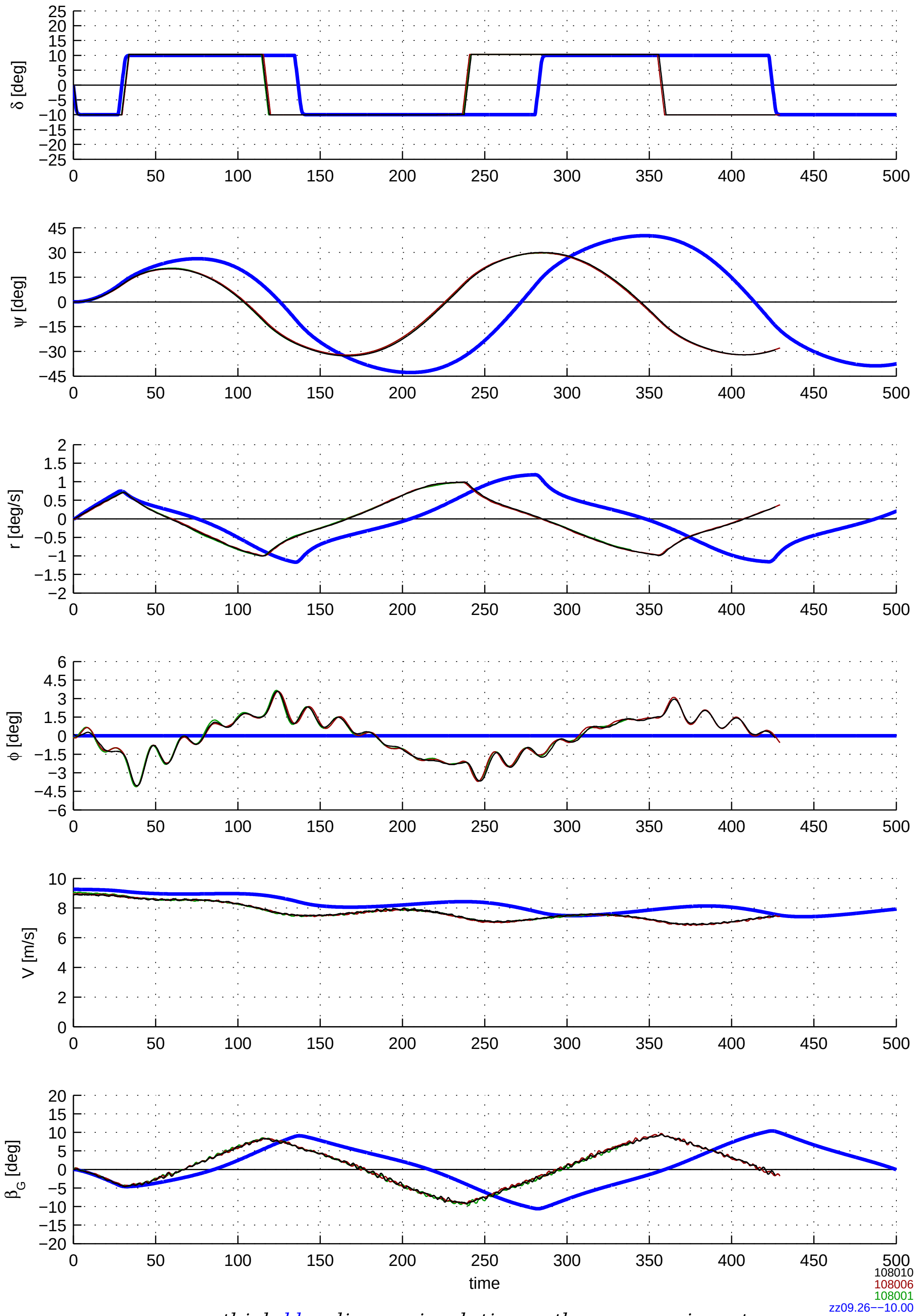

thick blue lines: simulation, others: experiments

ZIG-ZAG 10°/10° SB, V_0 = 18 kn, TRACK

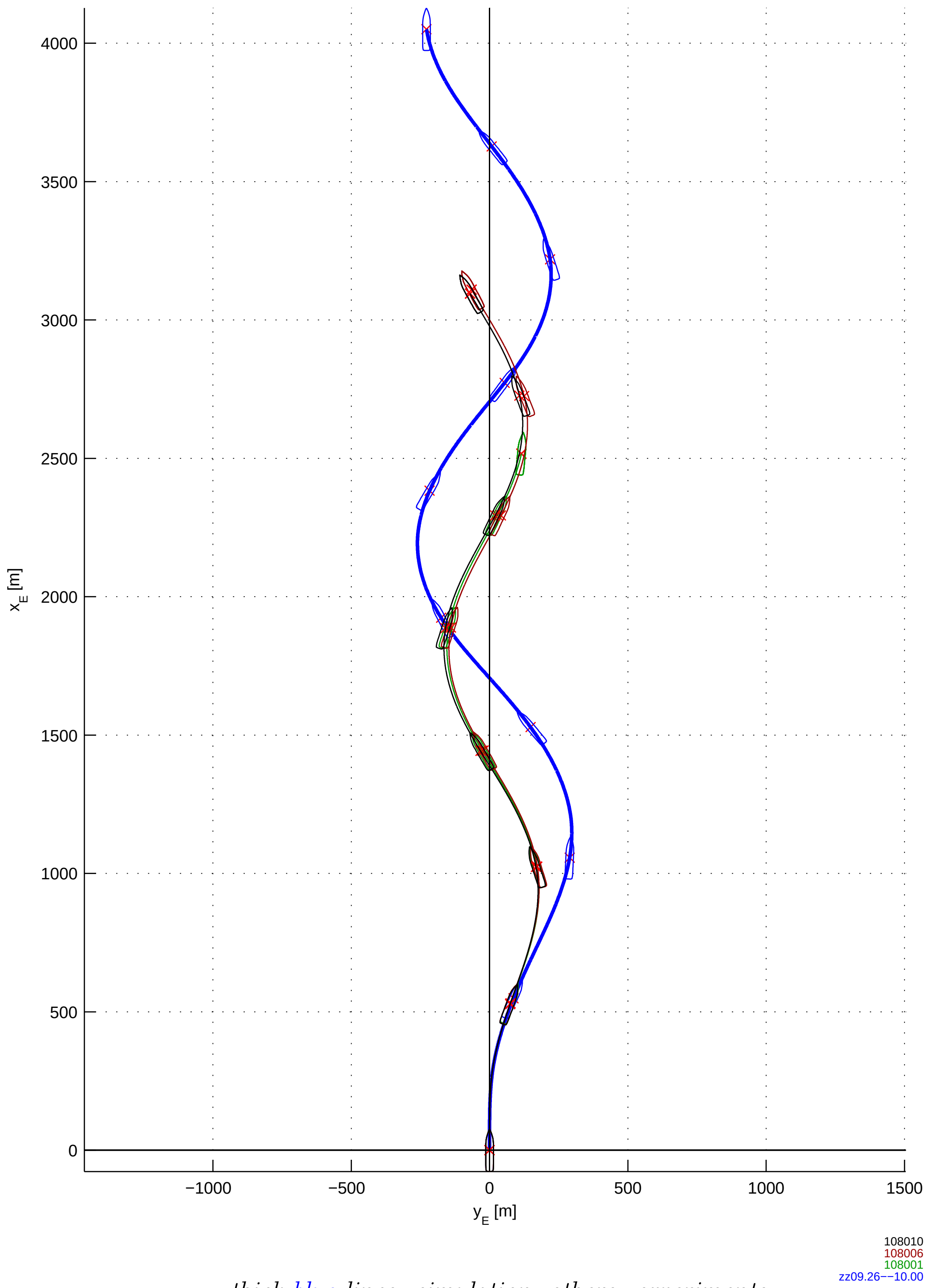

thick blue lines: simulation, others: experiments

ZIG-ZAG 20°/20° PS, V_0 = 18 kn, TIMESERIES

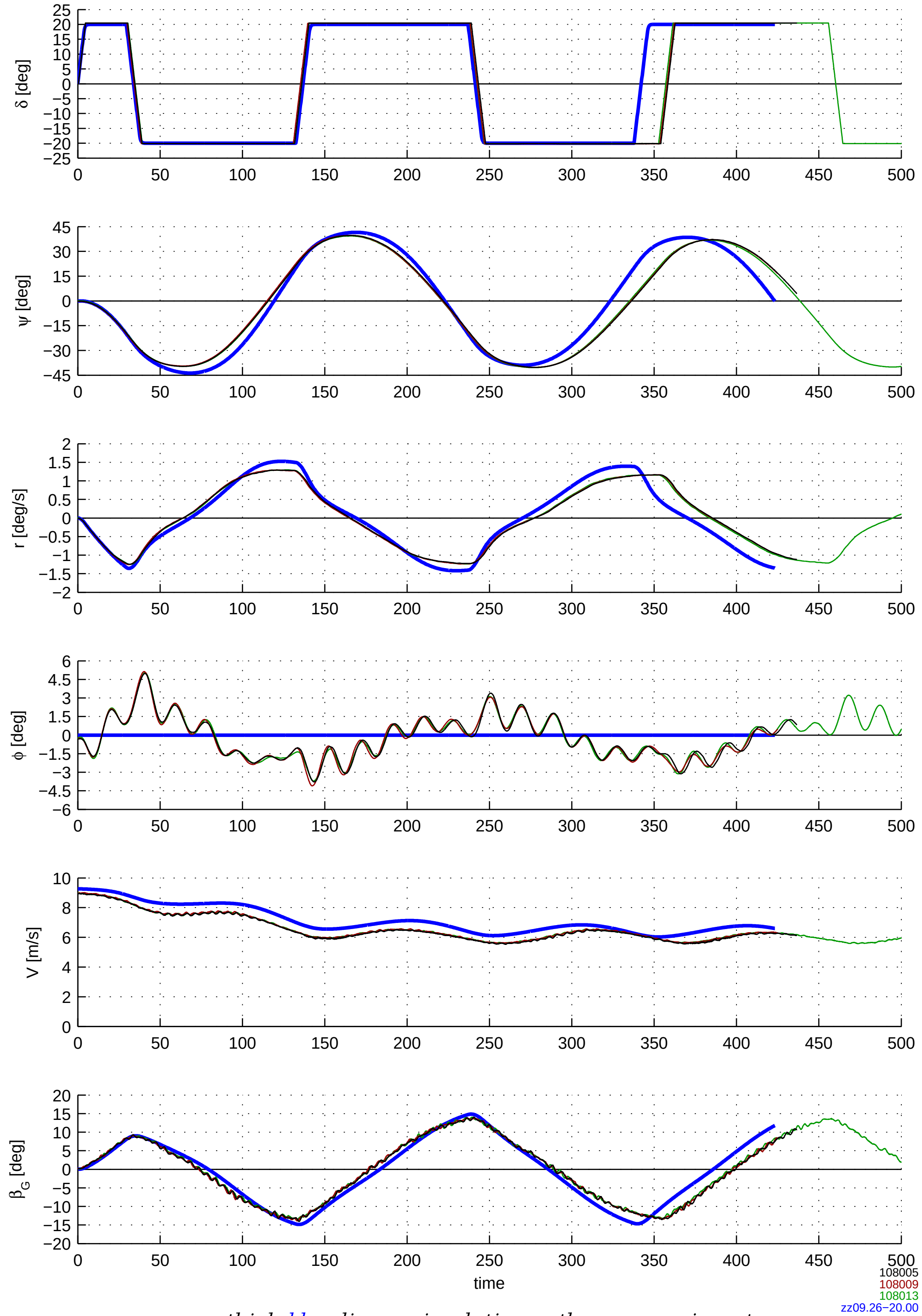

thick blue lines: simulation, others: experiments

ZIG-ZAG 20°/20° PS, V_0 = 18 kn, TRACK

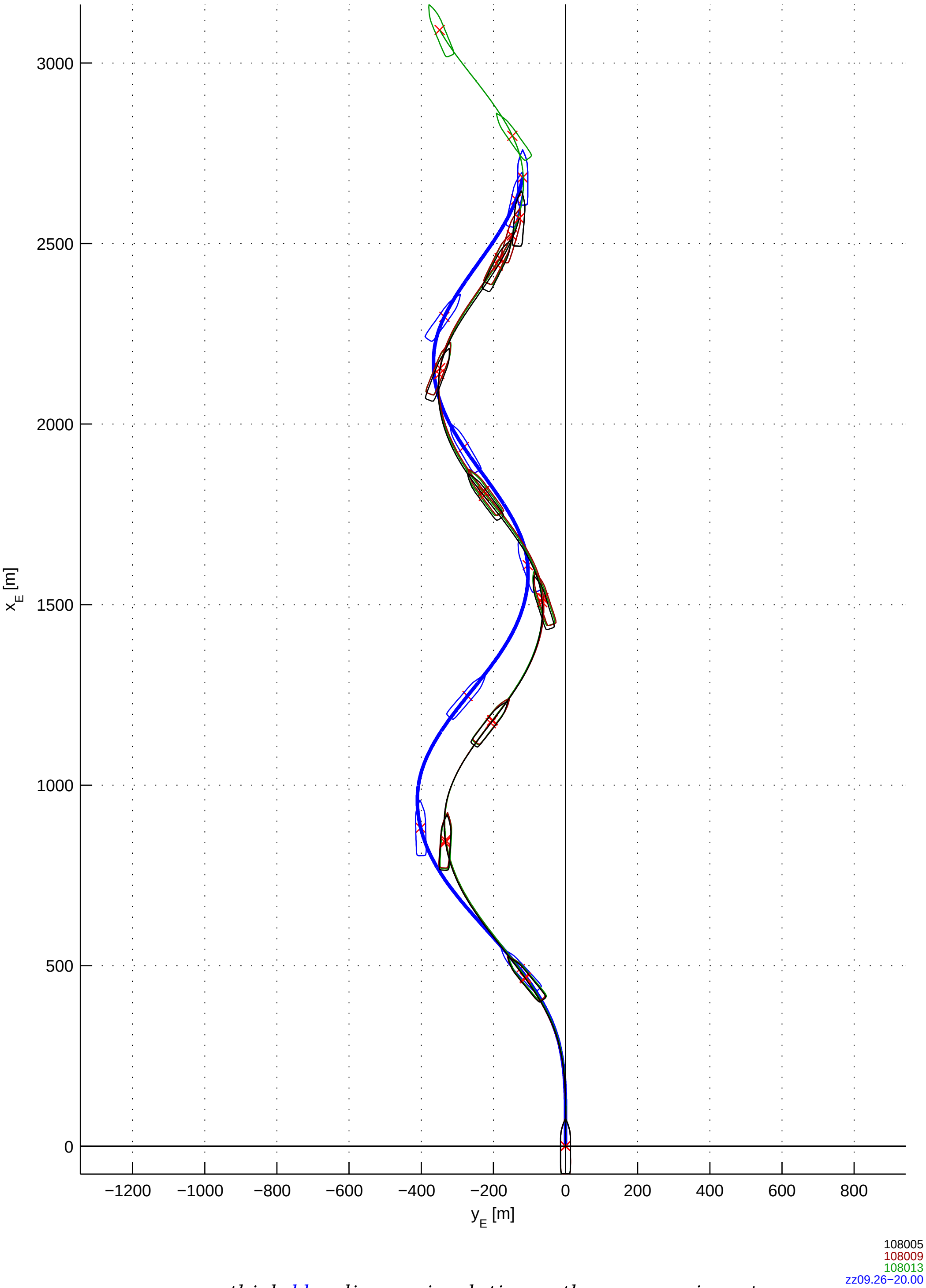

thick blue lines: simulation, others: experiments

ZIG-ZAG 20°/20° SB, V_0 = 18 kn, TIMESERIES

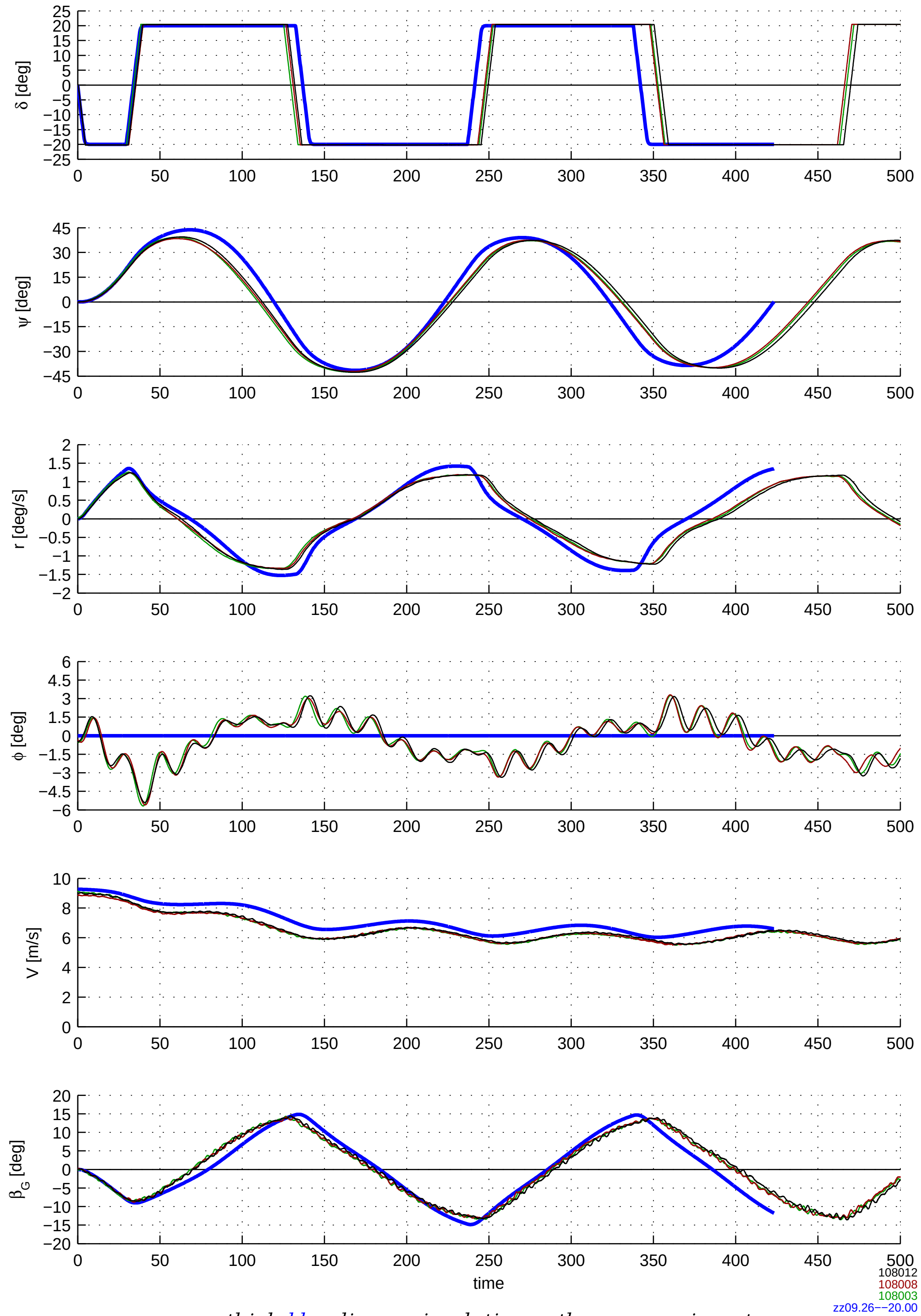

thick blue lines: simulation, others: experiments

ZIG-ZAG 20°/20° SB, V_0 = 18 kn, TRACK

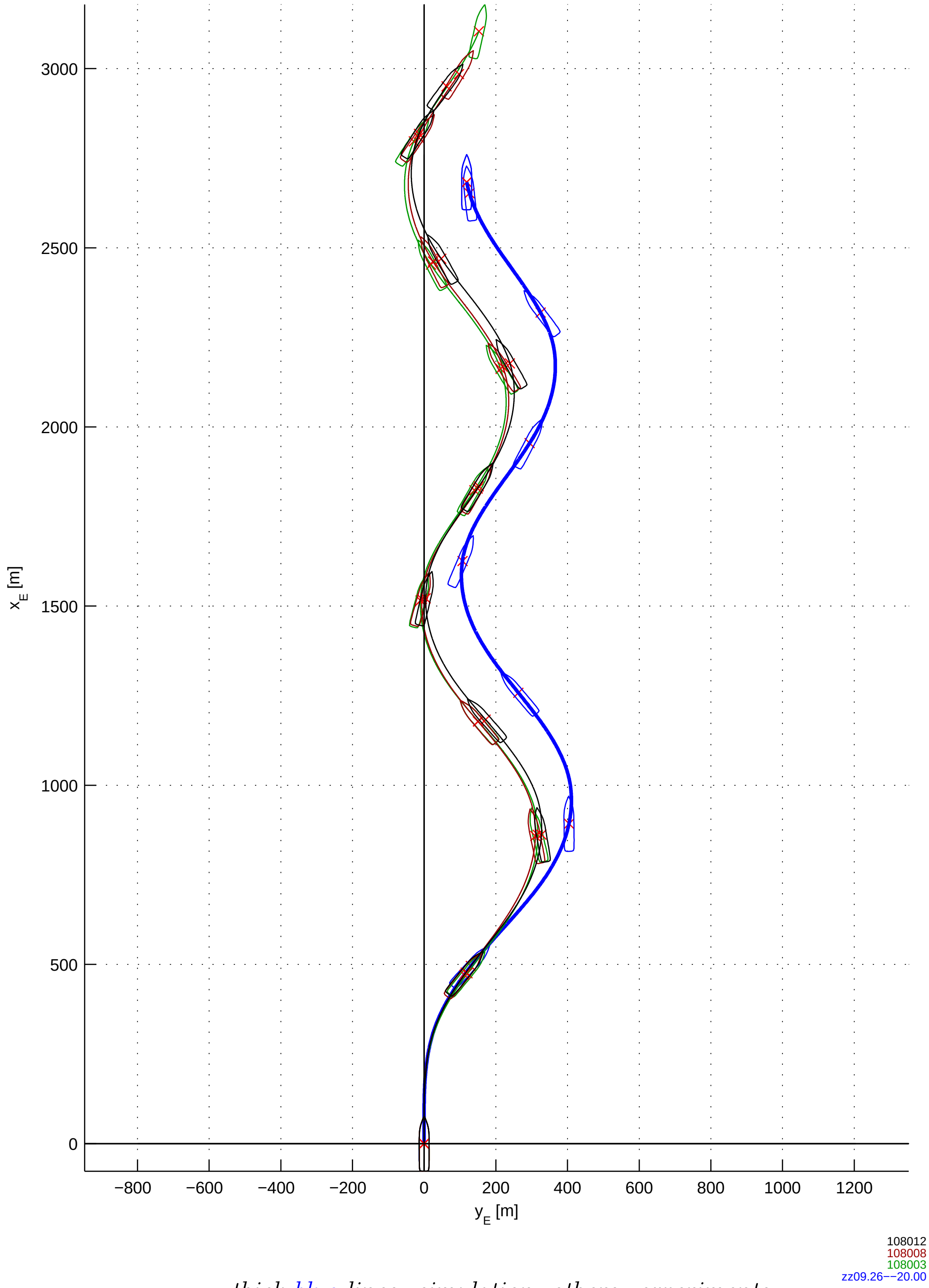

thick blue lines: simulation, others: experiments

TURNING CIRCLE 35° PS, V_0 = 10 kn, TIMESERIES

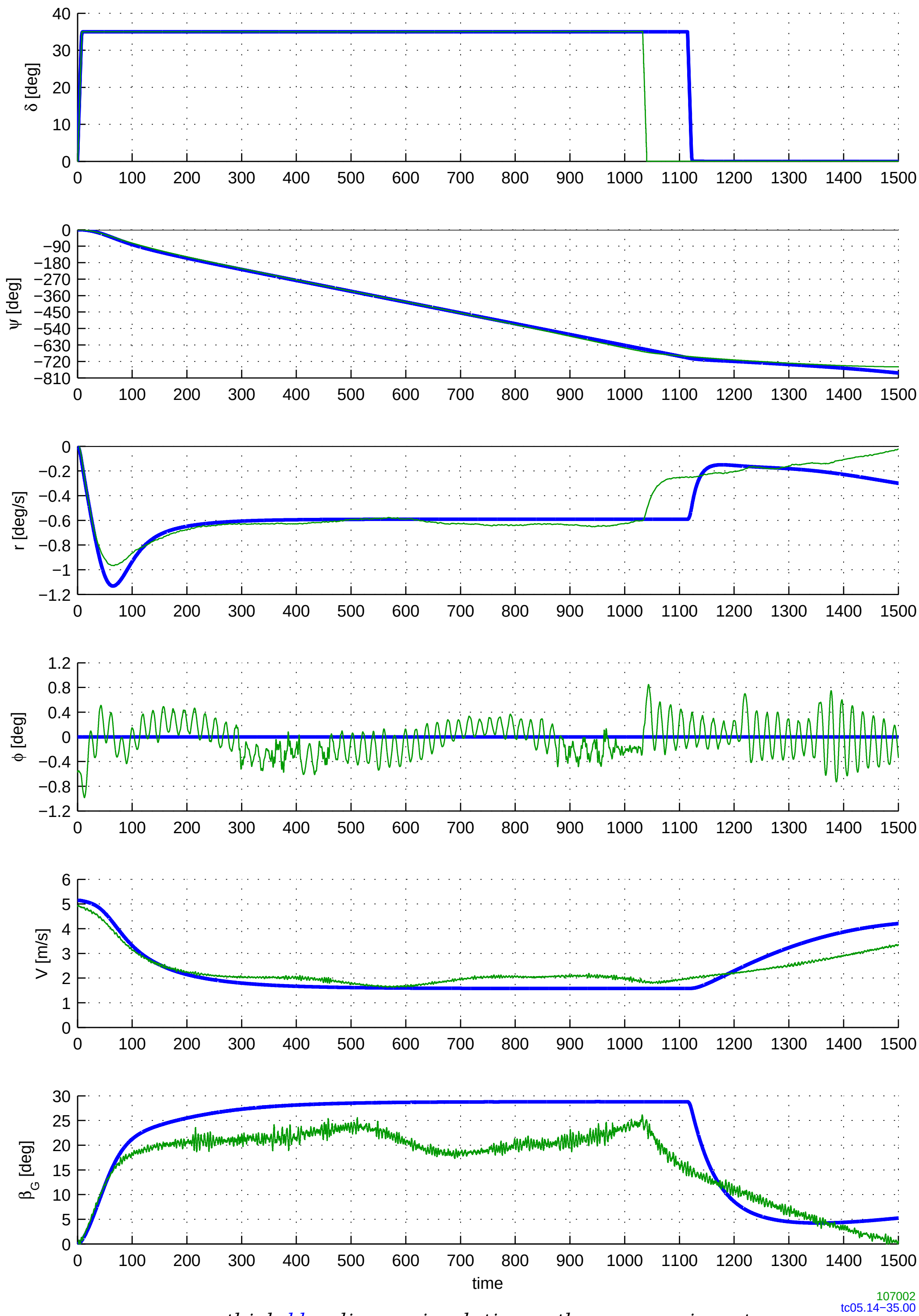

thick blue lines: simulation, others: experiments

TURNING CIRCLE 35° PS, V_0 = 10 kn, TRACK

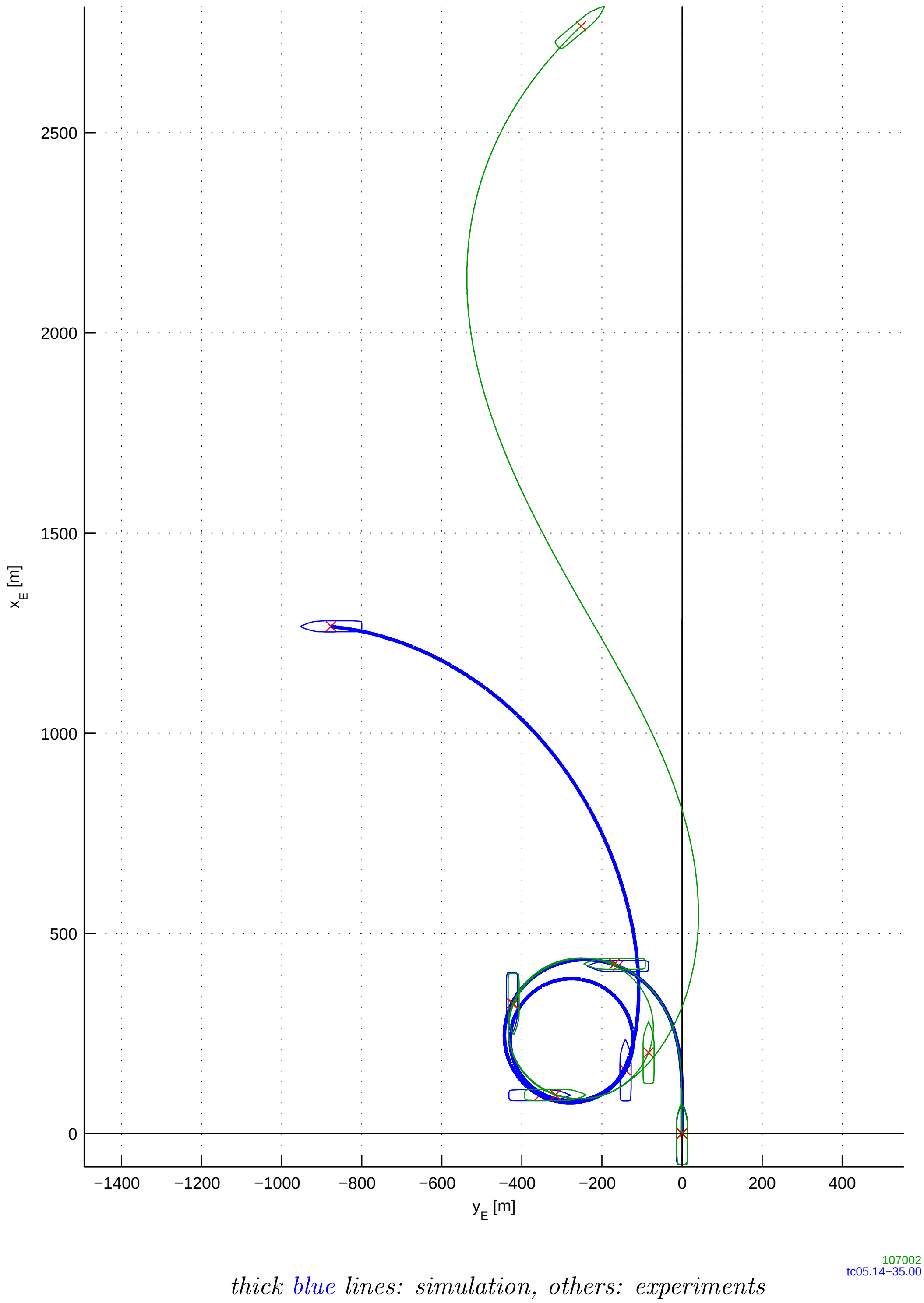

thick blue lines: simulation, others: experiments

TURNING CIRCLE 35° SB, $V_0 = 10$ kn, TIMESERIES

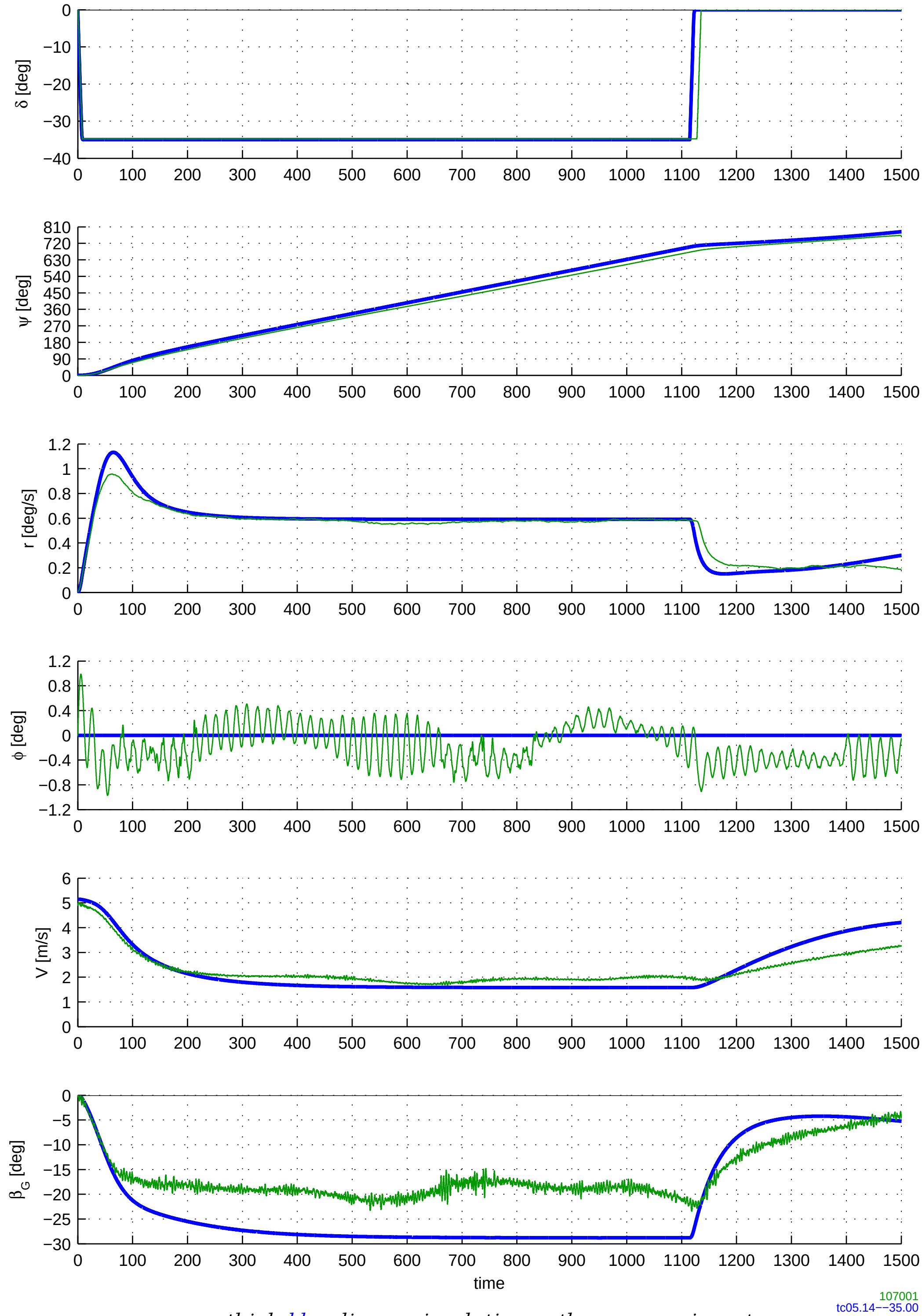

thick blue lines: simulation, others: experiments

TURNING CIRCLE 35° SB, V_0 = 10 kn, TRACK

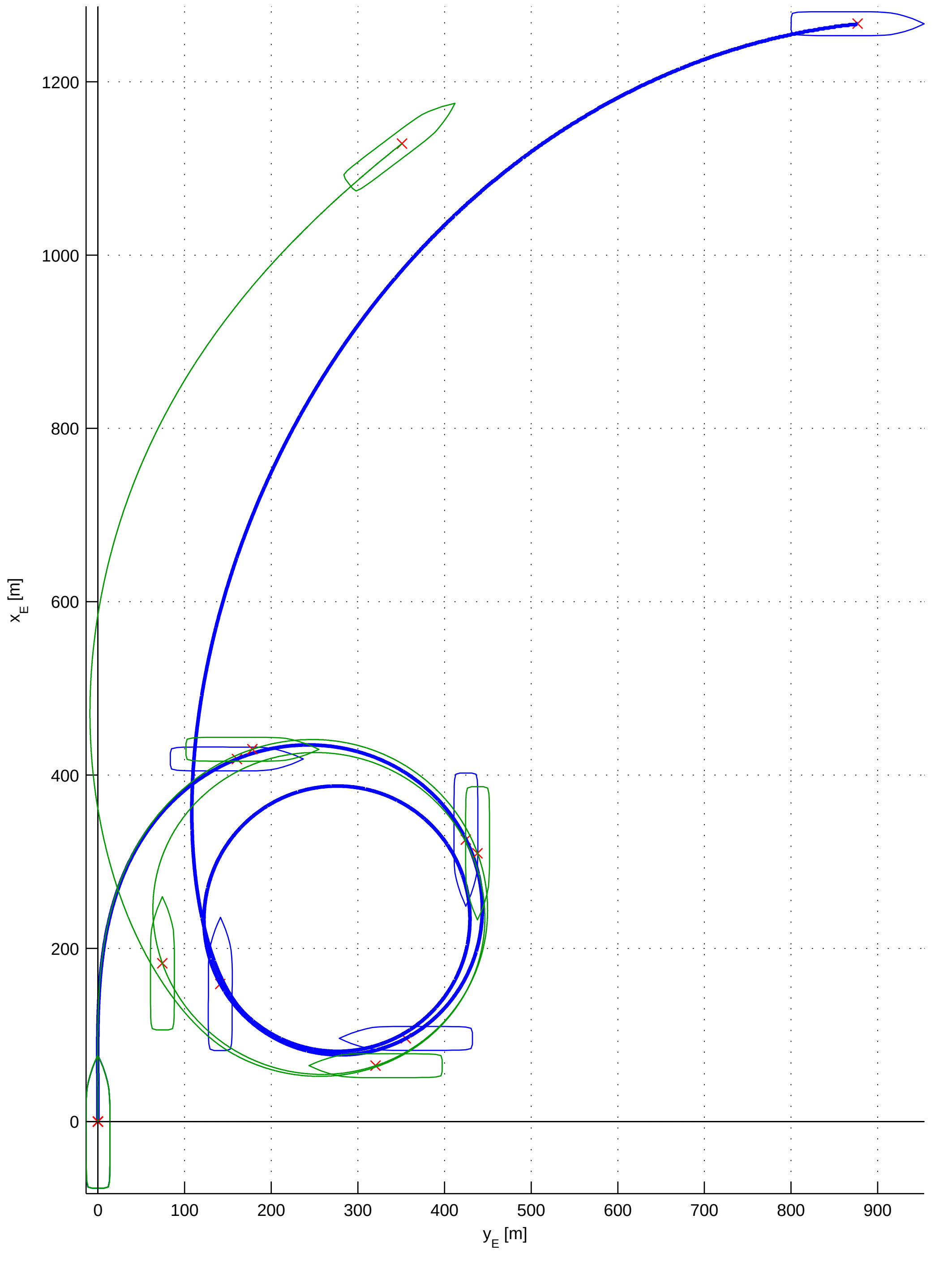

thick blue lines: simulation, others: experiments

TURNING CIRCLE 25° PS, V_0 = 10 kn, TIMESERIES

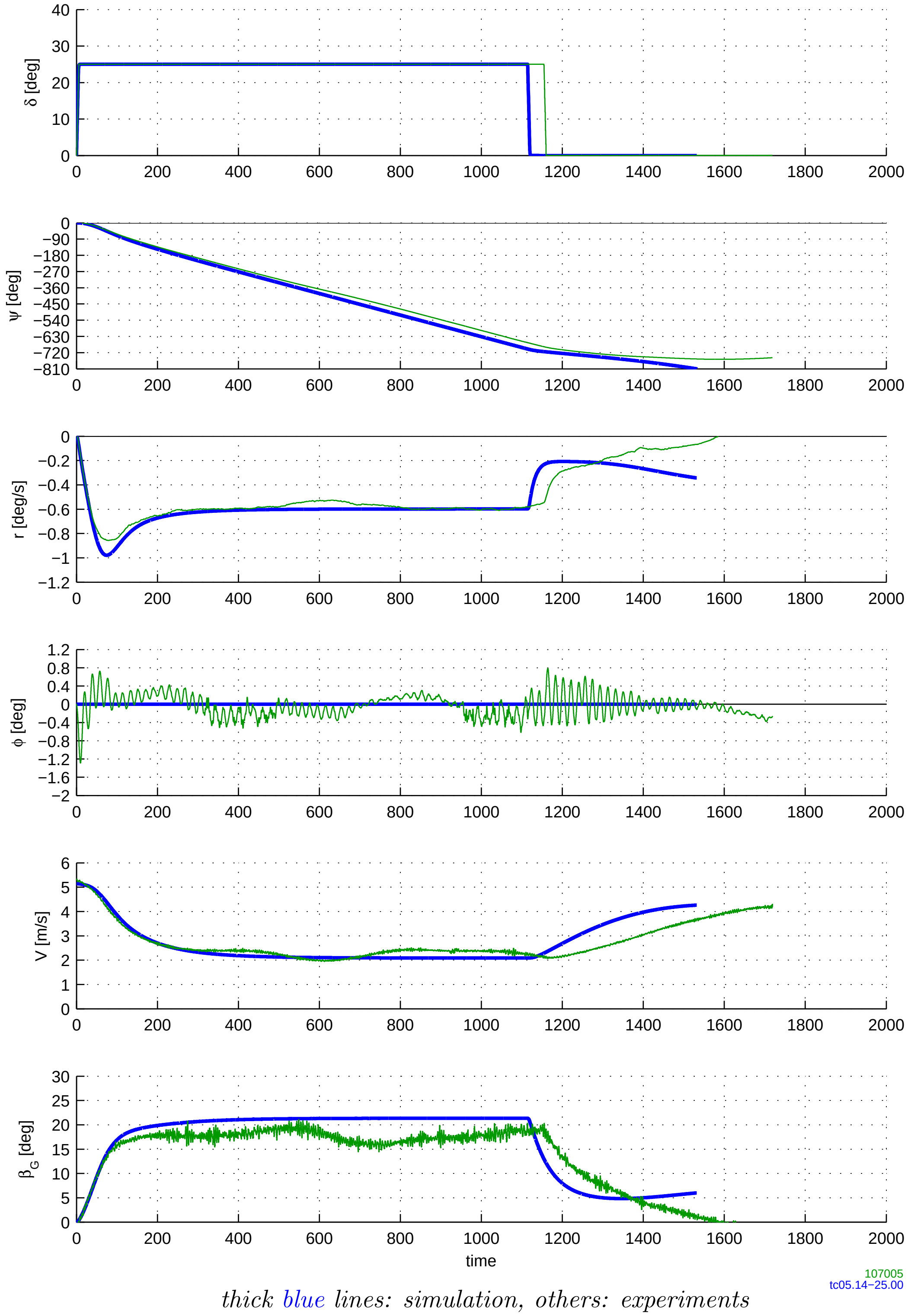

thick blue lines: simulation, others: experiments

TURNING CIRCLE 25° PS, V_0 = 10 kn, TRACK

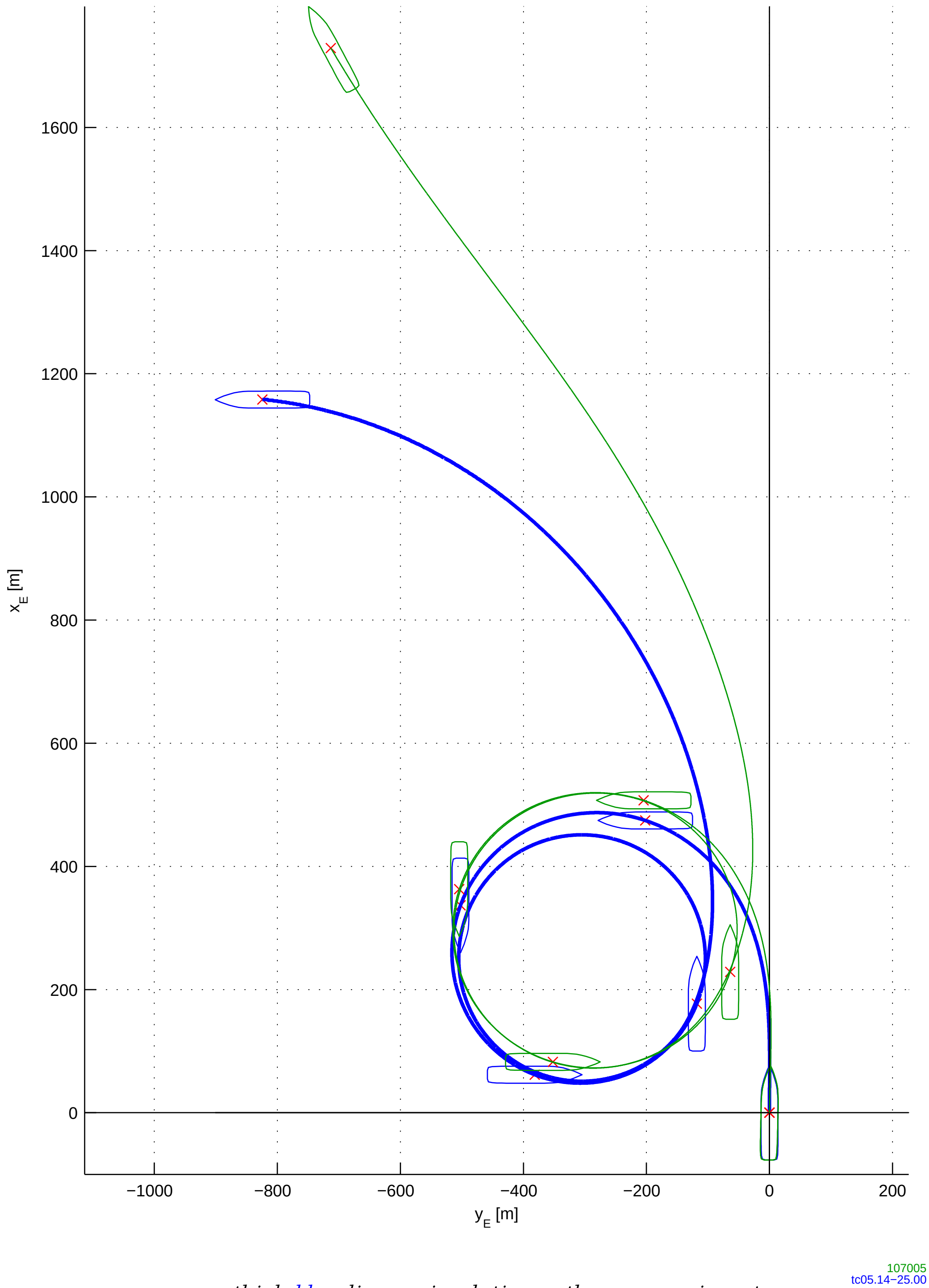

thick blue lines: simulation, others: experiments

TURNING CIRCLE 25° SB, V_0 = 10 kn, TIMESERIES

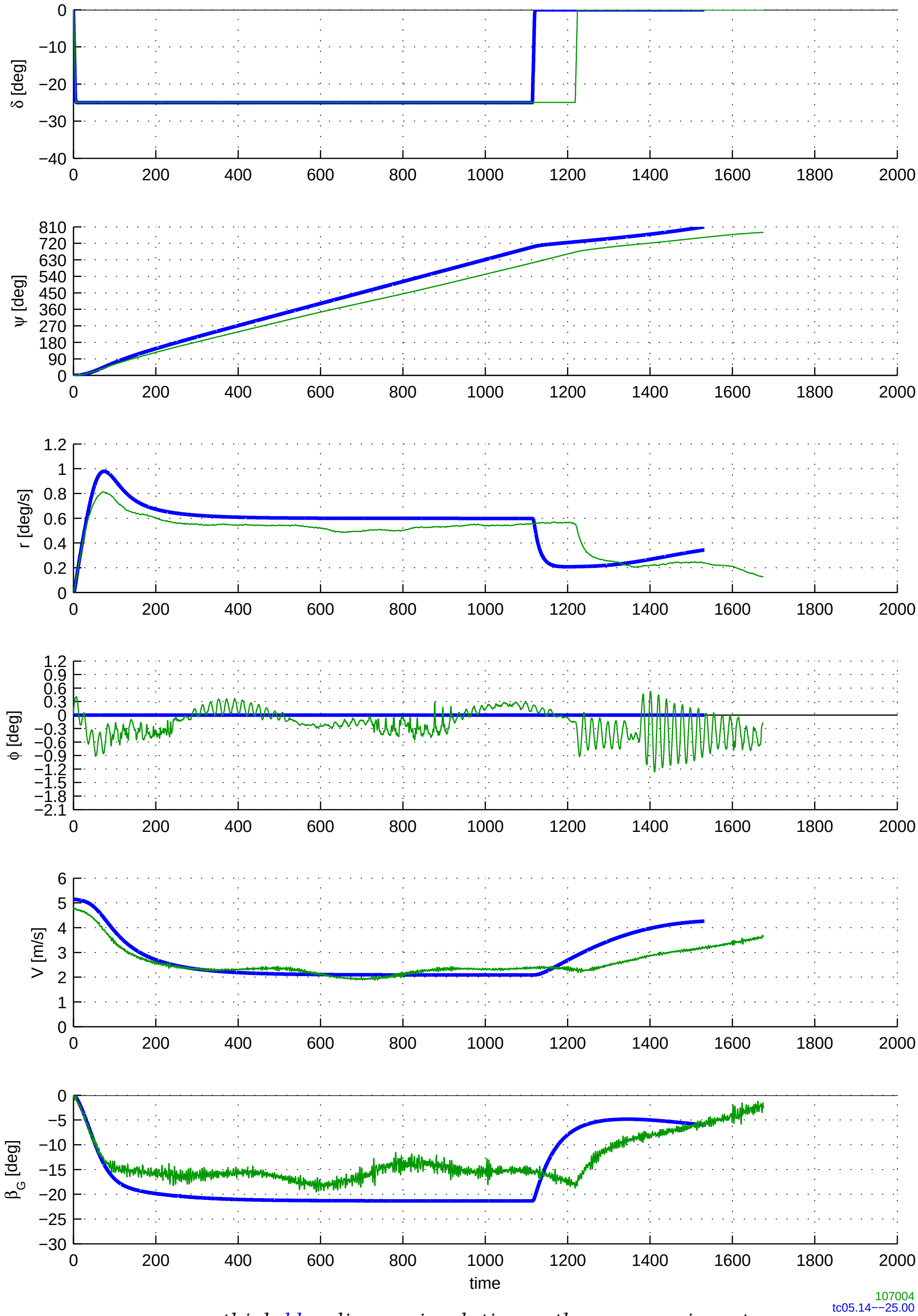

thick blue lines: simulation, others: experiments

TURNING CIRCLE 25° SB, V_0 = 10 kn, TRACK

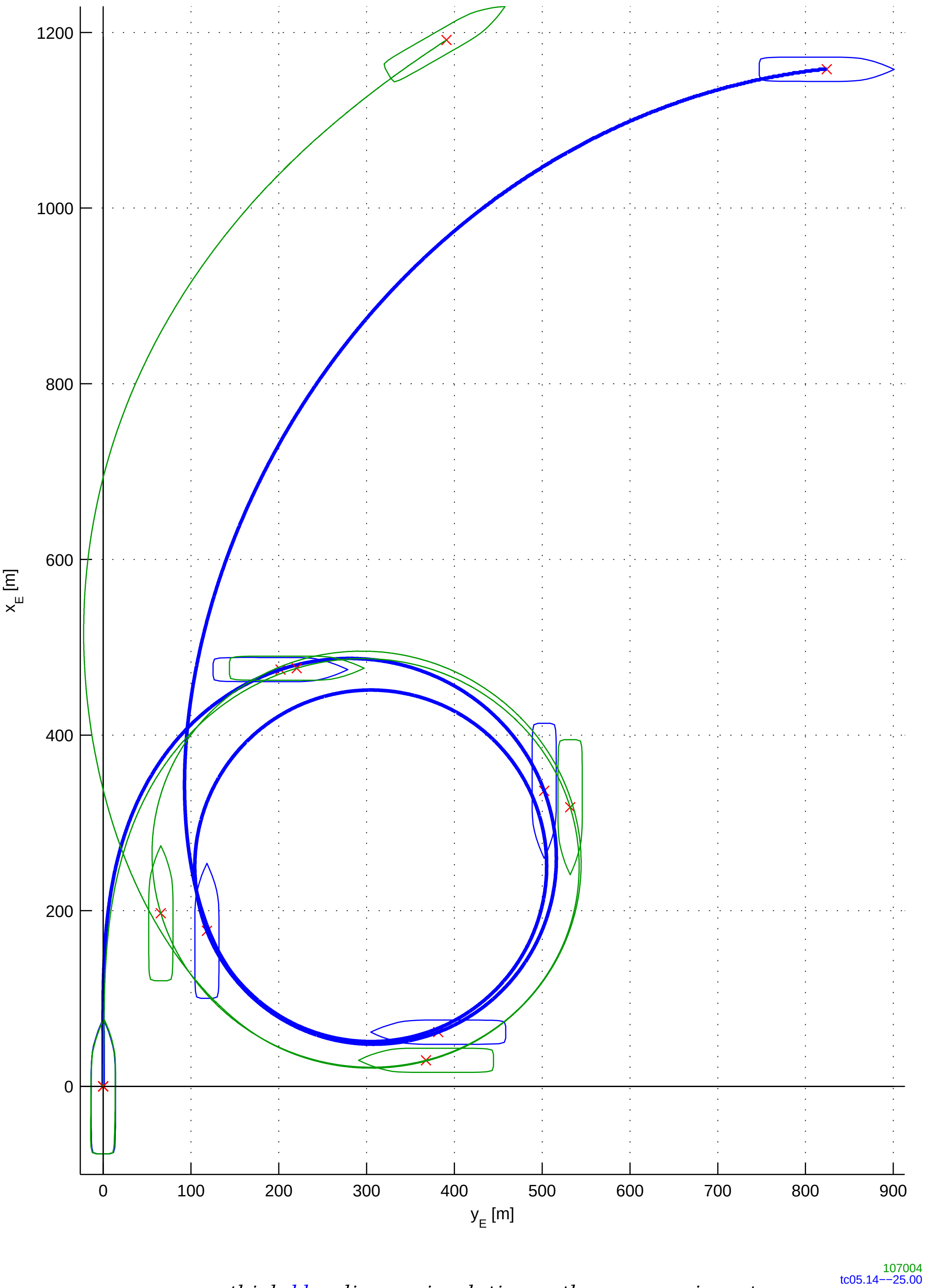

thick blue lines: simulation, others: experiments

TURNING CIRCLE 15° PS, V_0 = 10 kn, TIMESERIES

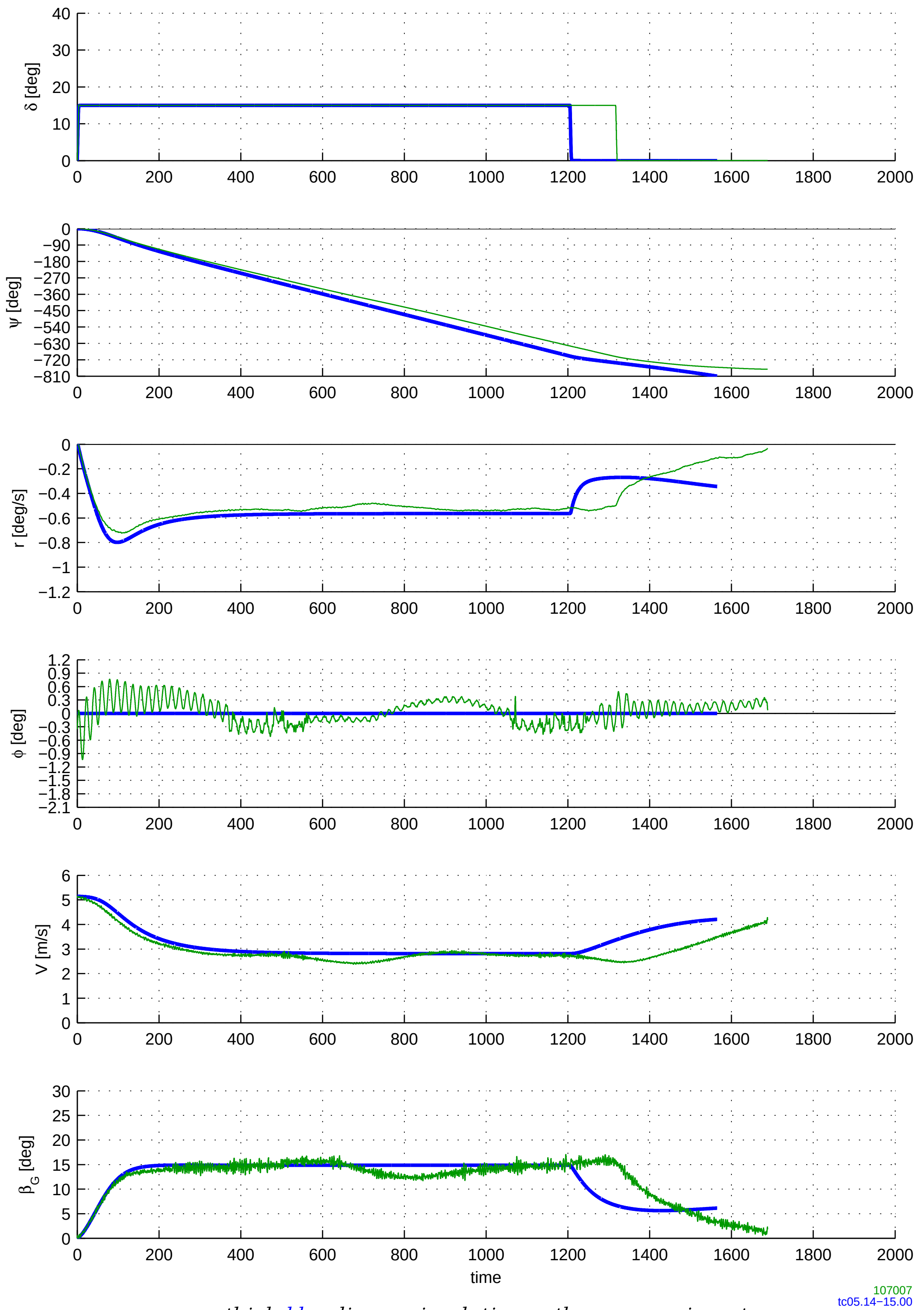

thick blue lines: simulation, others: experiments

TURNING CIRCLE 15° PS, $V_0 = 10$ kn, TRACK

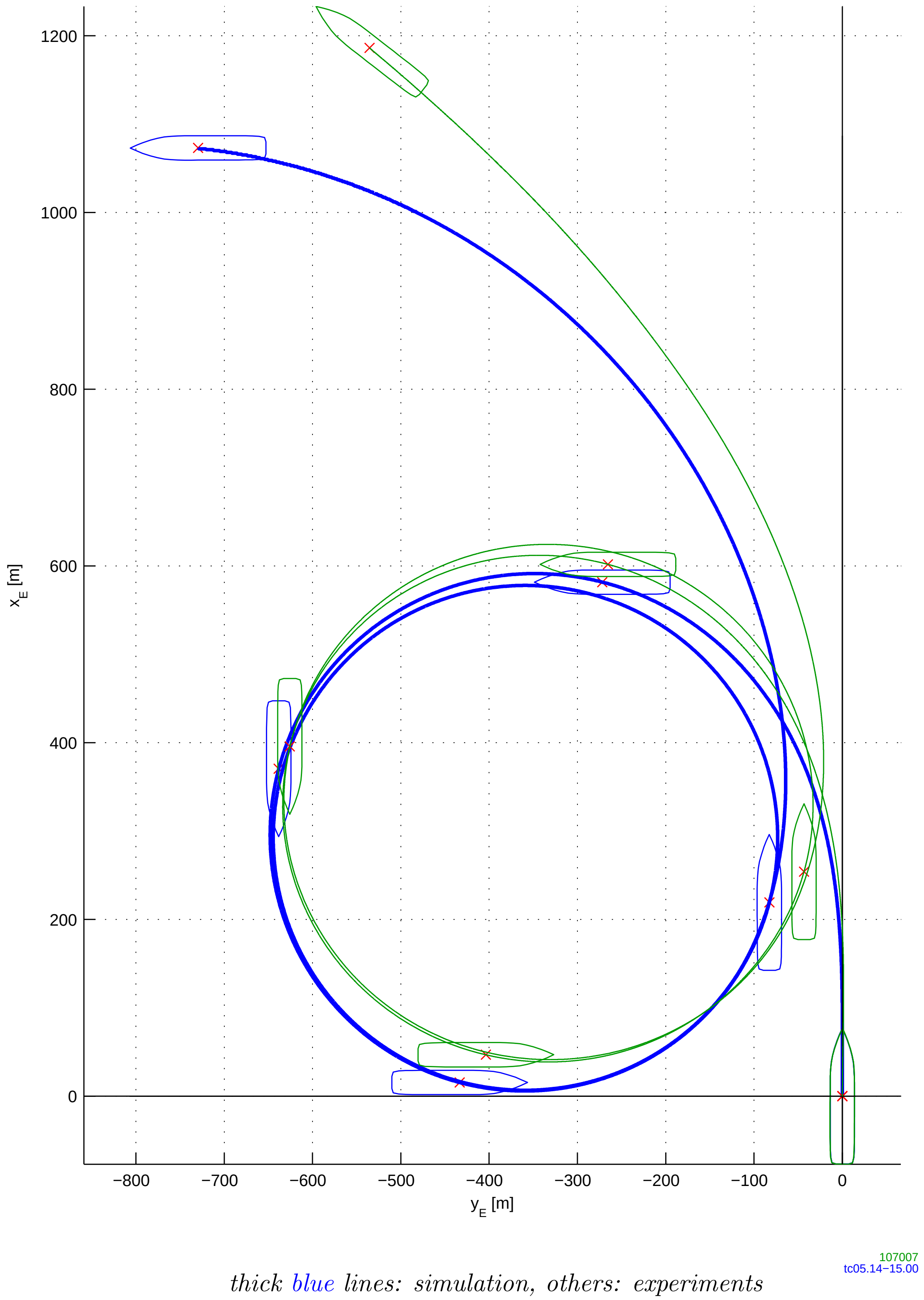

thick blue lines: simulation, others: experiments

TURNING CIRCLE 15° SB, V_0 = 10 kn, TIMESERIES

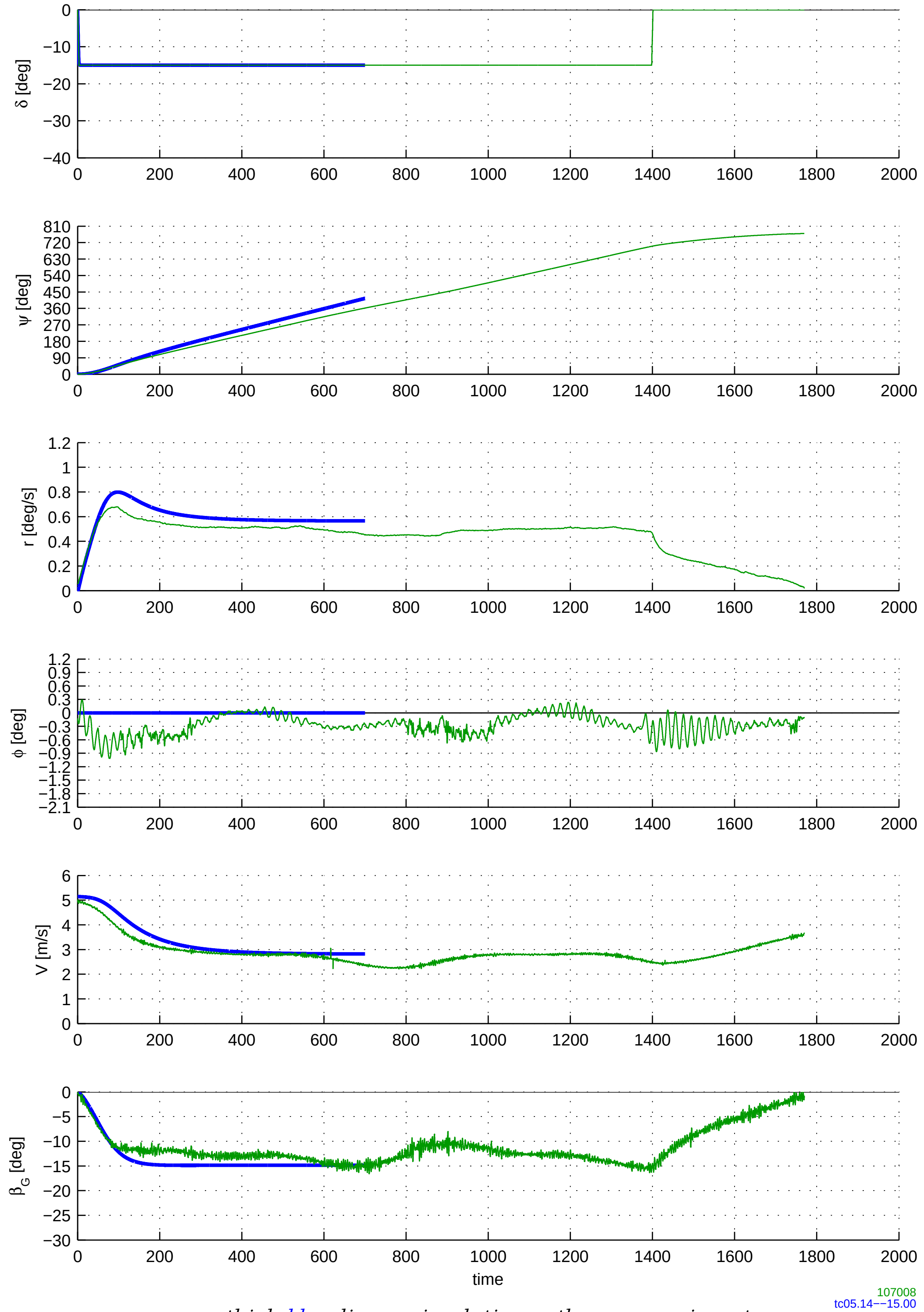

thick blue lines: simulation, others: experiments

TURNING CIRCLE 15° SB, V_0 = 10 kn, TRACK

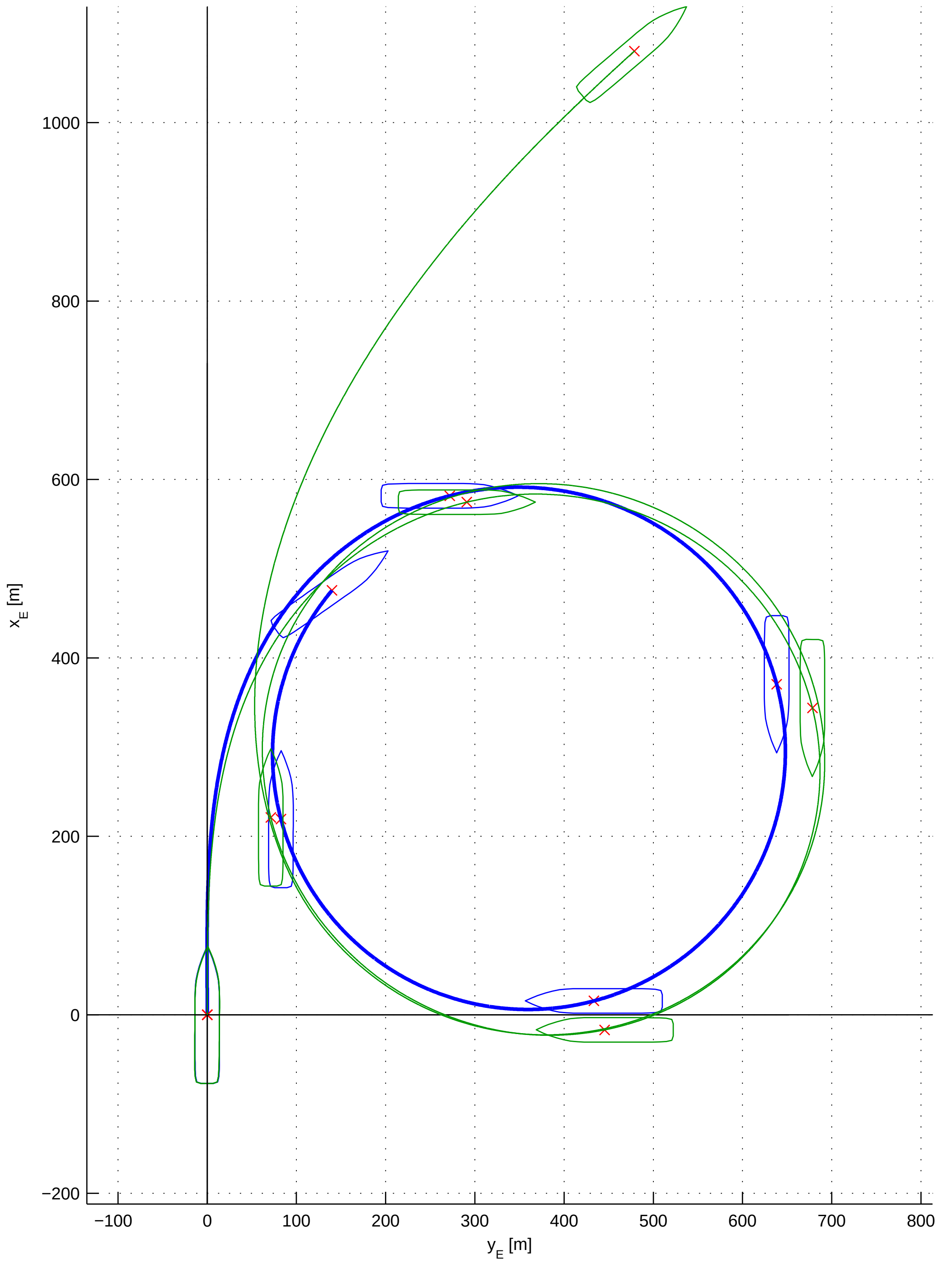

thick blue lines: simulation, others: experiments

TURNING CIRCLE 35° PS, V_0 = 18 kn, TIMESERIES

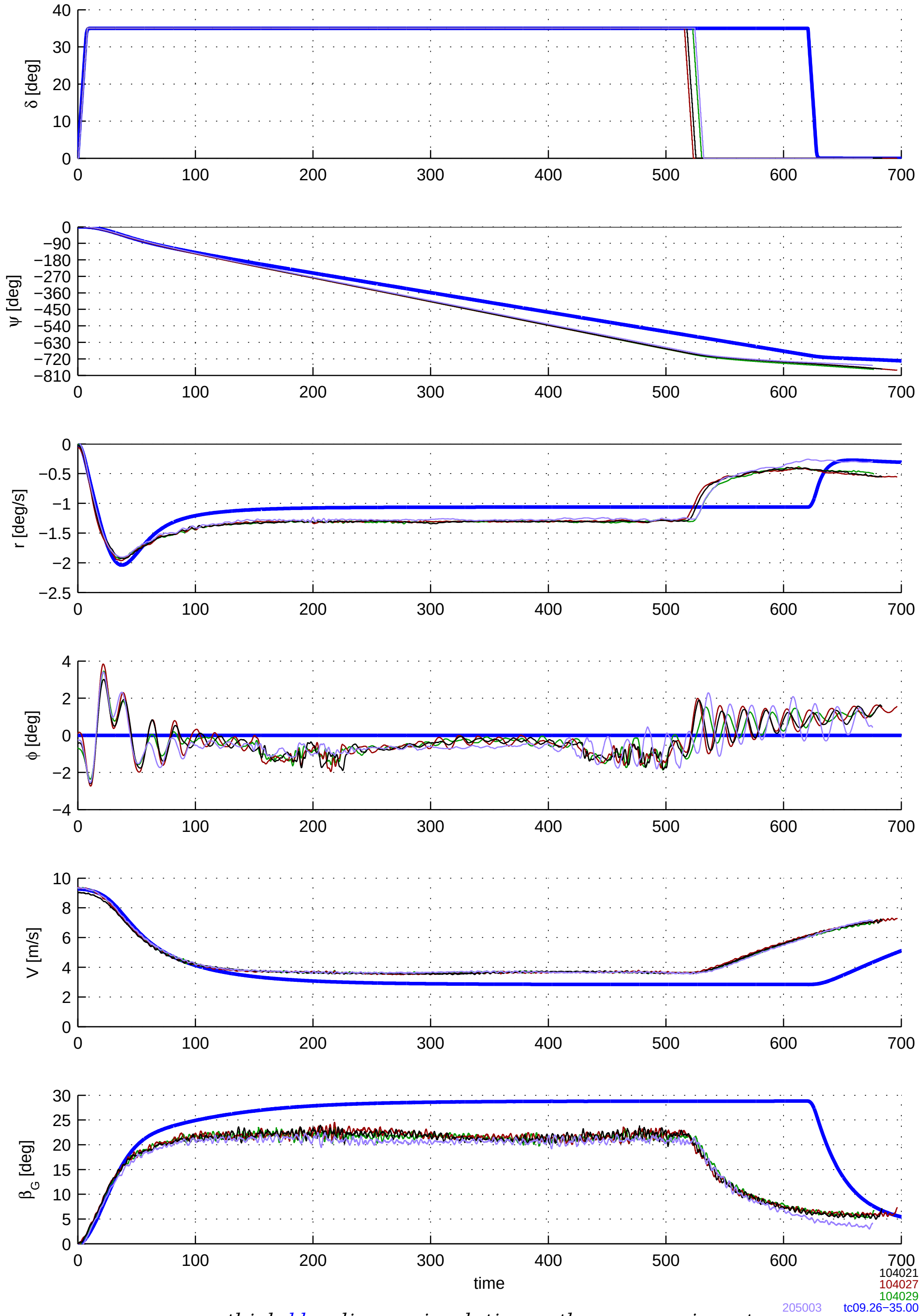

thick blue lines: simulation, others: experiments

TURNING CIRCLE 35° PS, V_0 = 18 kn, TRACK

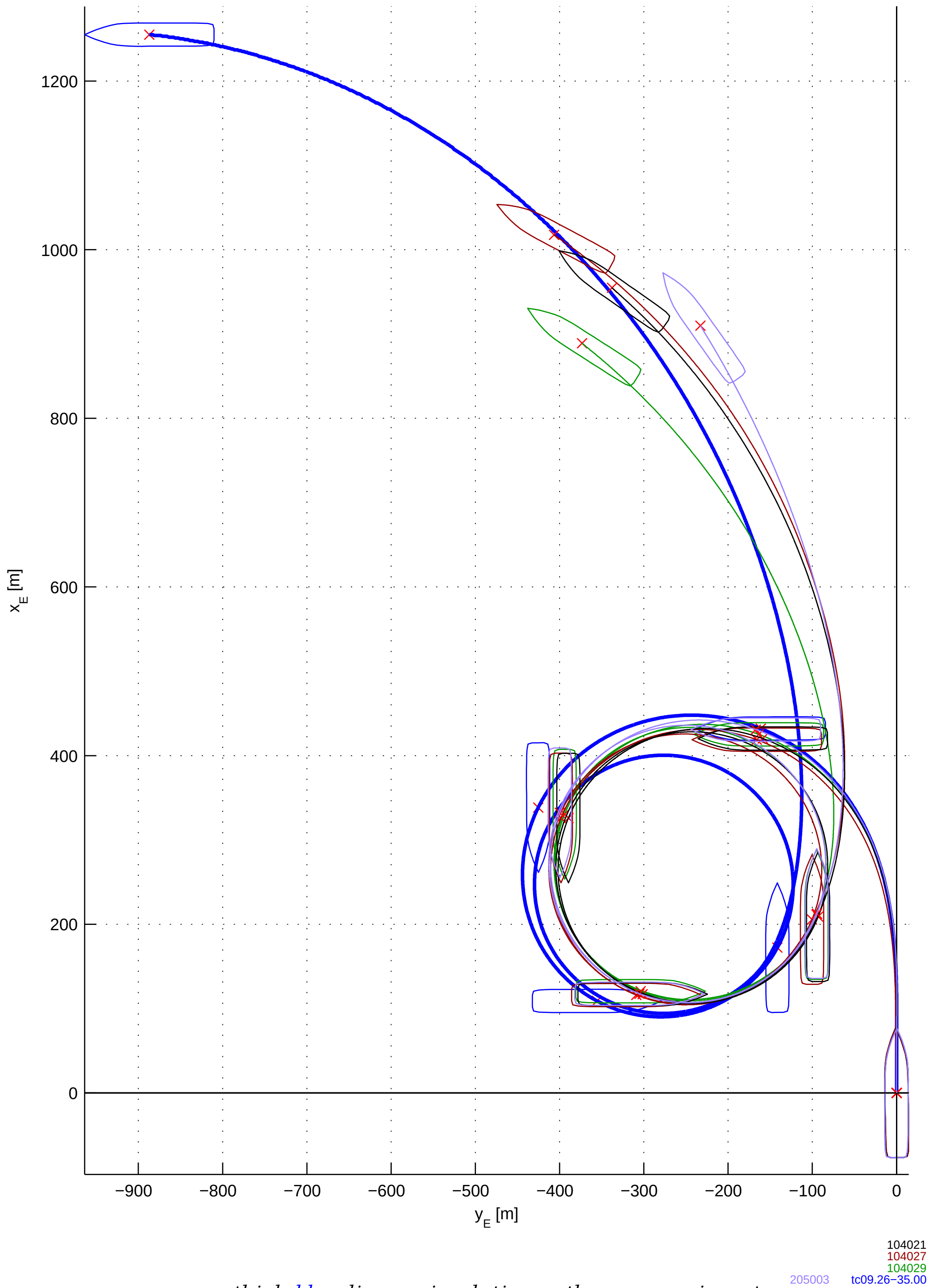

thick blue lines: simulation, others: experiments

TURNING CIRCLE 35° SB, V_0 = 18 kn, TIMESERIES

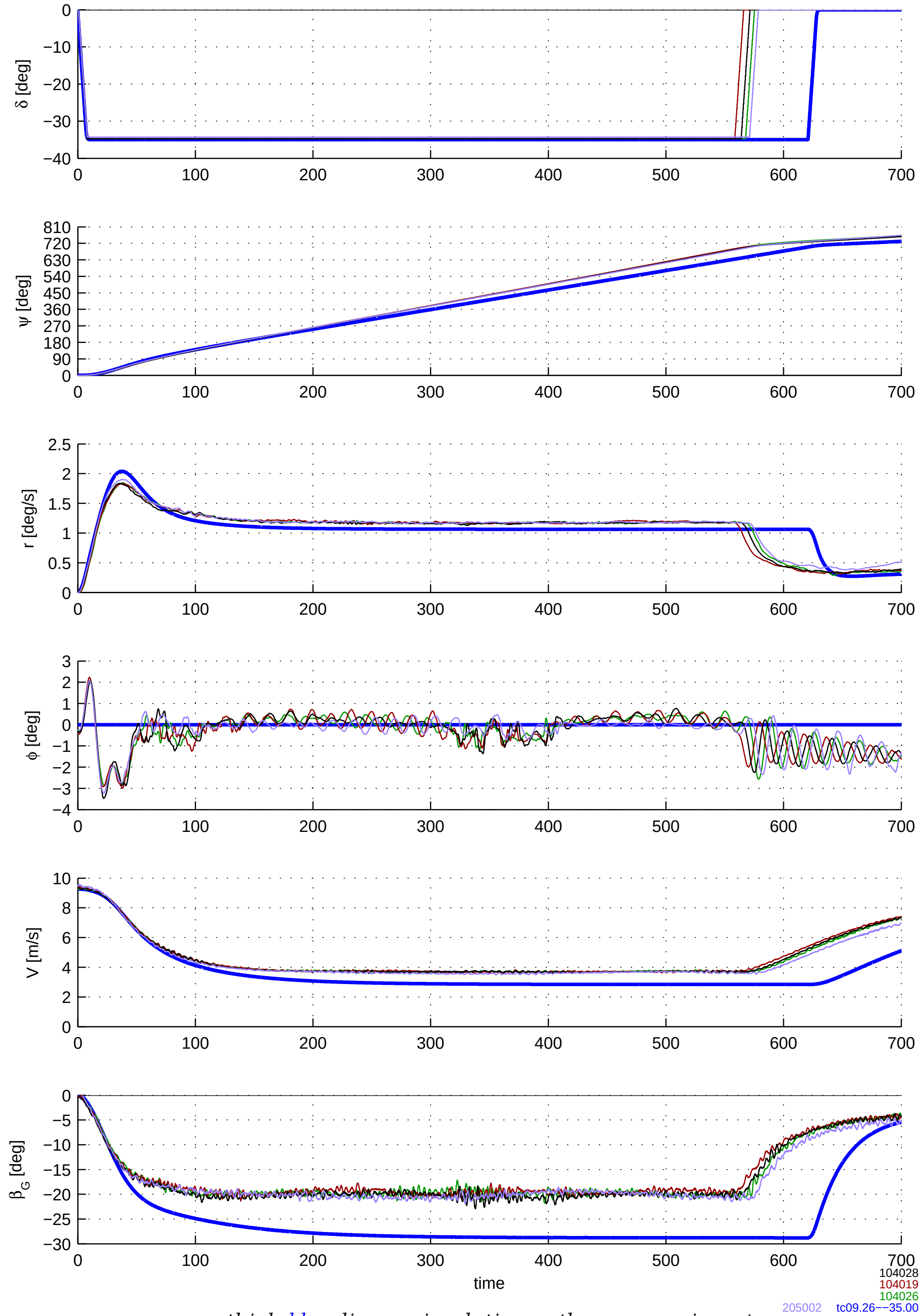

thick blue lines: simulation, others: experiments

TURNING CIRCLE 35° SB, V_0 = 18 kn, TRACK

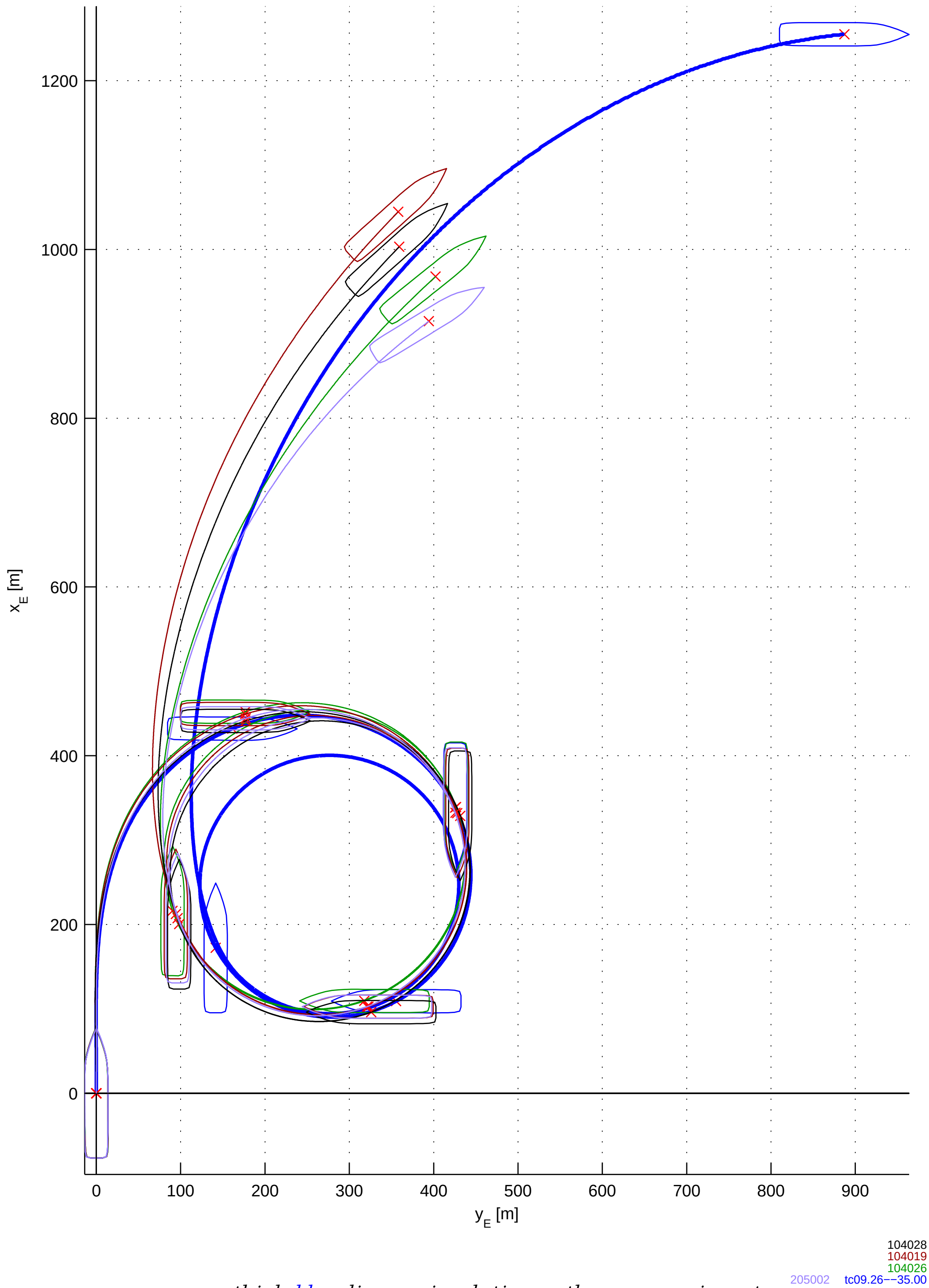

thick blue lines: simulation, others: experiments

TURNING CIRCLE 25° PS, V_0 = 18 kn, TIMESERIES

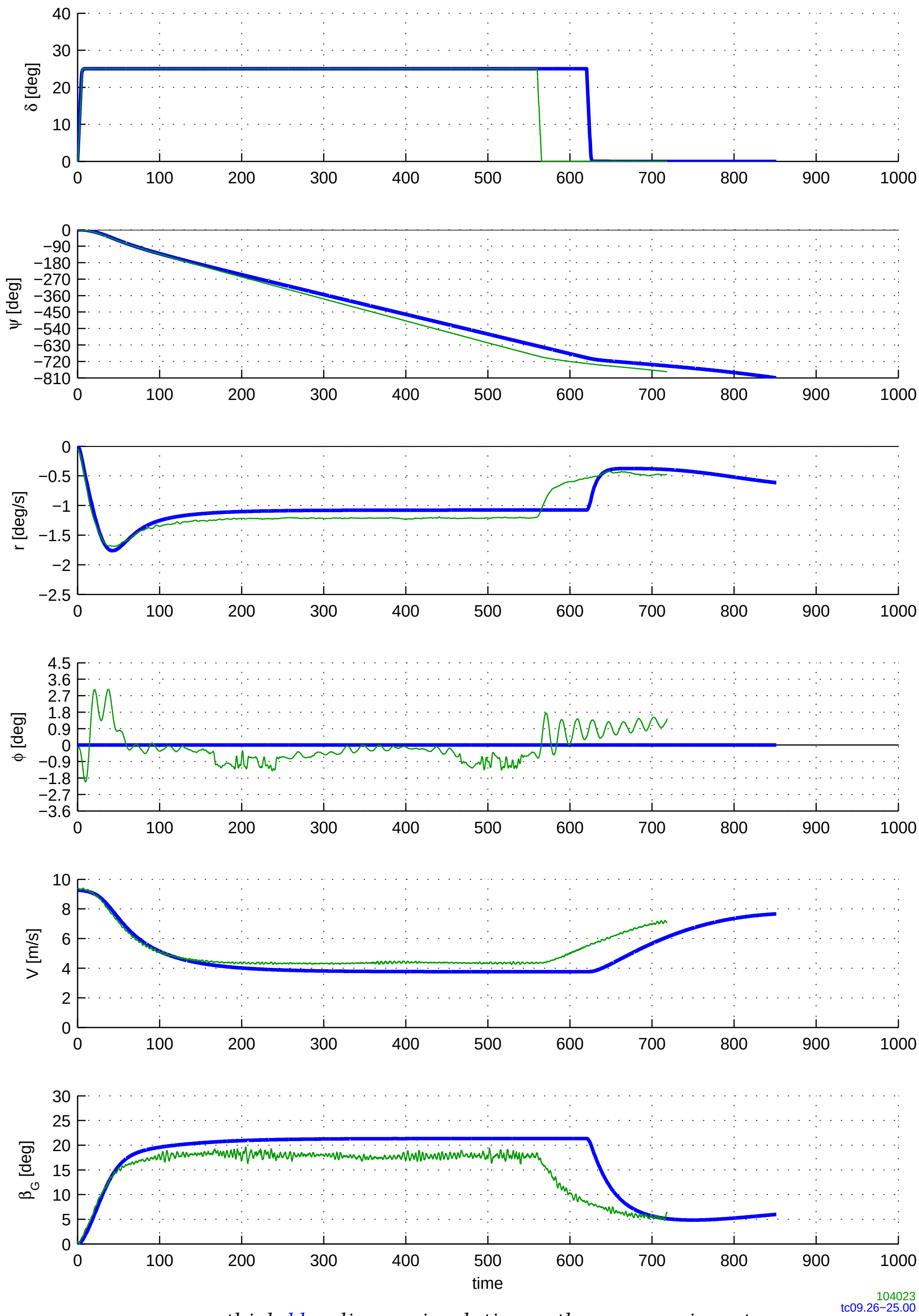

thick blue lines: simulation, others: experiments

TURNING CIRCLE 25° PS, $V_0 = 18$ kn, TRACK

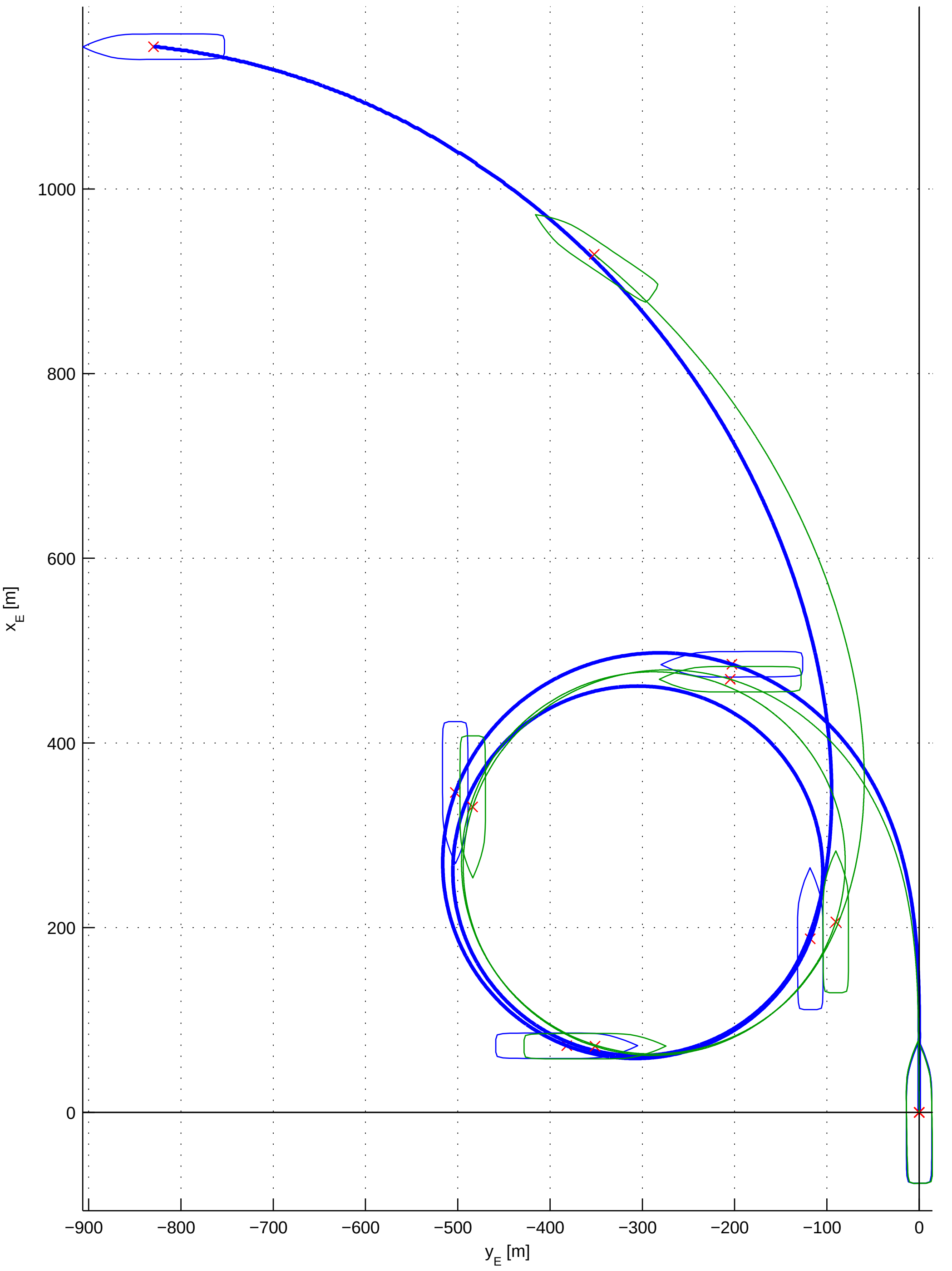

thick blue lines: simulation, others: experiments

TURNING CIRCLE 25° SB, V_0 = 18 kn, TIMESERIES

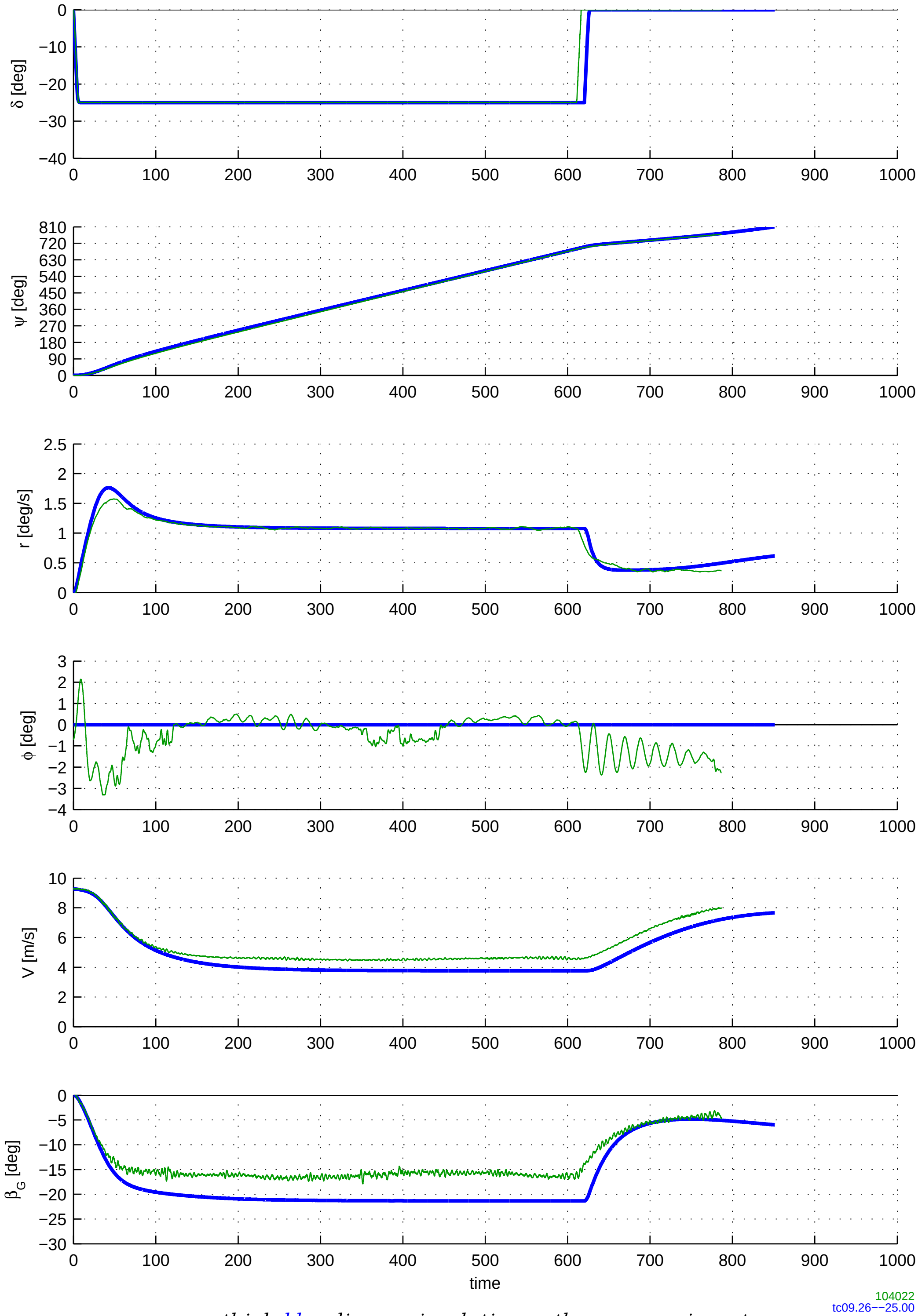

thick blue lines: simulation, others: experiments

TURNING CIRCLE 25° SB, V_0 = 18 kn, TRACK

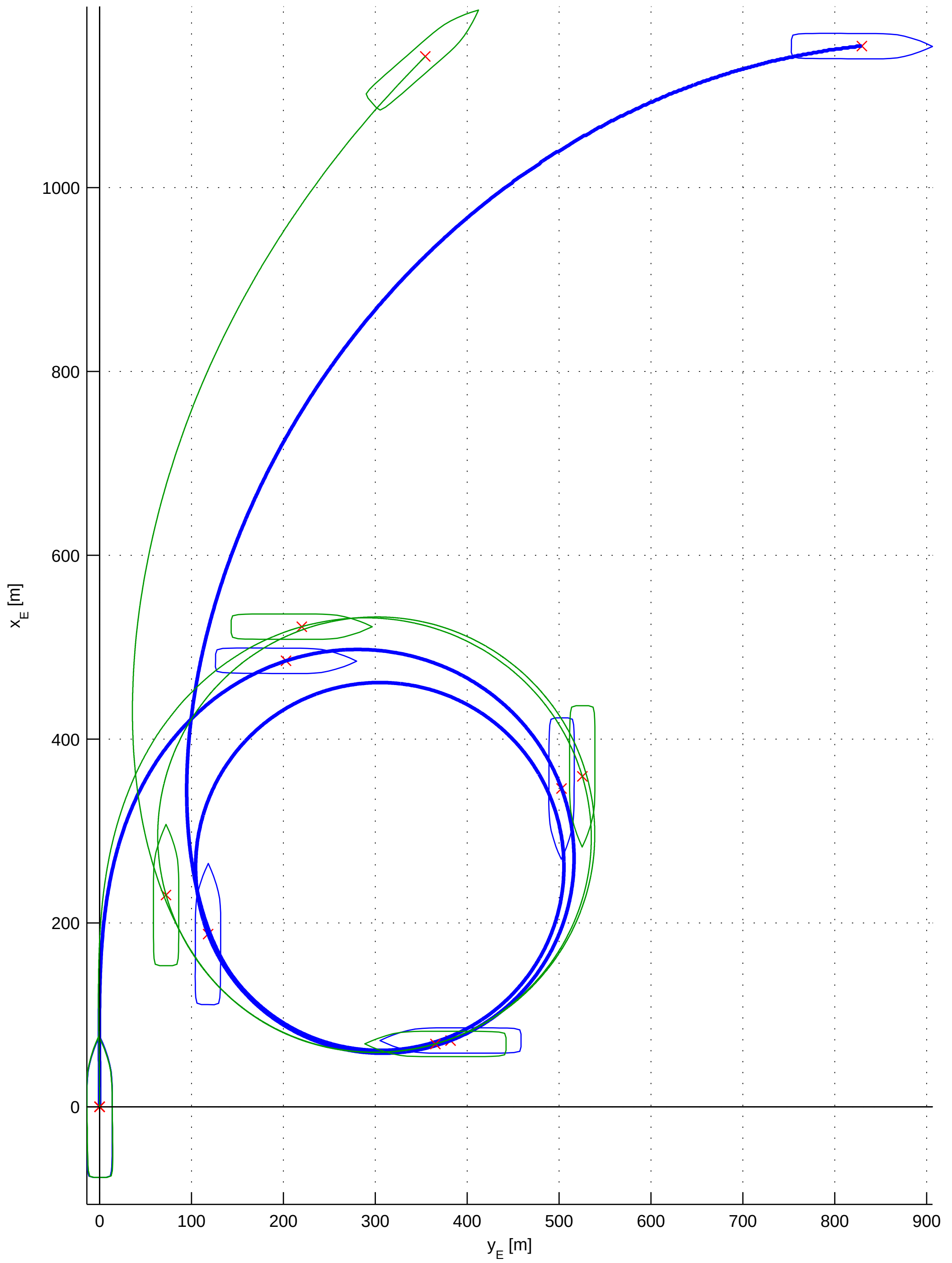

thick blue lines: simulation, others: experiments

TURNING CIRCLE 15° PS, V_0 = 18 kn, TIMESERIES

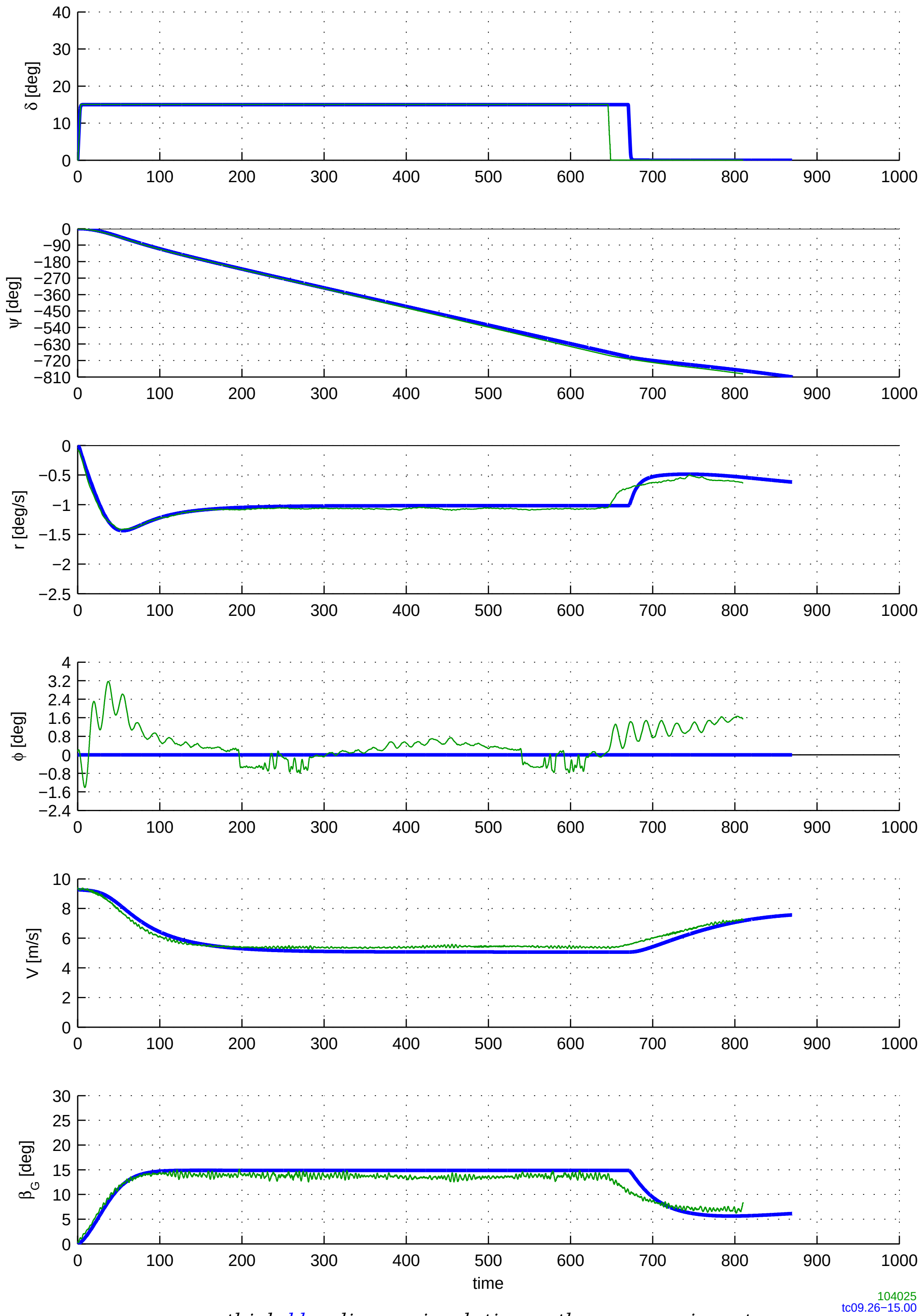

thick blue lines: simulation, others: experiments

TURNING CIRCLE 15° PS, $V_0 = 18$ kn, TRACK

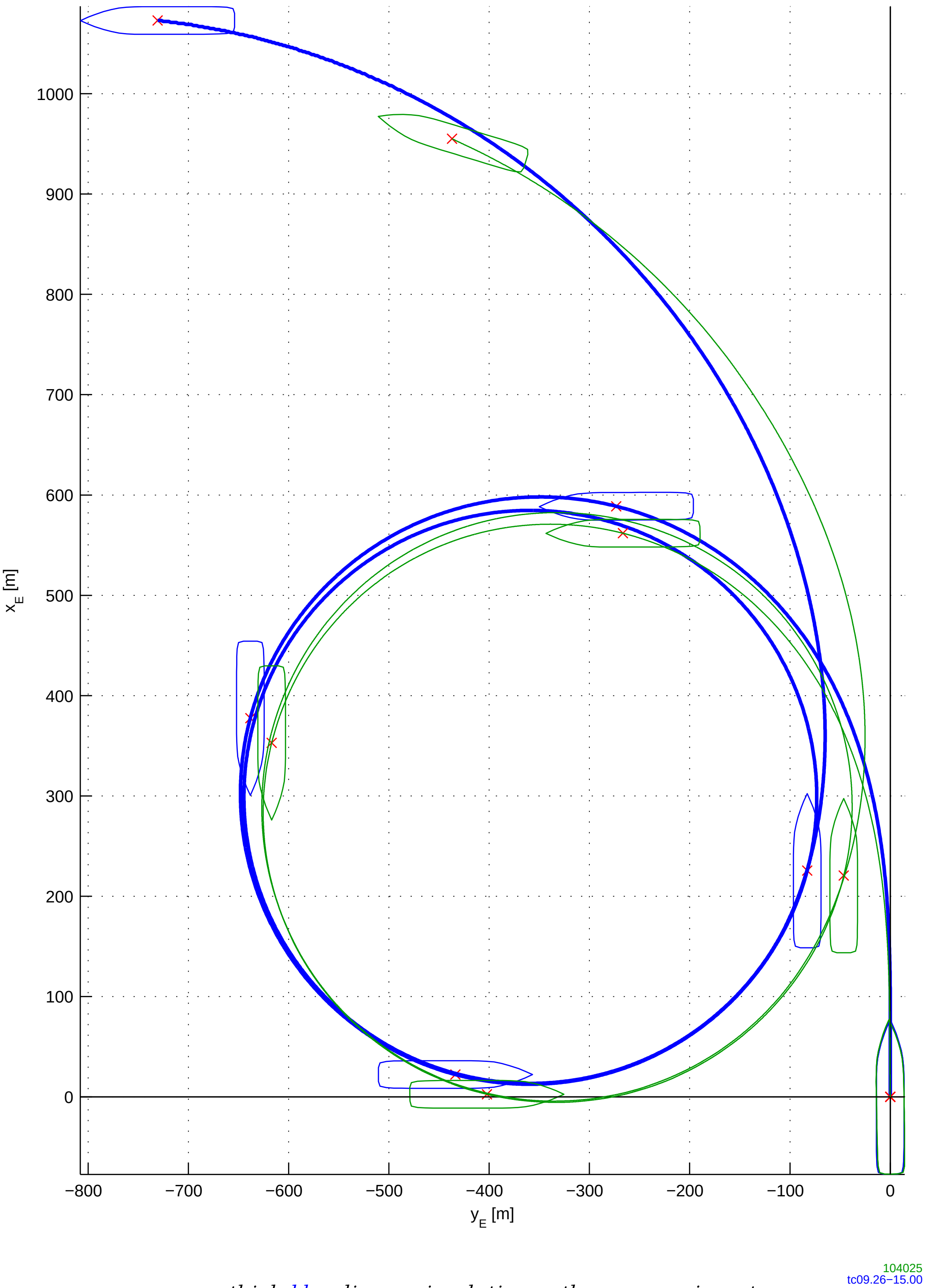

thick blue lines: simulation, others: experiments

TURNING CIRCLE 15° SB, V_0 = 18 kn, TIMESERIES

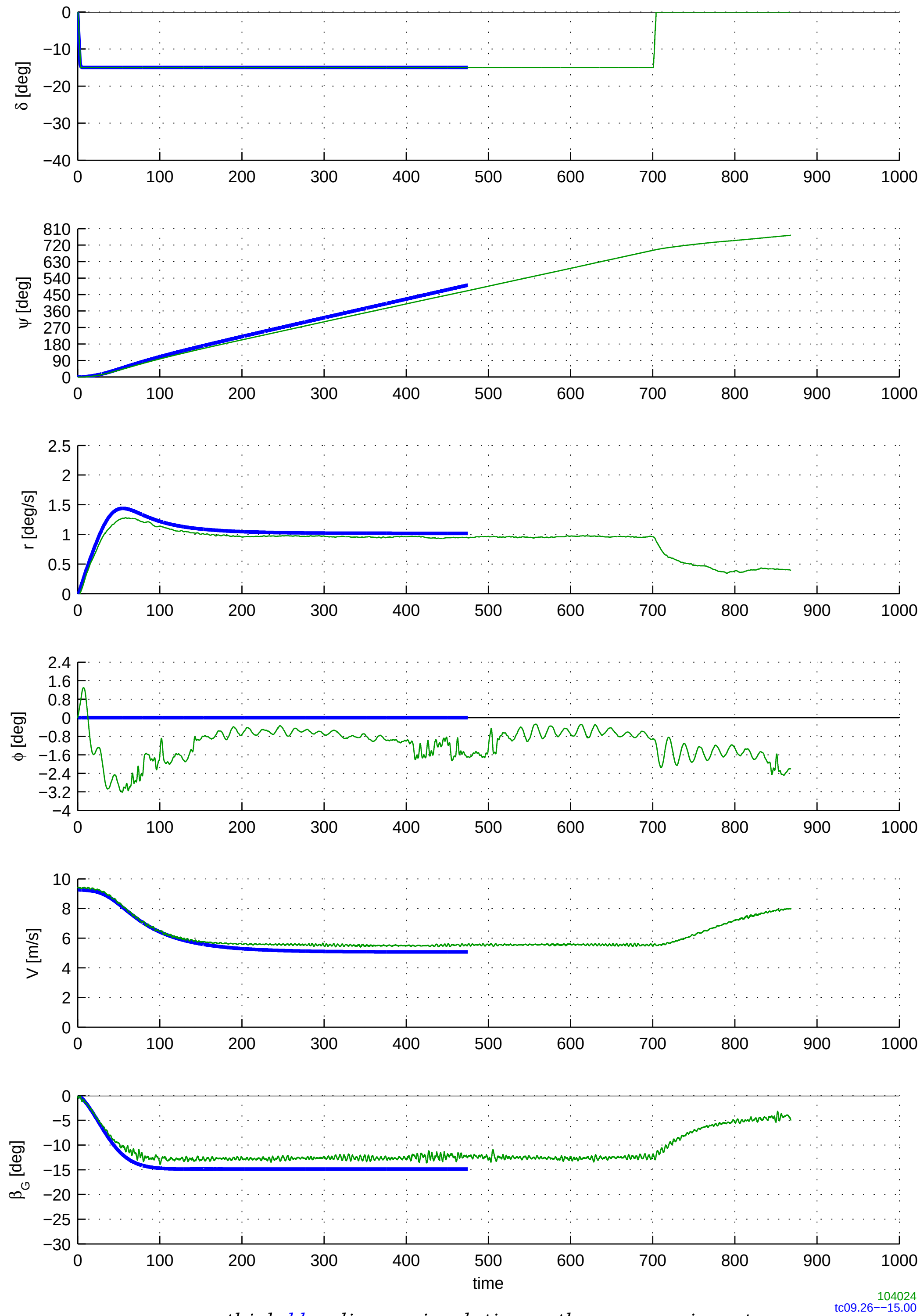

thick blue lines: simulation, others: experiments

TURNING CIRCLE 15° SB, $V_0 = 18$ kn, TRACK

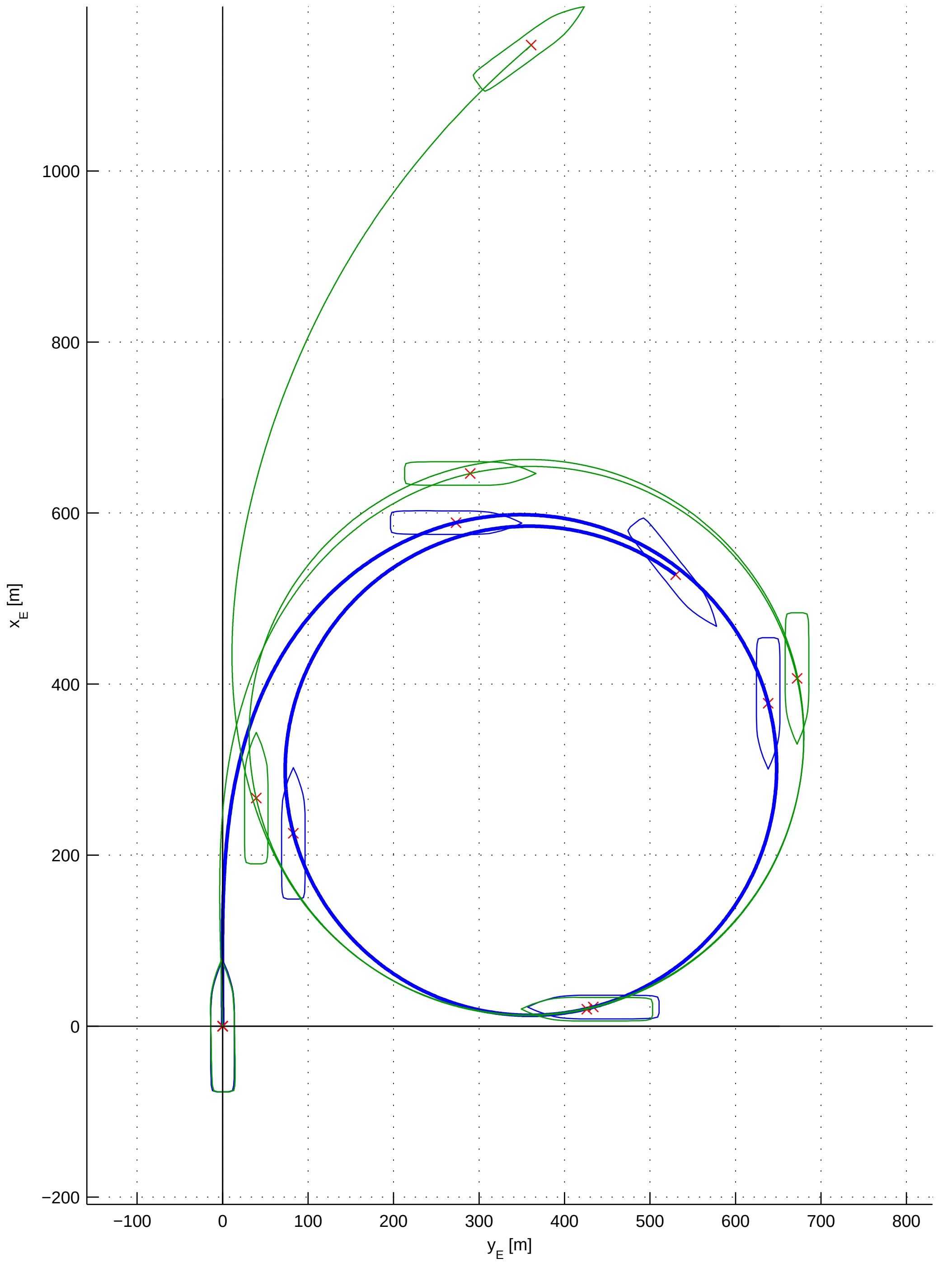

thick blue lines: simulation, others: experiments

The present work was initiated in order to improve traditional manoeuvring simulations based on empirical equations to model the forces and moments on the ship. With the evolution of the capability of viscous-flow solvers to predict forces and moments on ships, it was decided to develop a practical method to simulate the manoeuvrability of ships in which viscous-flow solvers are utilised and to investigate whether this improves the accuracy of manoeuvring predictions.

In this thesis, it is demonstrated that good predictions of the loads on the hull in manoeuvring motion can be obtained for a wide range of ship types. The trends in the forces and moments as a function of the drift angle or yaw rate are simulated well.

By using hydrodynamic manoeuvring coefficients derived from the CFD calculations, it is shown that it is possible to improve the prediction of ship manoeuvres compared to predictions using coefficients based on empirical equations. A considerable improvement in the turning circle predictions was obtained. The prediction of the yaw checking and course keeping and initial turning abilities based on zig-zag simulations improved as well, but further improvements are required for more reliable assessment of the manoeuvring performance.